



Study of the internal structure of the proton with the PANDA experiment at FAIR

Alaa Dbeyssi

► To cite this version:

Alaa Dbeyssi. Study of the internal structure of the proton with the PANDA experiment at FAIR. Other [cond-mat.other]. Université Paris Sud - Paris XI, 2013. English. NNT : 2013PA112180 . tel-00906761

HAL Id: tel-00906761

<https://theses.hal.science/tel-00906761>

Submitted on 16 Dec 2013

HAL is a multi-disciplinary open access archive for the deposit and dissemination of scientific research documents, whether they are published or not. The documents may come from teaching and research institutions in France or abroad, or from public or private research centers.

L'archive ouverte pluridisciplinaire **HAL**, est destinée au dépôt et à la diffusion de documents scientifiques de niveau recherche, publiés ou non, émanant des établissements d'enseignement et de recherche français ou étrangers, des laboratoires publics ou privés.



27 Septembre 2013

IPNO-T-13-04

Thèse

Présentée par

DBEYSSI Alaa

*Pour obtenir le grade de Docteur ès Sciences
De l'Université Paris Sud*

**Study of the internal structure of the proton with
the PANDA experiment at FAIR**



École Doctorale 517-PNC

Study of the internal structure of the proton with the PANDA experiment at FAIR

Thesis submitted for the degree of
Doctor of Philosophy (Nuclear Physics)
by

Alaa Dbeyssi

(Lebanese CNRS scholar)

Defended on September 27th 2013, in front of the jury:

President	T. SUOMIJARVI	IPNO, Paris-Sud
Examiner	P. GIANOTTI	INFN Frascati
Referee	M. GUIDAL	IPNO, Paris-Sud
Examiner	D. MARCHAND	IPNO, Paris-Sud
Examiner	J. RITMAN	FZ Jülich
Thesis advisor	E. TOMASI-GUSTAFSSON	IPNO, Paris-Sud
Referee	E. VOUTIER	LPSC Grenoble
Examiner	H. ZARAKET	Lebanese University

Remerciements

Ce travail de thèse s'est effectué dans le cadre d'une bourse du CNRS Liban, au sein de la collaboration PANDA à l'Institut de Physique Nucléaire d'Orsay. J'adresse mes remerciements à tous qui, par leur aide et leur soutien, ont contribué à la réalisation de ce travail.

En premier lieu, je remercie Dominique Guillemaud-Mueller, Faïçal Azaiez, Bernard Berthier, Jacques Guillot et Fadi Ibrahim de m'avoir accueilli au sein de l'Institut de Physique Nucléaire d'Orsay.

Je remercie les membres du jury de ma thèse, T. Suomijarvi, P. Gianotti, M. Guidal, D. Marchand, J. Ritman, E. Tomasi-Gustafsson, E. Voutier et H. Zaraket pour l'intérêt qu'ils ont porté à mon travail et pour leur disponibilité.

Je remercie ma directrice de thèse Egle Tomasi-Gustafsson pour son aide précieuse et sa disponibilité tout au long de ma thèse. Le travail avec une directrice de thèse comme Egle, avec ses qualités humains et son efficacité scientifique, a été très enrichissant pour moi. Je tiens également à remercier Mme Dominique Marchand, pour son aide depuis mon arrivé en France, pour son soutien, ses précieux conseils et pour le grand soin qu'elle m'a apporté à la correction de mon manuscrit. Elle m'a beaucoup aidé comme étant aussi la directrice de ma thèse.

Durant ces trois années, j'étais accueilli au sein du groupe PANDA de l'IPNO dirigé par T. Hennino et composé par B. Ramstein, R. Kunne, J. Van De Wiele, S. Ong, J. Boucher et B. Ma que je remercie beaucoup pour m'avoir soutenu, écouté et conseillé tout au long de la thèse. Je remercie la collaboration PANDA pour leur accueil.

J'adresse mes sincères remerciements à mes collaborateurs qui ont largement aidé à réaliser le travail présenté dans ce manuscrit. Le travail phénoménologique s'est effectué dans le cadre d'une collaboration avec professeurs E. A. Kuraev, G. I. Gakh et M. Konchatnyi. Les tests du couplage optique ont pu être effectués grâce à l'aide apportée par le service R&D détecteurs de l'IPNO, Mme Marie-Laure Boillot à l'ICMMO, et V. Dormenev à Giessen. M. Gumberidze a pris le temps de répondre à mes questions et résoudre les problèmes rencontrés dans la partie simulation avec PANDARoot.

Merci à toute l'équipe du service informatique et en particulier à Christophe Diarra pour le travail sur la grille de l'IPNO. Merci aussi à Monique, Sylvie et Annie.

Je remercie B. Tatischeff pour les discussions intéressantes que nous avons eues à l'heure du déjeuner.

Mes profondes remerciements à ma famille, mes amis et les gens de mon village "Deir Kouché" pour leurs soutiens et leurs encouragements.

Abstract

The proton is a bound state of quarks which are held together by the strong force, mediated by gluons. The understanding of the proton structure is presently one of the central issues in hadron physics. The present work reports on phenomenological and experimental studies related to the possibilities offered by the future antiproton beam at the FAIR facility at Darmstadt, in the momentum range between 1.5 and 15 GeV/c. After a classification of the reaction channels which are accessible in antiproton-proton annihilation, the main features of the PANDA detector are described. A chapter of this thesis is dedicated to the study of the optical coupling between crystals and photo-diodes in the electromagnetic calorimeter, which will be operated at low temperature (-25° C). Mechanical, thermal, optical properties and radiation hardness of two commercial glues are quantified.

Feasibility studies of the reaction $\bar{p}p \rightarrow e^+e^-$ for the Time-Like proton form factor measurements at PANDA are presented. The electromagnetic structure of the proton is parametrized in terms of electric G_E and magnetic G_M form factors. The electromagnetic interaction is well described by the theory of quantum electrodynamics. The traditional tool to determine proton electromagnetic form factors is polarized and unpolarized electron-proton elastic scattering, assuming that the interaction occurs through the exchange of one virtual photon. The crossed symmetry channels $\bar{p}p \leftrightarrow e^+e^-$ allow to access the Time-Like region. The background reactions are also studied, in particular the $\bar{p}p \rightarrow \pi^+\pi^-$ channel. The results obtained from a realistic Monte Carlo simulation using PANDARoot show that the proton form factor ratio can be measured at PANDA with unprecedented accuracy. The effects of radiative corrections due to real and virtual photon emission are considered.

Based on a model independent formalism, the calculation of the experimental observables for the $\bar{p}p \rightarrow e^+e^-$ reaction is extended to the annihilation into a heavy lepton pair which carries the same physical information on the proton structure as the electrons. In this case, the lepton mass can not be neglected. The same formalism is also applied in Space-Like region to the elastic scattering of protons from electrons at rest (pe -inverse kinematics). We suggest that the elastic pe scattering can be used to polarize and/or to measure the polarization of high energy proton (antiproton) beams, and allows a precise measurement of the proton charge radius.

Résumé

Le proton est un état lié de quarks qui sont maintenus ensemble par l'interaction forte dont les médiateurs sont les gluons. La compréhension de la structure du proton est actuellement l'une des questions centrales de la physique hadronique. Le présent travail rend compte des études phénoménologiques et expérimentales reliées aux possibilités offertes par le faisceau d'antiprotons qui sera disponible au futur complexe accélérateur FAIR à Darmstadt, dans la gamme d'impulsion entre 1.5 et 15 GeV/c. Après une classification des réactions qui sont accessibles dans l'annihilation proton-antiproton, les caractéristiques principales du détecteur PANDA sont décrites. Un chapitre de cette thèse est consacré à l'étude du couplage optique entre les cristaux et les photo-diodes du calorimètre électromagnétique, qui sera exploité à basse température (-25° C). Les propriétés mécaniques, thermiques, optiques et la résistance aux radiations de deux colles commerciales sont quantifiées.

Des études de faisabilité de la réaction $\bar{p}p \rightarrow e^+e^-$ pour la mesure des facteurs de forme du proton dans la région temps à PANDA sont présentées. La structure électromagnétique du proton est paramétrisée par ses facteurs de forme électrique G_E et magnétique G_M . L'interaction électromagnétique est bien décrite par la théorie de l'électrodynamique quantique. L'outil usuel pour déterminer les facteurs de forme électromagnétiques du proton est la diffusion élastique électron-proton polarisée et non polarisée, sous l'hypothèse que l'interaction se produit par l'échange d'un seul photon virtuel. La réaction croisée $\bar{p}p \rightarrow e^+e^-$ permet d'accéder à la région temps. Les réactions du bruit de fond sont également étudiées, en particulier la réaction $\bar{p}p \rightarrow \pi^+\pi^-$. Les résultats obtenus à partir d'une simulation Monte Carlo réaliste en utilisant le logiciel PANDARoot montre que le rapport des facteurs de forme du proton peut être mesuré à PANDA avec une précision sans précédent. Les effets des corrections radiatives dus à l'émission de photons réels et virtuels sont considérés.

Basé sur un formalisme modèle indépendant, le calcul des observables expérimentales pour la réaction $\bar{p}p \rightarrow e^+e^-$ est étendue à l'annihilation en une paire de leptons lourds qui porte la même information physique sur la structure du proton que les électrons. Dans ce cas, la masse du lepton ne peut pas être négligée. Le même formalisme est également appliqué dans la région espace à la diffusion élastique des protons par des électrons au repos (cinématique inverse). La diffusion pe -élastique puisse être utilisée pour polariser et/ou mesurer la polarisation des faisceaux de protons (antiprotons) de haute énergie, et elle permette également de mesurer le rayon de charge du proton.

Contents

1	Introduction	1
2	Physics with antiproton beams	5
2.1	Introduction	5
2.2	The Facility for Antiproton and Ion research at Darmstadt	7
2.3	The PANDA Experiment	8
2.4	Quark model	9
2.4.1	Hadrons in the quark model	9
2.4.2	Exotic hadrons	10
2.4.3	The $\bar{p}p$ system	11
2.5	Antiproton proton annihilation: the PANDA physics program	11
2.5.1	Total and elastic cross section	12
2.5.2	Production of light mesons	13
2.5.2.1	Total cross sections of light meson production	14
2.5.2.2	Probability of n pion production	16
2.5.2.3	$\pi^+\pi^-$ and K^+K^- channels	18
2.5.3	Production of charmonium and charmed mesons	19
2.5.4	Production of strange and charmed baryons	21
2.5.5	Electromagnetic processes and hadronic background	22
2.5.6	Other topics	24
3	Electromagnetic Form Factors of the proton	27
3.1	The concept of hadron electromagnetic form factors	27
3.1.1	Extension to a composite targets	28
3.1.2	Charge radius	29
3.1.3	Rosenbluth formula: magnetic contribution	30
3.2	Proton electromagnetic form factors	31
3.2.1	Model independent description	31
3.2.1.1	Space- and Time-Like region connection	34
3.2.1.2	The Sachs form factors	34
3.2.1.3	Boundary and asymptotic behavior	35
3.2.2	Experimental measurements of the electromagnetic proton form factors	35

CONTENTS

3.2.2.1	Data in Space-Like region	35
3.2.2.2	Data in Time-Like region	37
3.2.2.3	Unphysical region	39
3.2.3	Parametrizations of the proton form factors	40
3.2.3.1	Vector meson dominance model	40
3.2.3.2	Spin one hadrons, VMD inspired model	42
3.2.3.3	Perturbative QCD parametrization	43
3.2.4	General description in TL region	44
4	The PANDA detector setup	47
4.1	The targets	47
4.2	The magnets	48
4.3	Tracking System	49
4.4	Particle IDentification	52
4.5	Electromagnetic Calorimetry	53
4.5.1	Principles	53
4.5.2	Design and geometry	55
5	Tests of optical glues for the PANDA Electromagnetic Calorimeter	57
5.1	Thermal tests	58
5.2	Mechanical tests	60
5.3	Optical tests: transmittance measurements	61
5.4	Radiation hardness test	64
5.4.1	Gamma irradiation tests	65
5.4.2	Proton irradiation tests	66
5.5	Conclusion	66
6	Feasibility studies of proton form factor measurements at PANDA	69
6.1	Kinematics	70
6.2	Cross section and counting rate	71
6.3	PANDARoot software	72
6.3.1	Event generator	73
6.3.2	Digitization	73
6.3.3	Reconstruction	73
6.3.4	Particle IDentification	74
6.4	Simulation of the signal and the background	77
6.4.1	Monte Carlo parameters	77
6.4.2	Analysis	78
6.4.3	PID probability and kinematical Cuts	85
6.5	Expected statistical error on the proton FF ratio	85
6.5.1	Experimental observables	87
6.5.2	Extraction of the signal efficiency	87
6.5.3	Physical events	89

6.5.4	Normalization: observed events	90
6.5.5	Efficiency correction and fit	90
6.5.6	Error from the angular cut	91
6.6	Conclusion	94
7	QED radiative corrections to $\bar{p}p \rightarrow e^+e^-$ reaction using PHOTOS	95
7.1	PHOTOS	97
7.2	PHOTOS and the first order corrections	97
7.3	PHOTOS in PANDAROOT	98
7.4	Comparison of PHOTOS with analytical calculations	102
7.5	Conclusions	104
8	Elastic proton electron scattering	105
8.1	Kinematics and differential cross section	105
8.2	Proton charge radius	108
8.2.1	Hydrogen spectroscopy	109
8.2.2	Muonic hydrogen spectroscopy	109
8.2.3	Electron proton scattering	110
8.2.4	Proton charge radius measurement with pe elastic scattering . .	110
8.3	Polarization of high energy (anti)proton beams	113
8.4	Polarization transfer coefficients, T_{ij} , in the $p + \vec{e} \rightarrow \vec{p} + e$ reaction . .	114
8.5	High energy polarimetry	117
8.6	Polarization correlation coefficients, C_{ij} , in the $\vec{p} + \vec{e} \rightarrow p + e$ reaction .	117
9	Proton antiproton annihilation into massive leptons	121
9.1	Formalism	122
9.2	Kinematics	123
9.3	Unpolarized cross section in the CMS	124
9.3.1	Single spin observables: the analyzing power	126
9.3.2	Double spin polarization observables	127
9.3.2.1	Polarization transfer coefficients	128
9.3.2.2	Analyzing powers in polarized proton-antiproton collisions	128
9.3.2.3	Correlation coefficients: polarized lepton-antilepton pair	129
9.4	Triple spin polarization observables	130
9.5	Numerical results	131
9.6	Conclusion	134
10	Conclusions and perspectives	137
A	Lepton nucleon interaction: general formalism	141
A.1	The scattering amplitude	141
A.1.1	Leptonic current	142
A.1.2	Hadronic current	142

CONTENTS

A.2	Electromagnetic tensors	143
A.2.1	Leptonic tensor	143
A.2.2	Hadronic tensor	144
A.3	Polarized and unpolarized cross section	145
A.3.1	Polarization transfer coefficients $T_{ab}(S_i, \eta_j)$	145
A.3.2	Polarization correlation coefficients $C_{ab}(S_1, \eta_1)$	146
B	Polarization observables for the elastic proton electron scattering	147
B.1	Polarization transfer coefficients, T_{ij} , for $p + \vec{e} \rightarrow \vec{p} + e$	147
B.2	Polarization correlation coefficients, C_{ij} , for $\vec{p} + \vec{e} \rightarrow p + e$	148
C	Acronyms	149
D	List of publications	151
D.1	Journal Articles	151
D.2	Proceedings	152

List of Figures

2.1	Facility for Antiproton and Ion Research (FAIR, from [14]). The existing GSI facility is represented by the blue color. The planned FAIR facility is plotted in red color.	7
2.2	Total (black) and elastic (red) cross sections for the $\bar{p} + p$ reaction, as a function of the antiproton beam momentum. Data points are from [20], lines are from [23]. The contribution of inelastic events is also shown (green line).	12
2.3	Cross sections for different inelastic channels in the $\bar{p} + p$ reaction as a function of $p_{\bar{p}}$	14
2.4	Cross sections for different annihilation channels in the $\bar{p} + p$ reaction as a function of $p_{\bar{p}}$	15
2.5	Pion multiplicity in $\bar{p} + p$ annihilation as a function of $p_{\bar{p}}$, from Eq. 2.7 (black line) and from Eq. 2.8 (red line).	17
2.6	Probability for the emission of n pions in $\bar{p} + p$ annihilation as a function of pion multiplicity, from Eq. 2.9 for different incident momenta: at rest (red line), $p_{\bar{p}}=5$ GeV (green line), $p_{\bar{p}}=10$ GeV (blue line).	18
2.7	Pion (black circles) and kaons (red circles) cross section in the $\bar{p}p$ reaction as a function of $p_{\bar{p}}$, and their ratio (green circles).	19
2.8	Accessible hadrons with the antiproton beam at FAIR, from [18]. The upper scale displays the antiproton momentum and the lower one the hadron mass.	21
2.9	Factorization of DVCS into a hard part described by perturbative QCD and q soft part described by GPDs.	23
2.10	The diagram for the inverted WACS processes $\bar{p}p \rightarrow \gamma\gamma$ described by GDAs.	23
2.11	Factorization of $\bar{p}p \rightarrow e^+e^-\gamma$ into a hard sub-process and proton to photon transition distribution amplitude (TDA).	24
3.1	Schematic view of elastic scattering on a composite object [53].	28
3.2	Feynman diagram for the elastic electron proton scattering in the Born approximation.	32
3.3	Feynman diagram for the electron positron annihilation into proton antiproton pair.	33

LIST OF FIGURES

3.4	Spectral decomposition of the proton vertex based on the unitarity condition in the time-like region of momentum transfer squared.	33
3.5	Proton electric (left) and magnetic (right) FFs -normalized to one- in the SL region as a function of Q^2 , obtained with the Rosenbluth technique, divided by the dipole function G_D from Ref. [64].	36
3.6	Proton FF ratio $\mu_p G_E/G_M$ in the SL region as a function of Q^2 , obtained via the Rosenbluth technique (black points), and polarization method (green stars).	37
3.7	World data on the TL proton magnetic FF for $ G_E = G_M $, as function of q^2 . The vertical dashed line represents the kinematical threshold of the proton antiproton annihilation.	38
3.8	Proton electromagnetic FF ratio in TL region, as function of q^2 . Data are from Ref. [77] (red squares), from Ref. [78] (black triangles), from Ref. [79] (green circles), and from Ref. [80] (blue star).	39
3.9	Feynman diagram for $\bar{p} + p \rightarrow e^+ + e^- + \pi^0$ (a) for lepton pair emission from the antiproton and (b) from the proton.	40
3.10	The pQCD diagram describing at the first order the photon proton vertex. 43	
3.11	World data on the TL proton magnetic FF for $ G_E = G_M $, as function of q^2 . The lines are the predictions of the theoretical models from VMD (green solid line), pQCD (red dashed line), and from Ref. [97] (black dotted line).	45
3.12	Proton electromagnetic FF ratio in TL region, as functions of q^2 . The lines are the prediction of the theoretical models from VMD (green solid line), pQCD (red dashed line)), and from Ref. [97] (black dotted line). Data are from Ref. [77] (red squares), from Ref. [78] (black triangles), from Ref. [79] (green circles), and from Ref. [80] (blue star).	46
4.1	3D overview of the PANDA detector, from [18].	48
4.2	Basic layout of the MVD (top). The red inner parts are equipped with silicon hybrid pixel sensors. Double-sided silicon micro-strip detectors utilised in the outer layers are indicated in green. Bottom: Side view along the beam axis illustrating the polar angle coverage. The barrel and the forward part meet at a polar angle of $\theta = 40^\circ$	50
4.3	The Straw Tube Tracker (STT) of the target spectrometer seen from upstreams (left). Layout of the straw tubes in the STT in xy-view. The straws marked in green are parallel to the beam axis (right). The blue and red marked straw layers are skewed relative to the axially aligned straws in the same sector by a small angle of $+2.9^\circ$ and -2.9° , respectively.	51

4.4	Fractional energy loss per radiation length in lead as a function of energy (left), and photon interaction cross section as a function of energy in carbon and lead(right), from [20]. $\sigma_{p.e}$ denotes the atomic photoelectric effect, χ_{nuc} (χ_{nuc}) is the pair production from nuclear (electron) field, and $\sigma_{g.d.r.}$ the photonuclear interactions.	54
4.5	The barrel and forward endcap EMC, from [102].	55
5.1	Pictures of the interface of glue taken with an optical microscope after thermal test at $\mathcal{T} = 75^\circ \text{ C}$ (top left), 130° C (top right), 185° C (bottom left) and 240° C (bottom right).	59
5.2	Pictures of the interface of glue taken with an optical microscope after thermal test at $\mathcal{T} = 310^\circ \text{ C}$	59
5.3	Set-up for testing the mechanical resistance. The white metal block (on the bottom) induces the mechanical force.	60
5.4	Schematic representation of double beam spectrophotometers.	62
5.5	Varian Cary 5000 spectrophotometer (left). Copper plates of the spectrophotometer (right).	62
5.6	Optical transmittance as a function of the wavelength, with sample of two quartz glass plates without glue (black solid line) and with glue DC3145 at different temperatures: $+20^\circ \text{ C}$ (red dashed line), $+15^\circ \text{ C}$ (green dotted line), $+10^\circ \text{ C}$ (blue dashed-dotted line), 0° C (yellow long dashed-dotted line), -10° C (violet long dashed-triple dotted line), -20° C (cyan long dashed), -25° C (magenta long dashed-double dotted), -30° C (orange very long dashed line), -40° C (gray very long dashed-dotted line). The upper part of the spectra is magnified in the overlay.	63
5.7	Optical transmittance as a function of the wavelength, with a sample of two quartz glass plates without glue (black solid line) and with glue (RT600) at different temperatures: $+20^\circ \text{ C}$ (red dashed line), $+10^\circ \text{ C}$ (blue dashed-dotted line), 0° C (yellow long dashed-dotted line), -10° C (violet long dashed-triple dotted line), -20° C (cyan long dashed), -25° C (magenta long dashed-double dotted), -30° C (orange very long dashed line), -40° C (gray very long dashed-dotted line), -50° C (green dotted line)	64
5.8	Optical transmittance of the two quartz glasses, glued with DC3145, as function of the wavelength, before irradiation (black solid line) and after irradiation with different doses: 100 Gy (red dashed line), 250 Gy (green dotted line), 500 Gy (blue dashed-dotted line), 750 Gy (yellow long dashed-dotted line), 1000 Gy (violet long dashed-triple dotted line), at room temperature.	65
5.9	Same as Fig. 5.8 for the RT600 sample (left) and for the quartz glass sample (right).	66

LIST OF FIGURES

5.10	Optical transmittance of the two quartz glasses, glued with DC3145, as function of the wavelength, before irradiation (black solid line) and after irradiation (red dashed line) with a dose of $1. \times 10^{12}$ proton/cm ² (left) and 1.8×10^{13} proton/cm ² (right), at room temperature.	67
6.1	Ratio of the total proton antiproton annihilation cross section into a charged pion pair relative to an electron pair, as a function of total energy squared s	72
6.2	Standard chain of reconstruction in PANDARoot.	72
6.3	Pion STT dE/dx for a slice of momentum from Ref. [128], fitted with a Gauss function (blue) and Novosibirsk function (red).	76
6.4	Angular distribution in the CMS of a sample of reconstructed pions for positive (black) and negative (red) particles, obtained with the model of Ref. [33] for $s=13.9$ GeV ²	78
6.5	Angular distribution in the CMS for a sample of reconstructed events of the background (left) and the signal (right), for positive (black) and negative (red) particles, obtained with PHSP model for $s=8.2$ GeV ²	79
6.6	The difference $ \phi - \phi' $ for a sample of reconstructed events of the pion (left) and the electron (right) pairs, for $s=8.2$ GeV ²	79
6.7	The invariant mass for a sample of reconstructed pion (left) and electron (right) pairs, for $s=8.2$ GeV ²	80
6.8	Energy loss in the EMC over the reconstructed momentum for a sample of reconstructed events of the background (left) and the signal (right), as a function of the reconstructed momentum (Lab system), obtained with PHSP model for $s=8.2$ GeV ²	81
6.9	Same as Fig. 6.8 for the energy loss in the STT.	81
6.10	Same as Fig. 6.8 for the Cherenkov angle of the Barrel DIRC.	82
6.11	PID probability given by the EMC (black), EMC+STT (green) and total probability (red), for π^+ to be identified as e^+ (left) and π^- to be identified as e^- (right) for $s=8.2$ GeV ²	83
6.12	PID probability given by the EMC with respect to the probability given by the STT, for a pion to be identified as electron, for $s=8.2$ GeV ²	83
6.13	PID probability given by the EMC (black), EMC+STT (green) and total probability (red), for e^+ to be identified as e^+ (left) and e^- to be identified as e^- (right), for $s=8.2$ GeV ²	84
6.14	Number of fired crystals in the EMC, for a sample of reconstructed events of the background (left) and the signal (right), for positive (black) and negative (red) particles, for $s=8.2$ GeV ²	84
6.15	Angular distribution (left) of e^- (blue) and e^+ (green) in the CMS, for the MC events (top) and the reconstructed events after the cuts (bottom) obtained with PHSP model for $s=8.2$ GeV ² , in correspondence with the EMC geometry in the Lab system (right).	86
6.16	Scheme used for the extraction of statistical error on the proton FF ratio.	86

6.17	Signal efficiency for e^- (red), e^+ (black) and for their mean (green), obtained with PHSP model for $s=8.2$ GeV ²	88
6.18	Same as Fig. 6.17 for $s = 5.4$ GeV ² (left) and $s = 13.9$ GeV ² (right). . .	88
6.19	Angular distribution of the MC events obtained with PHSP model for e^- (blue) and e^+ (green) in the CMS, and following physical distribution (e^- (black) and e^+ (red)), before (top) and after the reconstruction and the cuts (bottom), for $s = 8.2$ GeV ² and $R = 1$	89
6.20	The observed events before efficiency correction $O(c)$ (forward events (blue circles) and backward events (orange squares)) and after efficiency correction $F(c)$ (forward events (red circles) and backward events (green squares)), as a function of $\cos^2 \theta$ for $s = 8.2$ GeV ² and $R = 1$. The line is the linear fit.	90
6.21	Same as Fig. 6.20 but for $s = 5.4$ GeV ² (left) and $s = 13.9$ GeV ² (right). The lines are the linear fit.	91
6.22	Expected statistical precision on the determination of the proton FF ratio for $R=1$, from Ref. [41] (yellow dashed band) and from the present simulation (magenta triangles) as a function of $s = q^2$, compared with the existing data. The statistical errors are extracted in the angular range $ \cos \theta \leq 0.8$	92
6.23	Ratio of the differential annihilation cross section into a pion pair relative to a charged electron pair in the CMS for $s=8.2$ GeV ² (back, solid line) and $s=13.9$ GeV ² (dashed, green line)	93
7.1	Feynman diagrams for the Born approximation and the first order correction in $\bar{p}p \rightarrow e^+e^-$	96
7.2	Dalitz plot of the emitted electron and positron energies in the CMS for $p_{\bar{p}} = 1.7$ GeV. The maximum energy of the emitted leptons is $\sqrt{s}/2=1.16$ GeV.	99
7.3	Electron-positron invariant mass and number of emitted γ 's per event for $p_{\bar{p}} = 1.7$ GeV.	100
7.4	Angular distribution of the emitted electron in the CMS, with and without PHOTOS for $p_{\bar{p}} = 1.7$ GeV.	100
7.5	Angular distribution of the emitted electron with PHOTOS for different cuts of the e^+e^- invariant mass (left). Ratio of the electron angular distribution with and without PHOTOS for \bar{p} momentum equal to 1.7 GeV (right).	101
7.6	Ratio of the electron angular distribution for $s=12.9$ GeV ² with and without PHOTOS [XPHCUT=0.01 with one photon emission] in the CMS for $E_{\gamma}^{max} = 50$ MeV (Black) and $E_{\gamma}^{max} = 100$ MeV (Red).	102

LIST OF FIGURES

7.7	RC factor δ , as a function of $\cos\theta$, according to Ref. [136] for $s=12.9$ GeV^2 and $E_\gamma^{\text{max}}=100$ MeV: vacuum excitations (magenta, dotted), odd contribution (red, long dashed) mainly from soft photon emission and from two photon exchange (blue, dot-dashed), FSR (green, dashed), total (black,solid).	103
8.1	Feynman diagram for the reaction $p(p_1) + e(k_1) \rightarrow p(p_2) + e(k_2)$. The transfer momentum of the virtual photon is $q = k_1 - k_2 = p_2 - p_1$. . .	106
8.2	(Left) Maximum value of the four momentum transfer squared (Q^2) as a function of the proton beam kinetic energy, E_p in GeV. (Right) Difference in kinetic energy between scattered protons and incoming protons, ΔE_p , for $E_p=100$ MeV, as a function of the sine of the proton scattering angle.	111
8.3	(Left)Energy of the recoil electron as a function of the cosine of the electron scattering angle for beam kinetic energy $E_p=100$ MeV. (Right) Differential cross section as a function of the cosine of the electron scattering angle for beam kinetic energy $E_p=100$ MeV.	112
8.4	Polarization transfer coefficients as a function of E_p for different angles of the recoil electron: $\vartheta = 0$ (black solid line), 10 mrad (red dashed line), 30 mrad (green dotted line), 50 mrad (blue dash-dotted line).	115
8.5	Same as Fig. 8.4 but for the spin correlation coefficients.	118
8.6	Variation of the differential quantities $C_{\ell\ell}^2(q^2)(d\sigma/dq^2)$ (left) and $C_{\ell\ell}^2(q^2)(d\sigma/dq^2)$ (right) [mb/GeV 2] as a function of incident energy for a polarized proton beam scattering from a polarized electron target $\vec{p} + \vec{e} \rightarrow p + e$, at different angles. Notations are the same as in Fig. 8.4.	119
8.7	Variation of the quantity F^2 [a.u.] as a function of proton kinetic energy E_p for a transverse polarized proton beam, scattered by a longitudinally polarized electron target ($\vec{p} + \vec{e} \rightarrow p + e$).	120
9.1	Energy of the τ^- lepton as a function of the emission angle for $E_1 = 6.85$ GeV (blue dash-dotted line), $E_1 = 15$ GeV (black solid line) and $E_1 = 30$ GeV (red dashed line), in the Lab system. The limiting angles are shown as vertical lines for the corresponding energy.	124
9.2	τ^+ emission angle ϑ' as a function of the τ^- angle ϑ in the Lab system. Notation as in Fig. 9.1.	125
9.3	Total cross section ratios $R_\ell = \frac{\sigma(\ell^+\ell^-)}{\sigma(e^+e^-)}$, for $\ell = \tau$ (red dashed line) and $\ell = \mu$ (blue solid line) as a function of $\sqrt{q^2}$. The shaded area illustrates the region below the physical threshold for $\bar{p} + p$ annihilation.	132
9.4	Differential cross section as a function of $\cos\theta$ (left) and $\cos^2\theta$ (right) for $q^2=15$ GeV 2 , assuming the VMD FF parametrization [165], for $\ell = \tau$ (red dashed line), $\ell = \mu$ (blue solid line). The calculation for $\ell = e$ (black dotted-dashed line) is hardly visible since it overlaps with the μ line.	133

9.5	(Left) Single spin asymmetry as a function of $\cos \theta$ for $q^2=15 \text{ GeV}^2$, for the parametrization of Ref. [165]. (Right) Ratio of the analyzing powers A_{yy}^C/A_{xx}^C in the CMS as a function of the total energy, with the parametrizations [165] (thin lines) and pQCD (thick lines). Notation as in Fig. 9.4.	134
9.6	Double polarization observables as a function of $\cos \theta$, for $q^2 = 15 \text{ GeV}^2$, using the VMD parametrization from Ref. [165] in CMS. Notation as in Fig. 9.4.	135
9.7	Double polarization observables as a function of $\cos \theta$, for $q^2 = 15 \text{ GeV}^2$, using the pQCD parametrization of FFs in CMS. Notation as in Fig. 9.4.	136

LIST OF FIGURES

List of Tables

2.1	The quantum numbers of the proton and antiproton systems	11
2.2	Quantum number of the S- and P-partial waves of the proton antiproton annihilation	11
2.3	Coefficients for the parametrization, Eq. 2.5, of selected inelastic channel cross sections.	15
2.4	Coefficients for the parametrization, Eq. 2.6, of selected inelastic channel cross sections.	16
2.5	Coefficients for the parametrizations of $\bar{p} + p \rightarrow K^+ + K^-$ and $\bar{p} + p \rightarrow \pi^+ + \pi^-$ cross sections.	19
3.1	Charge density, form factor and root mean squared radius [53].	30
6.1	Expected total cross section σ and number of counts N_E (in the full angular range ($\cos \theta = [-1, 1]$) and in the interval $ \cos \theta \leq 0.8$) from Eqs. 6.5 and 6.6 corresponding to an integrated luminosity $\mathcal{L} = 2 \text{ fb}^{-1}$, for different values of s	71
6.2	PID probability and kinematical cuts applied to the electron and pion reconstructed events.	85
6.3	Number of events after the PID probability and the kinematical cuts for the signal and the background, for $s=8.2 \text{ GeV}^2$	85
6.4	Values of R and \mathcal{A} according to different assumptions for $ G_E $	87
6.5	Efficiency integrated over the angular range $ \cos \theta \leq 0.8$ for different s values.	89
6.6	Expected statistical errors on the angular asymmetry and the proton FF ratio, for different s values. The second and the third columns are the theoretical values (simulation inputs). The fourth and the fifth columns are the results of the fit. The statistical errors are extracted in the angular range $ \cos \theta \leq 0.8$	91
6.7	Expected statistical errors on the proton FF ratio ΔR ($R = 1$) for different values of the angular cut.	93
7.1	RC factor δ in the CMS for $s=12.9 \text{ GeV}^2$, $E_\gamma^{max} = 100 \text{ MeV}$, given by PHOTOS and Refs. [136, 137].	104

LIST OF TABLES

8.1	Unpolarized cross section and polarized transfer cross sections (in mb) for different incident kinetic energies.	116
8.2	Integrated polarization transfer coefficients for different incident energies.	116

Chapter 1

Introduction

The understanding of the quark confinement, the possible existence of glueballs and hybrids and the origin of the hadronic masses are long-standing puzzles and represent a challenge for the understanding of strong interaction. The strong interaction has played a major role in the early universe, binds the nucleon (proton and neutron) within the atomic nucleus and dominates the interaction between the quarks within the hadrons. Among all possible realizations of quark and anti-quark configurations, the proton is the only stable hadron and consequently has been the subject of intensive studies. Mass, magnetic moment, magnetization and charge distribution, proton radius, polarization and excitation spectrum are studied both in theory and experiments since a long time. Nucleon structure observables like the electromagnetic form factors play a special role, since they serve as a sensitive testing ground for the understanding of the theoretical description. The experimental techniques have been substantially and continuously improved yielding new insights in nucleon structure. A recent breakthrough is due to the implementation of the polarization techniques.

The understanding of the electromagnetic structure of the nucleon is presently one of the central issues in hadron physics. The elastic electron nucleon scattering, where the interaction occurs through the exchange of a virtual photon, is an efficient tool to investigate the nucleon electromagnetic structure, which is parametrized in terms of the electric G_E and magnetic G_M form factors. The electromagnetic form factors are related to the charge and the magnetization distributions within the nucleon. This relation is straightforward in a non-relativistic approximation or in the Breit frame. The electromagnetic form factors are real functions of the momentum transfer squared in scattering processes (Space-Like), and become complex in the annihilation reactions (Time-Like). The Time-Like region is accessible through annihilation reactions, as $\bar{N} + N \leftrightarrow e^+ + e^-$. Crossing symmetry and analyticity relations connect the Time-Like with the Space-Like region. While in the last 50 years electron scattering experiments have allowed to explore the electromagnetic form factors in the Space-Like region in a large domain, the knowledge of the Time-Like form factors is scarce. Due to the low luminosity achieved up to now, data exist on the nucleon Time-Like form factors,

however no individual determination of the electric and magnetic form factors has been done so far. The unphysical region, below the threshold of the proton antiproton production, has never been experimentally accessed.

The progress on the understanding of the proton structure requires more experimental and theoretical efforts. Ambitious experimental programs are foreseen at the main accelerator facilities in this domain (experiments at Jefferson Laboratory (JLab), BESIII, Novosibirsk and PANDA at FAIR) with the aim to achieve a better precision and/or to access new kinematical regions. In Space-Like region, a discrepancy exists between the measured values of proton form factors using the Rosenbluth separation method and the GEp collaboration data (JLab) based on the polarization method. Calculations of quantum electrodynamics radiative corrections which are the suggested candidate to explain this discrepancy are model dependent and quantitatively inconsistent with each others. Future experiments will be a test of the validity of applying analyticity and unitarity on the nucleon form factors, as well as of the predictions of quantum chromodynamics in the asymptotic regime. Another interesting question to be addressed is related to the size of the proton. The recent measurement from the Lamb shift in muonic hydrogen (PSI) does not agree with the value based on electronic hydrogen as well as with elastic electron proton scattering experiments. This issue opens questions on the experimental methods and on the applied theoretical corrections, necessary to extract the radii.

The investigation of theoretical and experimental aspects related to the possibilities offered by the antiproton beams at the future Facility for Antiprotons and Ion Research (FAIR) at Darmstadt, in the momentum range between 1.5 and 15 GeV/c, is reported in this work. In particular, the possibility of a precise measurement of the Time-Like electromagnetic proton form factors with the PANDA (antiProton ANnihilation at Darmstadt) detector at FAIR is studied. Through phenomenological, experimental and simulation studies, the present thesis is devoted to a better understanding of the internal dynamics of the proton. The outline of the thesis is as follows:

A. Experimental and simulation studies

Chapter 2: in this chapter a general introduction on the physics subjects opened by the availability of antiproton beams is given. The physics goals of FAIR and of the PANDA experiment are also discussed.

Chapter 3: this chapter is devoted to the physics of the proton electromagnetic form factors. The world data in Space-Like and Time-Like region are shown and the methods used to extract the form factors are described. Different parametrizations for the proton form factors are discussed in this chapter.

Chapter 4: the PANDA detector system is described in this chapter with an emphasis on the electromagnetic calorimeter. The electromagnetic calorimeter plays a crucial role for the identification of electromagnetic processes.

Chapter 5: this chapter is dedicated to the experimental aspect of my work. It reports on the results of tests for low temperature applications of two commercial optical glues for the electromagnetic calorimeter of PANDA at FAIR. Mechanical, thermal and optical properties have been studied, as well as radiation hardness to photon and proton radiation.

Chapter 6: feasibility studies for Time-Like proton form factor measurements at PANDA through the annihilation reaction $\bar{p}p \rightarrow e^+e^-$ are described here. Based on Monte Carlo simulation within the PANDARoot framework, the expected statistical error at which the proton form factor ratio will be measured at PANDA is extracted at different energies.

Chapter 7: this chapter presents a study of the effect of radiative corrections on the $\bar{p}p \rightarrow e^+e^-$ differential cross section. The radiative corrections are included in PANDARoot via the package PHOTOS. The results from the Monte Carlo simulation are compared to existing calculations in the kinematical domain of interest for PANDA.

B. Phenomenological studies and conclusions

Chapter 8: based on the formalism derived in the appendix A, the experimental observables for the elastic reaction induced by proton scattering from electrons are calculated in the Born approximation. Specific attention is given to the kinematical conditions, that is, to the specific range of incident energy and transferred momentum. The interest of this study is due to the three possible applications: 1) the possibility to build polarized antiprotons beams (which would open a wide domain of polarization studies at FAIR), 2) the possibility to build beam polarimeters for high-energy polarized proton beams, and 3) the possibility to make a precise measurement of the proton charge radius for very small values of transferred momenta.

Chapter 9: in this chapter, previous calculations of polarization observables for the annihilation reaction $\bar{p}p \rightarrow e^+e^-$ are extended to the case of heavy leptons, such as the μ and τ -leptons. The case when the beam and/or the target are polarized, as well as when the outgoing leptons are polarized are considered. We give the dependence of the unpolarized cross section, angular asymmetry, and various polarization observables on the relevant kinematical variables in the center of mass system, paying particular attention to the effect of the mass induced terms.

Chapter 10: This chapter summarizes the results of this thesis work. Conclusions and perspectives are given here.

All along the manuscript, if not indicated, $c = \hbar = 1$ is assumed.

Most part of this work has been published and/or discussed in oral presentations. The list of publications is given in Appendix D.

Chapter 2

Physics with antiproton beams

2.1 Introduction

Over the past century, the concept of symmetry has been playing a key role for the understanding of subatomic particles, the fundamental building blocks of the universe, and the forces binding them. It was accepted that all subatomic particles (neutrino excluded) can have a mirror or antimatter counterpart with opposite charge and right- or left-handed spin. Experiments employing or generating antimatter particles provide important information about these fundamental particles and forces. Matter antimatter collisions may generate particle-antiparticle pairs, which provide essential knowledge of the characteristics of the elementary units of which the universe is composed.

The existence of the antimatter was first predicted in 1928, when Paul Dirac combined the quantum theory, as proposed by Erwin Schrödinger and Werner Heisenberg, and the Einstein's special relativity in one equation to describe the motion of the electron. The Dirac equation for spin 1/2 particles has positive as well negative energy solutions. The negative energies were first interpreted [1] as a sea filled with particles and vacuum obeying the Pauli exclusion principle. The situation was clarified in 1932 when Carl Anderson detected the first anti-electron, the positron [2]. While studying the tracks of cosmic particles, Anderson noticed an additional track characterized by the same mass as an electron but with a positive charge. In 1955, antiprotons were produced and identified at the Berkeley Bevatron by Emilio Segrè and Owen Chamberlain [3] who received the Nobel prize for physics in 1959. The velocity, the momentum, as well as the sign and the magnitude of the electric charge of the antiprotons were measured. One year later, at the same place, the anti-neutron was discovered in the charge exchange process followed by the \bar{n} annihilation [4].

After the Berkeley discoveries of the antinucleons, experiments with antiprotons were carried out at Brookhaven and CERN in the '60s and '70s by stopping antiprotons in hydrogen and deuterium filled bubble chambers (annihilation at rest) [5]. Even with the limited statistics and momentum resolution achieved in these experiments,

they demonstrated that the nucleon antinucleon ($\bar{N}N$) annihilation is a powerful tool to discover meson resonances. However, the annihilation $\bar{N}N$ at rest was restricted at that time to the study of initial states with orbital angular momentum $L = 0$. Compared to the electron positron annihilation at rest, where only γ rays can be produced, the substantial annihilated energy in $\bar{N}N$ leads to a variety of mesons, as well as lepton pairs populating the final states.

Progress in the $\bar{N}N$ low energy experimental field was achieved with the cooled antiproton beam of the Low-Energy Antiproton Ring (LEAR) [6], constructed in 1982 at CERN. Antiprotons were produced by focusing incident proton beams from the CERN Proton Synchrotron (PS) on a nuclear (Be) target. By means of stochastic cooling, the LEAR facility provided antiproton beams in the momentum range from 105 MeV to 2 GeV with low emittance and momentum spread of $\delta p_{\bar{p}}/p_{\bar{p}} \sim 0.1\%$ [7]. The stochastic cooling uses the electrical signals that the individual charged particles generate to control the emittance of the particle beam in the accelerators and in the storage rings. The LEAR antiproton storage ring has been operated until 1996 providing an intensive experimental study of low and medium energy antiproton annihilations. Its successor, the Antiproton Decelerator (AD) [8] delivers antiproton beams at momenta of 100 and 300 MeV, at intensities up to $\sim 2 \times 10^7$ per minute [9].

The highest energy (980 GeV) and luminosity ($\mathcal{L} = 10^{30} \text{ cm}^{-2} \text{ s}^{-1}$) antiproton facility was at Fermilab. Before the commissioning of the Tevatron, limited number of medium energy \bar{p} experiments at Fermilab, E760 and E835, have been focusing on the observation and measurement of charmonium states [10, 11]. For the first time a high energy polarized antiproton beam was obtained at Fermilab from the parity violating decay of anti- Λ^0 hyperons [12, 13], although the intensity was limited to $\sim 10^5 \bar{p}/\text{s}$. Pion reactions measured with this beam gave insight into the spin dependence of the underlying partonic processes and add new inputs regarding the debated question of the spin structure of protons.

Antiproton experiments held at Berkeley, LEAR and Fermilab opened new fields of physics. Particle physics topics such as charmonium studies, open charm and hyperon production, the search for glueballs and gluonic hybrid states predicted by the Quantum Chromodynamics (QCD) theory and the study of the hadron structure through the electromagnetic probe need to be addressed at a new facility offering intermediate antiproton energy beams. This will push back the frontiers of the accessible kinematics and achievable precision.

2.2 The Facility for Antiproton and Ion research at Darmstadt

A new international Facility for Antiproton and Ion Research (FAIR) [14] is under construction at Darmstadt (Germany). The FAIR project (Fig.2.1) is developed in cooperation with an international community of 45 countries and more than 2500 scientists and engineers. The existing GSI accelerators UNILAC (UNiversal Linear ACcelerator) and SIS18 (synchrotron with a maximum magnetic rigidity of 18 Tm) will be used as injector for the new system. The heart of FAIR is a double ring accelerator SIS100/300 of 1.1 km diameter, which will be used to accelerate protons and heavy ions at energies in the range of tens of GeV.

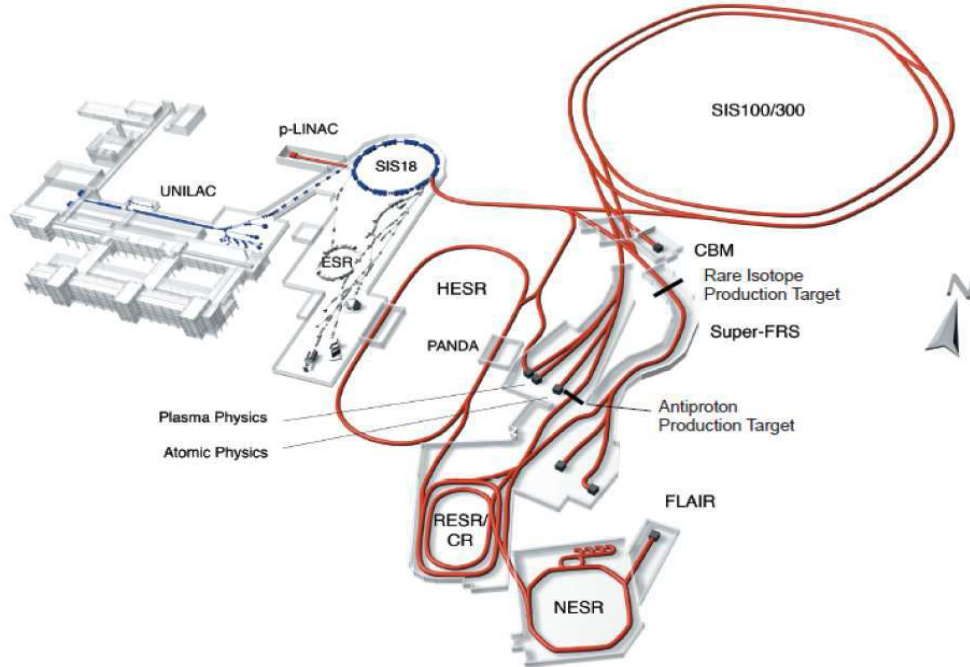


Figure 2.1: Facility for Antiproton and Ion Research (FAIR, from [14]). The existing GSI facility is represented by the blue color. The planned FAIR facility is plotted in red color.

Antiprotons will be produced by a metal target bombarded with the proton beams from SIS100. The \bar{p} beams will be pre-cooled in a system of storage and cooler rings and then injected in the High Energy Storage Ring (HESR), or in the New Experimental Storage Ring (NESR).

The energy resolution of the \bar{p} beam in HESR will benefit from stochastic and electron cooling. The electron cooling is a method of reducing the energy spread, angular divergence, and geometric size of a charged particle beam by merging with

an electron beam with which it exchanges energy. HESR is dedicated to supply the PANDA experiment with high intensity antiproton beams over a broad momentum range from 1.5 GeV to 15 GeV. Two operation modes will be available at HESR:

- high resolution mode in the momentum range from 1.5 GeV to 9 GeV. This operation mode provides a very high momentum resolution $\delta p_{\bar{p}}/p_{\bar{p}} \leq 4 \times 10^{-5}$ at a moderate luminosity of $\mathcal{L} = 2 \times 10^{31} \text{ cm}^{-2} \text{ s}^{-1}$;
- high luminosity mode in the full momentum range with greater momentum spread ($\delta p_{\bar{p}}/p_{\bar{p}} \sim 10^{-4}$) and luminosity $\mathcal{L} = 2 \times 10^{32} \text{ cm}^{-2} \text{ s}^{-1}$.

The NESR will be also equipped with stochastic and electron cooling. NESR will serve to cool and decelerate stable and radioactive ions as well as antiprotons for low energy experiments and trap experiment at FLAIR (Facility for Low Antiproton and Ion Research).

The physics program of the FAIR project spans a broad range of research fields: The NUSTAR [15] program is dedicated to Nuclear Structure, Astrophysics and Reactions with Rare-isotope beams. Another fold of the FAIR program deals with Atomic, Plasma Physics as well as Applications such as applied physics for material science and biology (APPA collaboration [16]). The third part concerns strong interaction studies in hadron physics and hadronic matter. In this field, two experiments are part of the base program: the Compressed Baryonic Matter (CBM Collaboration [17]) and the PANDA experiments. Using high energy ion beams, CBM will study the nuclear matter phase diagram and the quark gluon plasma.

2.3 The PANDA Experiment

The PANDA (antiProton ANnihilation at DArmstadt) experiment [18] is one of the key projects planned at the future Facility FAIR. The PANDA physics program aims to achieve precise studies and quantitative understanding of non perturbative QCD. The QCD is well understood at high energies, where the strong coupling constant is small and perturbation theory can be applied.

The scientific programme of PANDA covers charmonium spectroscopy, search for gluonic excitations, open charm spectroscopy, hypernuclear and electroweak physics, and electromagnetic processes. The experiment will benefit from the high intensity antiproton beams which will be provided by the HESR of FAIR in the range of momentum between 1.5 GeV and 15 GeV. The large acceptance of the PANDA detector (see chapter 4) for both charged and neutral particles, together with the foreseen high quality of the antiproton beam, will create an ideal environment to collect high statistics data.

Experiments with antiprotons are considered as a unique playground. The specificity of the annihilation of an antiproton beam with nucleons is the production of

different hadronic and electromagnetic channels with definite quantum numbers. This section will describe some of the interesting physics which can be addressed in $\bar{p}p$ annihilation, in the energy range of the PANDA experiment.

2.4 Quark model

Hadrons, strongly interacting particles, are bound states of quarks and gluons. The theory of the strong interaction is the QCD, the quantum field theory of color charged fermions (the quarks) and bosons (the gluons), based on the non-abelian gauge group SU(3).

The quantum numbers describe conserved quantities in the dynamics of the quantum system. Noether's theorem states that there is a one-to-one correspondence between conservation laws and symmetries of physical systems. For example, the conservation of energy follows from the time-invariance of physical systems, and the space isotropy gives rise to the conservation of the angular momentum.

Quarks (antiquarks) are strongly interacting spin 1/2 fermions ($s=1/2$) and have baryon number $\mathcal{B} = 1/3$ ($-1/3$). They are also defined by the quantum numbers of charge Q , and flavour: Isospin I , Isospin 3rd-component I_3 , Strangeness S , Charm C , Bottomness B and Topness T . The conservations of Q and I_3 have not been shown to be violated. Flavour quantum numbers are violated by the weak interaction and the Baryon number by the Chiral anomaly.

The charge and the flavour quantum numbers are related through the generalized Gell-Mann-Nishijima formula:

$$Q = I_3 + \frac{Y}{2}, \quad Y = \mathcal{B} + S + C + B + T, \quad (2.1)$$

where Y is called the Hypercharge quantum number.

2.4.1 Hadrons in the quark model

The quark model, developed by Murray Gell-Mann, is a classification scheme for hadrons in terms of their valence quarks, the quarks and antiquarks which give rise to the quantum numbers of the hadrons. They characterize the dynamical and the decay properties of the hadron. The quark-gluon sea has no effect on the quantum numbers, but determines other properties of the hadron, such as its internal electric charge and magnetic distribution.

Hadrons within the quark model can be either mesons consisting of a valence quark-antiquark pair with total baryon number $\mathcal{B} = 0$, or baryons (antibaryons) consisting of three valence quarks (qqq), with $\mathcal{B} = 1$ (-1). The baryon number of a particle is defined as the sum of the baryon number of its valence quark constituents:

$$\mathcal{B} = (n_q - n_{\bar{q}})/3. \quad (2.2)$$

Mesons are bosons made of one quark and one antiquark. They can be found in spin-1 triplet (three spin projections) and spin-0 singlet (one projection). Hadrons are classified according to the quantum numbers corresponding to the representation of the Poincaré group: J^{PC} , where J is the total angular momentum, P is the intrinsic parity, defined with the reflection of space, and C , the charge conjugation parity (C-parity), defined by the reflection of the antimatter universe. Poincaré group is the set of symmetries for the special relativity (translations in space and times, parity and time reversal, ...). For a meson of orbital momentum L , J , P , C are calculated as:

- $|L - s| \leq J \leq L + s$, where $s = 0$ or 1 .
- $P = (-1)^{L+1}$, where the 1 in the exponent arises from the intrinsic parity of the quark-antiquark pair.
- $C = (-1)^{L+s}$ for mesons which have no flavour as flavoured mesons have indefinite value of C .

Charged pions and the kaons are long-lived mesons and they can be detected before their decay. In the quark model, pions are a bound states of the light up and down quarks, and kaons are the bound states of a strange quark (or antiquark) and an up or down antiquark (or quark).

Baryons are fermion particles. The only stable baryon is the proton. Baryons that have non-zero strangeness, but zero Charm, Bottomness and Topness are called hyperons. The lightest of the hyperons is the Λ -hyperon. The hyperons are relatively long-lived. They decay via the weak interaction except the Σ^0 that decays electromagnetically (directly or through a series of decays) to a nucleon and one or more mesons. The hyperons do not normally form bound states but may occur in short-lived nuclei, called hypernuclei.

2.4.2 Exotic hadrons

Hadrons with valence configurations different from $\bar{q}q$ (mesons) and qqq (baryons) are called exotic hadrons. Exotic hadrons can be consisting of only quarks, such as the tetraquarks ($\bar{q}q\bar{q}q$) or the pentaquarks ($\bar{q}qqqq$). It is also possible that gluons could form compounds, either on their own creating glueballs (gg), or in combination with quarks forming so-called hybrids ($\bar{q}qg$ -mesons or $qqqg$ -baryons). For example, gluons can couple to quarks and antiquarks to form a color neutral object called hybrid meson.

Some quantum numbers allowed for these states coincide with the traditional $q\bar{q}$ mesons or qqq baryons. They are called cryptoexotic, or hidden-exotic hadrons. The other exotic hadron states have quantum numbers that cannot be fitted into the schematic system of the quark model. They could be either particles with anomalous flavour or charge, or particles with anomalous spin-parity quantum numbers. The identification of particles with such forbidden quantum numbers would thus prove the existence of exotic hadrons.

2.4.3 The $\bar{p}p$ system

The quantum numbers of the antiproton and proton are combined to establish the total quantum numbers of the initial $\bar{p}p$ system.

The baryon number and charge are additive scalars, while other quantum numbers are slightly more complicated to handle. The quantum numbers of the proton, the antiproton and the $\bar{p}p$ system are given in Tab. 2.1. L is the orbital angular momentum of the system. As in the case of quarks combination, the spin and isospin of the $\bar{p}p$ system can be obtained by treating these quantities as vectors. The charge conjugation of this system is given by $C = (-1)^{L+s}$. In addition, the system has also zero strangeness and charmness. All these quantum numbers put constraints on the possible final state particles that can occur in $\bar{p}p$ annihilation. Tab. 2.2 represents the allowed quantum numbers for $\bar{p}p$ annihilation, in S- and P-partial waves, within the quark model.

Quantum number	p	\bar{p}	$\bar{p}p$
Q	+1	-1	0
B	+1	-1	0
s	1/2	1/2	0, 1
J	1/2	1/2	0, 1, 2, ...
(I, I_3)	(1/2, 1/2)	(1/2, -1/2)	(1, 0), (0, 0)
P	+1	-1	$P = (-1)^{L+1}$

Table 2.1: The quantum numbers of the proton and antiproton systems

$^{2I+1, 2s+1}L_J$	$^{1,1}S_0$	$^{3,1}S_0$	$^{1,3}S_1$	$^{3,3}S_1$	$^{1,1}P_1$	$^{3,1}P_0$	$^{3,3}P_0$	$^{1,3}P_1$	$^{3,3}P_1$	$^{1,3}P_2$	$^{3,3}P_2$
J^{PC}	0^{-+}	0^{-+}	1^{--}	1^{+-}	1^{+-}	0^{++}	0^{++}	1^{++}	1^{++}	2^{++}	2^{++}

Table 2.2: Quantum number of the S- and P-partial waves of the proton antiproton annihilation

In addition to the quantum number conservation, the channels induced by the $N\bar{N}$ annihilation can also be predicted by the Dynamical Selection Rules (DSRs) [19]. DSRs can explain the experimental evidence for the suppression of certain transitions which are allowed by the conservation of the J^{PC} quantum numbers. Such DSR can arise from several sources such as the initial or final states interactions or orbital spin structure of the transition channels. Based on the DSRs, different final states have different cross sections and different branching transition ($^1S_0, ^3S_0, \dots$) ratios.

2.5 Antiproton proton annihilation: the PANDA physics program

In this section an overview of the accessible processes induced by $\bar{p}p$ annihilation and of their cross sections is given.

2.5.1 Total and elastic cross section

The measurement of the total, elastic and inelastic, cross section is an important test of the theoretical models describing the annihilation of hadrons, as the Glauber and Regge theories. A good parametrization of the existing data, over a wide range of momentum, helps for the estimation of the counting rates of future experiment and contributes to the optimization of the detector design.

The world data for the total and the elastic cross sections for the $\bar{p} + p$ induced reactions are illustrated in Fig.2.2 as function of the laboratory antiproton momentum $p_{\bar{p}}$ expressed in [GeV]. They are taken from the compilation of Refs. [20, 21, 22] where references to the individual experiments can be found. The lines are the results from the new fit [23] which includes a low energy extension of the Regge theory based on the Glauber theory [24, 25]. In this parametrization, the expression of the total cross

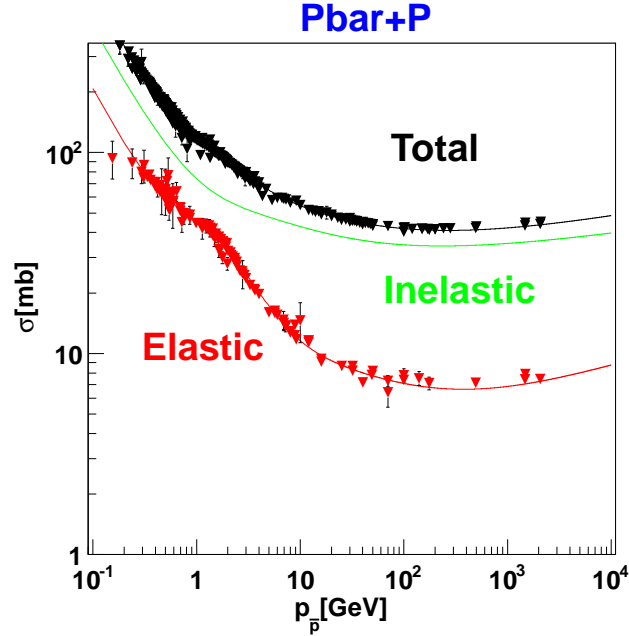


Figure 2.2: Total (black) and elastic (red) cross sections for the $\bar{p} + p$ reaction, as a function of the antiproton beam momentum. Data points are from [20], lines are from [23]. The contribution of inelastic events is also shown (green line).

section is factorized as:

$$\sigma_{\bar{p}p}^{tot}(mb) = \sigma_{asmpt}^{tot} \left[1 + \frac{C}{\sqrt{s - 4M^2}} \frac{1}{R_0^3} \left(1 + \frac{d_1}{s^{0.5}} + \frac{d_2}{s^1} + \frac{d_3}{s^{1.5}} \right) \right] \quad (2.3)$$

,

where:

$$\begin{aligned}\sigma_{asmpt}^{tot} &= 36.04 + 0.304 \left[\log \left(\frac{s}{33.0625} \right) \right]^2, \\ R_0 &= \sqrt{0.40874044 \sigma_{asmpt}^{tot} - B}, \\ B &= 11.92 + 0.3036 \left[\log \left(\frac{\sqrt{s}}{20.74} \right) \right]^2,\end{aligned}$$

and $C = 13.55 \pm 0.09$, $d_1 = -4.47 \pm 0.02$, $d_2 = 12.38 \pm 0.05$, $d_3 = -12.43 \pm 0.05$.

M is the proton mass and s is the total energy squared. The second factor in this formula describes the behaviour of the total cross section at low energies.

The expression of the elastic cross section is obtained by combining the approach of Refs. [24, 25] with the quasi-eikonal approximation of the reggeon theory [26]. This parametrization is valid in the range from 100 MeV up to 1000 GeV, and it can be written as:

$$\sigma_{pp}^{el} = \sigma_{asmpt}^{el} \left[1 + \frac{C}{\sqrt{s - 4M^2}} \frac{1}{R_0^3} \left(1 + \frac{d_1}{s^{0.5}} + \frac{d_2}{s^1} + \frac{d_3}{s^{1.5}} \right) \right] \quad (2.4)$$

where:

$$\begin{aligned}\sigma_{asmpt}^{el} &= 4.5 + 0.101 \left[\log \left(\frac{s}{33.0625} \right) \right]^2, \\ R_0 &= \sqrt{0.40874044 \sigma_{asmpt}^{tot} - B}, \\ B &= 11.92 + 0.3036 \left[\log \left(\frac{\sqrt{s}}{20.74} \right) \right]^2,\end{aligned}$$

and $C = 59.27 \pm 2.0$, $d_1 = -6.95 \pm 0.09$, $d_2 = 23.54 \pm 0.29$, $d_3 = -25.34 \pm 0.36$.

In the two previous equations, the total energy squared s and d_2 are expressed in $[\text{GeV}^2]$; R_0 in $[\text{GeV}^{-1}]$, B and C in $[\text{GeV}^{-2}]$; d_1 in $[\text{GeV}]$ and d_3 in $[\text{GeV}^3]$. The cross sections are in $[\text{mb}]$.

Fig. 2.2 shows that the elastic contribution amounts to $\sim 1/3$ of the total contribution. The difference between the total and elastic cross section parametrizations (green line) represents the contribution of inelastic events. It is of the order of 40 mb.

2.5.2 Production of light mesons

In proton antiproton annihilation, the production of light mesons such as the pions and kaons has a large cross section. Their spectrum has been widely measured by several experiment at Brookhaven and CERN facilities, and have been successfully interpreted within theoretical models, in particular, the statistical models (hot fireball picture). At PANDA, the analysis of these states as a function of the beam momentum will be important for two reasons:

- Their production mechanisms will shed light on the dynamical properties of the models based on QCD (quark counting rules).
- The knowledge of their cross sections is essential for the background studies, especially to the electromagnetic processes.

In this section, the annihilation cross sections of antiproton-proton into hadronic (pion and kaon) channels are considered and the related experimental data are compiled. Pion multiplicity in the final state is also analyzed in the kinematical domain accessible at PANDA. A parametrization for their cross sections is also given. This analysis is helpful for evaluating the total counting rates and serves as a basis to define trigger methods to extract reactions of interest in PANDA.

2.5.2.1 Total cross sections of light meson production

Experimental data on cross sections and angular distributions in $\bar{p}p$ annihilation concerning 230 final channels involving hadrons have been classified in Ref. [19]. Based on this compilation, that I updated using also Ref. [22], various cross sections for selected processes in the [0.01-10 mb] range have been collected and are illustrated in Figs. 2.3 and 2.4.

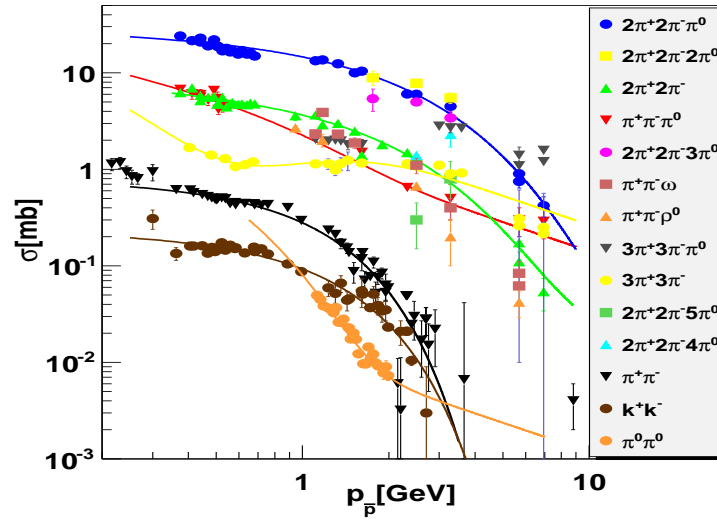


Figure 2.3: Cross sections for different inelastic channels in the $\bar{p} + p$ reaction as a function of $p_{\bar{p}}$.

The interest is focussed on the production of pions, or pions accompanied by nucleons. Fig. 2.3 shows that the most probable reaction involving pions, corresponds to more than three pions in the final state.

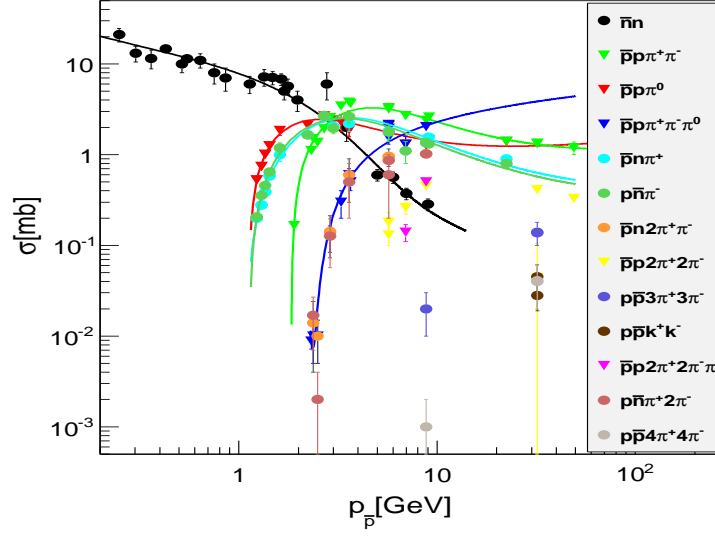


Figure 2.4: Cross sections for different annihilation channels in the $\bar{p} + p$ reaction as a function of $p_{\bar{p}}$.

The cross section for the reactions given in Fig. 2.3, and the charge exchange reaction presented in Fig. 2.4 can be parametrized as [27]:

$$\sigma = a e^{-b p_{\bar{p}}} + \frac{c}{p_{\bar{p}}}, \quad (2.5)$$

where $p_{\bar{p}}$ and σ are expressed in [GeV] and [mb] respectively. The coefficients a , b and c of the parametrization (Eq. 2.5) are given in Tab. 2.3 for the corresponding reactions.

Final state	a [mb]	b [GeV] ⁻¹	c [mb GeV]
$\pi^0 \pi^0$	3.88 ± 1.59	4.04 ± 0.36	0.01 ± 0.001
$\pi^+ \pi^- \pi^0$	8.16 ± 0.49	1.19 ± 0.05	0.33 ± 0.09
$2\pi^+ 2\pi^-$	6.86 ± 0.18	0.71 ± 0.018	0.25 ± 0.06
$3\pi^+ 3\pi^-$	-8.99 ± 0.53	2.23 ± 0.11	2.13 ± 0.72
$2\pi^+ 2\pi^- \pi^0$	24.28 ± 0.81	0.56 ± 0.008	0.007 ± 0.32
$\bar{n} n$	11.72 ± 1.082	0.7 ± 0.05	2.01 ± 0.31

Table 2.3: Coefficients for the parametrization, Eq. 2.5, of selected inelastic channel cross sections.

In Fig. 2.4 the cross sections for the production of proton-antiprotons (neutrons) with different numbers of charged and neutral pions (the other reactions with a larger number of pions are less probable) are illustrated. From threshold the cross sections

increase with the incident energy until a certain value of $p_{\bar{p}}$ for all reactions, except for the charge exchange reaction ($\bar{p} + p \rightarrow \bar{n} + n$) which has a sizeable cross section for $p_{\bar{p}} < 3$ GeV.

Above the corresponding threshold, the production of several pions accompanied by a proton-antiproton pair is more probable for a large incident energy than when the pions are produced alone. Consequently, the most probable reactions are the production of (4,5) pions, or the charge exchange reaction, but when the incident momentum increases it is necessary to evaluate, either the production of a larger number of pions (6,7 see following paragraph), or of a lower number (2,3) but accompanied by a proton-antiproton pair.

The difference between the behaviour of the cross sections can be explained at small incident energy by the effect of threshold. At threshold emitted particles are produced at rest. The pion final states can be obtained by the proton-antiproton annihilation at rest, but their production with a nucleon requires a certain threshold different from zero.

The cross section in [mb] for reactions given in Fig. 2.4 can be best parametrized as [27]:

$$\sigma = a_2 e^{b_2 p_{\bar{p}}} + c_2 / p_{\bar{p}} + d_2 \log(p_{\bar{p}}), \quad (2.6)$$

where a_2 , b_2 , c_2 and d_2 are given in Tab. 2.4, and $p_{\bar{p}}$ is expressed in GeV.

Final state	a_2 [mb]	b_2 [GeV] $^{-1}$	c_2 [mb GeV]	d_2 [mb]
$\bar{p}p\pi^0$	-39.59 ± 2.44	1.63 ± 0.01	7.12 ± 0.42	0.29 ± 0.03
$\bar{p}p\pi^+\pi^-$	-46.41 ± 0.86	0.83 ± 0.01	18.39 ± 0.44	0.21 ± 0.01
$\bar{p}p\pi^+\pi^-\pi^0$	99.34 ± 0.63	2.24 ± 0.02	-3.49 ± 0.09	1.15 ± 0.03
$\bar{p}n\pi^+$	-33.07 ± 1.36	0.99 ± 0.02	12.28 ± 0.73	0.07 ± 0.04
$p\bar{n}\pi^-$	-33.33 ± 1.25	1.06 ± 0.034	11.33 ± 0.75	0.06 ± 0.04

Table 2.4: Coefficients for the parametrization, Eq. 2.6, of selected inelastic channel cross sections.

2.5.2.2 Probability of n pion production

The existing experimental data on pion production in the $\bar{p}p$ annihilation are limited to a momentum up to ~ 10 GeV. In this section a phenomenological analysis of the pion multiplicity in the final state based on statistical models for $\bar{p}p$ annihilation is considered. A comparison to the experimental data and an extension to high energy, as accessible by the PANDA experiment, is performed.

The statistical models consider the emission of particles from a *fireball* of a volume Ω . The Fermi statistical model [28] is the simplest example: in the center of mass system (CMS), the incoming proton and antiproton appear as Lorentz-contracted spheres. After their annihilation, the total energy of the system is concentrated in a region of

space of volume Ω , which is sufficient to populate a large number of final states. This model suggests that statistical equilibrium will be obtained, and thus each final state, which is accessible via the strong interaction from the given initial state is excited according to its statistical weight. The statistical weight takes into account the spin and isospin weight factors. In the original Fermi model, only systems of non-interacting final state pions, confined in an arbitrary normalization volume were considered.

The statistical bootstrap model [29] is a more complex picture of the Fermi model where the strong interactions between the final state pions which lead to the formation of resonances are taken into account. In this model, the average pion multiplicity from $\bar{p} + p$ annihilation depends linearly on \sqrt{s} as is illustrated in Fig. 2.5.

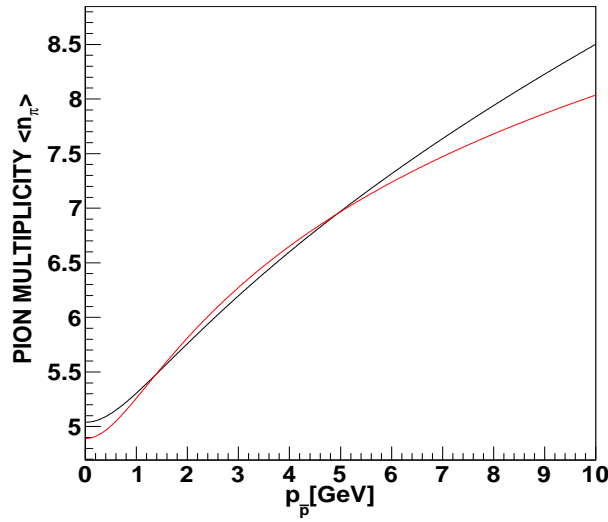


Figure 2.5: Pion multiplicity in $\bar{p} + p$ annihilation as a function of $p_{\bar{p}}$, from Eq. 2.7 (black line) and from Eq. 2.8 (red line).

In the bootstrap model, the dependence on $p_{\bar{p}}$ [GeV] can be parametrized as:

$$\langle n_\pi \rangle = 2.6 + 1.3 \left(1.76 + 1.88 \sqrt{0.88 + p_{\bar{p}}^2} \right)^{0.5}. \quad (2.7)$$

$\langle n_\pi \rangle$ is the pion multiplication.

A similar parametrization, which applies to the range $s^{1/2} \leq 30$ GeV, can be found in Ref. [30]:

$$\langle n_\pi \rangle = 2.65 + 1.78 \log \left(1.76 + 1.88 \sqrt{0.88 + p_{\bar{p}}^2} \right). \quad (2.8)$$

These two parametrizations reproduce the experimental data. For energies above the threshold, the average pion multiplicity for e^+e^- and $\bar{p}p$ at the same center of mass (CM) energy is essentially the same.

The n pion emission probability as a function of the pion multiplicity is illustrated in Fig. 2.6 for different momenta and can be parametrized as:

$$P(n_\pi) = \frac{1}{\sqrt{2\pi}D} e^{-\frac{(n_\pi - \langle n_\pi \rangle)^2}{2D^2}}, \quad \frac{D^2}{\langle n_\pi \rangle} = 0.174 \left(1.76 + 1.88 \sqrt{0.88 + p_{\bar{p}}^2} \right)^{0.2}. \quad (2.9)$$

where $\langle n_\pi \rangle$ is the pion multiplication and $P(n_\pi)$ is the probability for the n -pion emission, obtained from Eq. 2.7, which is consistent with the existing experimental values. The standard deviation D^2 increases with $\langle n_\pi \rangle$ and with $p_{\bar{p}}$.

The pion multiplicity in the final state of the $\bar{p} + p$ annihilation depends on the incident energy. In Fig. 2.6 it is seen that the contribution of six and seven pions (any charge state) in the final state is larger than the five pion contribution for $p_{\bar{p}} > 5$ GeV. At lower momenta, five pion emission has the largest contribution: the annihilation at rest is dominated by the emission of 5 five pions.

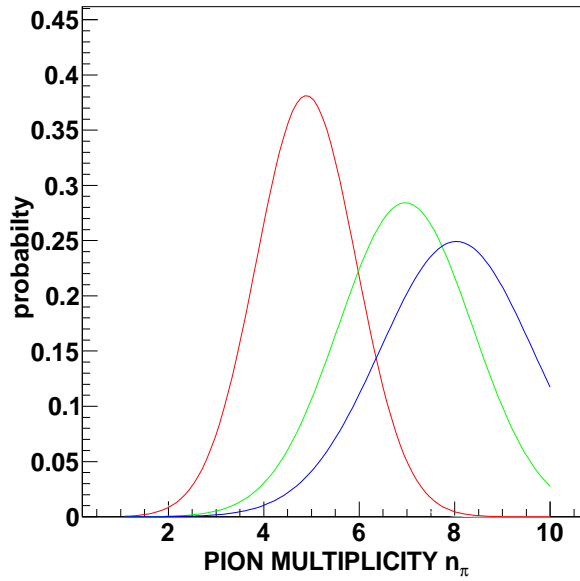


Figure 2.6: Probability for the emission of n pions in $\bar{p} + p$ annihilation as a function of pion multiplicity, from Eq. 2.9 for different incident momenta: at rest (red line), $p_{\bar{p}}=5$ GeV (green line), $p_{\bar{p}}=10$ GeV (blue line).

2.5.2.3 $\pi^+\pi^-$ and K^+K^- channels

Experimental measurements of pion and kaon cross sections can be found at the same value of incident energy, which allows the calculation of their ratio for a given incident momentum (Fig. 2.7).

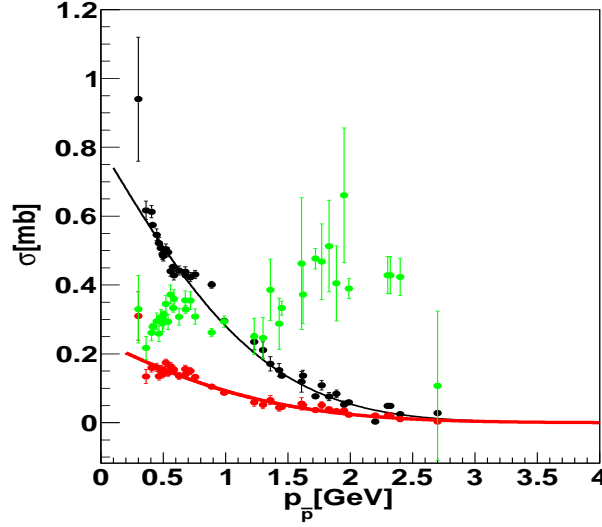


Figure 2.7: Pion (black circles) and kaons (red circles) cross section in the $\bar{p}p$ reaction as a function of $p_{\bar{p}}$, and their ratio (green circles).

The measurement of this ratio at PANDA with the high energy antiproton beams gives useful information on the reaction mechanism and opens the investigation of related phenomena, such as the excitation of physical vacuum through $\bar{p}p$ annihilation [31]. Fig. 2.7 shows that this ratio depends on the momentum, and tends to unity at high energy. The description of this ratio is a challenge for theoretical models [32, 33]. The $\pi^+\pi^-$ and K^+K^- cross sections can be parametrized as [27]:

$$\sigma = a_3 e^{-(b_3 p_{\bar{p}} + c_3 p_{\bar{p}}^2 + d_3)}. \quad (2.10)$$

a_3 , b_3 , c_3 and d_3 are given in the Tab. 2.5, and $p_{\bar{p}}$ is expressed in GeV.

Final state	a_3 [mb]	b_3 [GeV] $^{-1}$	c_3 [GeV] $^{-2}$	d_3
$\pi^+\pi^-$	1.34 ± 0.91	0.79 ± 0.06	0.29 ± 0.025	0.49 ± 0.68
K^+K^-	0.81 ± 1.99	0.75 ± 0.1	0.19 ± 0.04	1.23 ± 2.44

Table 2.5: Coefficients for the parametrizations of $\bar{p}+p \rightarrow K^++K^-$ and $\bar{p}+p \rightarrow \pi^++\pi^-$ cross sections.

2.5.3 Production of charmonium and charmed mesons

The charmonium spectroscopy is one of the the main motivations for the PANDA experiment. Charmonium is a bound state of charmed and anti-charmed ($\bar{c}c$) quarks. The

charmonium system can be understood as a non-relativistic bound state where the $c\bar{c}$ spectrum can be computed within the framework of non relativistic (heavy-quark) potential models. In this way, masses and widths are obtained by solving the Schrödinger equation. Precision measurements of the charmonium spectra and comparison with theory calculations will provide better understanding of the QCD and give information on the quark confinement potential.

The experimental techniques used for the measurement of charmonium spectra can be classified into two groups.

The first one is based on e^+e^- annihilations (BaBar [34], BELLE [35], BESIII [36]). In e^+e^- annihilations, direct formation is possible only for the states with the same quantum numbers as the photon ($J^{PC} = 1^{--} : J/\psi, \psi'$ and $\psi(3770)$). All other states can be produced in the radiative decays of the vector states. Charmonium states produced at the B-factories are observed via the decays of the B-meson.

The second one is based on the $\bar{p}p$ annihilation (LEAR [6], Fermilab E760/E835 [37] and PANDA). In $\bar{p}p$ collisions, the coherent annihilation of the 3 quarks in the proton with the 3 antiquarks in the antiproton populates directly the states with all non-exotic quantum numbers. The antiproton beam provides high resolution in mass and width for all charmonium states because in this case they are directly produced and their measurement will depend only on the beam parameters. However this technique suffers, in comparison with e^+e^- annihilation, from the hadronic background.

The charmonium spectrum can be described actually as follows:

- Below the threshold of the open charm $\bar{D}D$ mesons ($\sqrt{s} = 3.73$ GeV), all the 8 charmonium states have been observed:
 - Extensive measurements of the masses and widths of the ψ states have been performed at e^+e^- machines where they are produced directly via a virtual-photon exchange.
 - The available data on the states $h_c[J^{PC} = 1^{+-}]$, $\eta_c(1S)$, and $\eta_c(2S)[0^{-+}]$ require more precision.
- Above the threshold, the spin triplet S-wave $\psi(4040) [\psi(3^3S_1)]$, $\psi(4415) [\psi(4^3S_1)]$, as well as the D-wave $\psi(3770) [\psi(1^3D_1)]$, and $\psi(4160) [\psi(2^3D_1)]$ have been found. Many charmonium states have been recently observed (i.e, $Z_c(3900)$ by BESIII [38], $Z_c(4050, 4250, 4430)$ by the Belle collaboration [39, 40], ...). While some of these states appear to be consistent with conventional $c\bar{c}$, others do not. This region needs to be explored in more details to find the missing D-wave states, and explain the newly discovered states ($X, Y, Z, c\bar{c}, \dots$)

The spectrum can be divided into two parts:

- Not all the predicted charmonium states have been discovered.

- Different states have been recently found but their interpretation is not clear.

In $\bar{p}p$ annihilation, the resolution in mass and width of charmonium states is determined by the precision in the measurement of the beam energy and beam energy spread respectively. The key ingredient for the PANDA physics program is a high-intensity and a high-resolution beam of antiprotons in the momentum range of 1.5 to 15 GeV. Such a beam gives access to a center-of-mass energy range from 2.2 to 5.5 GeV in $\bar{p}p$ annihilations. In this range, a rich spectrum of hadrons with various quark configurations can be studied as it is illustrated in Fig. 2.8.

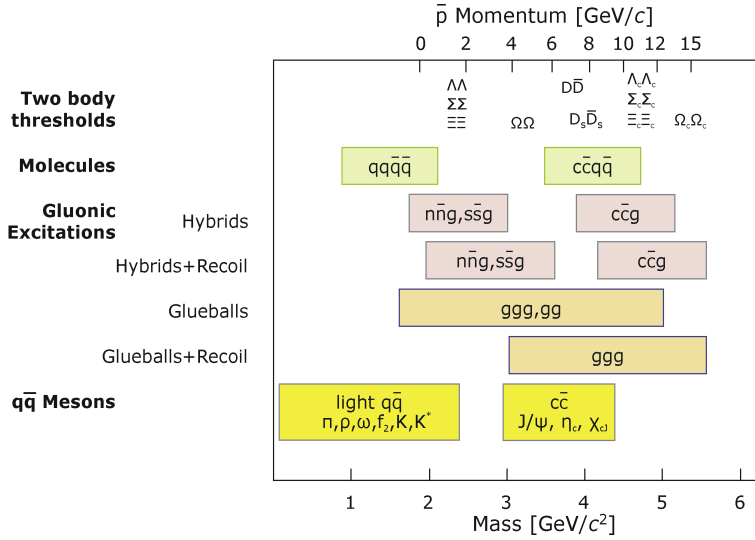


Figure 2.8: Accessible hadrons with the antiproton beam at FAIR, from [18]. The upper scale displays the antiproton momentum and the lower one the hadron mass.

Search of gluonic excitations, hybrids and glueballs, where the gluons act as principal component, is also a main goal of PANDA. In particular, hadronic states which contain charmed quarks and gluon-rich matter become experimentally accessible. The additional degrees of freedom carried by the gluons allow these hybrids and glueballs to have J^{PC} exotic quantum number. The $\bar{p}p$ annihilation is intrinsically a gluon rich process which can create gluonic excitations in a direct way. PANDA will extend the search for those objects into the charmonium mass range with high statistics and spin-parity analysis in fully exclusive measurements.

2.5.4 Production of strange and charmed baryons

In $\bar{p}p$ annihilation, a large fraction of the inelastic cross section is associated with channels resulting in a baryon anti-baryon pair in the final state [18]. Charmed and strange baryon spectroscopy provides an ideal tool for studying the dynamics of the light quarks in the environment of a heavy quark. Data on charmed and strange baryons are needed. A particular benefit of using antiprotons in the study of (multi)

strange and charmed baryons is that in $\bar{p}p$ annihilation no production of extra kaons or D mesons is required for strangeness or charm conservation respectively. This reduces the energy threshold as compared to pp collisions and thus the number of background channels. In addition, the requirement that the patterns found in baryon and anti-baryon channels have to be identical reduces the systematic experimental errors.

2.5.5 Electromagnetic processes and hadronic background

The PANDA experiment offers also the opportunity to investigate the electromagnetic structure of the proton through the production of virtual or real photons. Nevertheless it has to be pointed out that the measurement of electromagnetic processes in $\bar{p}p$ annihilation represents an experimental challenge due to the smallness of their cross section with respect to the huge hadronic background.

The reactions of interest for proton electromagnetic form factor measurements in the Time-Like region involve two leptons in the final state and no hadrons ($\bar{p} + p \rightarrow \ell^+ + \ell^-$, $\ell = e, \mu, \tau$), or two leptons and a pion for the near threshold and the unphysical kinematical regions ($\bar{p} + p \rightarrow \ell^+ + \ell^- + \pi^0$). The related cross sections are in the [nb] scale. The reactions involving hadrons in the final state are orders of magnitude larger than the channels of interest. For each electron produced, about 10^6 pions are produced in the similar kinematical region. Therefore, pions have to be identified from electrons in the simulation at the level of $\sim 10^{-8}$. In fact, two (three) pion production is the reaction that constitutes the background which is the most difficult to eliminate [41]. Concerning the annihilation reaction $\bar{p} + p \rightarrow \ell^+ + \ell^-$, channels with more than three hadrons in the final state will be efficiently identified due to the large acceptance of the PANDA detector and the good tracking resolution. The larger background is then expected to come from the annihilation into two hadrons as $\bar{p}p \rightarrow \pi^+\pi^-$, $\bar{p}p \rightarrow \pi^0\pi^0$ and $\bar{p}p \rightarrow K^+K^-$. The cross sections for the neutral (charged) hadron channels production are about five (six) orders of magnitude larger than for the reaction of interest. Concerning $\bar{p}p \rightarrow \pi^0\pi^0$, photons from the π^0 can produce e^+e^- pairs after conversion in the material. One (or both) pion via Dalitz decay can also give e^+e^- pair(s) but with probability $10^{-2}(10^{-4})$. For $\bar{p}p \rightarrow K^+K^-$, kaons, being heavier, have lower probability of misidentification than pions. The detailed study of $\bar{p}p$ annihilations into two charged pions and the related simulation analysis within the PANDARoot framework will be the subject of chapter 6.

In addition to the proton Time-Like form factors, the consideration of the so-called Generalized Parton Distributions (GPDs) is one of the aspects which can provide deep insight about the internal structure of the nucleon (for a recent review see Ref. [42] and references therein). The GPDs give detailed information on the longitudinal momentum and transverse position distribution of the constituent quarks and gluons, they allow to probe the nucleon as a 3-dimensional object. QCD factorisation theorems at the amplitude level allow to access GPDs in various hard exclusive reactions such as

the Deep Virtual Compton Scattering (DVCS) $ep \rightarrow ep\gamma$ (Fig. 2.9), where the photon is emitted from the nucleon, or the Wide Angle Compton Scattering $\gamma p \rightarrow \gamma p$ (WACS). The factorisation theorem allows to describe these processes into a hard perturbative QCD and a soft part parametrized by GPDs. Their crossed channels can be accessible in antiproton proton annihilation at the PANDA experiment. The crossed diagram of WACS is the exclusive annihilation of proton antiproton into two photons $\bar{p}p \rightarrow \gamma\gamma$ (Fig. 2.10) at large polar angle in the CMS [43]. The corresponding amplitudes that parametrise the soft part of this process (i.e. the counterparts of GPDs) are called generalised distribution amplitudes (GDAs).

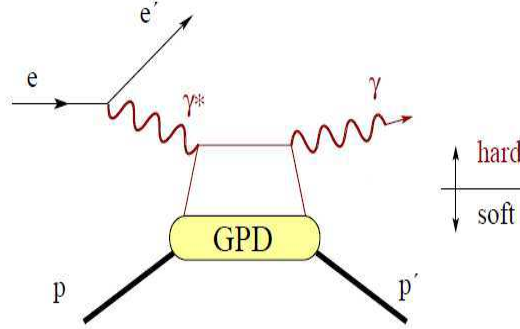


Figure 2.9: Factorization of DVCS into a hard part described by perturbative QCD and a soft part described by GPDs.

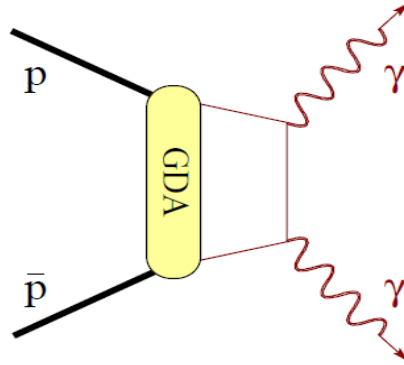


Figure 2.10: The diagram for the inverted WACS processes $\bar{p}p \rightarrow \gamma\gamma$ described by GDAs.

The annihilation reaction, $\bar{p}p \rightarrow \pi^0\gamma$, where one photon is replaced by a pseudo-scalar meson can be also described by GPDs and measured at PANDA. The main background for the crossed channel Compton scattering $\bar{p}p \rightarrow \gamma\gamma$ ($\bar{p}p \rightarrow \gamma\pi^0$) comes from reactions with neutral hadrons in the final state, like $\bar{p}p \rightarrow \pi^0\pi^0$. The number of the exclusive background events considered is roughly two to three orders of magnitude

higher than the number of events of interest [18].

Drell-Yan (DY) processes, $\bar{p}p \rightarrow \mu^+\mu^-X$, are considered also as a standard tool for probing the partonic structure of hadrons. It can be used to get information on transverse spin effects and transverse momentum within the nucleon. The DY process is an electromagnetic effect in which a quark and antiquark from a pair of interacting hadrons annihilate to give a lepton pair at high energy hadron-hadron colliders. PANDA offers a unique opportunity to measure these processes in $\bar{p}p$ annihilation probing both the sea and the valence quark region. The exclusive DY annihilation reaction $\bar{p}p \rightarrow \gamma^*\gamma \rightarrow e^+e^-\gamma$ can be also measured at PANDA. This process can be factorized (Fig. 2.11), at large invariant mass of the lepton pair (hard scale), by a hard sub-process amplitude and the so-called Transition Distribution Amplitudes (TDAs) that parametrize the transition of a proton into a virtual photon [44]. TDAs are non perturbative objects describing the transition between two particles.

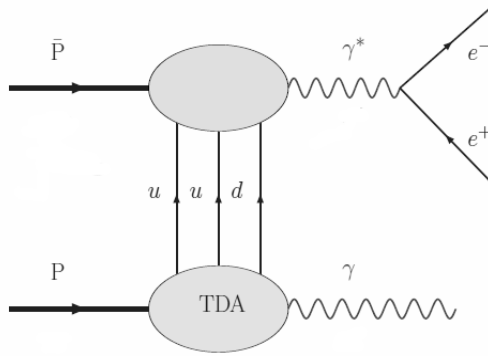


Figure 2.11: Factorization of $\bar{p}p \rightarrow e^+e^-\gamma$ into a hard sub-process and proton to photon transition distribution amplitude (TDA).

The same theoretical framework can also be applied to other reactions involving mesons in the final state, like $\bar{p}p \rightarrow \gamma^*\pi(\gamma^*\rho)$ [45]. Crossing symmetry relates these reactions to backward deep electro-production which may be accessed at electron accelerators. As in previous cases, reactions involving two or more hadrons, in particular pions, in the final state ($\bar{p}p \rightarrow \pi^0\pi^0$, $\bar{p}p \rightarrow \pi^+\pi^-\pi^0$, $\bar{p}p \rightarrow \pi^+\pi^-\rho^0$,...) constitute an important background for the measurement of channels with creation of a lepton pair.

2.5.6 Other topics

Let us mention other major topics in proton antiproton annihilation which will be addressed at PANDA and are described in Ref. [18]:

- Hypernuclear physics: a full domain of research which is of great interest for the PANDA collaboration is the hypernuclear physics. Besides hyperon-hyperon production, double hypernuclei will be produced and studied. Hypernuclei are

nuclear system in which one or more nucleons are replaced by one or more hyperons. A new quantum number, strangeness, is introduced into the nucleus, adding a third axis to the nuclear chart. The hyperon is not restricted by the Pauli principle in populating all possible nuclear states, in contrast to neutrons and protons. The hunting of the H-dibaryon "uuddss" [46] is one of the main challenges.

- Study of hadrons in the nuclear matter: the study of medium modifications of hadrons embedded in hadronic matter is aimed at understanding the origin of hadron masses in the context of spontaneous chiral symmetry breaking in QCD and its partial restoration in a hadronic environment. So far experiments have been focused on the light quark sector. The high-intensity antiproton beam will allow an extension of this program to the charm sector both for hadrons with hidden and open charm.

Chapter 3

Electromagnetic Form Factors of the proton

3.1 The concept of hadron electromagnetic form factors

Since the beginning of the last century, electron scattering has been considered as an effective tool for the study of the nucleon and nuclear structure. The cross section for the electron scattering in the Coulomb field of a static nucleus was first described by the well known Rutherford's formula (1911) [47]. It applies to non relativistic, spin zero, point-like particle scattering. The non relativistic approach is justified if the momenta of the particles are much smaller than their masses. The Rutherford formula for the electron scattered from a static point charge is:

$$\frac{d\sigma}{d\Omega} = \frac{Z^2\alpha^2}{16E_k^2 \sin^4(\vartheta/2)}, \quad (3.1)$$

where $d\Omega = 2\pi d \cos \vartheta$ is the solid angle of the scattered electron at polar angle ϑ in the laboratory (Lab) frame. E_k is the kinetic energy of the incident electron, $\alpha = e^2/(4\pi)$ is the electromagnetic coupling constant (e is the elementary charge) and Z is the atomic number of the target.

In 1929, N. F. Mott [48] gave for the first time a quantum mechanical formula for the scattering of unpolarized relativistic electrons off an atomic nucleus, considered as point-like particle, in the Born approximation. The Mott's formula describes the case where the incident particle (electron) is assumed to carry a spin (and a Dirac magnetic moment), but the structure-less scattering center (the nucleus) has neither spin nor magnetic moment. It was derived for the elements that satisfy the inequality $Z\alpha \ll 1$ (approximation of Mott). The Mott differential cross section, neglecting the target

recoil, is written as follows:

$$\frac{d\sigma^{Mott}}{d\Omega} = \frac{Z^2 \alpha^2 \cos^2(\vartheta/2)}{4\epsilon_1^2 \sin^4(\vartheta/2)}, \quad (3.2)$$

where ϵ_1 is the total energy of the incident electron in the Lab frame. Corrections to the Mott's formula, for more massive nuclei (large Z), have been later investigated (1948) and summarized in Refs. [49, 50].

3.1.1 Extension to a composite targets

The scattering amplitude of an incident particle with momentum \vec{p} and charge $Z_a e$ (which can be associated to a plane wave vector $\vec{k} = \vec{p}/\hbar$) on a unit charge e_j at a position ρ_j (Fig. 3.1), is defined by:

$$A_j = Z_a e e_j e^{i\vec{k} \cdot \vec{\rho}_j} e^{i\vec{k}' \cdot (\vec{r} - \vec{\rho}_j)} = Z_a e e^{i\vec{k}' \cdot \vec{r}} e_j e^{i\vec{q} \cdot \vec{\rho}_j} \quad (3.3)$$

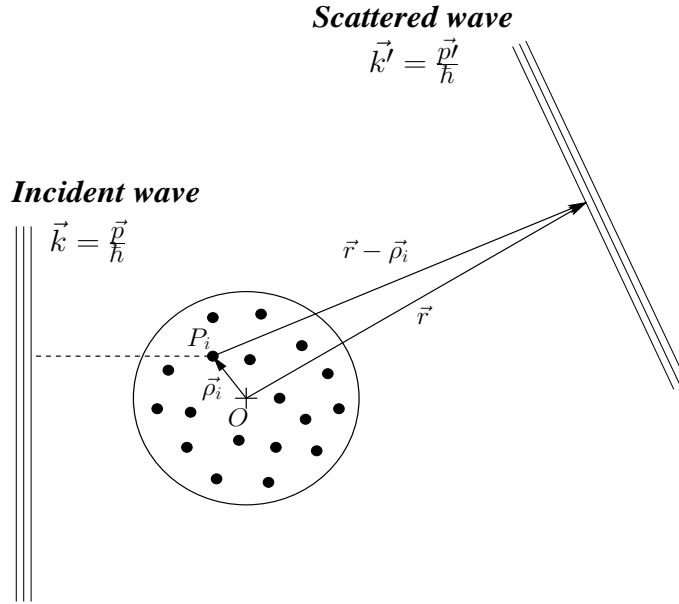


Figure 3.1: Schematic view of elastic scattering on a composite object [53].

The scattering generates a spherical wave, that can be observed at large distances as a plane wave $\vec{k}' = \vec{p}'/\hbar$. In Eq. 3.3, $\vec{r} - \vec{\rho}_j$ is the vector from the observation point to the charge e_j , and $\vec{q} = \vec{p} - \vec{p}'$ ($\hbar = 1$) is the momentum transfer. The factor $e^{i\vec{k} \cdot \vec{\rho}_j}$ defines the phase of the incident plane wave at the interaction point, and $e^{i\vec{k}' \cdot (\vec{r} - \vec{\rho}_j)}$ determines the phase of the scattered wave at the observation point. Similarly to optics, the total

scattered amplitude on the nucleus can be calculated as the sum of the amplitudes on the individual charges (neglecting the interactions between charges):

$$A = \sum_j A_j = Z_a e e^{i\vec{k}' \cdot \vec{r}} \sum_j e_j e^{i\vec{q} \cdot \vec{\rho}_j}. \quad (3.4)$$

In quantum mechanics, $\vec{\rho}_j$ represent the position operators of the internal motion in the target. By neglecting the target recoil effect (non relativistic limit), the last term is replaced by the corresponding mean value in the ground state of the target:

$$\langle j | \sum_j e_j e^{i\vec{q} \cdot \vec{\rho}_j} | j \rangle = \int \rho(\vec{x}) e^{i\vec{q} \cdot \vec{x}} d\vec{x}, \quad (3.5)$$

where $\rho(\vec{x})$ is the charge density at distance \vec{x} from the center of the target. This allows to introduce the notion of form factor (FF), normalized to the full charge volume as:

$$F(\vec{q}) = \frac{\int \rho(\vec{x}) e^{i\vec{q} \cdot \vec{x}} d\vec{x}}{\int \rho(\vec{x}) d\vec{x}}, \quad \int \rho(\vec{x}) d\vec{x} = Z_t e, \quad (3.6)$$

where Z_t is the atomic number of the target.

The first consideration of the finite nuclear size effects on the electron scattering appeared with Guth (1943) in Ref. [51]. Later, M. E. Rose (1948) [52], Smith (1951) [54] and others (see [55] and references therein), have shown that the elastic scattering formula of an incident point charge on a nucleus with finite size, must have the form:

$$\frac{d\sigma}{d\Omega} = \frac{d\sigma^{Mott}}{d\Omega} \left| \int \rho(\vec{x}) e^{i\vec{q} \cdot \vec{x}} d\vec{x} \right|^2 \quad (3.7)$$

The resulting cross section is equivalent to the cross section for scattering from a point source multiplied by the FF squared.

3.1.2 Charge radius

For small values of the momentum transfer, one can develop $F(\vec{q})$ in a Taylor series expansion on $\vec{q} \cdot \vec{x}$:

$$\begin{aligned} F(\vec{q}) &= \frac{1}{Z_t e} \int d\vec{x} e^{i\vec{q} \cdot \vec{x}} \rho(\vec{x}) \\ &= \frac{1}{Z_t e} \int d\vec{x} \left[1 + i\vec{q} \cdot \vec{x} - \frac{1}{2}(\vec{q} \cdot \vec{x})^2 + \dots \right] \rho(\vec{x}) \\ &= \frac{1}{Z_t e} \int_0^\infty r^2 dr \int_0^{2\pi} d\varphi \\ &\quad \int_{-1}^1 d \cos \vartheta \left[1 + i|\vec{q}|r \cos \vartheta - \frac{1}{2}|\vec{q}|^2 r^2 \cos^2 \vartheta \right] \rho(\vec{x}). \end{aligned} \quad (3.8)$$

The second term in the series expansion (Eq. 3.8) does not give any contribution, as $\vec{q} \cdot \vec{x} = |\vec{q}|r \cos \vartheta$ and $\int_{-1}^1 \cos \vartheta d \cos \vartheta = 0$.

In case of spherical symmetry, one can write:

$$F(\vec{q}) \sim 1 - \frac{1}{6} |\vec{q}|^2 \langle r_c^2 \rangle + O(q^2), \quad (3.9)$$

The mean square root charge radius of the target, $\langle r_c^2 \rangle$, is defined as:

$$\langle r_c^2 \rangle = \frac{\int_0^\infty r^4 \rho(r) dr}{\int_0^\infty r^2 \rho(r) dr}, \quad (3.10)$$

and the FF (Eq. 3.6):

$$F(\vec{q}) = \frac{4\pi \int \frac{r}{|\vec{q}|} \sin(qr) \rho(r) dr}{4\pi \int_0^\infty r^2 \rho(r) dr}. \quad (3.11)$$

The typical shapes of charge density of the target, in case of spherical symmetry, and the corresponding form factors (FFs) (Eq. 3.11) and radii (Eq. 3.10) are shown in Table 3.1.

density $\rho(r)$	form factor $F(\vec{q})$	charge radius $\langle r_c^2 \rangle$	name of model
δ	1	0	point-like
e^{-ar}	$\frac{a^4}{(\vec{q} ^2 + a^2)^2}$	$\frac{12}{a^2}$	dipole
$\frac{e^{-ar}}{r}$	$\frac{a^2}{ \vec{q} ^2 + a^2}$	$\frac{6}{a^2}$	monopole
$\frac{e^{-ar^2}}{r^2}$	$e^{- \vec{q} ^2/(4a^2)}$	$\frac{1}{2a}$	Gaussian
ρ_0 for $r \leq R$ 0 for $r \geq R$	$\frac{3(\sin X - X \cos X)}{X^3}$ $X = \vec{q} R$	$\frac{3}{5}R^2$	square well

Table 3.1: Charge density, form factor and root mean squared radius [53].

In a non relativistic approach the four momentum transfer squared is $q^2 \sim -|\vec{q}|^2$.

3.1.3 Rosenbluth formula: magnetic contribution

The first evidence of the non point-like structure of the proton appeared in 1928 with the measurement of its anomalous magnetic moment. Stern [56] observed that the proton magnetic moment was ~ 2.8 times higher than expected for a point-like particle.

Elastic scattering of high energy electrons taking into account the magnetic moment of the proton has been considered first by Rosenbluth in 1950 [57]. He showed that there

is a contribution to the elastic scattering cross section due to both the Dirac and the Pauli (anomalous) components of the proton's magnetic moment. Rosenbluth gave a relativistic formula for the elastic ep differential cross section which takes into account the spin of both electron and proton, and the structure of the proton through the contribution of its anomalous magnetic moment. The Rosenbluth formula was given in terms of effective charge and anomalous magnetic moments which are functions of the momentum transfer squared. The effective charge of the electron differs from its natural charge due to radiative corrections to the scattering. The modification of the proton charge and anomalous magnetic moment are assumed to be due to the action of a virtual meson field.

Later, phenomenological FFs, F_1 and F_2 have been introduced by Foldy and Salzman [58, 59], Yennie, Levy, and Ravenhall [60]. Foldy and Salzman provided the most general form of the electromagnetic current of the nucleon in terms of two invariant functions which depend only on invariants, the mass of the nucleon and the momentum transfer squared. The explicit derivation of the electromagnetic current of proton is described in the appendix A. F_1 was introduced to take care of the dependence on the charge and the Dirac magnetic moment. F_2 is an independent quantity and takes care of the dependence on the Pauli magnetic moment. Based on the Rosenbluth and Foldy formalism, Hofstadter [55] wrote the differential cross section of the elastic ep scattering as follows:

$$\frac{d\sigma}{d\Omega} = \left(\frac{d\sigma^{Mott}}{d\Omega} \right) \frac{\epsilon_2}{\epsilon_1} [F_1^2 + \tau F_2^2 + 2\tau \tan^2(\vartheta/2)(F_1 + F_2)^2], \quad \tau = -q^2/4M^2,$$

where ϵ_1 (ϵ_2) is the energy of the incident (scattered) electron in the Lab system. F_1 and F_2 (Dirac and Pauli FFs) are functions of the momentum transfer squared q^2 . The factor ϵ_2/ϵ_1 describes the recoil of the target.

3.2 Proton electromagnetic form factors

3.2.1 Model independent description

Nucleon electromagnetic FFs describe the modifications of the point-like photon-nucleon vertex due to the structure of nucleons. They represent a phenomenological contribution of the strong interaction in the electromagnetic processes involving non point-like particles. The number of independent electromagnetic FFs is determined by the spin of the hadron taking into account symmetry properties of the electromagnetic interaction under the Charge, Parity, and Time transformations. In a P and T invariant theory, the structure of any particle of spin S is parametrized in terms of $(2S+1)$ FFs. Protons and neutrons are described by two FFs, Dirac (F_1) and Pauli (F_2), which are functions of one kinematical variable, the momentum transfer squared. The deuteron (spin one particle) is described by three FFs, charge, electric, and quadrupole. The

scalar particles, with spin zero, have one FF.

Schematically, at small momenta (large internal distances) FFs probe the size of the nucleon. At high energies (short distances) they encode information on the quark substructure of the nucleon as described by the QCD. Their behavior should follow scaling laws, predicted by perturbative QCD (pQCD). The precise knowledge of FFs in a wide kinematical region probes the transition region, from non perturbative to perturbative QCD. FFs also contain important information on nucleon radii and vector meson coupling constants.

The traditional way to determine proton electromagnetic FFs consists in the measurement of electron-proton elastic scattering, assuming that the interaction occurs through the exchange of a virtual photon (Fig. 3.2): 1- the electromagnetic interaction of leptons ($e\gamma^*e$ vertex) is well defined by the theory of Quantum ElectroDynamics (QED); 2- the mechanism of the reaction is well known (one photon exchange), and 3- the vertex describing the interaction of the virtual photon with the proton ($p\gamma^*p$) contains the unknown structure, being parametrized in terms of the proton FFs.

The elastic electron proton scattering ep involves negative values of momentum transfer squared q^2 defined as:

$$q^2 = q_0^2 - \vec{q}^2 = (k_1 - k_2)^2 < 0, \quad (3.12)$$

where k_1 (k_2) is the four vector of the electron in the initial (final) state. The region accessible through the scattering channel is called Space-Like (SL) region (the space component of the four momentum transfer squared, q^2 , is larger than the time component). In SL region it is convenient to use the positive quantity $Q^2 = -q^2 > 0$ instead of q^2 .

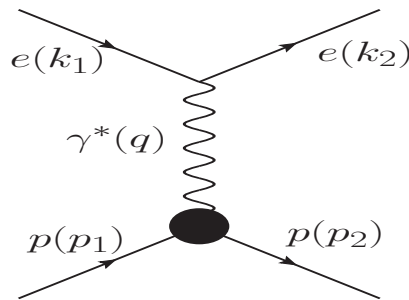


Figure 3.2: Feynman diagram for the elastic electron proton scattering in the Born approximation.

Information on proton electromagnetic FFs can be also extracted in the crossed symmetry channels: $e^+e^- \rightarrow \bar{p}p$ (Fig. 3.3) and $\bar{p}p \rightarrow e^+e^-$. Crossing symmetry, which holds at the tree level, states that the same amplitude describes the crossed

processes, which occur in different kinematical regions. Therefore, the cross section of the annihilation channels is described by the same functions F_1 and F_2 introduced to parametrize the elastic electron proton scattering.

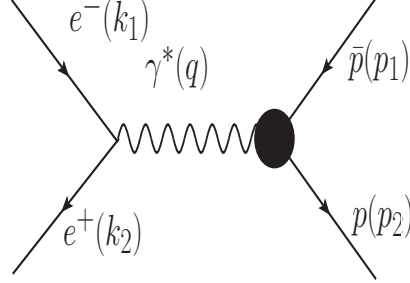


Figure 3.3: Feynman diagram for the electron positron annihilation into proton antiproton pair.

The annihilation channels involve positive values of the momentum transfer squared (Time-Like (TL) region):

$$q^2 = s = (p_1 + p_2)^2 = (k_1 + k_2)^2, \quad q^2 > 4M^2, \quad (3.13)$$

where p_1 (p_2) and k_1 (k_2) are the four vectors of the antiproton (proton) and electron (positron). $q^2 = 4M^2$ is the kinematical threshold of the proton antiproton production. The unitarity applied to the S-matrix elements of the considered processes and implemented through the optical theorem [61], constrains FFs to be real in SL region and complex in TL region. Using the optical theorem, the imaginary part of the hadronic current J which describes the coupling of the virtual photon to the proton-antiproton pair can be decomposed as (Fig. 3.4):

$$\text{Im} [\langle \bar{p}(p_1)p(p_2)|J|0 \rangle] \sim \sum_n \langle \bar{p}(p_1)p(p_2)|J^\dagger|n \rangle \langle n|J|0 \rangle, \quad (3.14)$$

where n runs over all the on-shell hadronic intermediate states allowed by conservation laws.

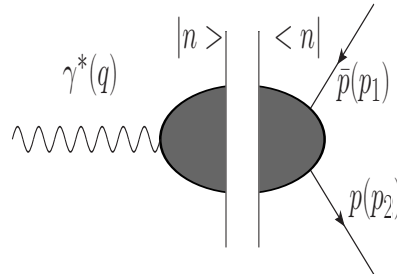


Figure 3.4: Spectral decomposition of the proton vertex based on the unitarity condition in the time-like region of momentum transfer squared.

The lightest hadronic state to be considered, which carries the same quantum numbers as the $p\bar{p}$ system and hence the first that opens, is $\pi^+\pi^-$. Therefore, the TL proton FFs acquire an imaginary part different from zero at $q^2 \geq 4m_\pi^2$ (the threshold of $\pi^+\pi^-$ creation). The region for $0 < q^2 < 4M^2$ is called the unphysical region.

3.2.1.1 Space- and Time-Like region connection

Based on unitarity and analyticity, dispersion relations give a unified frame for the description of FFs in the whole kinematical region $-\infty < q^2 < \infty$. Using SL and TL data as input, they can give predictions about the behavior of FFs (assumed analytical functions) in the regions where data are absent.

Let us consider the FFs as function of the variable $z = q^2$ taken as the real axis in the complex plane. The Schwarz reflection principle ($(F_i^*(z) = F_i(z^*))$) allows to analytically continue a function from one side of the plane to the other side, if along a part of the real axis the function does not contain singularities. The singularities exist whenever the variable q^2 has values for which the particles in intermediate states become on-mass-shell. From the previous section, we deduce that FFs have singularities at $q^2 \geq 4m_\pi^2$. Using the Cauchy theorem and the Schwarz reflection principle one can write the dispersion relation for the proton FFs as follows:

$$F(q^2) = F(0) + \frac{1}{\pi} \int_{4m_\pi^2}^{\infty} \frac{\text{Im}F(x)}{x - q^2} dx. \quad (3.15)$$

In addition, the asymptotic behavior of the nucleon FFs is driven by the Phragmén-Lindelöf theorem [62] which applies to analytical functions of complex variables:

$$\lim_{q^2 \rightarrow -\infty} |F^{SL}(q^2)| = \lim_{q^2 \rightarrow +\infty} |F^{TL}(q^2)| \quad (3.16)$$

The Phragmén-Lindelöf theorem states that: *given an analytic function $F(z)$, such that $|F(z)| \rightarrow a$ as $z \rightarrow \infty$ along a straight line, and $|F(z)| \rightarrow b$ as $z \rightarrow \infty$ along another straight line, if $F(z)$ is regular and bounded in the angle between these two lines, then $a = b$ and $|F(z)| \rightarrow a$ uniformly in this angle.* Identifying z with the q^2 axis, in TL region the imaginary part of FFs should vanish and the relative phase (between the SL and TL FF) is equal to zero or π . This prediction which constitutes an additional argument to the analytical nature of the FFs can be experimentally verified at PANDA.

3.2.1.2 The Sachs form factors

The Sachs FFs, electric G_E and magnetic G_M , were introduced [63] as a linear combinations of Dirac's and Pauli's FFs. They are expressed in terms of F_1 and F_2 as:

$$G_E = F_1 - \tau F_2, \quad G_M = F_1 + F_2, \quad \tau = -q^2/4M^2, \quad (3.17)$$

where M is the nucleon (proton in the present case) mass. The motivation of considering these combinations is due to the fact that, in a specific frame called the Breit

frame, the Sachs FFs are related to the scalar and vector parts of the electromagnetic current. Moreover in this system as in the case of non relativistic approximation, G_E and G_M correspond respectively to the three-dimensional Fourier transforms of the charge and magnetic spatial distributions within the nucleon. In the Breit frame, the energy of the virtual photon vanishes, and the transferred 4-momentum is $q = (0, \vec{q})$.

3.2.1.3 Boundary and asymptotic behavior

The Dirac and Pauli FFs are normalized at $Q^2 = 0$ according to the proton charge for F_1 and to the anomalous magnetic moment for F_2 :

$$F_1(0) = 1, \quad F_2(0) = \mu_p - 1, \quad (3.18)$$

where $\mu_p = 2.792847351(28)$ is the proton magnetic moment in units of nuclear magnetons. Using Eq. 3.17, the normalization of the Sachs FFs at $Q^2 = 0$ are:

$$G_E(0) = 1, \quad G_M(0) = \mu_p. \quad (3.19)$$

In TL region, at the threshold of proton antiproton annihilation, the following relation holds:

$$G_E(4M^2) = G_M(4M^2). \quad (3.20)$$

This follows from Eq. 3.17 setting $\tau = 1$. It is physically related to the fact that at threshold only one amplitude, corresponding to the s -wave, contributes to the reaction.

3.2.2 Experimental measurements of the electromagnetic proton form factors

3.2.2.1 Data in Space-Like region

In SL region, the electric G_E and magnetic G_M FFs have been measured up to momentum transfer squared $Q^2 = -q^2 = 8.83 \text{ (GeV)}^2$ in elastic ep scattering using the Rosenbluth separation method. $G_M(Q^2)$ has been extracted up to $Q^2 \simeq 31 \text{ (GeV)}^2$ based on the assumption $\mu_p G_E = G_M$. The Rosenbluth method consists in measurements of the unpolarized elastic electron proton differential cross section at different angles for a fixed value of Q^2 [55].

In Lab frame, the differential cross section for unpolarized $ep \rightarrow ep$ scattering (Eq. 3.12) is written in terms of the Sachs proton FFs as:

$$\begin{aligned} \frac{d\sigma}{d\Omega} &= \left(\frac{d\sigma^{Mott}}{d\Omega} \right) \frac{\epsilon_2}{\epsilon_1} \frac{1}{\mathcal{E}(1+\tau)} (\tau G_M^2 + \mathcal{E} G_E^2) \\ \mathcal{E}^{-1} &= 1 + 2(1+\tau) \tan^2(\vartheta/2), \tau = Q^2/(4M^2), \end{aligned} \quad (3.21)$$

where \mathcal{E} is the virtual photon polarization.

The FFs are determined through the \mathcal{E} -dependence of the reduced elastic differential cross section defined by:

$$\sigma^{red}(\vartheta, Q^2) = \tau G_M^2 + \mathcal{E} G_E^2. \quad (3.22)$$

The linear dependence of the reduced cross section $\sigma^{red}(\vartheta, Q^2)$ (after extracting kinematical factors) as a function of \mathcal{E} allows to determine $G_E(Q^2)$ and $\tau G_M(Q^2)$ as the slope and the intercept. At higher Q^2 , this method leads to large uncertainties on the extraction of G_E , due to the fact that the magnetic contribution to the differential cross section is accompanied by the kinematical factor τ . The world data [64] on the proton FFs, extracted with the Rosenbluth separation method are shown in Fig. 3.5. Up to $\sim 8 \text{ (GeV)}^2$, the behavior of the magnetic and electric FFs were described by a dipole function, according to:

$$G_M(Q^2)/\mu_p = G_E(Q^2) = G_D(Q^2), \quad G_D(Q^2) = (1 + Q^2/0.71)^{-2}. \quad (3.23)$$

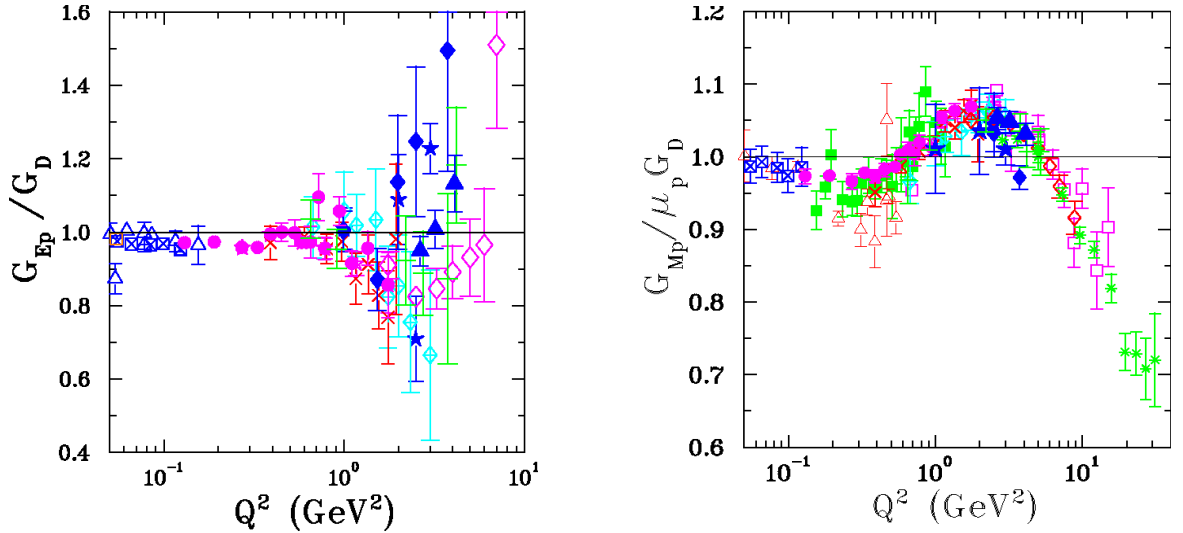


Figure 3.5: Proton electric (left) and magnetic (right) FFs -normalized to one- in the SL region as a function of Q^2 , obtained with the Rosenbluth technique, divided by the dipole function G_D from Ref. [64].

Polarization method:

In the recent years, and with the developments of polarized, high intensity electron beams, hadron polarimeters and large acceptance spectrometers, it was possible to extract proton FFs using the polarization method suggested by Akhiezer and Rekalo in 1968 [65, 66]. The GEp collaboration at JLab, measured the ratio of the proton FFs in a scattering experiment of a polarized electron beam on an unpolarized proton target. The measurement of the longitudinal (P_ℓ) and transverse (P_t) polarizations of the outgoing proton, allows to determine the ratio $R = G_E/G_M$ by:

$$R = \frac{G_E}{G_M} = -\frac{P_t}{P_\ell} \frac{\epsilon_1 + \epsilon_2}{2M} \tan(\vartheta/2), \quad (3.24)$$

The measurements have been done up to $Q^2 \simeq 8.9 \text{ (GeV)}^2$ (see [67] and references therein). The data show that the electric and magnetic distributions in the proton are different, contrary to what was earlier assumed. A monotonic decrease of the ratio $\mu_p G_E/G_M$ with Q^2 , deviating from unity as Q^2 increases, was observed. Fig. 3.6 illustrates the existing data on the proton FF ratio, obtained from the Rosenbluth (from Ref. [68],[69] and [70], black points) and the polarization (Akhiezer-Rekalo) (from Ref. [71],[72],[67],[73] and [74], green stars) methods.

The difference of the ratio from unity is attributed to the electric FF, as the magnetic contribution is assumed to be well known from the cross section (at large momentum transfer it represents more than 90%). The discrepancy between the data extracted from two different methods is likely to be attributed to radiative corrections. The probability to radiate one or more photons from a few GeV electron may reach 40%. Radiative corrections are applied at first order to unpolarized data and are neglected in polarization experiments, as they factorize and cancel (at first order). Higher order corrections should be considered at high Q^2 .

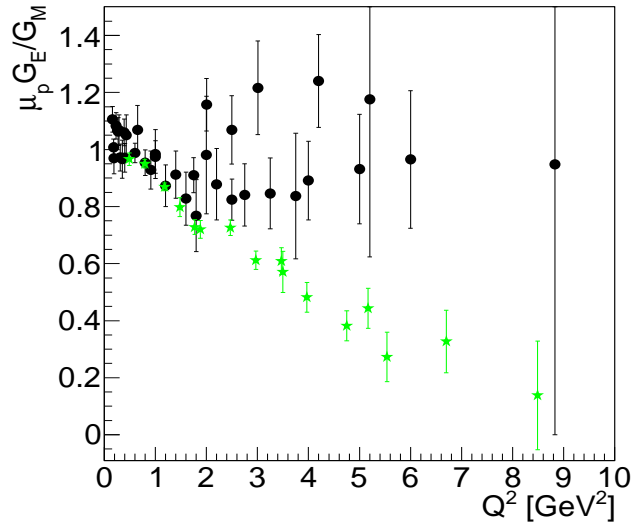


Figure 3.6: Proton FF ratio $\mu_p G_E/G_M$ in the SL region as a function of Q^2 , obtained via the Rosenbluth technique (black points), and polarization method (green stars).

3.2.2.2 Data in Time-Like region

The proton FFs have been measured in TL region, where they are complex functions of q^2 , through the annihilation reactions $\bar{p}p \leftrightarrow e^+e^-$. In the Born approximation, the differential cross section for the annihilation reaction $\bar{p}p \rightarrow e^+e^-$ in the CMS, is expressed as a function of the proton electromagnetic FFs as [75]:

$$\begin{aligned}\frac{d\sigma}{d\cos\theta} &= \mathcal{N}\mathcal{D}, \quad \mathcal{N} = \frac{\pi\alpha^2}{2\beta s}, \quad \beta = \sqrt{1 - \frac{1}{\tau}}, \quad \tau = \frac{s}{4M^2}, \quad s = q^2 \\ \mathcal{D} &= (1 + \cos^2\theta)|G_M|^2 + \frac{1}{\tau}\sin^2\theta|G_E|^2,\end{aligned}\tag{3.25}$$

where α is the electromagnetic coupling constant, and θ is the scattering angle of the electron (in CMS). The differential cross section for the reaction $e^+e^- \rightarrow \bar{p}p$ has the same angular dependence as Eq. 3.25 but a different phase space factor.

The total cross section, integrated over the full angular distribution range is:

$$\sigma_{tot} = 8\mathcal{N}(2\tau|G_M|^2 + |G_E|^2).\tag{3.26}$$

The measurement of the differential cross section at a fixed energy allows one to determine the ratio $R = |G_E|/|G_M|$. With a precise knowledge of the normalization and the luminosity, a separate determination of $|G_E|$ and $|G_M|$ is feasible. Due to the low luminosity achieved in the experiments, an effective FF $|G_M| = |G_E|$ has been extracted from the measurement of the total cross section (Eq. 3.26).

Fig. 3.7 displays the data on the effective magnetic FF as a function of q^2 obtained in $\bar{p}p \leftrightarrow e^+e^-$ experiments. The few existing data on the proton FF ratio in TL region are reported in Fig. 3.8.

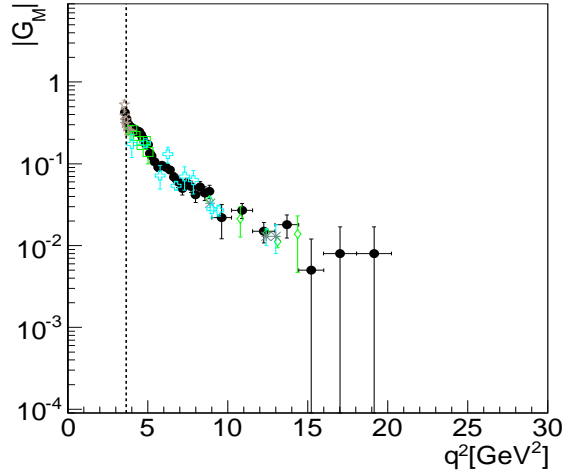


Figure 3.7: World data on the TL proton magnetic FF for $|G_E| = |G_M|$, as function of q^2 . The vertical dashed line represents the kinematical threshold of the proton antiproton annihilation.

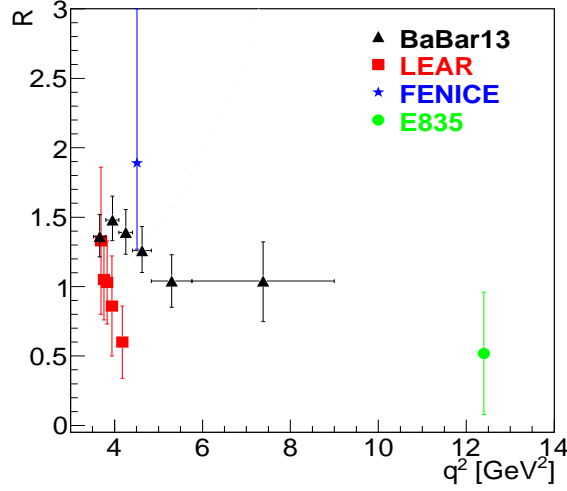


Figure 3.8: Proton electromagnetic FF ratio in TL region, as function of q^2 . Data are from Ref. [77] (red squares), from Ref. [78] (black triangles), from Ref. [79] (green circles), and from Ref. [80] (blue star).

3.2.2.3 Unphysical region

In proton antiproton annihilation (TL region), the selection of a pair of leptons accompanied by a pion in the final state allows access to electromagnetic proton FFs in the so-called unphysical region. This idea was suggested by M. P. Rekalo [76]. Assuming the dominance of t and u channel exchange diagrams, the emission of a pion by the proton or the antiproton lowers the momentum squared q^2 of a virtual photon which subsequently decays into a lepton pair (Fig. 3.9). This mechanism allows q^2 values to be reached under the $4M^2$ threshold in the TL region of transferred momenta. This reaction is related by crossing symmetry to pion electroproduction which has been widely studied. However it is not straightforward to find relations between the observables in the annihilation and scattering channels due to excitation of nucleon resonances.

Different models have been considered to describe the annihilation mechanism of $\bar{p}p \rightarrow e^+e^-\pi^0$ [81, 82, 83]. In particular, in Ref. [83], the dependence of the differential cross section and polarization observables in the $\bar{p}p \rightarrow e^+e^-\pi^0$ reaction on the polarizations of the proton target and antiproton beam (the produced electron may be unpolarized or longitudinally polarized) have been derived in a general form using hadron electromagnetic current conservation and P-parity invariance of the hadron electromagnetic interaction. The expressions of the observables are given in terms of six independent amplitudes (in general complex functions of three kinematical variables) which fully describe the considered reactions in the one-photon-exchange approximation.

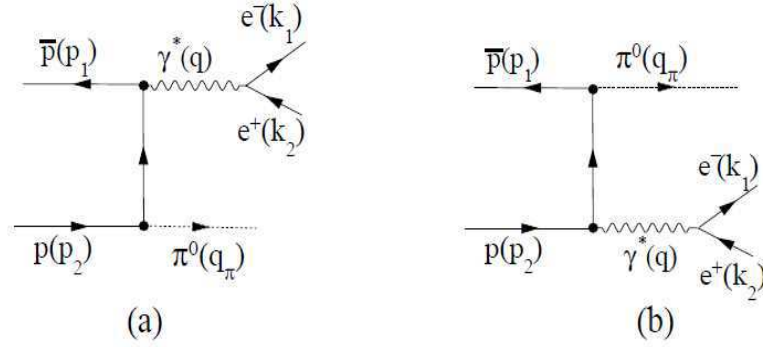


Figure 3.9: Feynman diagram for $\bar{p} + p \rightarrow e^+ + e^- + \pi^0$ (a) for lepton pair emission from the antiproton and (b) from the proton.

Experimentally, the unphysical region for the proton FFs has never been explored. Feasibility studies based on Monte Carlo (MC) simulations [84, 85] showed the possibility of proton FF measurements in the unphysical region at PANDA.

3.2.3 Parametrizations of the proton form factors

The calculation of the nucleon FFs from QCD is complicated as it requires, in the few GeV momentum transfer region, non-perturbative methods. Many theoretical attempts have been made to understand the existing data in SL region. Different models exist to describe the non-perturbative structure of the nucleon but not all of them describe all four nucleon FFs and not all of them can be extended in the TL region. In this section, a short overview of a few theoretical predictions used in this field, and which are based on the Vector Meson Dominance (VMD) model and perturbative QCD (pQCD) is given.

3.2.3.1 Vector meson dominance model

The earliest models to explain the global features of the nucleon FFs, such as its approximate dipole behavior ($\sim [Q^2]^{-2}$) were the VMD models. In this picture the photon couples to the nucleon through the exchange of intermediate vector mesons ($\omega, \phi, \rho, \dots$) which have the same quantum numbers as the photon (total spin 1 and odd parity $J^P = 1^-$). VMD models give a simple parametrization of the nucleon FFs based on a few number of parameters of physical meaning (masses, coupling constants,...). The VMD models describe SL FFs, where most of the data exist, and have the necessary analytical properties to be extended into the TL region.

In 1973 a parametrization for the SL nucleon FFs was suggested by F. Iachello, A. D. Jackson and A. Lande [86] based on the VMD model, predicting a linear decrease of the proton FF ratio, in agreement with the result from the GEp polarization transfer

experiments which appeared in 2010 [67]. The nucleon FFs were described as the product of an intrinsic nucleon FF, $g(Q^2)$, and a term describing the interaction of the nucleon cloud with the electromagnetic field. In order to take into account the different coupling to the isoscalar (ω, ϕ, \dots) and isovector (ρ, \dots) vector mesons, the Dirac and Pauli nucleon FFs are expressed as follow:

$$F_i = F_i^S + F_i^V, \quad i = 1, 2, \quad (3.27)$$

where F_i^S and F_i^V are the isoscalar and isovector FFs respectively and they have the following dependence in Q^2 :

$$\begin{aligned} F_1^S(Q^2) &= \frac{1}{2}g(Q^2) \left[(1 - \beta_\omega - \beta_\phi) + \beta_\omega \frac{M_\omega^2}{M_\omega^2 + Q^2} + \beta_\phi \frac{M_\phi^2}{M_\phi^2 + Q^2} \right], \\ F_1^V(Q^2) &= \frac{1}{2}g(Q^2) \left[(1 - \beta_\rho) + \beta_\rho \frac{M_\rho^2}{M_\rho^2 + Q^2} \right], \\ F_2^S(Q^2) &= \frac{1}{2}g(Q^2) \left[(-0.12 - \alpha_\phi) \frac{M_\omega^2}{M_\omega^2 + Q^2} + \alpha_\phi \frac{M_\phi^2}{M_\phi^2 + Q^2} \right], \\ F_2^V(Q^2) &= \frac{1}{2}g(Q^2) \left[3.706 \frac{M_\rho^2}{M_\rho^2 + Q^2} \right]. \end{aligned} \quad (3.28)$$

The parameters $\beta_\rho = 0.672$, $\beta_\omega = 1.102$, $\beta_\phi = 0.112$ and $\alpha_\phi = -0.052$ are adjusted to fit the SL data [86]. They represent the product of the $V\gamma$ and VNN coupling constants. The standard values of the masses $M_\rho = 0.765$ GeV, $M_\omega = 0.783$ GeV and $M_\phi = 1.019$ GeV and width $\Gamma_\rho = 0.112$ GeV were used. The effect of the width for ω and ϕ was neglected. The finite width of the ρ was described using the formalism of Refs. [87, 88], where the following change has been applied to Eq. 3.28:

$$\begin{aligned} \frac{M_\rho^2}{M_\rho^2 + Q^2} &\rightarrow \frac{M_\rho^2 + 8\Gamma_\rho m_\pi/\pi}{M_\rho^2 + Q^2 + (4m_\pi^2 + Q^2)\Gamma_\rho\alpha(Q^2)/m_\pi}, \\ \alpha(Q^2) &= \frac{2}{\pi} \left[\frac{Q^2 + 4m_\pi^2}{Q^2} \right]^{1/2} \ln \left[\frac{\sqrt{Q^2 + 4m_\pi^2} + \sqrt{Q^2}}{2m_\pi} \right]. \end{aligned} \quad (3.29)$$

The intrinsic form factor $g(Q^2)$ was parametrized by a dipole function:

$$g(Q^2) = (1 + \gamma Q^2)^{-2}, \quad \gamma = 0.25 \text{ (GeV)}^{-2}. \quad (3.30)$$

In 2004 this model was analytically extended to the TL region [89] introducing a complex phase in the expressions of the intrinsic FF and the ρ meson term:

$$g(q^2) = \frac{1}{(1 - \gamma e^{i\theta} q^2)^2}. \quad (3.31)$$

The phase factor $\theta = 53^\circ$ was adjusted to fit the data on $|G_M^p|$ in the TL region.

The ρ meson term becomes, for $q^2 \geq 4m_\pi^2$:

$$\frac{M_\rho^2}{M_\rho^2 - q^2} \rightarrow \frac{M_\rho^2 + 8\Gamma_\rho m_\pi / \pi}{M_\rho^2 - q^2 + (4m_\pi^2 - q^2)\Gamma_\rho \alpha(q^2)/m_\pi + i\Gamma_\rho 4m_\pi \beta(q^2)}, \quad (3.32)$$

where

$$\alpha(q^2) = \frac{2}{\pi} \left[\frac{q^2 - 4m_\pi^2}{q^2} \right]^{1/2} \ln \left[\frac{\sqrt{q^2 - 4m_\pi^2} + \sqrt{q^2}}{2m_\pi} \right], \quad (3.33)$$

and

$$\beta(q^2) = \sqrt{\frac{\left(\frac{q^2}{4m_\pi^2} - 1\right)^3}{\frac{q^2}{4m_\pi^2}}}. \quad (3.34)$$

3.2.3.2 Spin one hadrons, VMD inspired model

The deuteron is a spin one hadron and it has been largely discussed in the literature as it is the lightest nucleus. Data on the three SL deuteron FFs, using the electron deuteron elastic scattering, are available up to momentum transfer squared $Q^2 = 1.9 \text{ GeV}^2$. The individual determination of the three deuteron FFs requires the measurement of the differential cross section and at least one polarization observable, usually the tensor polarization, t_{20} , of the scattered deuteron in unpolarized ed scattering. In the TL region, the measurement of deuteron FFs is beyond the experimental possibilities, but information on the TL spin one hadrons can be extracted from the reaction $e^+ + e^- \rightarrow \rho^- + \rho^+$.

VMD has been also extended to spin one hadrons and successfully applied to the deuteron [90]. In Ref. [91], one can find a simple parametrization, based on VMD approach, for the electromagnetic FFs of the ρ -meson. The parametrization reproduced the theoretical predictions from Ref. [92] in SL region. The extension of the model to TL region was made by analytical continuation, introducing an imaginary part through widths for the effective particles carrying the electromagnetic interaction. Recently, the BaBar collaboration has detected four pions identifying the $e^+ + e^- \rightarrow \rho^+ + \rho^-$ reaction [93]. The results were given in terms of helicity amplitudes. This unique experimental data point puts a constraint on pre-existent ρ -meson FF parametrizations. I have been involved in a work [94] establishing a correspondence between the formalism of Ref. [91] and the helicity amplitudes for the reaction $e^+e^- \rightarrow \rho^+\rho^-$ in order to analyse the constraint on the TL ρ -meson FFs measured by the BaBar collaboration. We showed that, keeping the same parametrization form, a small readjustment of the mass parameters (mass of the effective particles) allows to correctly reproduce the helicity amplitudes measured in the BaBar experiment.

3.2.3.3 Perturbative QCD parametrization

In the high Q^2 -limit, where a perturbative treatment of the strong interaction is possible, QCD predicts [95, 96] the asymptotic behavior of the nucleon FFs by considering both dimensional scaling laws and hadronic helicity conservation.

At asymptotically large values of Q^2 , the photon has sufficiently large virtuality to see the nucleon made of three collinear quarks. To keep the nucleon intact, the momentum transferred by the photon has to be shared among the constituent quarks. At least, two massless gluons must be exchanged, and each gluon propagator contributes with a factor $1/Q^2$ (Fig. 3.10). One associates the gauge coupling constant to each quark gluon vertex.

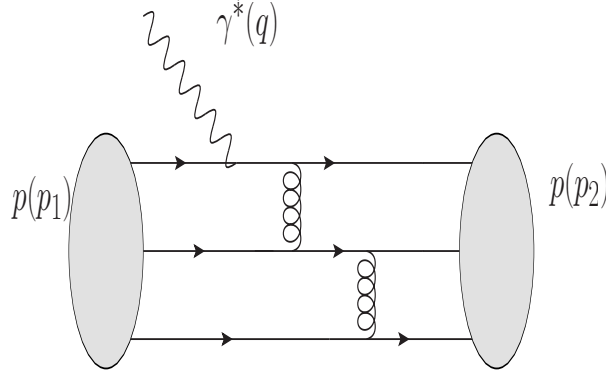


Figure 3.10: The pQCD diagram describing at the first order the photon proton vertex.

QCD can predict only the Q^2 -dependence of the nucleon FFs which must be the same for G_E and G_M , as it depends only on the number of the valence quarks involved in the reaction:

$$G_E(Q^2) = G_M(Q^2) \sim \frac{\alpha_s^2(Q^2)}{Q^4}. \quad (3.35)$$

The coupling constant $\alpha_s(Q^2)$ is determined in SL region as:

$$\alpha_s = g_s^2(Q^2)/(4\pi) \sim \frac{1}{\beta_0 \ln(Q^2/\Lambda^2)}, \beta_0 = 11 - \frac{2}{3}n_f, \quad Q^2 > \Lambda^2, \quad (3.36)$$

where Λ is the QCD scale constant and $n_f = 3$ is the number of flavors.

The analytical extension of the pQCD parametrization to the TL region can be done with the following replacements:

$$Q^2 \rightarrow -q^2, \quad \ln(Q^2/\Lambda^2) \rightarrow \ln(q^2/\Lambda^2) - i\pi, \quad q^2 > \Lambda^2. \quad (3.37)$$

The negative sign in the logarithmic function induces the imaginary part for the TL FFs. In terms of the Sachs FFs, one can write:

$$G_{E,M} = \frac{A}{(q^2)^2 [\ln(q^2/\Lambda^2) - i\pi]^2}, \quad |G_{E,M}| = \frac{A}{(q^2)^2 [\ln^2(q^2/\Lambda^2) + \pi^2]}. \quad (3.38)$$

The value of the coefficient A is obtained with a fit to the TL experimental data for $|G_M| = |G_E|$. The fit gives for the proton the value $A = 89.54 \text{ GeV}^2$ with $\Lambda = 0.3$. The pQCD parametrization assumes relative phase between G_M and G_E equal to zero. The measurement of this relative phase in experiments using polarization observables will be a test of the validity of such an assumption.

3.2.4 General description in TL region

The understanding of the new measurements of the SL and TL nucleon FFs and the future plans of precise measurements on nucleon FFs motivate the necessity of new qualitative models of the nucleon, which are able to explain the existing data in the whole kinematical region and to give useful predictions. Existing models may reproduce reasonably well the experimental finding of the fast decreasing of the electric FF (G_E) at large momentum transfer, after a fitting. The VMD model, which describes the nucleon as a charged center of valence quarks surrounded by a meson cloud, predicted such behavior before the data appeared. Note that such parametrization contains an implicit constrain for the neutron and proton FFs which must be fitted simultaneously. In Ref. [97], a new qualitative model which can be applied to both proton and neutron, in all the kinematical region (SL and TL), was derived. This model gives also an explanation for the decrease of G_E at large momentum transfer but with a nucleon picture completely different from the one given by the VMD. In addition, it gives empirical evidence that nucleons behave as point-like particles at threshold [98]. As this model was not used for the numerical applications of this thesis, we limit ourself to display here only the outline of its formalism:

- The model leaves unchanged the pQCD predictions ($\sim Q^{-4}$) for the magnetic FF (G_M), based on the quark counting rules.
- A correction to the expression of G_E which is related to the scalar part of the electromagnetic field is provided by the central region of the nucleon. At large value of the momentum transfer squared, the central region of the nucleon is assumed to be electrically neutral, due to the strong gluonic field. In such condition, a phenomena similar to the screening of a charge in a plasma occurs reducing the electromagnetic field and producing an additional suppression of the electric FF with respect to $\sim Q^{-4}$.
- The formalism was derived in the Breit frame for SL region and in the CMS for the TL region, allowing to give a unified expression for the TL and SL FFs which are functions of the invariant Q^2 .

In SL region, the model predicts:

$$G_E(Q^2) = \frac{G_M(Q^2)}{\mu_p} (1 + Q^2/q_1^2)^{-1} \quad (3.39)$$

and in TL region, Q^2 was replaced by $q^2 - 4M^2$ in order to have the implicit normalization $|G_E| = |G_M| = 1$ at threshold:

$$|G_M(q^2)| = [1 + (q^2 - 4M^2)/q_2^2]^{-2} \Theta(q^2 - 4M^2) \quad (3.40)$$

$$|G_E(q^2)| = |G_M(q^2)| [1 + (q^2 - 4M^2)/q_1^2]^{-1} \Theta(q^2 - 4M^2). \quad (3.41)$$

$\Theta(q^2 - 4M^2)$ avoids poles in the unphysical region. q_1 and q_2 are parameter fit.

The data for $|G_M| = |G_E|$ together with the predictions of the models presented here are shown in Fig. 3.11. First, one can see that the VMD model (green color) is not able to reproduce the data on the TL FFs, in particular at large momentum transfer squared. However, the data are well reproduced by pQCD (red color) and the new model following Eq. 3.40 with $q_1^2=3.6 \text{ GeV}^2$ and $q_2^2=1.2 \text{ GeV}^2$ (black color). The few existing data on the proton FF ratio in TL region are reported in Fig. 3.12.

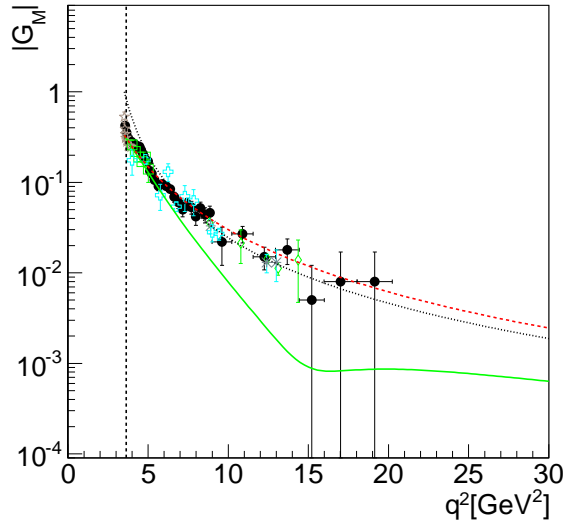


Figure 3.11: World data on the TL proton magnetic FF for $|G_E| = |G_M|$, as function of q^2 . The lines are the predictions of the theoretical models from VMD (green solid line), pQCD (red dashed line), and from Ref. [97] (black dotted line).

The nucleon models cannot be definitely discriminated with the present status on the experimental measurements. At least, in SL region where large sets of data exist, the discrepancy between the results coming from the Rosenbluth separation and polarization methods have to be understood.

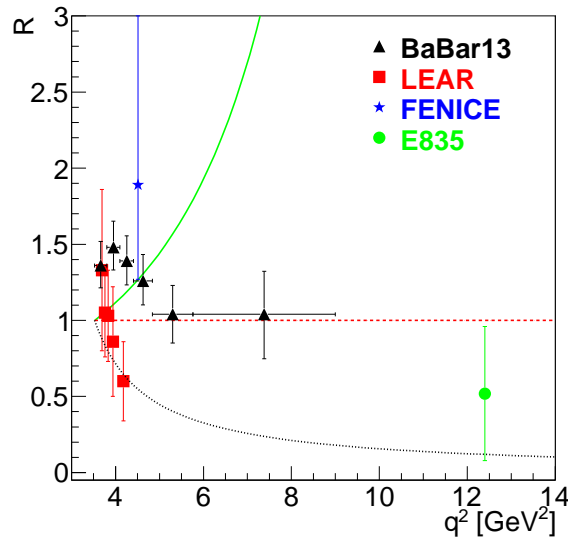


Figure 3.12: Proton electromagnetic FF ratio in TL region, as functions of q^2 . The lines are the prediction of the theoretical models from VMD (green solid line), pQCD (red dashed line), and from Ref. [97] (black dotted line). Data are from Ref. [77] (red squares), from Ref. [78] (black triangles), from Ref. [79] (green circles), and from Ref. [80] (blue star).

Chapter 4

The PANDA detector setup

The foreseen program of the PANDA experiment, described in chapter I, requires a high performance detector. PANDA will be installed at the HESR for antiprotons of the future FAIR facility. The detector will be composed of two magnetic spectrometers: the target spectrometer, based on a superconducting solenoid magnet surrounding the interaction point, and the forward spectrometer based on a dipole magnet, for small angle tracks. The main requirements of the PANDA detector are:

- high rate capability (2×10^7 annihilations/s).
- nearly 4π solid angle.
- good momentum resolution.
- high vertex resolution.
- good charged particle identification.
- efficient event selection.

The experimental setup is shown in Fig 4.1 for both target and forward spectrometers. The different sub-detectors, the beam-line and the target system are also displayed.

4.1 The targets

Hydrogen target systems will be used for antiproton-proton reactions at PANDA. In order to reach the average maximum design luminosity of $2 \times 10^{32} \text{cm}^{-2} \text{s}^{-1}$, a target thickness of about 4×10^{15} hydrogen atoms per cm^2 is required assuming 10^{11} stored antiprotons with a production rate of $2 \cdot 10^7 \text{s}^{-1}$ in the HESR ring. Two complementary techniques are under study: the cluster-jet target and the pellet target. Both techniques are capable of providing sufficient densities for hydrogen at the interaction point and meet a large fraction of the experiment requirements. Cluster jet targets provide a

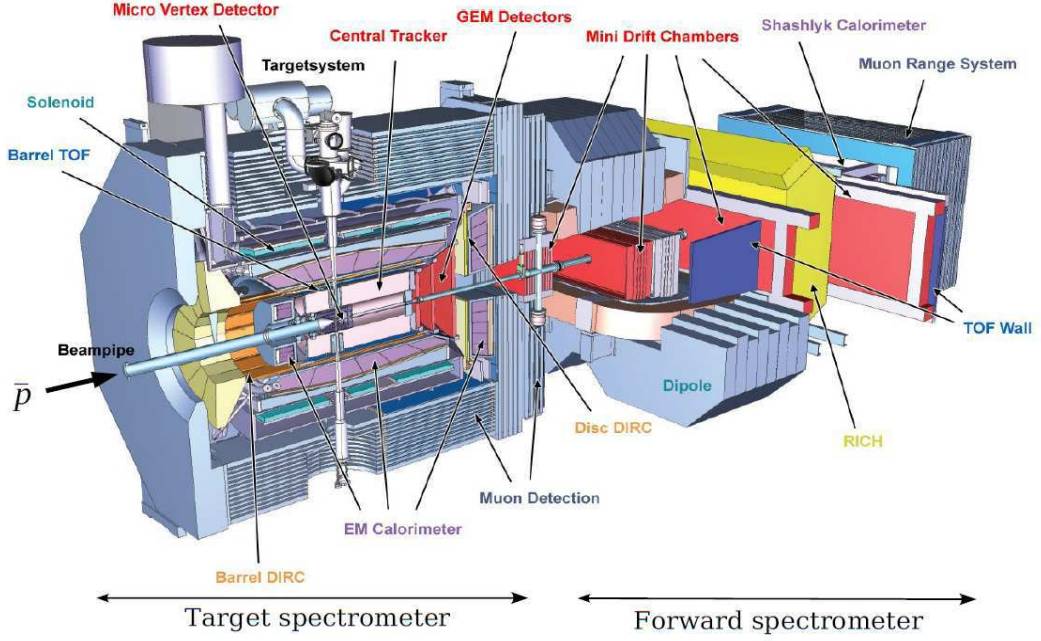


Figure 4.1: 3D overview of the PANDA detector, from [18].

homogeneous and adjustable target density without any time structure. However the lateral spread of the cluster jet leads to an uncertainty in the definition of the interaction point along the beam axis of several millimeters. Pellet targets provide a stream of frozen molecule droplets, called pellets, which drop vertically with a fixed frequency off from a fine nozzle into vacuum. The advantage of this target is the high resolution in the vertex position ($50 \mu\text{m}$) that can be reached thanks to the large number of interactions expected in every pellet and to the foreseen pellet tracking system. A very precise positioning of the target is crucial for the exact definition of the primary interaction vertex. However, pellet targets suffer from a non-uniform time distribution, which results in larger variations of the instantaneous luminosity as compared to a cluster jet target. Cluster-jet and pellet source will be installed alternatively depending on the experimental program to be investigated. For the nuclear target part of the PANDA physics program, wire or fiber targets will be used.

4.2 The magnets

In high energy particle experiments, the magnet systems are used to bend charged particles so that their momenta can be measured. This bending is due to the Lorentz force which is proportional to the mass and velocity of the particle; low-momentum

particles curve significantly in comparison to those of high-momentum which curve very little. The amount of the curvature can be quantified and the particle momentum is determined from this value. High magnetic field is needed for very energetic particles to curve enough for the determination of their momentum. A uniform direction and strength magnetic field allows measurements to be made very precisely. However, particles with very low momenta in a strong magnetic field will be curved so strongly that they will loop repeatedly in the field and most likely not be measured.

The magnetic field in the target spectrometer of PANDA detector will be provided by a superconducting solenoid coil with an inner radius of 105 cm and a length of 2.8 m. The maximum magnetic field is 2 T. The field homogeneity should be better than 2% over the volume of the vertex detector and the central tracker.

As part of the forward spectrometer, a dipole magnet with a large opening of about 1 m in height (gap), 3 m wide and 2.5 m long will provide a bending power of 2 T.m and will be used for the momentum reconstruction of charged particles emitted at forward angles. The dipole magnet provides bending power with a B-field perpendicular to the forward tracks. The forward magnetic spectrometer will allow the reconstruction of charged particle tracks from 0° up to 10° horizontally (5° vertically) with a momentum resolution of 1%. The resulting deflection of the antiproton beam at the maximum momentum of 15 GeV will be 2.2° .

The magnet designs are described in more details in Ref. [99].

4.3 Tracking System

High resolution measurement of charged particle trajectories will be provided by three tracking systems in the target spectrometer: the Micro Vertex Detector, the Central Tracker and the Gas Electron Multiplier Stations.

Micro Vertex Detector (MVD): MVD [100] is the innermost sub-detector system of the target spectrometer, optimized for the detection of secondary decay vertices of short lived particles such as the D-mesons and hyperon decays. The MVD is also designed to improve the transverse momentum resolution and Particle IDentification (PID) using the information on the energy loss of slow particles in this sub-detector.

The MVD is based on radiation hard silicon pixel detectors with fast individual pixel readout circuits and silicon strip detectors. It consists (Fig. 4.2) of four barrel layers in the central part, with an inner radius of 2.5 cm and an outer radius of 13 cm, surrounding the beam pipe and of eight detector discs arranged perpendicular to the beam, in order to achieve the best acceptance for the forward part of the particle spectrum.

Central Tracker: the Straw Tube Tracker (STT) [101] is the central tracking detector designed for the tracking of charged particles in the PANDA target spectrometer. The STT aims for a precise spatial reconstruction of the helical trajectories of charged

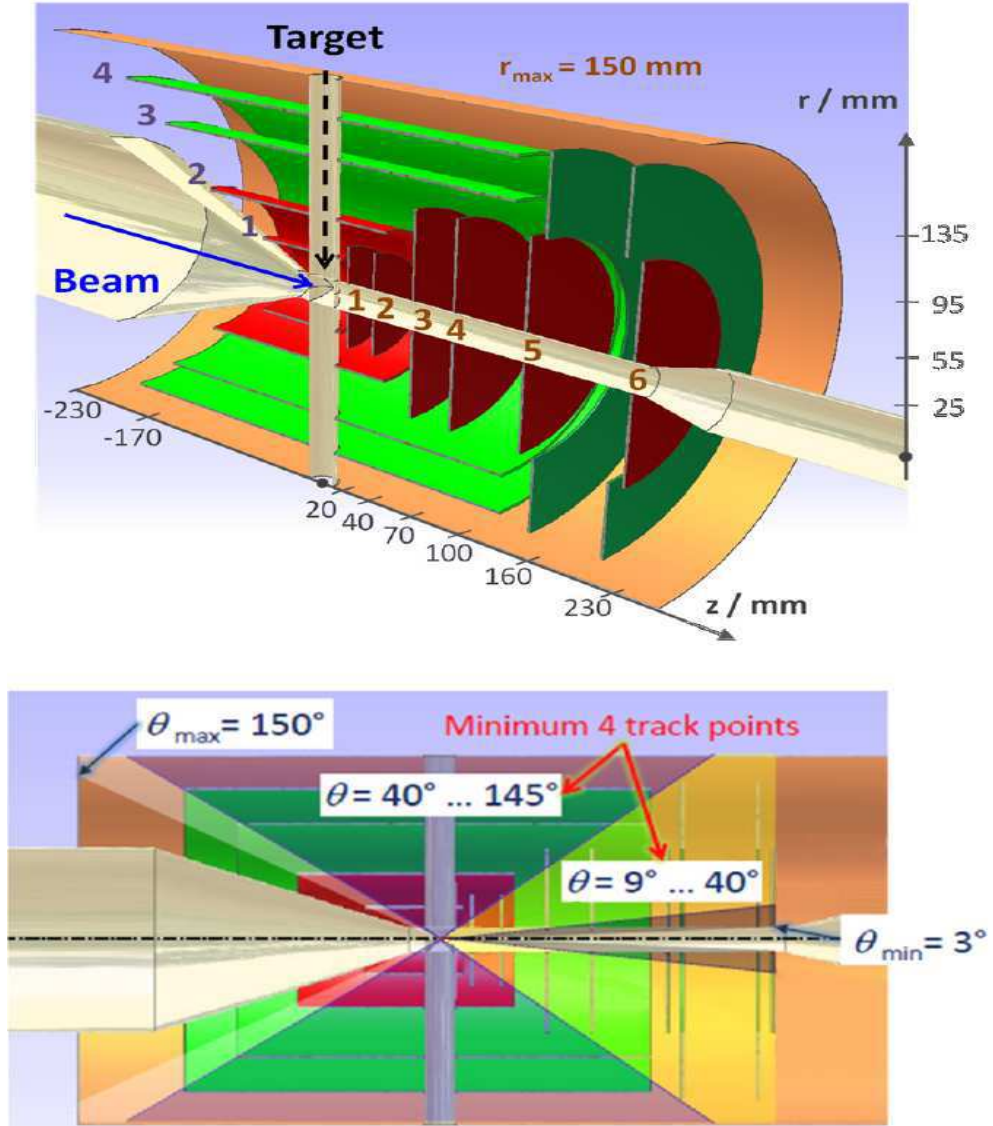


Figure 4.2: Basic layout of the MVD (top). The red inner parts are equipped with silicon hybrid pixel sensors. Double-sided silicon micro-strip detectors utilised in the outer layers are indicated in green. Bottom: Side view along the beam axis illustrating the polar angle coverage. The barrel and the forward part meet at a polar angle of $\theta = 40^\circ$.

particles in a broad momentum range from about a few 100 MeV/c up to 8 GeV. The STT will play an important role for PID from the measurement of the energy loss (dE/dx), in particular in the momentum region below 1 GeV.

The STT (Fig. 4.3) consists of 4636 single straw tubes arranged in a large cylindrical volume around the beam-target interaction point. The STT will cover the polar angles from 22° to 140° . It encloses the MVD for the inner tracking and is followed in the beam direction by a vertical setup of Gas Electron Multiplier disks for adding track points in the forward polar angle range.

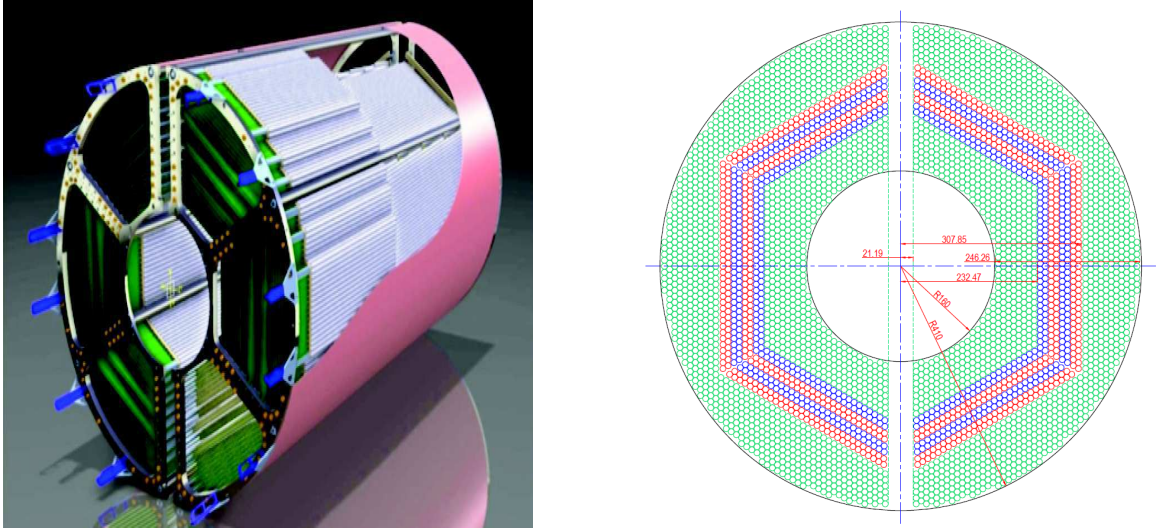


Figure 4.3: The Straw Tube Tracker (STT) of the target spectrometer seen from upstreams (left). Layout of the straw tubes in the STT in xy-view. The straws marked in green are parallel to the beam axis (right). The blue and red marked straw layers are skewed relative to the axially aligned straws in the same sector by a small angle of $+2.9^\circ$ and -2.9° , respectively.

Straws are gas-filled (Argon and CO_2 mixture) cylindrical aluminized mylar tubes with a conductive inner layer as cathode and an anode wire stretched along the cylinder axis. An electric field between the wire and the outer conductor separates electrons and positive ions produced by a charged particle along its trajectory through the gas volume. The energy loss (dE/dx) of a charged particle in the straw gas volume can be derived from the number of ionization electrons per track length (dx) for the generated straw signal.

Gas Electron Multiplier (GEM) Stations : particles emitted at angles below 22° which are not fully covered by the STT will be tracked by three planar stations placed approximately 1.1 m, 1.4 m and 1.9 m downstream of the target. Each of the stations consists of double planes with two projections per plane. The stations will be equipped with Gaseous micro-pattern detectors based on GEM foils as amplification stages. The Gaseous micro-pattern detectors based on GEM foils can sustain the high

counting rate of particles peaked at the most forward angles. The maximum expected particle flux in the first chamber in the vicinity of the 5 cm diameter beam pipe will be about $3 \times 10^4 \text{ cm}^{-2} \text{ s}^{-1}$.

The Forward Tracker (FT) consists of three pairs of planar tracking stations (six straw tube chambers), one pair will be placed in front, one behind the dipole magnet, and the third one will be placed inside the magnet gap in order to track low momentum particles hitting the magnet yoke.

4.4 Particle IDentification

Cherenkov Detectors: charged particles traversing a medium of refractive index n and $\beta = v/c > 1/n$ (v is the velocity), larger than the Cherenkov threshold $\beta_{th} = 1/n$, emit Cherenkov photons at an angle $\theta_c = \arccos(1/\beta n)$. A particle is then identified by combining the measured value of θ_c angle with the information on the particle momentum from the central tracker.

In the PANDA detector, the Detection of Internally Reflected Cherenkov (DIRC) light will be used for PID at polar angles between 22° and 140° (Barrel DIRC). It will consist of 1.7 cm thick fused silica (artificial quartz) slabs, with refractive index $n=1.47$, surrounding the beam line at a radial distance of 45 cm to 54 cm. This provides PID from rather low momenta of 0.8 GeV up to about 5 GeV.

The light will be imaged by lenses onto Micro-Channel Plate PhotoMultiplier Tubes (MCP PMTs) which are insensitive to magnet fields. This fast light detector type allows a more compact design and the readout of two spatial coordinates.

For particles at polar angles between 5° and 22° , a similar concept of radiator, based on fused silica will be used. It consists of a disc shape radiator (Disc DIRC) of 2 cm thick and radius 110 cm.

Time of Flight (TOF) Detector will provide PID for slow particles at polar angles from 22° to 140° . The TOF is related to the relative velocity of the particle, $t = l/(\beta c)$, where l is the path length, of the order of 50-100 cm in the target spectrometer. In order to be able to optimize the separation of most of the different types of produced particles (e, μ, π, p, K), the time resolution must be better than 100 ps.

The TOF detector will be placed between the central tracker and the Barrel DIRC, and consists of $\sim 2 \times 2 \text{ cm}^2$ scintillator tiles readout by silicon photomultipliers. It can be also used to detect photon conversions in the DIRC radiator.

Muon Detectors: The detection of muons is important, in particular for the physics topics related to the electromagnetic processes, i.e, Drell-Yan channels, semi-leptonic meson decays and J/Ψ decays. It is also important for proton FF measurements (see chapter 9).

The Muon detector will be implemented in the yoke of the solenoid magnet to separate primary muons from pions and the secondary muons coming from pion decays.

In the barrel region the yoke is segmented in a first layer of 6 cm iron followed by 12 layers of 3 cm thickness with 3 cm gap for tracking detectors. The endcap is divided into 5 layers of 6 cm iron plus a removable muon filter of 5 additional layers of 6 cm iron. Aluminium drift tubes will be used as detectors.

4.5 Electromagnetic Calorimetry

The Electromagnetic Calorimeter (EMC) is the central component of the PANDA detector [102]. It is designed to measure the high-energy photons over a dynamic range from few MeV up to 15 GeV. EMC is constituted by blocks of radiation sensitive material, where particles lose their energy by producing secondary particles. The energy loss in the scintillator material of the EMC, combined with the information on the particle momentum from the tracking system, will be used for the charged PID, i.e., for electron-hadron separation. Electrons deposit all their energy in an electromagnetic shower, while muons and hadrons lose only a smaller fraction of their kinetic energy by ionization processes.

4.5.1 Principles

Electron and photon interaction with matter: high energy electrons and positrons predominantly lose their energy while interacting with matter via Bremsstrahlung radiation. At low energy, the loss is dominated by the ionization or the excitation of an atom with atomic number Z , although other processes such as Møller scattering, Bhabha Scattering and positron annihilation can contribute to the energy loss in this region. Fig. 4.4 (left) shows the electron energy loss in lead ($Z=82$) as a function of the electron energy. One can see that the rate of the Bremsstrahlung radiation is nearly proportional to the energy, while the ionization process rate varies logarithmically with the electron energy. The energy at which the two rates are equal is called the critical energy E_c , and it is expressed as [103]:

$$E_c = 800(\text{ MeV})/(Z + 1.2). \quad (4.1)$$

The energy loss of photons can be characterized by three main processes: photo-electric effect, Compton scattering and electron positron pair production. The photon interaction cross section with lead as a function of the photon energy is shown in Fig. 4.4 (right). At high energy, the pair production dominates where a photon with energy larger than $2m$ (m is the mass of the electron) is converted into an electron-positron pair.

Electromagnetic shower: a high energy incident electron (positron) or photon on a thick absorber initiates an electromagnetic cascade, through pair production and Bremsstrahlung in the Coulomb field of the atomic nucleus and the electrons of the matter. Therefore secondary particles (electrons, positrons and photons) are generated

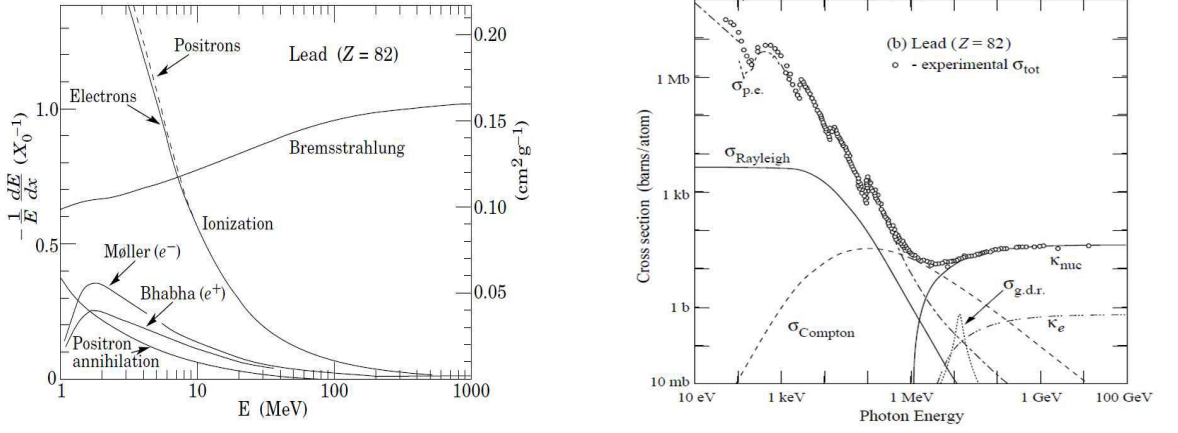


Figure 4.4: Fractional energy loss per radiation length in lead as a function of energy (left), and photon interaction cross section as a function of energy in carbon and lead(right), from [20]. $\sigma_{p.e}$ denotes the atomic photoelectric effect, $\chi_{nuc}(\chi_{nuc})$ is the pair production from nuclear (electron) field, and $\sigma_{g.d.r.}$ the photonuclear interactions.

with lower energy. The process continues until the energy of electrons and positrons falls below the critical energy E_c .

The spread of the shower is mainly focused in the longitudinal direction due to the high incoming longitudinal momentum. The radiation length, X_0 ($[g][\text{cm}^{-2}]$), measures the longitudinal spread of an electromagnetic cascade. It is defined as the distance over which a high-energy electron loses $1/e$ of its energy by Bremsstrahlung [103]. It is also defined as the $7/9$ of the mean free path for pair production by a high-energy photon. The active material of the EMC must have a sufficient thickness in terms of radiation length in order to absorb the complete electromagnetic shower. The transverse development of the shower can be measured in terms of Molière radius R_M . It is defined as the radius of a cylinder containing in average 90% of the shower's energy deposition. The shape of an electromagnetic shower can be used as input for PID. In the material with small Molière radius, the largest fraction of the electromagnetic shower is contained in a few modules, while a hadronic shower with similar energy is spread over a large number of scintillators.

The deposited energy in the EMC converts into an electrical signal (ionization charge) or a light signal (scintillators, Cherenkov light), which can be measured.

Energy resolution: the energy resolution of a calorimeter is usually parametrized as [104]:

$$\sigma(E) = a\sqrt{E} \oplus b \oplus cE, \quad (4.2)$$

where the symbol \oplus means the addition in quadrature. a is the stochastic term (shower fluctuations, sampling fluctuations, dead material at the front of the calorimeter),

b stands for the background (noise term) and c is a constant term related to the non-uniformities in signal collection and bad detector calibration. The energy spread increases with the energy of the incident particle.

4.5.2 Design and geometry

The physics program of the PANDA experiment, focusing on high precision spectroscopy of charmonium states and of exotic hadrons in the charmonium region requires a wide dynamic range for the energy deposition. Besides, the expected high counting rates (about $2 \cdot 10^7$ annihilations/s) and the geometric compact design of the target spectrometer require a fast scintillator material with short radiation length and Molière radius.

The PANDA detector consists of a target and a forward EMC. The target EMC surrounds the interaction point and provides an almost 4π coverage (5° up to 165°). It consists of three parts, the central barrel, the forward (Fig. 4.5) and the backward endcaps. The Lead-tungstate PbWO_4 crystals will be used as detector material

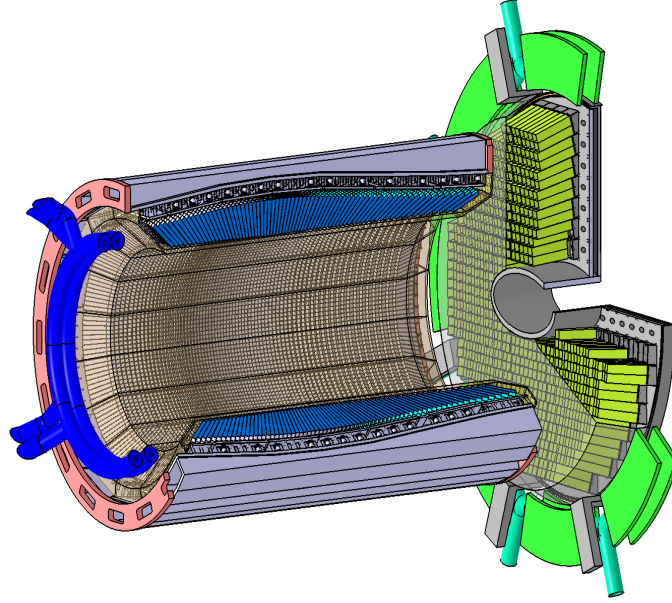


Figure 4.5: The barrel and forward endcap EMC, from [102].

in the target EMC of PANDA detector. The central barrel of the EMC (22° - 140°) is composed of 11360 crystals arranged in 16 identical sectors (slices). The forward (backward) endcap covers the angles from 5° - 10° up to 22° (from 147.5° up to $\sim 165^\circ$). The crystals will be 20 cm long, approximately $22 \times X_0$ in order to achieve an energy resolution below 2% at 1 GeV at a tolerable energy loss due to longitudinal leakage of the shower. Tapered crystals with a front size of $2 \times 2 \text{ cm}^2$ will be mounted in the barrel EMC. The forward endcap EMC will be a planar arrangement of 3600 tapered crystals with roughly the same dimensions as in the barrel part, and the backward

endcap EMC is composed by 592 crystals.

Scintillating material: PbWO_4 (PWO) is a high-density inorganic scintillator with sufficient energy and time resolution for photon and electron detection. The PbWO_4 is characterized by rapid scintillation process with a short decay time ($\tau=6.5$ ns), which is an advantage over the high rate of events expected at PANDA (10^7 interactions/s). These crystals were used in the Compact Muon Solenoid experiment at CERN and for the e1-DVCS experiment held in Hall B at JLab [105]. PANDA will use the second generation of PbWO_4 (PWO-II) where the light yield is improved by about a factor two compared to PWO of PWO_4 . Due to the extreme experimental conditions and requirements for the PANDA physics, the EMC will be operated at a temperature of $T=-25^\circ\text{C}$ to take advantage of the increase of the scintillation light of PbWO_4 by a factor of four compared to the room temperature [106].

Readout: the readout of the crystals will be performed by large area avalanche photo diodes (LAAPDs) in the barrel and in the backward endcap. This type of photo-detector has several advantages: compactness, a total thickness of $\sim 200\mu\text{m}$, high quantum efficiency of 70 – 80% at the wavelength of the maximum emission intensity of lead tungstate, insensitivity to magnetic fields and low cost mass production. For the forward endcap the vacuum photo-triodes (VPTs) will be used. The VPTs have lower gain and lower quantum efficiency, however, they are more radiation hard, have lower dark current and lower capacitance, which provides advantages for operation in a high hit-rate environment (forward endcap).

The PANDA group at IPNO took in charge the design the development of the cooling system for the barrel EMC crystals. During my thesis, I was involved in experimental tests of the optical coupling between the crystals and the LAAPDs where the transmittance of two optical glues has been measured at $T=-25^\circ\text{C}$.

The EMC of the forward spectrometer relies on a shashlyk type calorimeter. It is located 7 m downstream of the target and will cover an area of about 3 m^2 . The discrimination between neutral pions and single gammas is extremely important for forward EMC in experiments seeking to find isolated photons at low rate. Cherenkov and TOF detectors will be also used in the forward spectrometer for PID. Muon detectors similar to that of the target spectrometer but suited to higher momenta will be employed to discriminate pions from muons and to detect the pion decay in the forward spectrometer.

Chapter 5

Tests of optical glues for the PANDA Electromagnetic Calorimeter

The photon detection in extreme high luminosity environment and within a large energy range, from a few MeV to 15 GeV, is a more stringent requirement of PANDA compared to previous experiments and demands new solutions for detectors, associated with electronics, and data acquisition. In particular, a low energy threshold of ≤ 3 MeV for an individual detector module (required for low energy pion detection) demands the maximization of the PbWO_4 light output [107] and the light detection efficiency. In fact, the luminescence yield of PbWO_4 is relatively low about 17-20 phe/MeV at 18°C for a crystal length of 200 mm.

The cooling operation of the PANDA EMC requires a functional test of all components in a low temperature environment. In particular, the optical properties of the glue between the crystal and the avalanche photo diode (APD) should not deteriorate or age.

The main criteria for the choice of the optical glue between the APD and the crystal are the following:

- It should be easy to handle;
- The glue has to keep the object in place for at least 10 years;
- It must be transparent for the scintillation light in the wavelength range of 300-800 nm even at $\mathcal{T} = -25^\circ\text{C}$;
- Its properties should not be deteriorated under ageing and radiation.

Commercial glues usually report the chemical and mechanical characteristics, but the behavior of the transmittance in the specific environment of a particle accelerator requires dedicated studies. Such studies will be the subject of this chapter.

Most of the relevant properties have been tested by the CMS (Compact Muon Solenoid) collaboration [108] for several samples of glues [109]. The work presented here is focusing on:

- measurements of mechanical and thermal resistance,
- transparency and radiation hardness at low temperatures,

of two different glues: the **Dow Corning (3145 RTV MIL-A-46146)** (DC3145) [110] and **ELASTOSIL RT 600** (RT600) [111]. The DC3145 is a high strength adhesive silicone and it is typically used for bonding of sensitive electronic components. This glue is used in the CMS EMC. The RT600 is also a silicone compound obtained by mixing the two components, Elastosil A + B with a ratio of 9:1. Both glues have been previously tested on radiation hardness as well as mechanical properties and long term ageing effects but only at room temperature [109].

In the first part of this chapter, the mechanical stability is investigated in conjunction with the impact of large temperature gradients. Then the effect of low temperatures on the properties of optical transparency is described. At the end, the radiation hardness to photon and proton radiation is presented.

5.1 Thermal tests

The setup of the EMC at a low temperature can have harmful effects on the adhesive glue used as optical coupling between crystals and APDs. In the PANDA experiment, the glue will be exposed during the cooling process to a temperature difference $\Delta\mathcal{T} \approx 50^\circ \text{C}$, starting at room temperature. Assuming the expansion coefficient to be constant as a function of the temperature, it is expected that the effects are the same in equivalent ranges, for example for a temperature change from $\mathcal{T} = 75^\circ \text{C}$ to $\mathcal{T} = 25^\circ \text{C}$.

A sample is prepared by gluing under pressure two Heraeus Suprasil quartz glasses [112] of dimensions $20 \times 20 \text{ mm}^2$ and thickness 0.02 mm by a drop of glue (DC3145) to form a central spot of about 1 cm diameter.

The procedure consisted in warming up the sample on a heating plate and instantly cooling down to room temperature, by sliding it on a support. The temperature of the sample was measured by a thermocouple type K. After exposing the glue to different gradients of temperature up to 300°C , the glue interface was inspected with an optical microscope (using the computer program Motic 2000) for inhomogeneities or cracks.

The images did not show any effect of cracks or vaporization up to 75°C (Fig. 5.1). In order to test the transition temperature when the glue changes its properties, the sample was heated up to 130°C , 185°C , 240°C , up to 310°C , respectively. Only at the last temperature value, the glue shows physical changes with appearance of vapour bubbles (Fig. 5.2).

The thermal tests confirm that the glue will withstand large variations of temperature. In order to check if this property holds on a long time period, an additional

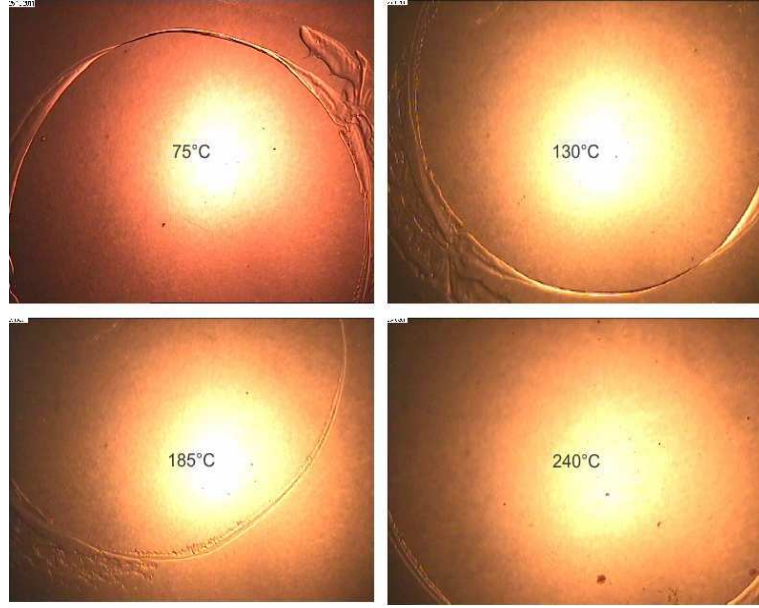


Figure 5.1: Pictures of the interface of glue taken with an optical microscope after thermal test at $\mathcal{T} = 75^\circ \text{C}$ (top left), 130°C (top right), 185°C (bottom left) and 240°C (bottom right).

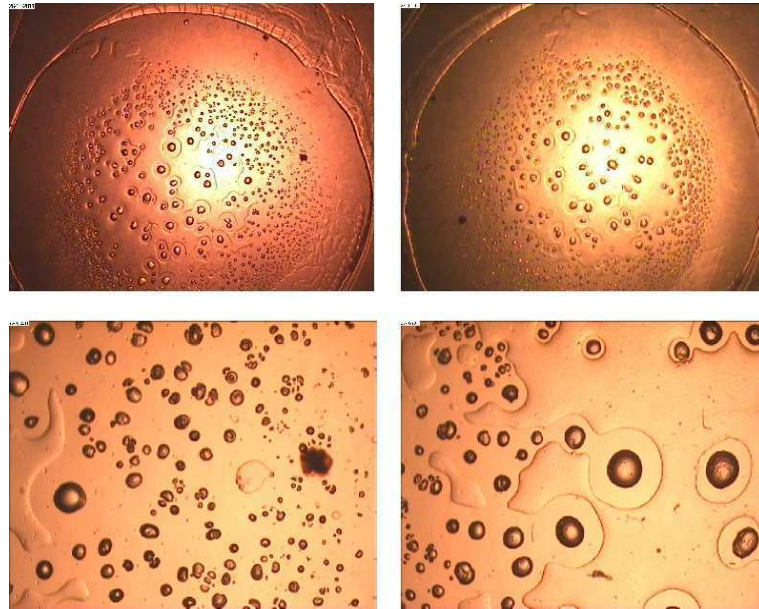


Figure 5.2: Pictures of the interface of glue taken with an optical microscope after thermal test at $\mathcal{T} = 310^\circ \text{C}$.

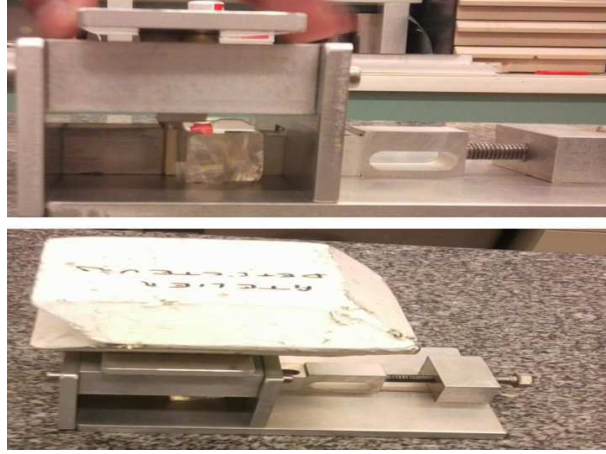


Figure 5.3: Set-up for testing the mechanical resistance. The white metal block (on the bottom) induces the mechanical force.

sample was left in a freezer at -20°C for one month. No variation was observed, besides vapour condensation on the glass itself.

5.2 Mechanical tests

During the cooling phase of the detector, the different expansion coefficients of the materials of the APDs and of the scintillators induce mechanical stress on the glue, which can be estimated. The thermal expansion coefficients of the APD and of the PbWO_4 crystal are, respectively:

$$\lambda_{APD} = 2 \times 10^{-6}/^{\circ}\text{C}, \quad \lambda_{\text{PbWO}_4} = 10 \times 10^{-6}/^{\circ}\text{C}. \quad (5.1)$$

The APDs have an active area of $14 \times 7 \text{ mm}^2$, and contact surface $S = L \times \ell = 18 \times 9 \text{ mm}^2$. The thermal expansion undergone by the glue, due to the difference of the two materials, for $\Delta\mathcal{T} = 50^{\circ}\text{C}$ is:

$$\Delta L = \Delta\mathcal{T} \times \Delta\lambda \times L = 7.2 \text{ } \mu\text{m}, \quad \Delta\lambda = 8 \times 10^{-6}/^{\circ}\text{C}. \quad (5.2)$$

Assuming a rigidity of the glue of $R = 30000 \text{ MPa}$, the equivalent force which is applied to the glue during the cooling is:

$$F = W \times R \times \Delta L/L = 5 \text{ N}, \quad (5.3)$$

corresponding to 0.5 kg (where W is the working area, $W = 50 \text{ } \mu\text{m} \times \ell$). In order to test the mechanical resistance of the glue, a specific device was built within the "Service Détecteurs de l'IPNO" (Fig. 5.3). An APD, glued on the crystal, is fixed at the center of the device. A cylinder sliding from the top, creates a vertical force on the APD.

Additional weight can be added on the top of the device. Each applied weight (5.5, 11, 16.5, 22 kg, ...) is kept in place for a period of time of four hours. A comparator was used to measure the slip between the crystal and the APD, if applicable.

The glue DC3145 shows a strong mechanical resistance. The system withstood higher and higher weights, up to a limit of 63 kg, when the crystal was damaged due to break-up. Such strong resistance will prevent replacing the APD in case of damage. Finally, when the calorimeter will be in place, replacements are not foreseen. However, during the test procedure, it would be possible to unglue the APD using ethyl alcohol. After immersing a sample formed by the "crystal + DC3145 + APD" for a period of about two hours in ethyl alcohol, the APD has been easily separated without inducing any crack inside and even on the surface of the crystal. The ethyl alcohol does not damage the properties of the crystal. This was verified by putting a crystal in alcohol for two days where also no change in the crystal was observed.

The mechanical test was also applied on the second glue RT600 with the same procedure. The system supported only a maximum weight equal to 0.86 kg but split up very easily under a weight of 1.53 kg showing a significantly lower mechanical resistance of the glue.

5.3 Optical tests: transmittance measurements

Transmittance measurements at low temperature were done, at the "Institut de Chimie Moléculaire et des Matériaux d'Orsay", in order to verify that the glues do not lose or change transparency in the interesting wavelength range. Similar tests have been done before [113, 114] but at our knowledge not at low temperatures. Due to the luminescence of PbWO_4 , the relevant emission spectrum is located between 300 nm and 600 nm. However, we extended this range from 190 to 800 nm: on the short wavelength side, in order to inspect the transition towards complete absorption, and on the long wavelength side, since the stability of the photo sensor performance can be monitored independently at longer wavelength. The absorption of radiation by the molecules in the UV/visible domain (considered here) is due to the transition of an electron from a molecular orbital to another with higher energy. The transmittance of a sample, denoted T , is given by the ratio of an incident beam intensity I_0 and the corresponding transmitted intensity I ($T = I/I_0$). The absorption coefficient is defined as $A = -\log T$.

The measurements were done with a double beam spectrophotometer Varian Cary 5000 with two light sources, a deuterium lamp in the range 185-350 nm and a tungsten lamp in the range 350-3500 nm. A schematic diagram of a double-beam UV-V spectrophotometer is shown in Fig. 5.4. The beam emitted by the source crossed a monochromator which selected a narrow, adjustable wavelength range for the beam. The beam was then divided in two beams: one passed through the sample, and the other one served as reference. The calibration was insured by an automatic procedure. A cryostat was integrated in the spectrophotometer. The temperature was adjusted by

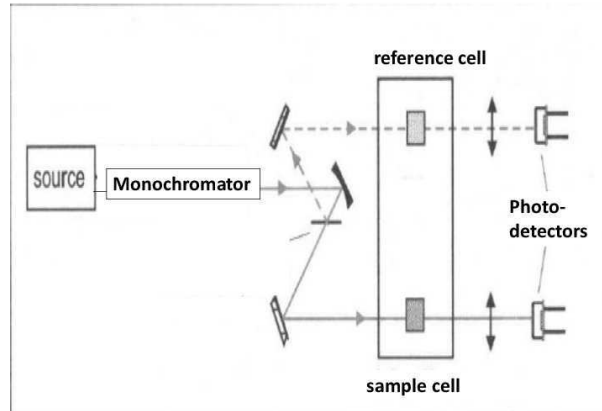


Figure 5.4: Schematic representation of double beam spectrophotometers.

thermal conduction, with the help of liquid nitrogen. The sample was fixed between two copper plates (Fig. 5.5). The plates had a hole of 5 mm diameter for the optical beam to pass through the sample. The hole had to be large enough to have a homogeneous spot on the glued sample. However a compromise had to be found, because a large hole would prevent a homogeneous distribution of the temperature on the quartz glass, which is not a good conductor.



Figure 5.5: Varian Cary 5000 spectrophotometer (left). Copper plates of the spectrophotometer (right).

Three samples were prepared: two samples with two quartz glasses glued by DC3145 and RT600, and a third sample with two quartz glasses without glue. The measurement of the transmittance was done by comparing the transmitted beam with the reference beam. An automatic scan in the chosen domain of wavelengths was done.

After setting a new temperature value, it was necessary to wait 15 min for stabilizing the system, as well as verify and regularly fill the level of the liquid nitrogen. The automatic zero of the system was periodically reset.

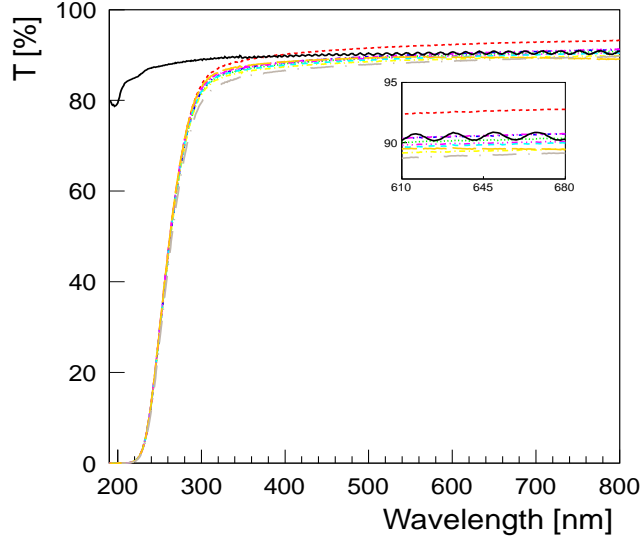


Figure 5.6: Optical transmittance as a function of the wavelength, with sample of two quartz glass plates without glue (black solid line) and with glue DC3145 at different temperatures: $+20^{\circ}\text{C}$ (red dashed line), $+15^{\circ}\text{C}$ (green dotted line), $+10^{\circ}\text{C}$ (blue dashed-dotted line), 0°C (yellow long dashed-dotted line), -10°C (violet long dashed-triple dotted line), -20°C (cyan long dashed), -25°C (magenta long dashed-double dotted), -30°C (orange very long dashed line), -40°C (gray very long dashed-dotted line). The upper part of the spectra is magnified in the overlay.

Series of measurements were performed for temperatures ranging from 20°C down to -40°C for DC3145 and -50°C for RT600. Reference spectra of the transmittance of the sample with the two quartz glasses without glue as well as without sample were also taken. The results are shown in Fig. 5.6 for the glue DC3145 and in Fig. 5.7 for RT600. All the spectra have been normalized to the run without sample.

In Fig. 5.6, one can see that the spectra with the glued sample show a very similar behavior at the different temperatures: below 220 nm the transmittance is zero (total absorption), then the transmittance increases above $T \approx 80\%$ with increasing wavelength from $\lambda = 290\text{ nm}$. The discontinuity of each spectra around $\lambda = 349\text{ nm}$ is due to the transition between the two lamps. Comparing to the spectrum of the sample without glue (solid black line), one can notice that the transparency loss is mainly due to the quartz glasses. The effect of the glue appears between 190-300 nm, which is not a relevant domain for PbWO and does not depend on the temperature. The spectra corresponding to the different temperatures are overlapping: the small differences are on the level of uncertainties in the adjustment of the set-up and instrumental accuracies. The oscillations on the spectra are due to the light reflection on the two quartz glasses.

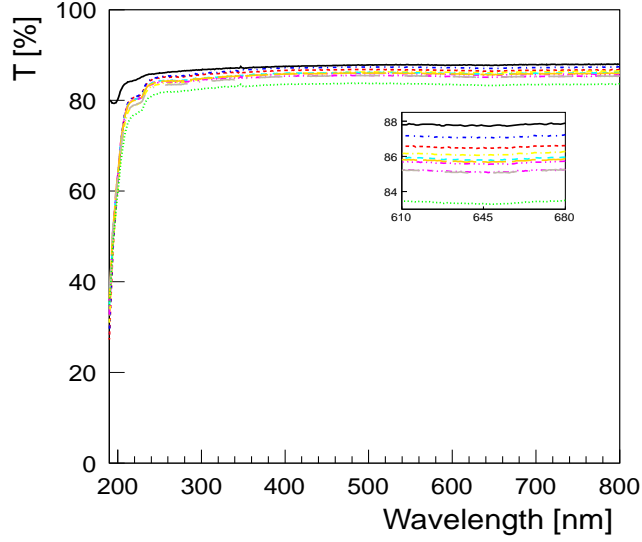


Figure 5.7: Optical transmittance as a function of the wavelength, with a sample of two quartz glass plates without glue (black solid line) and with glue (RT600) at different temperatures: +20° C (red dashed line), +10° C (blue dashed-dotted line), 0° C (yellow long dashed-dotted line), -10° C (violet long dashed-triple dotted line), -20° C (cyan long dashed), -25° C (magenta long dashed-double dotted), -30° C (orange very long dashed line), -40° C (gray very long dashed-dotted line), -50° C (green dotted line)

Similar results were obtained for the glue RT600 (Fig. 5.7). The difference between the curves is of the order of 2%, which is also the error inherent to the measurement. An additional measurement performed at $T = -50^\circ \text{C}$ shows a significantly larger gap. In general, RT600 has a superior transparency in the region between 200 and 300 nm compared to DC3145.

5.4 Radiation hardness test

Radiation damage studies on the glue DC3145 have been performed at room temperature by the CMS collaboration using three types of radiation: gammas with an integrated dose of 4000 Gy, slow neutrons of 1 MeV energy and 70 MeV protons with an integrated fluence of 2×10^{13} particles/cm² [109].

Although the results showed a slight sensitivity of the glue to gamma radiation, this glue was considered suitable for the CMS-ECAL detector.

In collaboration with the PANDA group at Giessen, a series of additional irradiation tests with gamma quanta and proton beams have been performed.

5.4.1 Gamma irradiation tests

Radiation hardness tests with gamma-quanta were performed with a Co-60 source in the Radiation Center of the University of Giessen. The dose rate was 2.32 Gy/min. Samples of a single quartz glass (0.21 ± 0.01 mm thickness), DC3145 glue (0.18 ± 0.03 mm thickness) and RT600 glue (0.03 ± 0.01 mm thickness) were tested. The effective thicknesses of layers of both glues were calculated by subtracting the two quartz plates from the overall thickness of the sample. The pure quartz sample was tested separately to evaluate the contribution of the identified damage.

Transmittance spectra of each sample were measured before and after irradiation with integrated doses of 100, 250, 500, 750 and 1000 Gy, respectively. The transmittance spectra were measured with the spectrophotometer Hitachi U-3200 in 30 minutes after the irradiation.

The results (Figs. 5.8, 5.9) show an excellent resistance to γ -radiation up to a dose of 1000 Gy in all cases. This holds for the quartz glasses glued with both glues as well as, for comparison, the sample without glue. The maximum dose of 1000 Gy is larger than the expected integral dose in the forward part of the PANDA EMC after more than 10 years of operation. Therefore one can conclude that both glues are sufficiently resistive to gamma irradiation compared to the radiation damage on the crystal itself.

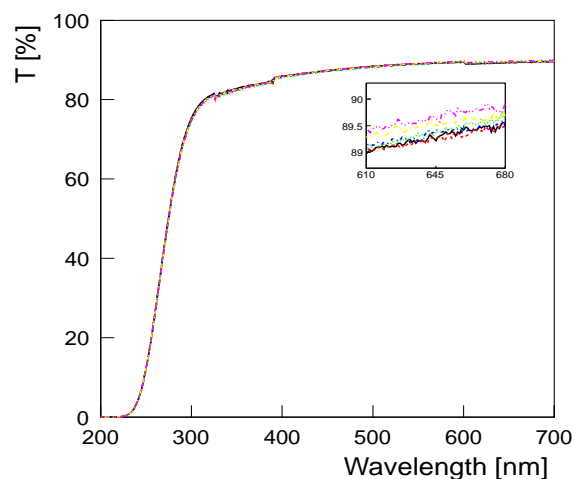


Figure 5.8: Optical transmittance of the two quartz glasses, glued with DC3145, as function of the wavelength, before irradiation (black solid line) and after irradiation with different doses: 100 Gy (red dashed line), 250 Gy (green dotted line), 500 Gy (blue dashed-dotted line), 750 Gy (yellow long dashed-dotted line), 1000 Gy (violet long dashed-triple dotted line), at room temperature.

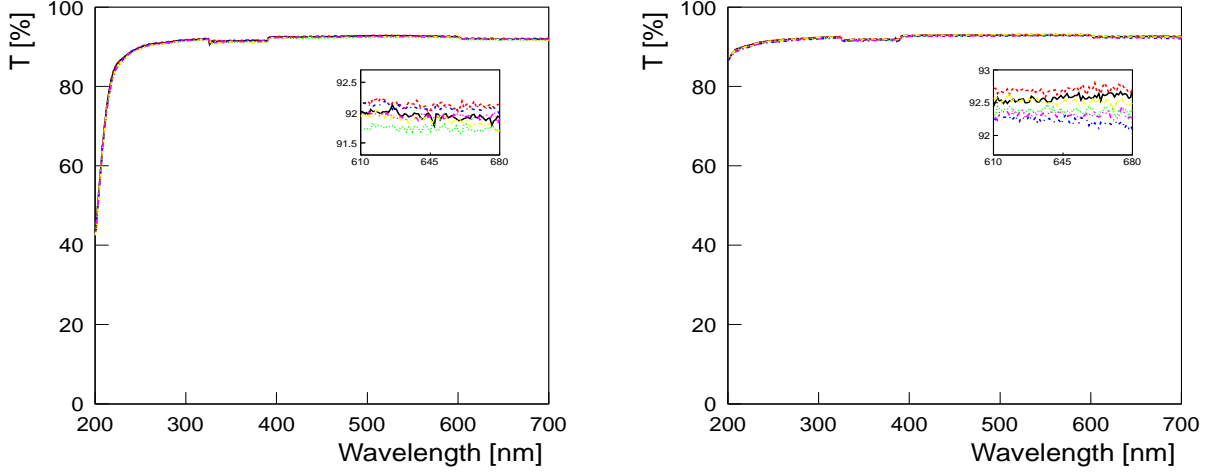


Figure 5.9: Same as Fig. 5.8 for the RT600 sample (left) and for the quartz glass sample (right).

5.4.2 Proton irradiation tests

Since DC3145 has a stronger mechanical resistance and is easier to manipulate (one component product), it appears to be preferable than RT600 for this PANDA application. Therefore, the irradiation studies with a proton beam were performed only with DC3145.

The tests with two samples of DC3145 were performed with a 150 MeV proton beam at the irradiation beam-line of the AGOR facility at KVI (Groningen, The Netherlands). The proton beam was defocused and homogenized by scatter foils to illuminate full area of the samples. The first sample (0.12 ± 0.03 mm thickness) was irradiated with the total fluence of 10^{12} protons/cm², and the second one (0.08 ± 0.02 mm thickness) with $1.8 \cdot 10^{13}$ protons/cm². Transmittance measurements before and after irradiation were done with a spectrophotometer Hitachi U-3200. The results are presented in Fig. 5.10. No significant damage of the transmittance even after irradiation with the higher fluence can be observed.

5.5 Conclusion

In this chapter, the mechanical, thermal, optical properties and the radiation hardness of two commercial glues (DC3145 and RT600) have been studied. The results show that the DC3145 glue meets the requirements of the PANDA-EMC operational conditions. Therefore, the PANDA collaboration has chosen the DC3145 for the optical coupling between the LAAPDs and PWO crystals for the EMC.

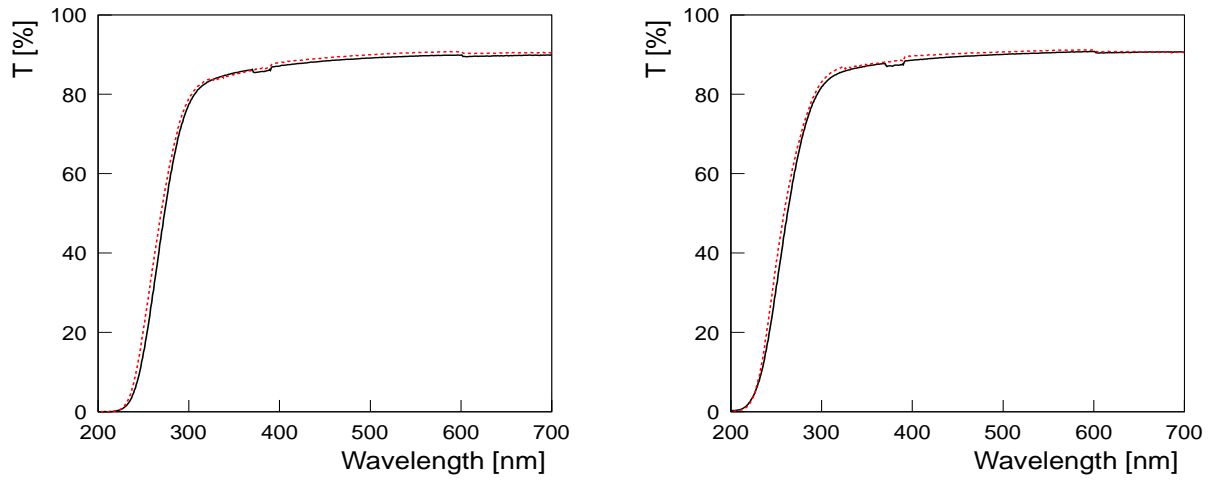


Figure 5.10: Optical transmittance of the two quartz glasses, glued with DC3145, as function of the wavelength, before irradiation (black solid line) and after irradiation (red dashed line) with a dose of $1. \times 10^{12}$ proton/cm² (left) and 1.8×10^{13} proton/cm² (right), at room temperature.

Chapter 6

Feasibility studies of proton form factor measurements at PANDA

This chapter is dedicated to the feasibility study of measuring EM FFs of the proton through the annihilation reaction $\bar{p}p \rightarrow e^+e^-$. Based on MC simulations within the framework of the PANDARoot software, an estimation of the statistical precision at which the proton FF ratio can be determined at PANDA is presented. The feasibility studies described here are divided into three parts:

1. The study of the suppression of the main background ($\bar{p}p \rightarrow \pi^+\pi^-$) versus the signal ($\bar{p}p \rightarrow e^+e^-$) efficiency. For this purpose the full simulation of these 2 channels has been performed within PANDARoot software and it is described in this section.
2. The description of the procedure to extract the information from the relevant spectra.
3. The evaluation of the statistical errors on the extracted proton FF ratio from the events of the reaction $\bar{p}p \rightarrow e^+e^-$. Note that the procedure developed here will be applied directly to the experimental data.

A previous study on the feasibility of proton FF measurement was performed within the BABAR framework [115] and published in Ref. [41] for the preparation of the physics performance report for PANDA [18]. The BABAR framework contains the PANDA geometry. The interest of doing the present analysis is twofold. First, the conception and the design of the detector has been optimized since the PANDA report has been published in 2009. Second, a new software (PANDARoot) has been developed and the necessary routines have to be created and/or tested according to the intrinsic physics cases. Therefore we present here the updated analysis dedicated to the extraction of the TL proton FFs at PANDA.

The study of the background suppression requires first the evaluation of the counting rates of the signal and the background. After describing the kinematics of these reactions in section 6.1, the evaluation of the counting rates is done in section 6.2. The

standard chain of the full simulation with PANDARoot is described in section 6.3. The different models used for the event generators, the reconstruction and the calculation of the PID probability are also explained. Based on the properties of the kinematics and the PID information from the sub-detectors, the procedure to identify and analyze the signal and the background is discussed in section 6.4. Finally, the angular asymmetry $\mathcal{A} \pm \Delta\mathcal{A}$ and the proton FF ratio $R \pm \Delta R$ are extracted in section 6.5 using a fitting procedure.

6.1 Kinematics

Let us consider the reaction:

$$\bar{p}(p_1) + p(p_2) \rightarrow h^-(k_1) + h^+(k_2), \quad h = e, \pi, \quad (6.1)$$

where the four-momenta of the particles are written in parentheses. The analysis presented in this chapter is mainly done in the CMS, in a coordinate frame where: the z -axis is directed along the antiproton momentum ($z \parallel \vec{p}$), the y -axis is directed along the vector $\vec{p} \times \vec{k}$ (\vec{k} is the momentum of the negative particle in the final state in CMS) and the x -axis in order to form a left handed coordinate system. In this frame the four-momenta are:

$$\begin{aligned} p_1 &= (E, \vec{p}), \quad p_2 = (E, -\vec{p}), \\ k_1 &= (E, \vec{k}), \quad k_2 = (E, -\vec{k}), \quad \vec{p} \cdot \vec{k} = pk \cos \theta, \end{aligned} \quad (6.2)$$

The kinematics is also described with the azimuthal angle ϕ . The cylindrical symmetry of the unpolarized binary reactions around the beam axis implies an isotropic distribution in ϕ .

The reactions $\bar{p}p \rightarrow e^+e^-$ and $\bar{p}p \rightarrow \pi^+\pi^-$ are two body final state processes. The electrons or pions in the pair are emitted back to back in the CMS. Each of the final particles, having equal mass, carries half of the total energy of the system, \sqrt{s} , where the invariant s is defined as follows:

$$s = q^2 = (p_1 + p_2)^2 = (k_1 + k_2)^2, \quad E = \sqrt{s}/2. \quad (6.3)$$

In the Lab system where the proton target is at rest, the invariant s is written as follows:

$$s = 2M(E_1 + M), \quad (6.4)$$

where E_1 is the energy of the antiproton beam in the Lab frame and M is the proton mass. The mass of the electron and of the pion are smaller than the proton mass, and then there is no limitation on the angular range of the produced particles in the Lab system (see section 9.2).

In the present case, the signal and the background have very similar kinematics as the mass of the electron is sufficiently close to the pion mass, compared to other

hadrons. Therefore the kinematics plays a minor role in the electron/pion separation. However the kinematical selection helps for the suppression of the hadronic contribution related to the channels with more than two particles in the final states, or secondary particles which come from the interaction of primary particles with the detector material.

6.2 Cross section and counting rate

In the Born approximation, the differential cross section for the annihilation reaction $\bar{p}p \rightarrow e^+e^-$ (in the CMS), as a function of the proton electromagnetic FFs was derived in chapter 3 (Eq. 3.25). The total cross section, integrated over the full angular distribution range was also given (Eq. 3.26):

$$\sigma_{tot} = 8\mathcal{N}(2\tau|G_M|^2 + |G_E|^2). \quad (6.5)$$

The evaluation of the counting rate as a function of the energy needs a model for the proton FFs. The parametrization from Ref. [116], which is obtained by a fit to the TL data assuming $|G_E| = |G_M|$, is used:

$$|G_E| = |G_M| = \frac{22.5}{1 + s [GeV^2]/3.6} G_D, \quad G_D = (1 + s [GeV^2]/0.71)^{-1}. \quad (6.6)$$

The expected cross section and the number of counts are given in Tab. 6.1 for three values of the total energy squared s (which correspond to three values of the energy (E_1) and momentum ($p_{\bar{p}}$) of the antiproton beam in the Lab system), assuming an integrated luminosity $\mathcal{L} = 2 \text{ fb}^{-1}$ which is expected for each data point at one value of q^2 in four month data taking at PANDA, 100% efficiency and full acceptance.

$s [\text{GeV}^2]$	$E_1 [\text{GeV}]$	$p_{\bar{p}} [\text{GeV}]$	$\sigma [\text{pb}]$	$N_E[-1, 1]$	$N_E[-0.8, 0.8]$
5.4	1.	1.7	538	1.07×10^6	8.34×10^5
8.2	2.5	3.3	32	6.4×10^4	4.9×10^4
13.9	5.47	6.4	1	1.94×10^3	1.46×10^3

Table 6.1: Expected total cross section σ and number of counts N_E (in the full angular range ($\cos\theta = [-1, 1]$) and in the interval $|\cos\theta| \leq 0.8$) from Eqs. 6.5 and 6.6 corresponding to an integrated luminosity $\mathcal{L} = 2 \text{ fb}^{-1}$, for different values of s .

In chapter 2, the existing experimental data on the total cross section $\sigma^{\pi^+\pi^-}$ for the background annihilation process $\bar{p}p \rightarrow \pi^+\pi^-$, was compiled and parametrized (Eq. 2.10). Using this parametrization and Eq. 6.5 for the electron total cross section $\sigma^{e^+e^-}$, the ratio $\sigma^{\pi^+\pi^-}/\sigma^{e^+e^-}$ is shown in Fig. 6.1 as a function of the total energy squared s . One can see that this ratio takes its maximum ($\sim 10^5$) around $s = 6 \text{ GeV}^2$, and then it decreases rapidly with the energy as expected from the quark counting rules: the hadronic cross sections should decrease faster at large s than the electromagnetic channels, as the number of constituent quarks is larger [95].

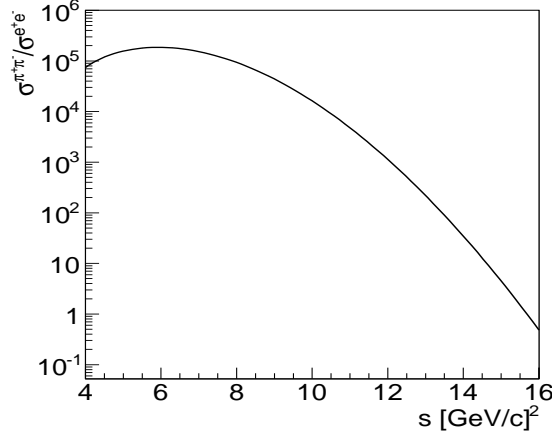


Figure 6.1: Ratio of the total proton antiproton annihilation cross section into a charged pion pair relative to an electron pair, as a function of total energy squared s .

6.3 PANDARoot software

PANDARoot is the offline software for the PANDA detector simulation and event reconstruction. It is implemented in FairRoot [117], a common framework for the future FAIR experiments, which is currently used to simulate detector performances and to optimize different detector concepts. The reconstruction code is developed in the frame of PANDARoot which contains the design of the PANDA detector.

The software is based on the ROOT [118] and Virtual MC [119] packages where the transport models Geant3 [120] and Geant4 [121] are implemented. Different reconstruction algorithms for tracking and PID are under development and optimization in order to achieve the performance requirements of the experiment. The simulation using the PANDARoot framework can be described as in Fig. 6.2.

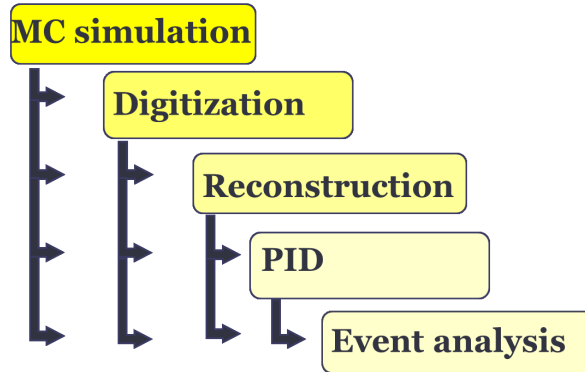


Figure 6.2: Standard chain of reconstruction in PANDARoot.

6.3.1 Event generator

Physics and background events can be produced by different event generators according to the physics case, such as EvtGen, Dual Parton Model (DPM), PYTHIA and Ultra relativistic Quantum Molecular Dynamics (UrQMD). Additional generators are developed within the collaboration for specific physics case needs (i.e. for electromagnetic FFs, DY, Hypernuclei, etc.) and inserted into the code.

EvtGen [122] is an event generator used by several collaboration (BaBar, CLEO, D0, Belle...), well suited for the physics of B-meson decays, for complex sequential decays and CP violating decays. It allows to generate the resonances of interest, taking into account the known decay properties, including angular distributions, polarization, etc., and allows the user to define the decay models of his choice. EvtGen uses the formalism of spin density matrices which takes into account the spin effects and provides the possibility to study the angular distributions of particles in the final state. A decay table lists the possible decay processes, their branching ratio and their decay model.

For the simulation of the produced particles, the DPM based generator, can be used in the case of $\bar{p}p$ annihilation. DPM [123] is based on Regge theory, which gives the energy dependence of hadron-hadron cross sections assuming various exchanges of particles between projectile and target in the t-channel. It gives the possibility to simulate inelastic interactions as well as elastic $\bar{p}p$ -scattering.

In case of antiproton nucleus collisions, the UrQMD model [124] is used for generating the annihilation background. It is a microscopic model based on phase space description of nuclear reactions. It describes the phenomenology of hadronic interactions at low and intermediate energies ($\sqrt{s} < 5$ GeV) in terms of interactions between known hadrons and their resonances. At higher energies, $\sqrt{s} > 5$ GeV, the excitation of colour strings and their subsequent fragmentation into hadrons are taken into account.

6.3.2 Digitization

The digitization is the second step of the simulation. It follows the propagation of the generated particles through the PANDA detector by using the GEANT3 or GEANT4 transport codes which takes into account the interactions of the particles with the detector material and their decays (interaction point, energy losses,...) in terms of hits. The digitization models the signals and their processing in the front-end-electronics of the individual detectors, producing a digitized detector response as similar as possible to the real data.

6.3.3 Reconstruction

The momentum values and the vertex coordinates of each charged particle are reconstructed by merging the information from all the tracking detectors present in the spectrometer. In the target spectrometer, tracking is provided by the MVD surrounding the interaction point, the STT arranged in a cylindrical volume around the beam

axis, and the GEM stations for forward angle tracks. The track object provides information about a charged particle path through the space. It contains a collection of hits in the individual tracking sub-detectors.

The momentum and the energy of the photon are reconstructed with the EMC sub-detectors. The continuous area formed by an electromagnetic shower of incident photon in the scintillator modules of the EMC is called cluster. The energy deposit and the position of all scintillator modules in a cluster allow the determination of the four vector of the initial photon.

6.3.4 Particle Identification

The charged tracks described by a set of parameters and their covariances are extrapolated to the different positions in the spectrometer using GEANE track follower [125]. The charged candidates are then filled with the track variables adding the information which is relevant for PID, i.e. dE/dx , Cherenkov angle, energy deposit in EMC, etc. The EMC clusters which are not correlated to charged tracks are considered as neutral particle candidates.

Several PID algorithms run over each candidate where the probability density functions are calculated. The PID software is divided in two different parts. In the first stage the recognition is done for each detector individually, so that final probabilities for all five particle hypothesis (e, μ , π , K and p) are provided. The probabilities are normalised uniquely by assuming the same fluxes for each particle species. In the second stage the global PID combines the information from all sub-detectors by applying a standard likelihood method.

For the simulation described in this chapter, PID information from the four sub-detectors EMC, STT, (Barrel and Disc) DIRC and MVD are used for the electron/pion separation. The PID algorithms of these sub-detectors which correspond to the PANDARoot version number 17878, are described below.

EMC PID algorithm: the PID probability given by the EMC and used in the present simulation, is called the "Bayesian EMC PID" [126]. The method uses a naive Bayes classifier to combine the three variables of the EMC: the energy deposit over the momentum, the lateral moment, and one Zernike moment [127]. The Zernike moments describe the energy distribution within a cluster by radial and angular dependent polynomials.

A naive Bayes classifier is a probabilistic classifier based on Bayes' theorem with strong independence assumptions. The Bayes theorem is expressed as:

$$P(c_j|d) = \frac{P(d|c_j)P(c_j)}{P(d)}, \quad (6.7)$$

where

- $P(c_j|d)$ is the probability of instance d being in class c_j . In the present case the

instance d corresponds to the three EMC variables, and the class c_j is attributed to the type of the particle (e, μ , π , K, p).

- $P(d|c_j)$ is the probability of generating the instance d in a given class c_j .
- $P(c_j)$ is the probability of occurrence of the class c_j .
- $P(d)$ is the probability of the instance d .

Naive Bayesian classifiers assume that attributes have independent distributions and thereby estimate:

$$P(d|c_j) = P(d_1|c_j) * P(d_2|c_j) * \dots * P(d_n|c_j). \quad (6.8)$$

The EMC probability was built with a MC data set of single tracks for each particle species in the momentum range between 0.2 GeV and 10 GeV. In the current version of PANDARoot, the Bayes method is only available for the EMC sub-detector.

STT PID algorithm: the PID probability for the STT sub-detector is calculated with samples of particles of each kind, simulated and fully reconstructed in a momentum range between 0.2 GeV and 5 GeV. Since at fixed momentum the dE/dx mean values are nearly Gaussian, the momentum range has been divided into intervals ~ 30 MeV/c large and for each interval the dE/dx distribution has been fitted with a Gaussian function. The extracted parameters of the fit, sigma σ and mean μ , as a function of the momentum, have been again best fitted with the following function:

$$f = \frac{p_0}{p^2} + p_1 \log p + p_2, \quad (6.9)$$

where p_i are fit parameters, and p is the momentum. The Gaussian function is missing the right shoulder of the distribution. Actually, ongoing work aims to include a new fit function, the "Novosibirsk function" for the STT PID in the code of PANDARoot. The Novosibirsk function is a Gaussian distribution with an extra parameter describing the tail (Fig. 6.3). It is given by:

$$f(x) = a_0 \exp \left[-0.5 \frac{\ln^2(1 + \lambda a_1(x - a_2))}{2a_1^2} \right], \quad \lambda = \sinh[a_1 \sqrt{\ln 4} / (\sigma a_1) \sqrt{\ln 4}], \quad (6.10)$$

where a_0 is a normalization factor, a_1 is the peak position of the distribution, σ is the resolution and a_1 is the tail parameter.

When a particle of unknown mass has to be identified following this procedure, the dE/dx and momentum are reconstructed and a point is identified in the plot of energy loss as a function of the momentum, where the regions are known. Then, for every particle hypothesis, the Gaussian corresponding to the reconstructed momentum of the track is chosen and it is evaluated at the measured track mean dE/dx. The resulting value, which comes from a standard normalized Gaussian, is the value of the

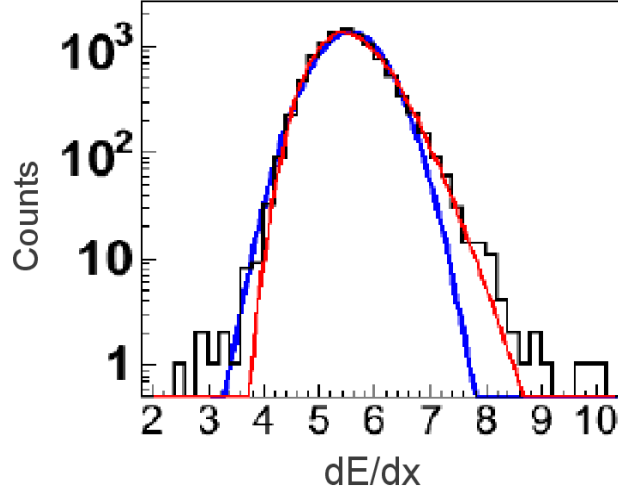


Figure 6.3: Pion STT dE/dx for a slice of momentum from Ref. [128], fitted with a Gauss function (blue) and Novosibirsk function (red).

probability density function for that hypothesis. In the momentum range $p < 0.2$ GeV and $p > 5$ GeV the procedure is not able to identify the type of the particle. The PID probability is splitted equally into the five particle types (0.2 for each type).

PID with other detectors: The DIRC sub-detector provides a PID probability using the information on the Cherenkov angle variable. The probability is calculated separately for the Barrel and the Disc components of the DIRC. The method is based on a fit of the difference between the expected Cherenkov angle in a medium of refractive index n , $\cos \theta_C = 1/(\beta n)$, and the reconstructed Cherenkov angle, for each particle type. The velocity $\beta = p/\sqrt{p^2 + m^2}$ is calculated using the tracking information on the momentum and the mass m of the particle. Additional help for the identification can be also obtained by energy loss information from the MVD detector, at the lowest momenta. In this case, the energy loss of particles with momenta below 1 GeV is parametrized using a Landau function.

Global PID: The global PID probability, which combines the relevant information of all sub-detectors associated with one track, has been realized with a standard likelihood method. Based on the likelihoods obtained by each individual sub-detector, the probability for a track originating from a particle type k is evaluated as follows:

$$P(k) = \frac{\prod_i P_i(k)}{\sum_j \prod_i P_i(j)} \quad (6.11)$$

where the product with index i runs over all considered sub-detectors and the sum with index j runs over the five particle types.

6.4 Simulation of the signal and the background

The complete simulation (from the MC generation level to the event analysis level) of a large number of events may take very large time. With the basic equipment at IPNO, an event is treated in ~ 3.5 sec. The time of the simulation can be reduced by splitting the total number of events into sub-jobs which can be run all in parallel. However this requires a large number of central processing units (CPUs). To this aim, the PANDA grid is used here to generate the background and the signal channels. Note that previous studies and tests of the PANDARoot methods and versions were done on the grid of IPNO [129]. The role of a grid is to facilitate the use of computer resources (computing and storage) distributed over the internet and accessible by users from different disciplines. The grid consists of a resource center with several sites.

The PANDA experiment will use the grid of PANDA [130] as well as its computing infrastructure for simulations, reconstruction and data analysis. This grid encompasses now 19 sites from 13 institutes in 9 countries. It is based on AliEn (Alice Environment) middleware [131], developed by the ALICE collaboration at CERN. The grid monitoring and data production supervision are done via MonALISA [132]. The grid of PANDA is used now to run theoretical calculations, simulations and other jobs related to detector design and prototyping.

6.4.1 Monte Carlo parameters

The EvtGen generator is used to generate the signal ($\bar{p}p \rightarrow e^+e^-$) and the background ($\bar{p}p \rightarrow \pi^+\pi^-$). Since two charged pions in final state constitute the background which is the most difficult channel to be identified, the DPM generator for the other elastic and inelastic background channels has not been used in the present study. Using the phase space PHSP model (flat distribution in $\cos\theta$ in CMS), $10^8(10^6)$ events are generated for the reaction $\bar{p}p \rightarrow \pi^+\pi^-(e^+e^-)$ at each value of the three incident antiproton momenta $p_{\bar{p}} = 1.7, 3.3$ and 6.4 GeV ($s = 5.4, 8.2, 13.9$ GeV² respectively). An overall background suppression factor of the order of a few 10^8 leads to a contamination far below the percent level. The events are generated in the full range of the polar angle θ and azimuthal angle ϕ . Our simulation was the first large scale simulation on the PANDA grid. It allowed optimization of procedures and sharing jobs: a gain in time of a factor 4 was achieved from the beginning of the simulation in April 2013 to the end in June 2013 [133, 134].

In the PANDARoot code, a MC event generator for the process $\bar{p}p \rightarrow \pi^+\pi^-$, has been implemented [135]. The kinematic region covers the antiproton momentum range from 0.79 GeV to 12 GeV, in the Lab frame. For the low energy regime, the parametrization of the cross section is based on a Legendre polynomial fit to data from the (antiproton beam) CERN 28 GeV proton synchrotron. For the high energy regime, the predictions of Ref. [33] (see section 6.5.6) based on a Regge theory approach were used.

As an example, the MC events given by this generator at $p_{\bar{p}} = 6.4$ GeV, are illus-

trated in Fig 6.4. One can see that the angular distribution is forward and backward peaked for negative and positive pions respectively. This model predicts a factor of about $\sim 10^2$ between the rates at $\cos\theta \pm 1$ and the central region where no experimental data exist. Therefore, it is possible that a larger number of pions than predicted by the model will be produced in the central region. This generator was not used for the studies described in this chapter.

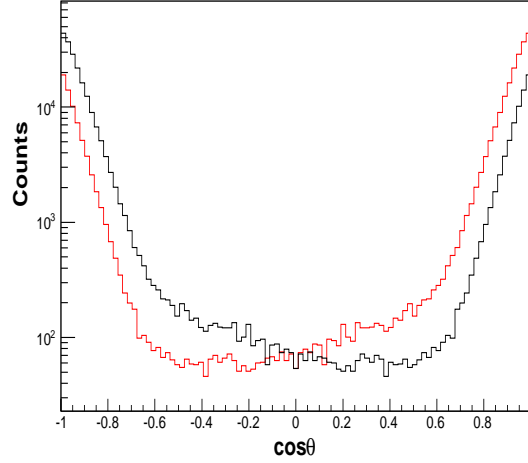


Figure 6.4: Angular distribution in the CMS of a sample of reconstructed pions for positive (black) and negative (red) particles, obtained with the model of Ref. [33] for $s=13.9 \text{ GeV}^2$.

Although the simulation, the reconstruction and the analysis have been fully performed for each 3 values of $s = q^2$ mentioned above, only the point at intermediate energy ($s = 8.2 \text{ GeV}^2$) will be illustrated in this section for the sake of clarity.

6.4.2 Analysis

The events for both channels have been analysed in two steps:

- First, the events which have one positive and one negative particle are selected. In the case when the track contains more than one positive or one negative particle (secondary particles which may produced by the interaction of generated primary particles with the detector materials), the pair (one positive + one negative) which is the best back-to-back in the CMS ($\theta + \theta' = 180^\circ$) is selected.
- Then, the reconstructed variables (kinematics, PID probabilities,...) of the selected events are analyzed and the best cuts which can suppress the pion background keeping at the same time the best possible efficiency for the signal are set.

Kinematics: the CMS angular distribution for the selected events before the cuts, is illustrated in Fig. 6.5 for the background (left) and the signal (right). Compared to the MC events, a fraction of about 82% (84 %) for the background (signal) is reconstructed and selected. The loss of $\approx 20\%$ corresponds mostly to forward and backward events ($\cos\theta \sim \pm 1$) due to the acceptance of the PANDA detector.

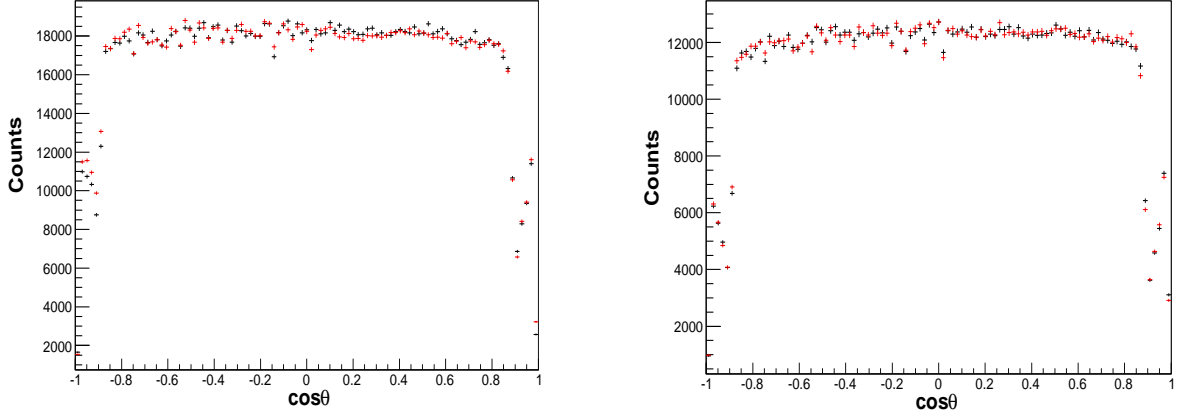


Figure 6.5: Angular distribution in the CMS for a sample of reconstructed events of the background (left) and the signal (right), for positive (black) and negative (red) particles, obtained with PHSP model for $s=8.2 \text{ GeV}^2$.

Fig. 6.6 shows the distribution in ϕ -angle for the electron and pion pairs. The azimuthal angles (ϕ for the negative and ϕ' for the positive particle) do not depend on the Lorentz transformation (the same in the CM and Lab system).

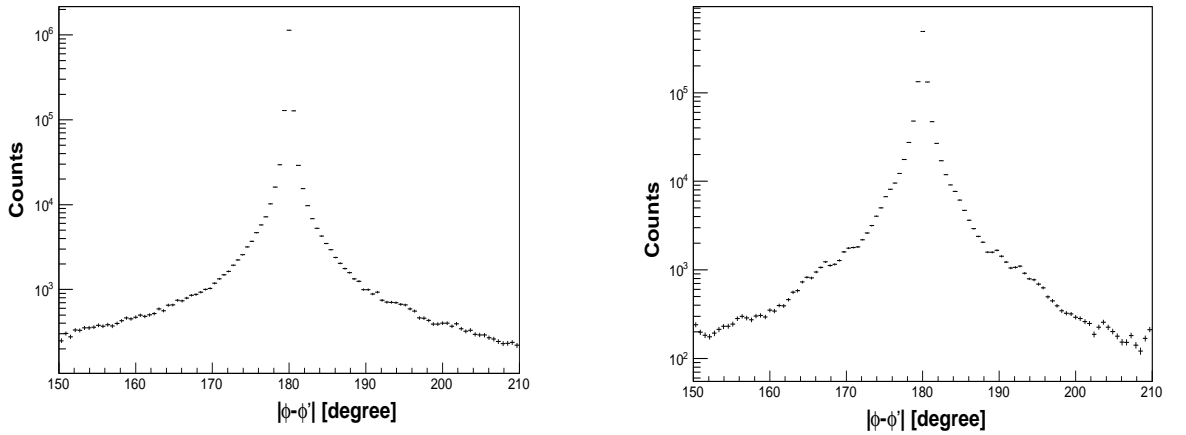


Figure 6.6: The difference $|\phi - \phi'|$ for a sample of reconstructed events of the pion (left) and the electron (right) pairs, for $s=8.2 \text{ GeV}^2$.

Unlike the momentum and energy of a charged particle, the polar angles (θ for the negative and θ' for the positive particle in CMS) as well as the azimuthal angles, in average are not affected by the Bremsstrahlung emission during the travel of the particle through the detector.

The reconstructed invariant mass (of the two charged pions and electrons) is defined as:

$$M_{inv} = \sqrt{(k_1 + k_2)^2}, \quad (6.12)$$

where k_1 and k_2 are the reconstructed four momenta of the negative and positive pions (or electrons) in the final state. The reconstructed invariant mass is shown in Fig. 6.7 for $s=8.2 \text{ GeV}^2$. The distribution has a maximum at the theoretical value of $\sqrt{s} \approx 2.86 \text{ GeV}$.

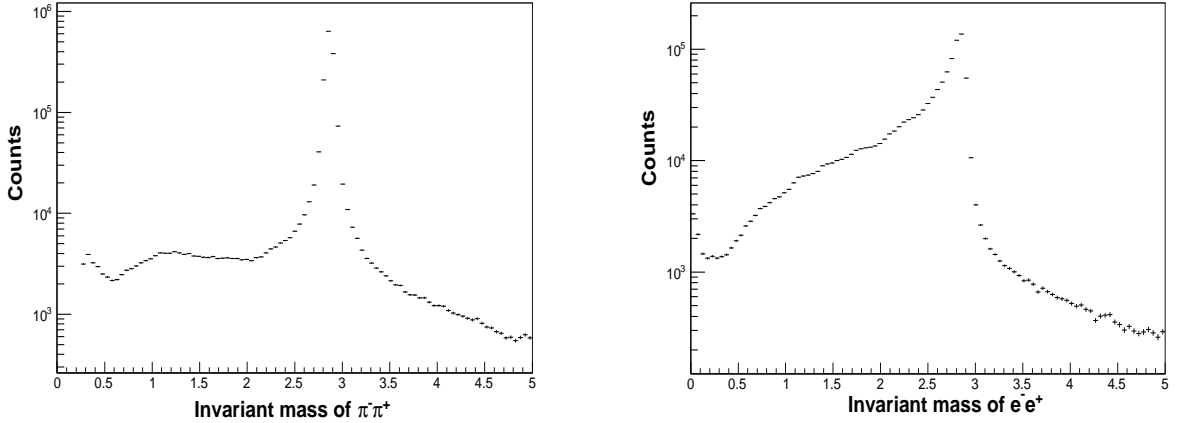


Figure 6.7: The invariant mass for a sample of reconstructed pion (left) and electron (right) pairs, for $s=8.2 \text{ GeV}^2$.

Reconstructed PID variables: the most sensitive variable in the EMC that can be used for the identification of charged particles is the ratio of the energy deposit (E_{EMC}) on the reconstructed momentum as shown in Fig. 6.8. For the signal (Fig. 6.8 right), this ratio is distributed around a mean value of about 1, with a width of the order of ~ 0.1 . The discontinuities that appear on the plot are due to the transition regions between the different parts of the EMC. For the background (Fig. 6.8 left), the distribution shows a double structure: a narrow peak at low “ $E_{EMC}/\text{momentum}$ ” values, which is due to energy loss by ionization, and another one around $E_{EMC}/\text{momentum}=0.4$ corresponding to the hadronic interactions. The tail of the latter extends to much higher values, causing background under the electron peak.

The energy loss per unit of length dE/dx in the STT is shown in Fig. 6.9 as a function of the reconstructed momentum.

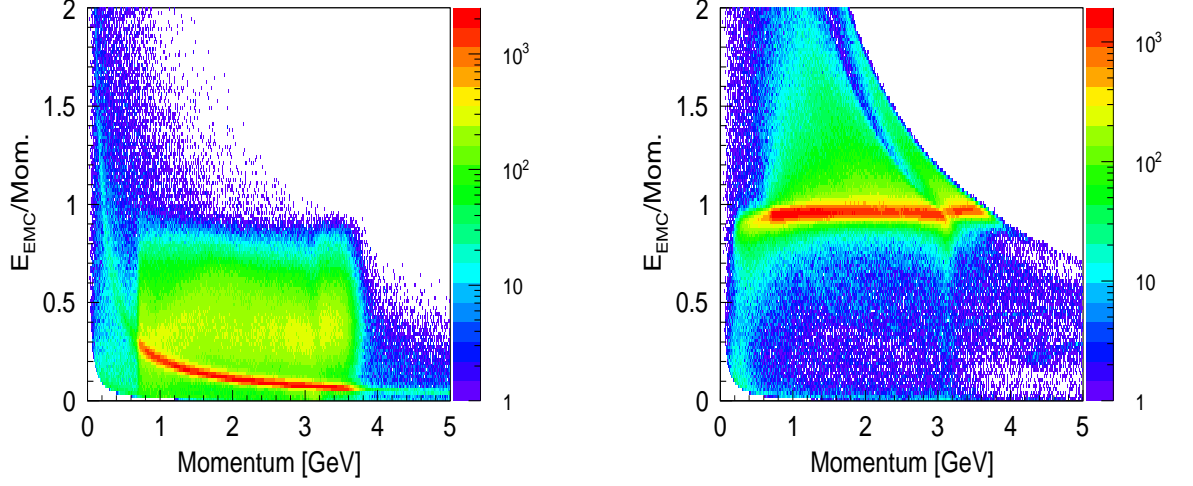


Figure 6.8: Energy loss in the EMC over the reconstructed momentum for a sample of reconstructed events of the background (left) and the signal (right), as a function of the reconstructed momentum (Lab system), obtained with PHSP model for $s=8.2 \text{ GeV}^2$.

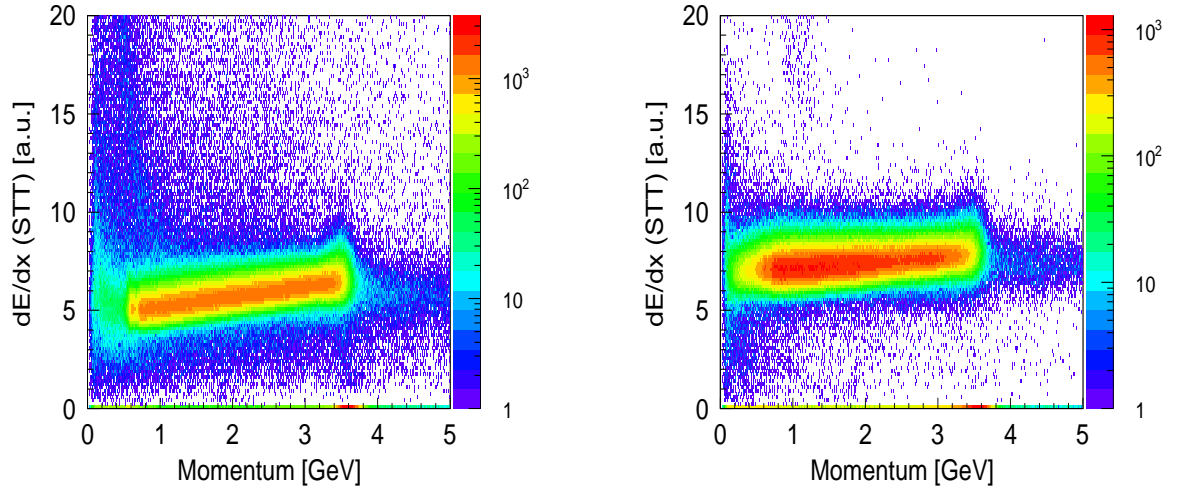


Figure 6.9: Same as Fig. 6.8 for the energy loss in the STT.

The Cherenkov angle provided by the Barrel DIRC is shown in Fig. 6.10. One can see that, at high energy, there is no possibility to disentangle electrons and pions using these two variables (dE/dx and θ_c).

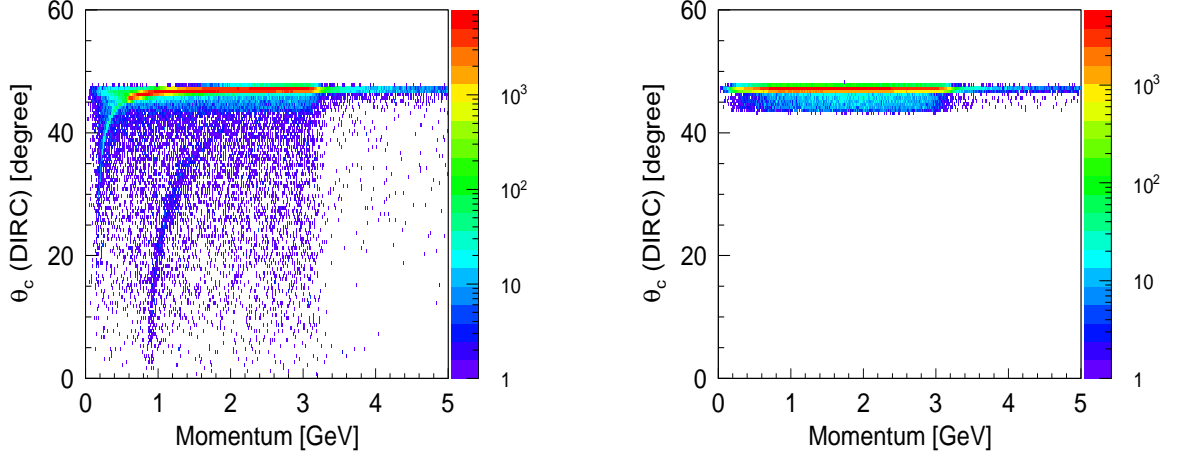


Figure 6.10: Same as Fig. 6.8 for the Cherenkov angle of the Barrel DIRC.

For the electron/pion separation, one can apply cuts on the variables shown in Figs. 6.8, 6.9, and 6.10 (hard cuts). However, with this method, a large fraction of the signal efficiency is lost. In the present analysis, PID cuts are rather applied on the probabilities given by the sub-detectors which are calculated on the basis of these variables.

PID probabilities for the detected particles to be identified as the signal: the probability for a pion to be identified as an electron, given by the sub-detectors EMC, STT, Barrel and Disc DIRC and MVD are shown in Fig. 6.11 for positive (left) and negative (right) pions. The distributions are maximum at PID probability equal to zero where the pions are well identified. The peak at 0.2, is related to the events when the method used to calculate the probability can not provide a decision about the type of the particle. In this case, the probability is splitted equally into the five particle types. The last bin of the histogram contains the events where the pions are identified as electrons (PID probability $P > 0.99$). The EMC is the most important detector for the electron identification. It is expected that the combined probability from the four sub-detectors improves the information on the type of the particle given by the EMC. This would be translated as a reduction of the number of events in the last bin of the histogram shown in Fig. 6.11, which in fact shows the opposite behavior. Eq. 6.11, used to combine the probabilities in PANDARoot, taking the case when only EMC and STT are hit, is written as:

$$P = \frac{P_{EMC} \cdot P_{STT}}{\sum_j P_{EMC}(j) \cdot P_{STT}(j)} \quad (6.13)$$

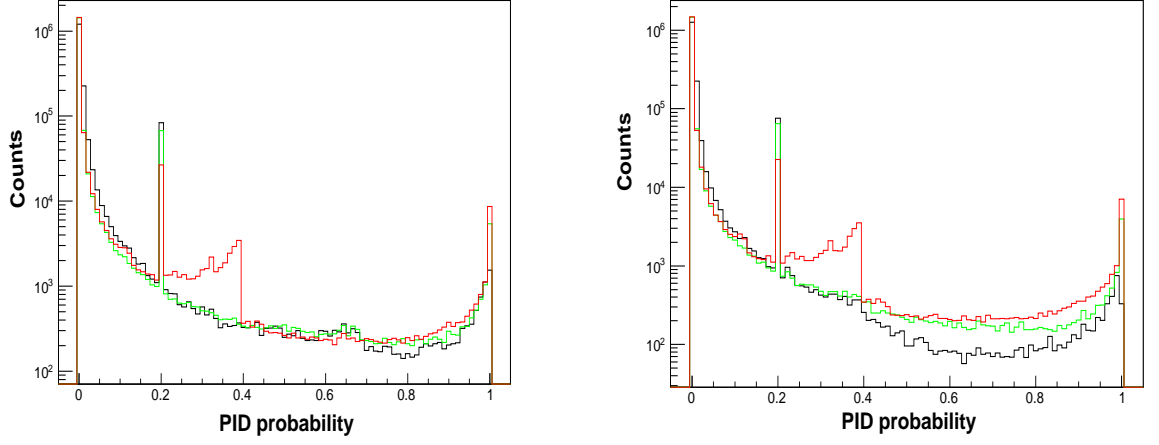


Figure 6.11: PID probability given by the EMC (black), EMC+STT (green) and total probability (red), for π^+ to be identified as e^+ (left) and π^- to be identified as e^- (right) for $s=8.2$ GeV².

For the pion events which have individual probabilities to be identified as the signal, $P_{EMC} \approx 0$ (well identified) and $P_{STT} = 1$ (misidentified), the combined probability is ~ 1 (misidentified). On the other hand, looking at the correlation which may exist between the sub-detectors EMC and STT (Fig. 6.12), it is seen that the large number of events, having electron P_{STT} equal to one, corresponds to P_{EMC} close to zero and vice versa. One can conclude that to enhance the rejection power of the background one should apply PID cuts, not only to the combined probability, but also on the individual probabilities P_i in order to eliminate the events with corresponding $P_i \sim 0$.

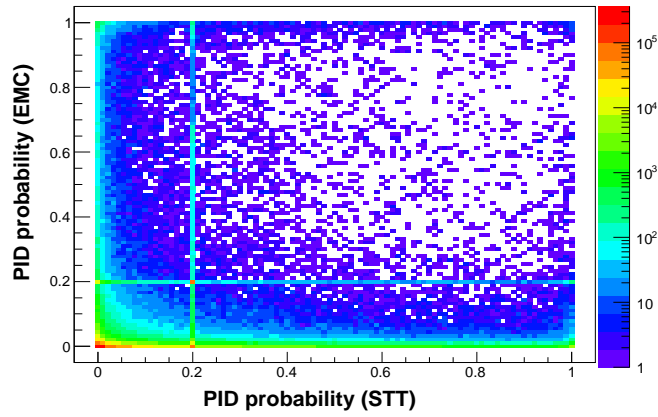


Figure 6.12: PID probability given by the EMC with respect to the probability given by the STT, for a pion to be identified as electron, for $s=8.2$ GeV².

For the signal, the PID probabilities are shown in Fig. 6.13. The distributions have their maximum at PID probability equal to one. These plots show that the combined probability increases the efficiency of the signal as expected from Eq. 6.11.

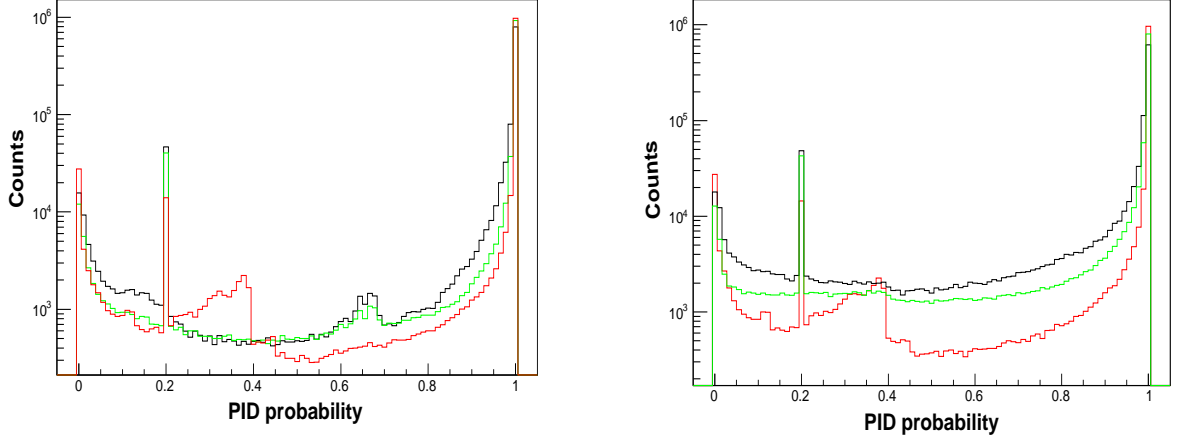


Figure 6.13: PID probability given by the EMC (black), EMC+STT (green) and total probability (red), for e^+ to be identified as e^+ (left) and e^- to be identified as e^- (right), for $s=8.2 \text{ GeV}^2$.

Number of fired crystals in the EMC: the number of fired crystals in the EMC (N_{EMC}) is also an important parameter which can be used for electron/pion separation. This variable is not taken into account by the Bayes PID probability calculated for the EMC and it depends on the kinematics of the reaction. Fig. 6.14 shows that a large fraction of the background events corresponds to less than 5 fired crystals, while the signal has a maximum in the region of $N_{EMC} > 5$.

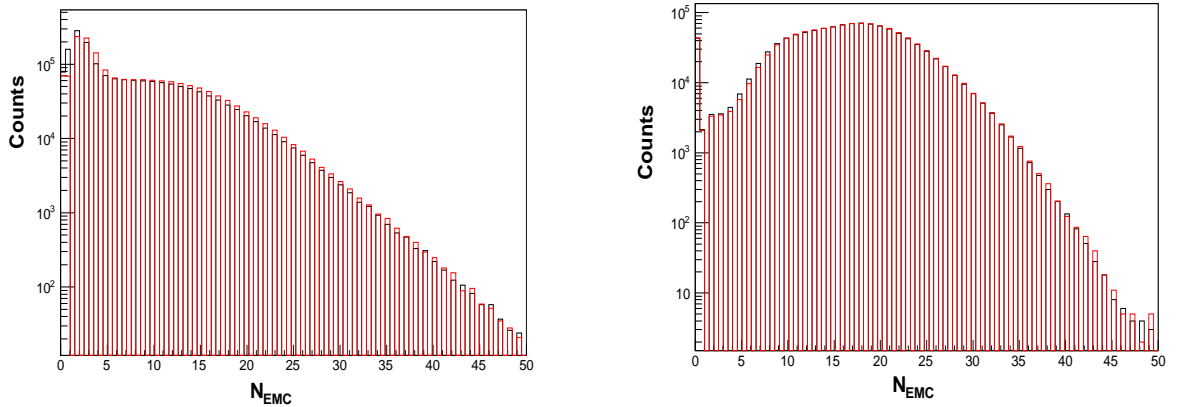


Figure 6.14: Number of fired crystals in the EMC, for a sample of reconstructed events of the background (left) and the signal (right), for positive (black) and negative (red) particles, for $s=8.2 \text{ GeV}^2$.

6.4.3 PID probability and kinematical Cuts

The cuts applied to the background and the signal events are reported in Tab. 6.2, for each value of the momentum transfer squared ($s = 5.4, 8.2$ and 13.9 GeV^2). The cuts are adjusted in order to kill the 3×10^8 events of the background, keeping at the same time the best possible values of the signal efficiency. The additional effect of the individual cut are reported for $s = 8.2 \text{ GeV}^2$ in Tab. 6.3.

$s[\text{GeV}^2]$	5.4	8.2	13.9
Combined PID probability	> 0.99	> 0.99	> 0.999
Individual PID_i	> 0.05	> 0.05	> 0.06
N_{EMC}	> 5	> 5	> 5
$\theta + \theta'$	$[178^\circ, 182^\circ]$	$[178^\circ, 182^\circ]$	$[175^\circ, 185^\circ]$
$ \phi - \phi' $	$[178^\circ, 182^\circ]$	$[178^\circ, 182^\circ]$	$[175^\circ, 185^\circ]$
Invariant mass [GeV]	no cut	> 2.14	> 2.5

Table 6.2: PID probability and kinematical cuts applied to the electron and pion reconstructed events.

Cut	pions [events]	Integrated efficiency
$\text{PID}^{tot} > 0.99, \text{PID}_i > 0.05$	693	61%
$N_{EMC} > 5$	268	60%
Kinematical cuts (θ, ϕ)	9	51%
$\sqrt{s} > 2[\text{GeV}]$	3, $[-0.8, 0.8]=1$	46%, $[-0.8, 0.8] = 54\%$
$\sqrt{s} > 2.135[\text{GeV}]$	0	44%, $[-0.8, 0.8] = 51.9\%$

Table 6.3: Number of events after the PID probability and the kinematical cuts for the signal and the background, for $s=8.2 \text{ GeV}^2$.

The reconstructed events for the signal, after applying the cuts, as well as the original MC events are shown in Fig. 6.15 (left) for $s=8.2 \text{ GeV}^2$. The drop of reconstructed events at $\cos \theta = 0.65$ ($\theta_{lab} \sim 22.3^\circ$) is due to the transition region between the forward and the barrel EMC (Fig. 6.15 right).

6.5 Expected statistical error on the proton FF ratio

The reconstructed electron events, after the full suppression of the $\pi^+\pi^-$ background, are used to extract the statistical error on the proton FF ratio following the scheme illustrated in Fig. 6.16.

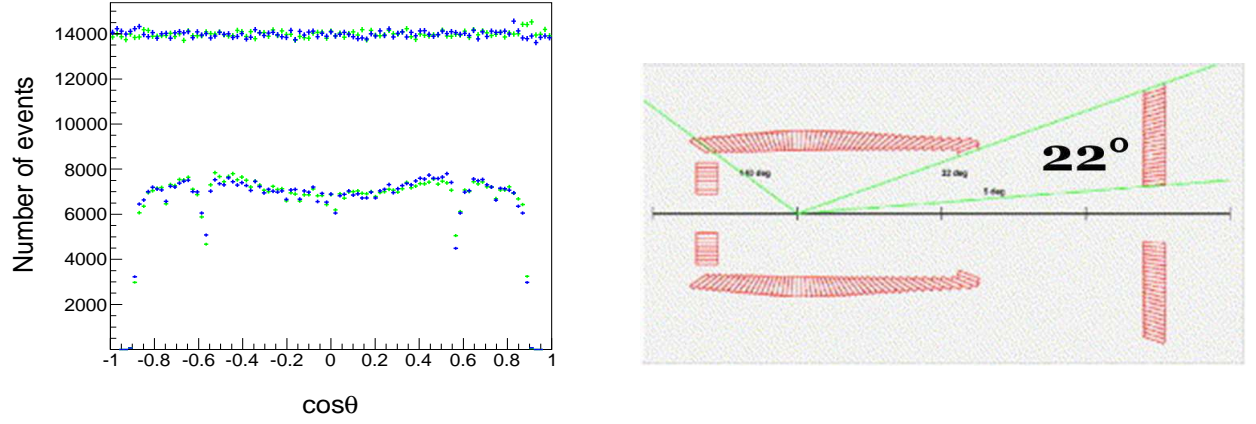


Figure 6.15: Angular distribution (left) of e^- (blue) and e^+ (green) in the CMS, for the MC events (top) and the reconstructed events after the cuts (bottom) obtained with PHSP model for $s=8.2 \text{ GeV}^2$, in correspondence with the EMC geometry in the Lab system (right).

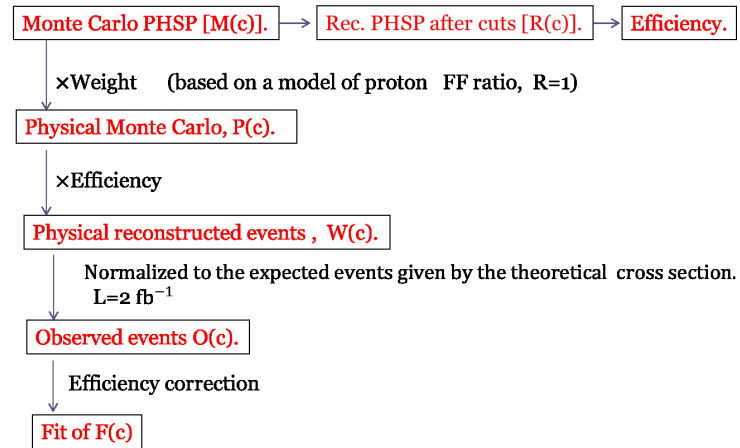


Figure 6.16: Scheme used for the extraction of statistical error on the proton FF ratio.

6.5.1 Experimental observables

The differential cross section for the electron pair production (Eq. 3.25) can be written as a function of the angular asymmetry \mathcal{A} as:

$$\frac{d\sigma}{d\cos\theta} = \sigma_0 [1 + \mathcal{A} \cos^2 \theta]. \quad (6.14)$$

\mathcal{A} is defined as the slope of the linear $\cos^2 \theta$ dependence, and σ_0 is the value of the differential cross section at $\theta = \pi/2$. They are functions of the proton FFs:

$$\sigma_0 = \mathcal{N} \left(|G_M|^2 + \frac{1}{\tau} |G_E|^2 \right), \quad \mathcal{A} = \frac{\tau |G_M|^2 - |G_E|^2}{\tau |G_M|^2 + |G_E|^2} = \frac{\tau - R^2}{\tau + R^2}, \quad (6.15)$$

where $R = |G_E|/|G_M|$ is the proton FF ratio. The angular asymmetry lies in the range $-1 < \mathcal{A} < 1$. Tab. 6.4 gives the values of \mathcal{A} under three assumptions of the electric FFs.

	R	\mathcal{A}
$ G_E = 0$	0	1
$ G_E = G_M $	1	$(\tau - 1)/(\tau + 1)$
$ G_E = 3 G_M $	3	$(\tau - 9)/(\tau + 9)$

Table 6.4: Values of R and \mathcal{A} according to different assumptions for $|G_E|$

The measurement of the angular asymmetry allows one to determine the FF ratio through the relation:

$$R = \sqrt{\tau \frac{1 - \mathcal{A}}{1 + \mathcal{A}}} \quad (6.16)$$

In the limit of small errors, as long as first order statistical methods work, the error on R can be obtained from standard error propagation on \mathcal{A} :

$$\Delta R = \frac{1}{R} \frac{\tau}{1 + \mathcal{A}^2} \Delta \mathcal{A}. \quad (6.17)$$

6.5.2 Extraction of the signal efficiency

The signal efficiency was extracted from the PHSP events for each $\cos \theta$ bin. The ratio between the PHSP reconstructed $R(c)$ (after the cuts), and the MC $M(c)$ events represents the signal efficiency as a function of the angular distribution (Figs. 6.17, 6.18), which can be written as:

$$\epsilon(c) = \frac{R(c)}{M(c)}, \quad c = \cos \theta. \quad (6.18)$$

To the content of each bin of the MC and reconstructed events, is attributed the error $\Delta M(c) = \sqrt{M(c)}$ and $\Delta R(c) = \sqrt{R(c)}$ respectively. The error on the efficiency is derived using Eq. 6.18 as follows:

$$\Delta\epsilon(c) = \sqrt{\frac{\epsilon(c)(1 + \epsilon(c))}{M(c)}} \quad (6.19)$$

Eq. 6.19 shows that, the statistical error on the efficiency depends on the number of MC events and it can be reduced to very small values.

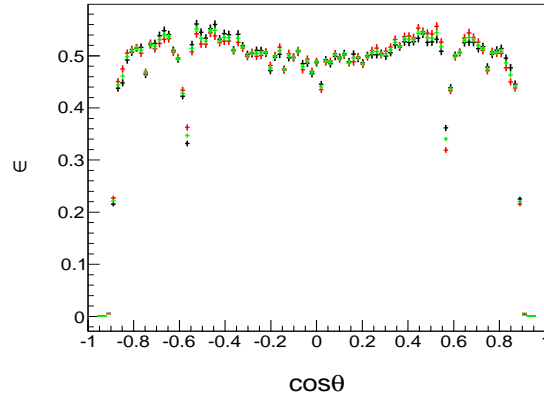


Figure 6.17: Signal efficiency for e^- (red), e^+ (black) and for their mean (green), obtained with PHSP model for $s=8.2 \text{ GeV}^2$.

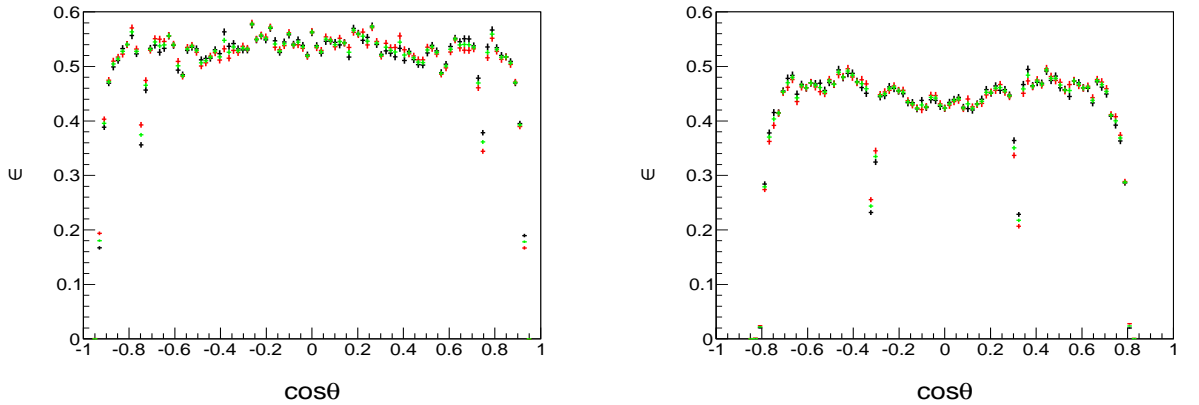


Figure 6.18: Same as Fig. 6.17 for $s = 5.4 \text{ GeV}^2$ (left) and $s = 13.9 \text{ GeV}^2$ (right).

Due to the drop of the efficiency in the region $\cos\theta > 0.8$, the analysis for the extraction of the proton FF ratio is limited to the angular range $\cos\theta = [-0.8, 0.8]$. The integrated efficiency in this region is given by Tab. 6.5 for the considered $s = q^2$ values.

$s \text{ [GeV}^2\text{]}$	5.4	8.2	13.9
$\epsilon[\%]$	54.36	51.9	43.8

Table 6.5: Efficiency integrated over the angular range $|\cos\theta| \leq 0.8$ for different s values.

6.5.3 Physical events

The PHSP events which have a flat distribution of $\cos\theta$ in CMS, do not contain the physics of the proton FFs. Physical events follow the angular distribution of Eq. 6.14. Therefore the MC histograms are rescaled by the weight $\omega(c) = 1 + \mathcal{A} \cos^2\theta$, where \mathcal{A} is given according to a model for G_M and G_E . The advantage of the PHSP model is that the same simulation can be used to test different models of the proton FFs at a fixed energy. Fig. 6.19 shows the angular distribution of the MC PHSP $M(c)$ events and physical $P(c)$ events, at $s=8.2 \text{ GeV}^2$, for the case:

$$R = \frac{|G_E|}{|G_M|} = 1, \quad \mathcal{A} = \frac{\tau - 1}{\tau + 1}. \quad (6.20)$$

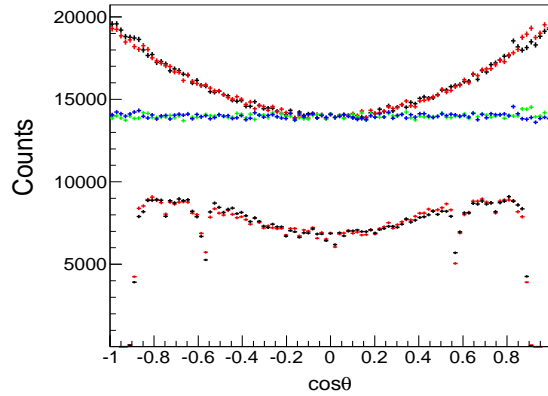


Figure 6.19: Angular distribution of the MC events obtained with PHSP model for e^- (blue) and e^+ (green) in the CMS, and following physical distribution (e^- (black) and e^+ (red)), before (top) and after the reconstruction and the cuts (bottom), for $s = 8.2 \text{ GeV}^2$ and $R = 1$.

The signal efficiency estimated following the PHSP events is applied on $P(c)$ to obtain the physical reconstructed events $W(c)$ (black color):

$$W(c) = P(c)\epsilon(c), \quad c = \cos\theta. \quad (6.21)$$

6.5.4 Normalization: observed events

The physical events $W(s)$ after the cuts are normalized according to the counting rate given by Tab. 6.4 which depends on the energy of the system and the luminosity of the experiment. The events which will be observed in the real experiment are estimated (with a luminosity of $\mathcal{L} = 2 \text{ fb}^{-1}$) as follow:

$$O(c) = W(c) \cdot \frac{N_E[-0.8, 0.8]}{\int_{-0.8}^{0.8} P(c) dc}, \quad c = \cos \theta, \quad (6.22)$$

with an error $\Delta O(c) = \sqrt{O(c)}$ since the experimental error will be finally given by the accumulated statistics of the detected events.

6.5.5 Efficiency correction and fit

The fit procedure is applied on the observed events after efficiency correction ($F(c)$):

$$F(c) = O(c)/\epsilon(c), \quad \Delta F(c) = \Delta O(c)/\epsilon(c) = \sqrt{O(c)}/\epsilon(c), \quad (6.23)$$

where the error on the efficiency $\Delta\epsilon(c)$ is neglected. For each s value, the distribution $F(c)$ as a function of $\cos^2 \theta$ is fitted with a two-parameter function (straight line). The linear fit function is:

$$y = a_0 + a_1 x, \quad \text{with } x = c^2, \quad a_0 \equiv \sigma_0, \quad a_1 \equiv \sigma_0 \mathcal{A}, \quad (6.24)$$

where a_0 and a_1 are the parameters to be determined by minimization. They are related to the physical FFs, through Eq. 6.15. The observed events, before ($O(c)$) and after ($F(c)$) efficiency correction are shown in Figs. 6.20 and 6.21.

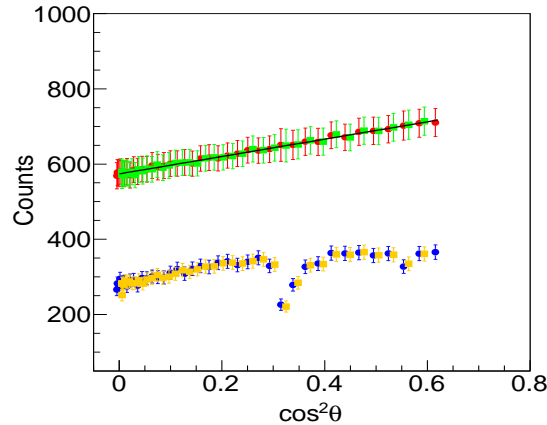


Figure 6.20: The observed events before efficiency correction $O(c)$ (forward events (blue circles) and backward events (orange squares)) and after efficiency correction $F(c)$ (forward events (red circles) and backward events (green squares)), as a function of $\cos^2 \theta$ for $s = 8.2 \text{ GeV}^2$ and $R = 1$. The line is the linear fit.

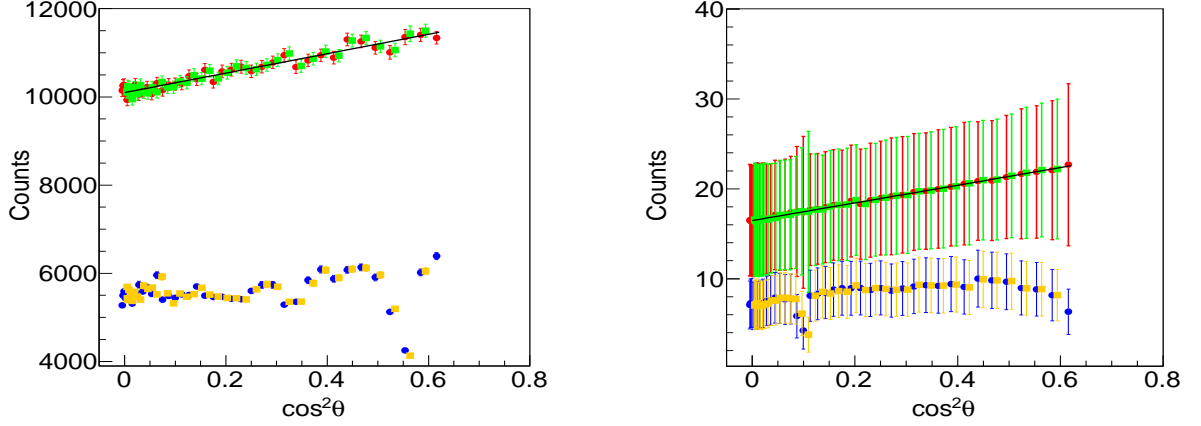


Figure 6.21: Same as Fig. 6.20 but for $s = 5.4 \text{ GeV}^2$ (left) and $s = 13.9 \text{ GeV}^2$ (right). The lines are the linear fit.

The result of the fit are reported in Tab. 6.6. The input values of R and \mathcal{A} are recovered within the error ranges. Note that the alignment of the points along the fitted function is driven by the high statistics (10^6) of the simulated events. Therefore the value of the χ^2 resulting from the fit is not significant.

$s \text{ [GeV}^2\text{]}$	R	A	$R \pm \Delta R$	$\mathcal{A} \pm \Delta \mathcal{A}$
5.4	1	0.21	0.992 ± 0.009	0.218 ± 0.009
8.2	1	0.4	0.997 ± 0.045	0.401 ± 0.038
13.9	1	0.59	1 ± 0.396	0.595 ± 0.255

Table 6.6: Expected statistical errors on the angular asymmetry and the proton FF ratio, for different s values. The second and the third columns are the theoretical values (simulation inputs). The fourth and the fifth columns are the results of the fit. The statistical errors are extracted in the angular range $|\cos\theta| \leq 0.8$.

The three points obtained from the present simulations and the world data on the proton FF ratio are shown in Figs. 6.22. Data are from Ref. [77] (red squares), Ref. [78] (black triangles), Ref. [79] (green circles), and Ref. [80] (blue stars). The yellow band is the result obtained in the previous analysis [41] within the BaBar framework. Note that the error bars are driven by the square root of the efficiency.

6.5.6 Error from the angular cut

The feasibility studies presented in this chapter showed that the suppression of the main background at the level of 10^{-8} is achieved keeping a sufficient signal efficiency for the proton FF measurement at PANDA. The physical distribution is not flat in $\cos\theta$, therefore the rejection power depends on the angular range. The differential cross section for the $\bar{p} + p \rightarrow \pi^+\pi^-$ process was parametrized in Ref. [33] reproducing

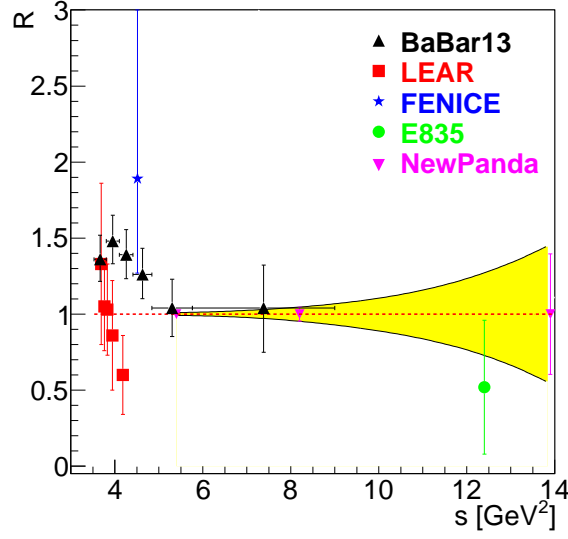


Figure 6.22: Expected statistical precision on the determination of the proton FF ratio for $R=1$, from Ref. [41] (yellow dashed band) and from the present simulation (magenta triangles) as a function of $s = q^2$, compared with the existing data. The statistical errors are extracted in the angular range $|\cos \theta| \leq 0.8$.

approximately the available data. At high energy, the t -dependence of the cross section is parametrized as:

$$\frac{d\sigma}{dt} = Cs^{-8}f(c), \quad f(c) = \frac{1}{2}(1 - c^2) = [2(1 - c)^{-2} + (1 + c)^{-2}]^2,$$

where

$$t = M^2 + M_\pi^2 - \frac{s}{2}(1 - \beta_\pi\beta_p c), \quad \beta_\pi = \sqrt{1 - \frac{4M_\pi^2}{s}}, \quad \beta_p = \sqrt{1 - \frac{4M^2}{s}},$$

Therefore

$$\frac{d\sigma}{dc} = \frac{d\sigma}{dt} \frac{dt}{dc} = \left(\frac{s}{2}\beta_\pi\beta_p\right) = \frac{C}{2}s^{-7}\beta_\pi\beta_p f(\theta), \quad c = \cos \theta,$$

where θ is the CM angle of π^- . For a better agreement with the experiment, the distribution in the forward and backward regions has been symmetrized around $c = 0$, and a value around $C=440 \text{ mb GeV}^{14}$ has been adjusted on the data.

The ratio of the differential cross section background/signal is shown in Fig. 6.23 for two values of s (8.2 and 13.9 GeV^2) and for the proton FF ratio $R = 1$. The ratio depends on the angle.

The range of $|\cos \theta| > 0.8$ where the ratio is larger than 10^6 is excluded from the present analysis due to the sudden drop of the efficiency in this region. The relative ratio is then maximum at $|\cos \theta| = 0.8$. In the real experiment, it is possible that the extraction of the proton FFs in the edge region becomes problematic. In this case one

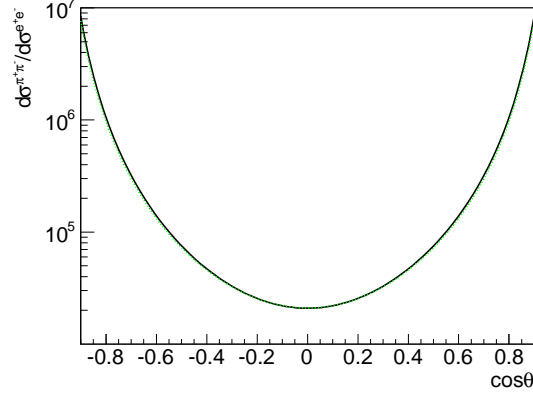


Figure 6.23: Ratio of the differential annihilation cross section into a pion pair relative to a charged electron pair in the CMS for $s=8.2 \text{ GeV}^2$ (back, solid line) and $s=13.9 \text{ GeV}^2$ (dashed, green line)

can limit the angular range. The effect of the angular cut on the expected statistical precision on the proton FF ratio is given in Tab. 6.7.

angular cut	$s=5.4 \text{ GeV}^2$	$s=8.2 \text{ GeV}^2$	$s=13.9 \text{ GeV}^2$
$ \cos \theta \leq 0.8$	0.009	0.045	0.396
$ \cos \theta \leq 0.7$	0.012	0.063	0.525
$ \cos \theta \leq 0.6$	0.018	0.094	0.764
$ \cos \theta \leq 0.5$	0.029	0.144	1.202
$ \cos \theta \leq 0.4$	0.052	0.258	2.209
$ \cos \theta \leq 0.3$	0.119	0.549	4.573

Table 6.7: Expected statistical errors on the proton FF ratio ΔR ($R = 1$) for different values of the angular cut.

The statistical error increases by reducing the angular range since the angular cut reduces the statistic. Reducing the angular range one can still extract a meaningful value, which does not compromise the quality of the experiment in comparison to the existing data at least for $s = 5.4$ and 8.2 GeV^2 . Note that in all previous experiments ([79], [77]), the proton FF ratio was extracted with an angular cut $|\cos \theta|$ smaller than 0.8, i.e. between 0.451 and 0.602 in Ref. [79].

This conclusion holds for $R = 1$. For the case of proton FF ratio $R = 0$, the angular distribution will be steeper, and the effect of the cut will be more evident. For $R=3$, on the other end, the asymmetry becomes negative, and the side bands count less than the central bins.

Different sources of systematic errors can affect the experimental result. For example, the experimental asymmetries or radiative corrections will change the linear dependence (in $\cos^2 \theta$) of the differential cross section for the electrons or positrons. MC simulations in Ref.[41] showed that the PANDA detector will be sensitive to a level of 5% of angular asymmetry. We did not repeat this study here as we do not expect significant differences with the results obtained from the present analysis.

6.6 Conclusion

A full simulation has been performed within the PANDARoot framework for three kinematical points, where 3×10^6 events have been simulated for the signal ($\bar{p}p \rightarrow e^+e^-$) and 3×10^8 events for the background ($\bar{p}p \rightarrow \pi^+\pi^-$). In comparison to the previous analysis [41], the description of the detector is more realistic as well as the different steps of reconstruction and analysis. The efficiency has improved by 5 to 10 %, although the experimental cuts will be finally set on the real data.

The knowledge of the TL electromagnetic FFs will be extended in a large kinematical range. The present results show that the statistical error at $q^2 \geq 14 \text{ GeV}^2$ will be comparable to the one obtained by BaBar at 7 GeV^2 .

The study of the precision of the determination of the individual FFs is underway. The absolute cross section measurement depends essentially on the precision achieved in the luminosity measurement.

Chapter 7

QED radiative corrections to $\bar{p}p \rightarrow e^+e^-$ reaction using PHOTOS

Electromagnetic FFs of the proton are determined in the TL region from the angular distribution of $\bar{p}p \leftrightarrow e^+e^-$ (Eq. 3.25), which holds in Born approximation. However, in an experiment, one never measures the Born cross section (at the lowest order in α^2). Since all the particles involved in this reaction are charged particles, in the presence of an electromagnetic field, they emit real and virtual photons. These emissions result in a modification of the physical quantities (as the cross section of the process of interest) and the experimental data must be corrected for these radiative effects. Radiative corrections (RC) depend on the kinematics of the reaction and are functions of the same kinematical variables which contain the physical information. In coincidence experiments, they are incorporated in Monte Carlo generator together with the acceptance corrections.

The RC are quantum effects which contribute to the observables at higher orders of the electromagnetic coupling constant. They play a role beyond the Born approximation.

The analytic calculations of RC are highly non trivial and should be developed keeping in mind the level of precision achievable in the experiment. The method to study RC on the observables is to classify the radiative processes according to the power of the fine structure constant (α) at the level of the cross section. Based on Feynman rules, to each vertex of the electromagnetic interaction one associates the charge e of the particle. Therefore, a factor $\alpha = e^2/(4\pi) = 1/137$ appears in the expression of the cross section which contain the modulus square of the reaction amplitude. This means that the Born cross section will be lowered by a factor α each time an additional electromagnetic vertex appears. The Born diagram of $\bar{p}p \rightarrow e^+e^-$ reaction is of the order α^2 (leading order).

The Feynman diagrams contributing to the next to leading order (α^3) are shown in Fig. 7.1 together with the Born diagram. They contain:

- the virtual corrections which come from the interference between the Born diagram (a) and the diagrams with one virtual photon emission (at the proton

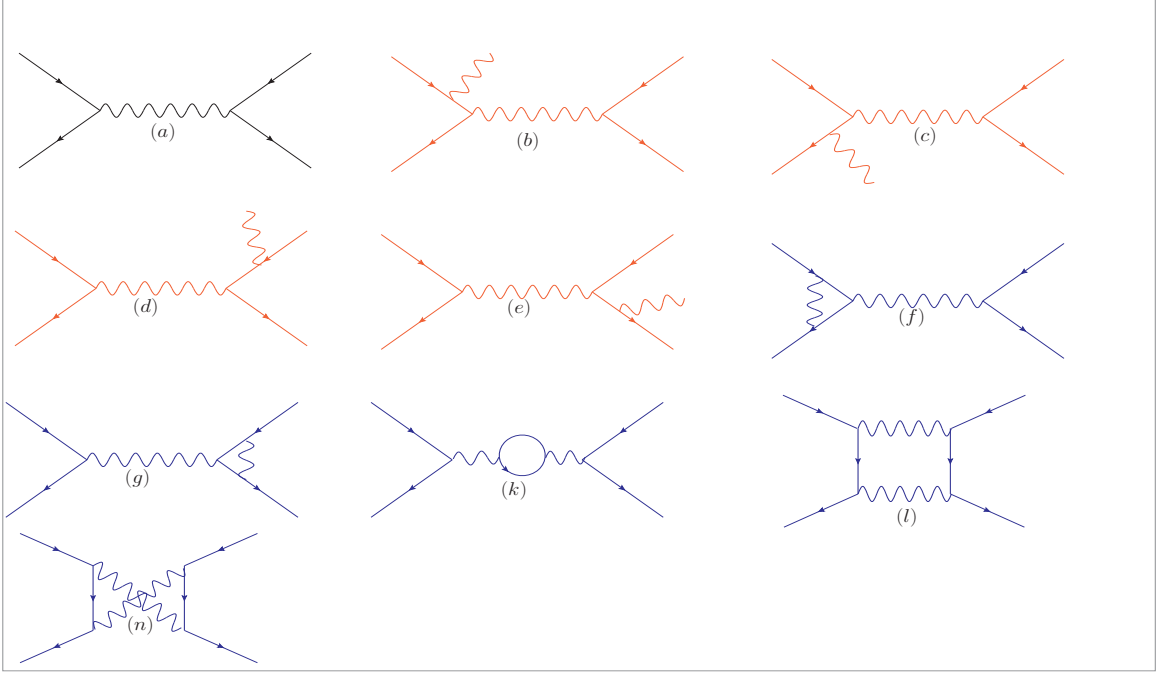


Figure 7.1: Feynman diagrams for the Born approximation and the first order correction in $\bar{p}p \rightarrow e^+e^-$.

vertex (f), the electron vertex (g), vacuum polarization (k) and two photon exchange (l,n)). Interference is possible only for the processes of the same final state;

- the Bremsstrahlung (real photon emission) from the initial (antiproton (b) and proton (c)) and final (electron (d) and positron (e)) states, and their interferences.

Self-energy corrections (emission and re-absorption from the same particle) also play a role and result in a renormalization of the mass and/or the energy of the particles. They contain ultraviolet divergences which are cancelled in the total correction. Note that kinematical effects (i.e. large momentum transfer, reaction mechanism, nucleon structure) may enhance some terms in the α -expansion series of the cross section and may compensate the α suppression. The so-called Structure Function (SF) method classifies the radiative processes according to $(\alpha/\pi)^n L^n$, $n = 0, 1, 2, \dots$ where $L = \ln(Q^2/\mu^2)$ ($\mu = m_e, \lambda_{QCD}, \dots$) is called the leading logarithm. The Leading Logarithmic (LL) approximation is limited to $(\alpha/\pi)L \sim 1$.

As previously mentioned, the radiative corrections are included in PANDARoot via the package PHOTOS. In this chapter, the effect of PHOTOS for RC estimation on the $\bar{p}p \rightarrow e^+e^-$ differential cross section is studied. First, the PHOTOS algorithm is described, then the data with and without corrections generated by PHOTOS are

shown. Finally the results are compared to existing calculations [136, 137, 138]. The effects of RC on the observables are illustrated and the degree of accuracy that can be obtained is discussed. The goal of this study is to evaluate the precision of the RC obtained with PHOTOS in the perspective of the TL electromagnetic FF measurement at PANDA.

7.1 PHOTOS

PHOTOS [139, 140] is a universal Monte Carlo algorithm for the simulation of QED radiative corrections in any decay of particle or resonance, occurring with a certain probability, independently of the physics process that was generated. Bremsstrahlung photons are added in a fraction of the events taking into account the event topology, the energy and the momentum conservation. PHOTOS allows to apply the corrections to simulated events from final state radiation (FSR), in LL approximation. The main characteristics of PHOTOS can be summarized as follows:

- For each event, PHOTOS generates real photons emitted by the particles in the final state, with corresponding reduction of the energy of the parent particle.
- Real photons are generated with energy above a certain value (E_γ^{min}).
- The number of generated events is not changed by applying PHOTOS.

7.2 PHOTOS and the first order corrections

The differential cross section of $\bar{p}p \rightarrow e^+e^-$ is written, in the Born approximation, as a function of $\cos^2\theta$ (where θ is the angle of the produced electron) in the CMS (Eq. 3.25). RC can be divided in odd and even contributions with respect to $\cos\theta$. Even contributions do not affect the slope of the $\cos^2\theta$ dependence of the cross section and act as a global normalization. Odd contributions arising from the interference between the initial and the final state and, at a lesser extent, the two photon exchange contribution, result in a distortion of the angular distribution. The RC given by PHOTOS can be described as follows:

- PHOTOS includes the Bremsstrahlung from the final state only. The Bremsstrahlung corrections lead to infrared singularities. These singularities are cancelled order by order by virtual corrections. In PHOTOS, instead of calculating the virtual corrections analytically, they are reconstructed numerically from the real photon corrections in the LL approximation.

The standard treatment of the Bremsstrahlung consists of separating the real photon contribution as:

- soft photon contribution with the emitted photon energy up to an infrared cut-off parameter (E_γ^{min}),

- hard photon contribution from photon energy E_γ^{min} up to an experimental cut (hard cut E_γ^{max}) depending on the energy resolution of the detector. Photons with energy under the hard cut are not seen by the detector and therefore they should be corrected theoretically.

The total RC should not depend on this soft parameter but they depend on the experimental cut applied on the hard photon emission.

- The contribution of the box diagrams (2γ exchange) and the initial state radiation are not included in PHOTOS. Their contribution is considered to be negligible. The radiation from the proton and antiproton is, in principle, small compared to the photon emission by electrons, as it is inversely proportional to the mass of the considered particle.
- The vacuum polarization is not taken into account in PHOTOS, its contribution can be considered as a normalization factor.
- The main contribution, at the first order, to the odd part of RC which comes from the interference between the initial and final state radiations is not calculated by PHOTOS and can affect the extraction of the FFs as it leads to a distortion in the electron angular distribution.

It has to be noted that, within PHOTOS, the number of real photons emitted from the final state can be larger than one, contributing to higher order RC.

7.3 PHOTOS in PANDAROOT

The PHOTOS package is implemented in the PANDARoot at the level of the event generator (EvtGen). PHOTOS is switched on by default and can be switched off by adding the expression “noPhotos” in the first line of the decay file used for the Monte Carlo simulation. PHOTOS *version 2.02* with the following DEFAULT settings was used for the present studies:

- $XPHCUT = 0.01$; XPHCUT defines the infrared cut-off parameter (defined in the previous section). It is related to the minimal energy of emitted photons in the CM of $\bar{p}p$ system by:

$$XPHCUT = \frac{E_{min}^\gamma}{\sqrt{s}/2}, \quad (7.1)$$

where the invariant s is the total energy squared of the system. Only photons with energy above the energy fixed by the cut-off parameter are generated.

- $ISEC = True$: double photon emission from the final state is included. The number of emitted photons from the final state is limited to 2.

- *INTERF = True*: the interference between photons emitted from an electron and a positron is included.

In this work, the effect of PHOTOS on the Monte Carlo energy and the angular distribution of the emitted electron-positron particles in $\bar{p} + p$ annihilation is studied. The present simulations are done assuming 4π detection. The detector acceptance, the reconstruction and the PID efficiency are not taken into account.

We have generated 10^6 events for the reaction $\bar{p}p \rightarrow e^+e^-$ with the proton FF ratio equal to unity ($|G_E| = |G_M|$). The results presented in this section correspond to antiproton momentum $p_{\bar{p}} = 1.7$ GeV ($s=5.4$ GeV²). Fig. 7.2 shows the correlation between the energy of the positron as a function of the energy of the electron in the CMS. The left plot represents the case when PHOTOS is switched off. The energy is splitted equally between the two leptons $E_{CM}^{e^+} = E_{CM}^{e^-} = \sqrt{s}/2$. The right plot corresponds to PHOTOS switched on. The energy of the leptons is reduced due to the γ emission, showing the typical radiative tail.

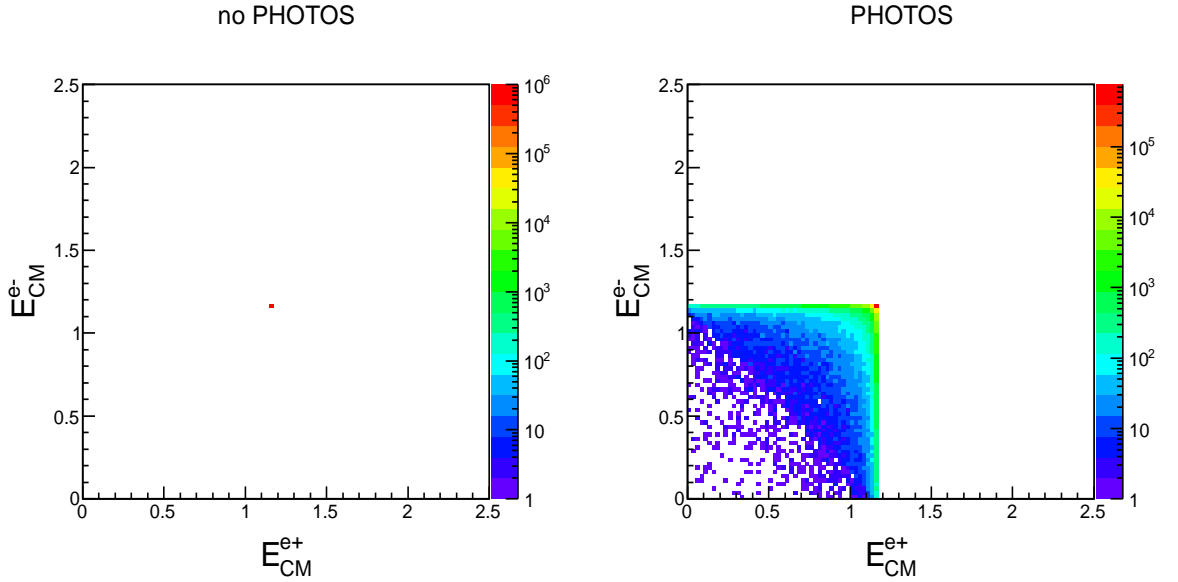


Figure 7.2: Dalitz plot of the emitted electron and positron energies in the CMS for $p_{\bar{p}} = 1.7$ GeV. The maximum energy of the emitted leptons is $\sqrt{s}/2=1.16$ GeV.

Fig. 7.3 (right) shows the number of γ 's emitted in each event. As it is expected from the settings of this version of PHOTOS, the maximum number of emitted photons per event is 2. The first column in this plot represents the case where there was no γ emission: photons with energy below E_{γ}^{min} are not generated. In the present case ($s = 5.4$ GeV² and $XPHCUT=0.01$), the minimal energy of the emitted photons in $\bar{p}p$ CMS is 11.6 MeV.

The invariant mass of e^+e^- is illustrated in Fig. 7.3 (left) where the red vertical line corresponds to events without photon emission ($\sqrt{s} = 2.32$ GeV). The discontinuity

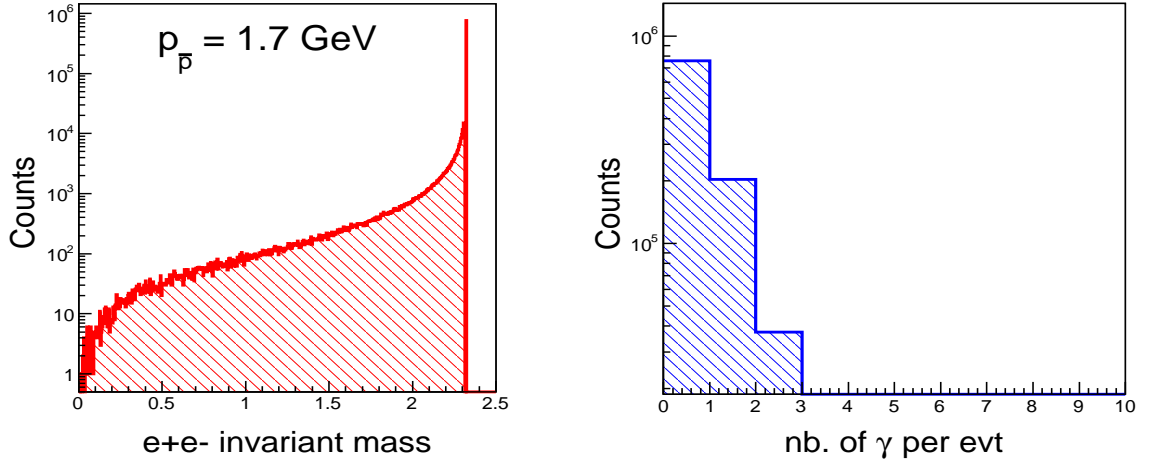


Figure 7.3: Electron-positron invariant mass and number of emitted γ 's per event for $p_{\bar{p}} = 1.7$ GeV.

of the spectra near ($\sqrt{s} = 2.32$ GeV) reflects the effect of the soft cut-off parameter ($XPHCUT$).

Looking at the angular distribution of the electron in CMS (Fig. 7.4), one can see that there is no quantitative difference between simulations done with and without PHOTOS. The reason for such a behavior is related to the fact that, up to now, full integration on the photon energies is performed and no hard cut which is related to the detector resolution has been applied.

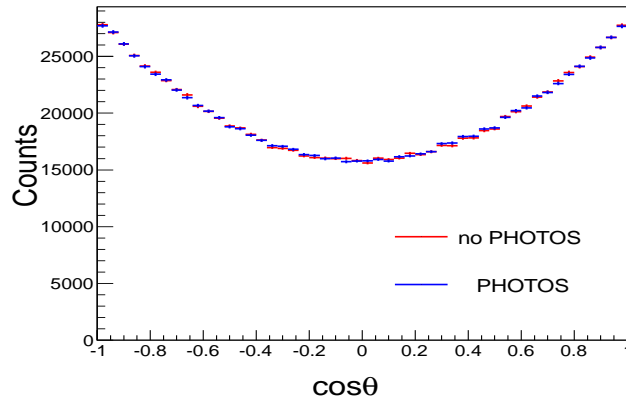


Figure 7.4: Angular distribution of the emitted electron in the CMS, with and without PHOTOS for $p_{\bar{p}} = 1.7$ GeV.

Instead of applying hard cut on the emitted photons, one can also apply cuts on the invariant mass of e^+e^- (Fig. 7.3, left). The angular distributions of the electron in the CMS corresponding to different cuts applied on the invariant mass of the lepton pair ($M_{e^+e^-} > 0.5, 1, 1.5, 2$ GeV) are shown in Fig. 7.5. In the case of two photon emission, the invariant mass and the energy of the photons are related in the $\bar{p}p$ CMS by the following relation:

$$s = M_{e^+e^-}^2 + 2\sqrt{s}(E_{\gamma_1} + E_{\gamma_2}). \quad (7.2)$$

The cuts on the invariant mass (from 0.5 to 2 GeV) correspond respectively to the following hard photon cuts on the sum of the two photon energies: 1.11, 0.95, 0.68, 0.3 GeV. Such cuts do not introduce any anisotropy in the angular distribution.

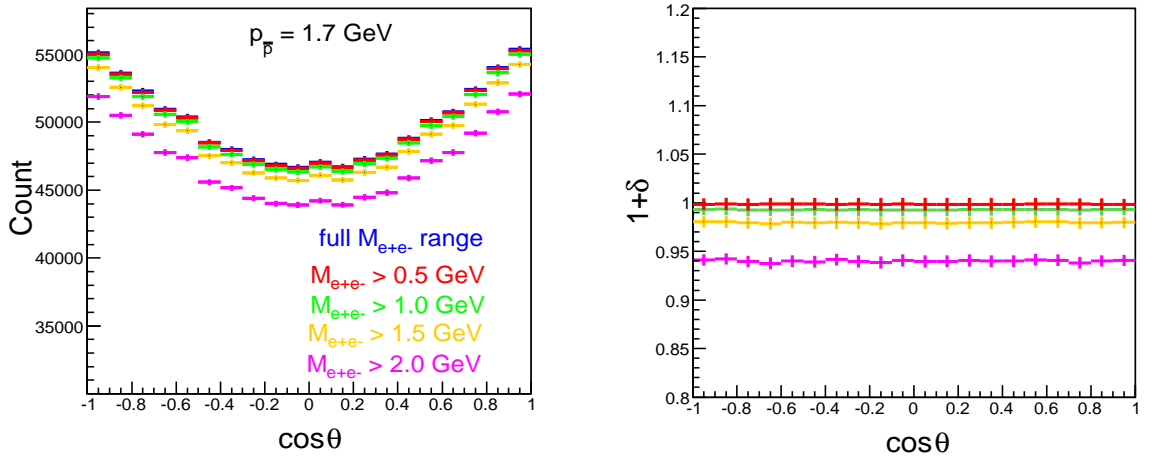


Figure 7.5: Angular distribution of the emitted electron with PHOTOS for different cuts of the e^+e^- invariant mass (left). Ratio of the electron angular distribution with and without PHOTOS for \bar{p} momentum equal to 1.7 GeV (right).

The differential cross section, including RC can be written as:

$$\frac{d\sigma^c}{d\Omega} = \frac{d\sigma^B}{d\Omega}(1 + \delta), \quad (7.3)$$

where Ω is the solid angle of the produced lepton (electron or positron). The factor δ determines the magnitude of the RC, and can be obtained from PHOTOS (as a function of the CM angle of electron or positron) by associating:

- $d\sigma^c/d\Omega$ to the angular distribution of the lepton where PHOTOS is switched on ($\bar{p}p \rightarrow e^+e^-\gamma$).
- $d\sigma^B/d\Omega$ to the angular distribution of the lepton in Born approximation ($\bar{p}p \rightarrow e^+e^-$) where PHOTOS is switched off.

From Fig. 7.5 (right), one can see that the $(1 + \delta)$ factor does not depend on the angle of the electron in the CMS. Applying the condition $M_{e^+e^-} > 2$ GeV, RC are of the order of 6% ($\delta = -0.06$).

7.4 Comparison of PHOTOS with analytical calculations

Let us consider another kinematical region, $s = 12.9$ GeV², which corresponds to an antiproton incident momentum $p_{\bar{p}} = 5.86$ GeV and compare the results from PHOTOS to RC calculations where different contributions at the first order (α^3) are taken into account. The results which we have obtained with PHOTOS (setting the option of one photon emission) applying the following hard cuts on the real photons, $E_{\gamma}^{max} = 50$ MeV and $E_{\gamma}^{max} = 100$ MeV, are shown in Fig. 7.6. These values of energies and cuts allowed a direct comparison with the existent analytical calculations of Refs. [136] and [137].

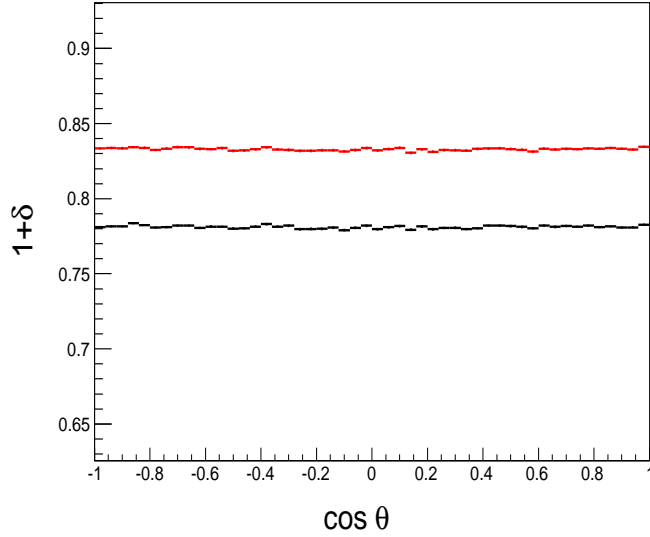


Figure 7.6: Ratio of the electron angular distribution for $s=12.9$ GeV² with and without PHOTOS [XPHCUT=0.01 with one photon emission] in the CMS for $E_{\gamma}^{max} = 50$ MeV (Black) and $E_{\gamma}^{max} = 100$ MeV (Red).

The calculation of RC from Ref. [136] is shown in Fig. 7.7 as a function of the electron angle, for $E_{\gamma} < 100$ MeV. The results have been generalized to next-to leading orders using the structure function method.

The different lines correspond to the following contributions to the cross section:

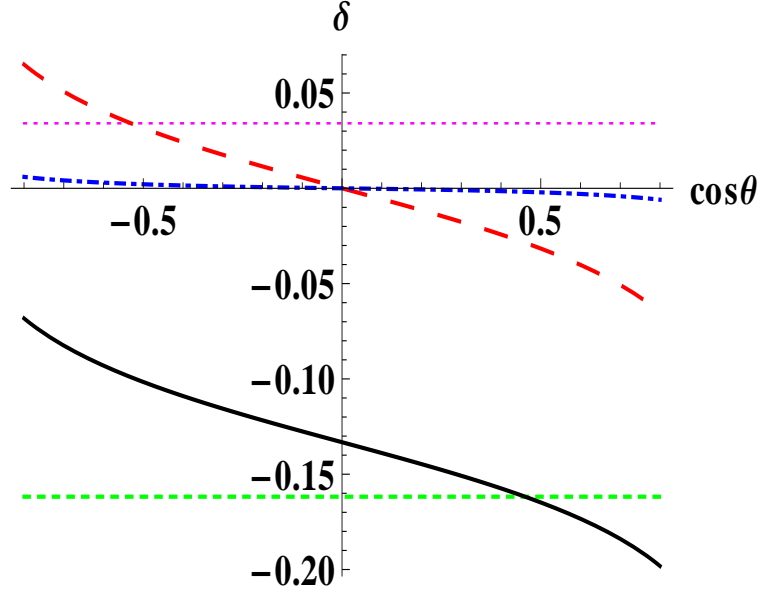


Figure 7.7: RC factor δ , as a function of $\cos \theta$, according to Ref. [136] for $s=12.9 \text{ GeV}^2$ and $E_\gamma^{max}=100 \text{ MeV}$: vacuum excitations (magenta, dotted), odd contribution (red, long dashed) mainly from soft photon emission and from two photon exchange (blue, dot-dashed), FSR (green, dashed), total (black, solid).

- the angle independent contributions: vacuum polarization (magenta, dotted), and final state radiation (FSR) (green, dashed).
- the odd contribution (red, long dashed): which comes mostly from the interference of initial-final state emission, and the two photon exchange (blue, dot-dashed).

The total correction is shown by the black solid line in Fig. 7.7. One can see that it is of the order of -6% at backward angle and reaches about -20% at forward angle.

In Ref. [137] a first order calculation was performed. The analytical calculation for the interference (initial-final state) contribution, taking into account the hadron structure parametrized in terms of proton FFs, gives a value for the total RC for $s=12.9 \text{ GeV}^2$ between -0.24 and -0.07 , and without interference -0.015 . However the precision on these numbers is affected by the hadron structure model. Moreover, the hadron after having emitted the photon can not be considered as on-shell particle.

In Tab. 7.1 the values extracted by PHOTOS are compared to the calculations [136] and [137]. The contribution of the two real photon emission and their interference using PHOTOS for $s = 12.9 \text{ GeV}^2$ and $E_\gamma^{max}=100 \text{ MeV}$ is about 3% . This is obtained by reproducing the same simulation with the 2 photon emission option.

Contribution	PHOTOS	Ref. [136]	Ref. [137]
2 γ exchange (box diagrams)	—	$[-0.005, 0.005]$	$[-0.01, 0.01]$
vacuum polarization	—	0.03	0.01
FSR	-0.17	-0.16	-0.17
Total RC	-0.17	$[-0.20, -0.06]$	$[-0.24, -0.07]$

Table 7.1: RC factor δ in the CMS for $s=12.9 \text{ GeV}^2$, $E_\gamma^{max} = 100\text{MeV}$, given by PHOTOS and Refs. [136, 137].

7.5 Conclusions

In this chapter the RC for proton antiproton annihilation into an electron pair using the PHOTOS package which is implemented in PANDARoot, have been estimated. The simulations were limited to the Monte Carlo generated events without taking into account the effects of PANDA detectors. The aim of this study is the evaluation of the precision of RC generated by the PHOTOS package with respect to the available analytical calculations.

The estimations have been done in the CMS for two values of the incident antiproton momentum ($p_{\bar{p}} = 1.7 \text{ GeV}$ and 5.86 GeV). In Lab system, it was checked that PHOTOS gives the expected angular dependence of radiative corrections. RC depend on the hard photon cut. A realistic value of this cut will be settled when the detector capability to detect the hard photons with a specific resolution will be demonstrated on real data.

The results given by the simulation are consistent with analytical calculations which have been computed for the considered reaction concerning the even contributions excepted the vacuum polarization which is not included in PHOTOS. Let us note that these contributions act as a global normalization and do not affect the procedure of extraction of the FF ratio described in chapter 6. On the other hand, odd contributions arising from the interference between the initial and the final state and the two photon exchange are not calculated by PHOTOS. Such contributions results in a distortion of the angular distribution affecting the extraction of FFs and increasing the systematic errors.

The systematic effects of the RC on the extracted proton FFs were not considered further. The development of a dedicated event generator taking into account even and odd contributions or the implementation in PHOTOS of the missing odd contributions is under discussion.

Chapter 8

Elastic proton electron scattering

In this chapter, the elastic scattering of proton beam on electron target (*pe*-inverse kinematics) is considered in the Lab frame and in the framework of a relativistic approach assuming the Born approximation. Using the formalism derived in the appendix A , the explicit expressions for the unpolarized cross section, the polarization observables, and the relations describing this specific kinematics are derived. The mass of the electron which is considered at rest is not neglected. Based on the specific properties of such a reaction, we consider the following applications:

- measurement of the proton charge radius at low momentum transferred;
- polarization of (anti)proton beams with energy in the GeV range;
- measurement of the polarization of (anti)proton beams.

The kinematical relations and the unpolarized cross section are studied in the first part of this chapter as well as the possibility to make a precise measurement of the proton charge radius using *pe* elastic scattering. The second part describes the transfer polarization observables from a polarized electron target to an unpolarized proton beam. Finally, the polarized cross section describing the spin correlation of the proton and the electron in the initial state is calculated and the figure of merit for a *pe*-polarimeter is estimated. In our analysis, atomic electrons are considered as electron targets. Liquid hydrogen targets for example are used as proton targets, but any reaction with such targets also involves reactions with atomic electrons, which can be considered at rest.

8.1 Kinematics and differential cross section

Let us consider the scattering of a proton beam on an electron target at rest (Fig. 8.1):

$$p(p_1) + e(k_1) \rightarrow p(p_2) + e(k_2), \quad (8.1)$$

where the particle momenta are indicated in parenthesis, and $q = k_1 - k_2 = p_2 - p_1$ is the exchanged four-momentum. We used the following notations (Lab frame):

$$p_1 = (E_1, \vec{p}_1), p_2 = (E_2, \vec{p}_2), k_1 = (\epsilon_1, \vec{k}_1), k_2 = (\epsilon_2, \vec{k}_2), \tau = -q^2/(4M^2). \quad (8.2)$$

where M is the proton mass.

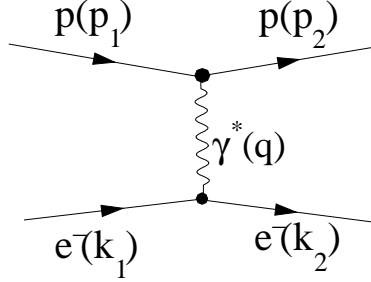


Figure 8.1: Feynman diagram for the reaction $p(p_1) + e(k_1) \rightarrow p(p_2) + e(k_2)$. The transfer momentum of the virtual photon is $q = k_1 - k_2 = p_2 - p_1$.

The expression of q^2 can be derived from energy and momentum conservation laws. For a given energy E_1 of the proton beam, the maximum value of the transferred momentum is:

$$(-q^2)_{max} = \frac{4m^2(E_1^2 - M^2)}{M^2 + 2mE_1 + m^2}, \quad (8.3)$$

where m is the electron mass. Being proportional to the electron mass squared, q^2 is restricted to very small values. This is a general characteristic of the hadron scattering by atomic electrons, even for relatively large energies of the incident hadrons.

The four momentum transfer squared is expressed as a function of the energy of the outgoing electron, ϵ_2 , as:

$$q^2 = (k_1 - k_2)^2 = 2m(m - \epsilon_2), \quad (8.4)$$

where

$$\epsilon_2 = m \frac{(E_1 + m)^2 + (E_1^2 - M^2) \cos^2 \vartheta}{(E_1 + m)^2 - (E_1^2 - M^2) \cos^2 \vartheta}, \quad (8.5)$$

and ϑ is the angle between the proton beam and the recoil electron momenta.

The angle and the energy of the recoil electron are related by:

$$\cos \vartheta = \frac{(E_1 + m)(\epsilon_2 - m)}{|\vec{p}_1| \sqrt{(\epsilon_2^2 - m^2)}}, \quad (8.6)$$

which shows that $\cos \vartheta \geq 0$ (the electron can never recoil backward). One can see from Eq. 8.5 that in the inverse kinematics, the available kinematical region is reduced to small values of ϵ_2 :

$$\epsilon_{2,max} = m \frac{2E_1(E_1 + m) + m^2 - M^2}{M^2 + 2mE_1 + m^2}, \quad (8.7)$$

being proportional to the electron mass. From momentum conservation, the energy and the angle of the scattered proton E_2 and ϑ_p are related by:

$$E_2^\pm = \frac{(E_1 + m)(M^2 + mE_1) \pm M(E_1^2 - M^2) \cos \vartheta_p \sqrt{\frac{m^2}{M^2} - \sin^2 \vartheta_p}}{(E_1 + m)^2 - (E_1^2 - M^2) \cos^2 \vartheta_p}, \quad (8.8)$$

which shows that to one proton angle ϑ_p correspond two values of the proton energy E_2 (and two corresponding values for the energy ϵ_2 and the angle ϑ of the recoil electron, as well as for the transferred momentum q^2). The two solutions coincide when the angle between the initial and final hadron takes its maximum value, which is determined by the ratio of the electron and scattered proton masses, $\sin \vartheta_{p,max} = m/M \ll 1$ (the square root in Eq. 8.8 is equal to zero). Hadrons are scattered from atomic electrons at very small angles, and the larger is the hadron mass, the smaller is the available angular range for the scattered hadron. From momentum and energy conservation, one can also show that the proton can not be scattered backward ($\cos \vartheta_p \geq 0$). This situation remind us of the experiment of Rutherford, Geiger and Marsden [47] consisting of the scattering of alpha (α) particles by a gold foil. It was expected, as mentioned above, that particles would pass through the gold foil with very little deflection (inverse kinematics). Surprisingly, alpha particles were found at large angles, some were even scattered backwards. This experiment led the way to the concept of the atom nucleus.

The expression of the differential cross section for unpolarized proton-electron scattering, in the coordinate system where the electron is at rest, can be written, in Born approximation, as:

$$\frac{d\sigma}{dq^2} = \frac{\pi\alpha^2}{2m^2\vec{p}_1^2} \frac{\mathcal{D}}{q^4}, \quad (8.9)$$

with

$$\mathcal{D} = q^2(q^2 + 2m^2)G_M^2(q^2) + 2[q^2M^2 + 2mE_1(2mE_1 + q^2)][F_1^2(q^2) + \tau F_2^2(q^2)]. \quad (8.10)$$

It can be written in terms of the Sachs FFs as:

$$\begin{aligned} \mathcal{D} = & q^2(q^2 + 2m^2)G_M^2(q^2) \\ & + 2[q^2M^2 + \frac{1}{1+\tau}(2mE_1 + \frac{q^2}{2})^2][G_E^2(q^2) + \tau G_M^2(q^2)]. \end{aligned} \quad (8.11)$$

Similarly to ep scattering, the differential cross section diverges as q^4 when $q^2 \rightarrow 0$ and allows to reach very large cross sections. This is a well known result, which is a consequence of the one photon propagator. The expression (8.11) differs from the Rosenbluth formula [57], as terms depending on the electron mass can not be neglected.

For all the numerical applications of this chapter, the proton structure is taken into account through the FFs using the dipole parametrization (Eq. 3.23). The standard dipole parametrization coincides with more recent parametrizations for $-q^2 < 1$

GeV². At higher q^2 , different choices may affect the cross section and the polarization observables. However as shown above, the maximum value of q^2 is so small in inverse kinematics that it justifies the choice of the dipole parametrization, and even of constant FFs, where the constants correspond to the static values.

As shown by Eq. 8.9, the cross section diverges for $q^2 \rightarrow 0$. This condition is obtained when the scattering angle $\vartheta_p \rightarrow 0$, or when the energy of the incident beam is very small. The region where the present calculation can be applied without divergences is determined as follows:

- At large impact parameter (defined as the perpendicular distance between the path of the projectile (proton) and the center of the field (atomic electron), or at small incident energy, Coulomb screening occurs. This can be taken into account by introducing a minimum scattering angle, which is related to the impact parameter (b). The classical (c) and quantum (q) expressions for the minimum scattering angle are given by [141]:

$$\vartheta_{p,min}^{(c)} = \frac{2e^2}{|\vec{p}_1|\beta b}, \quad \vartheta_{p,min}^{(q)} = \frac{\hbar}{|\vec{p}_1|b}, \quad (8.12)$$

where $\beta = |\vec{p}_1|/E_1$ is the relative velocity. The characteristic screening distance in the present case (atomic electrons) is the Bohr radius $b = 0.519 \times 10^5$ fm.

- When the incident energy is very low, the electron and proton may be trapped in a bound system, and elastic scattering based on one photon exchange cannot be applied to this process. The Born approximation corresponds to the first term of an expansion in the parameter α/v which should be less than one. The condition $\alpha/v < 0.1c$ (c is the speed of light) is satisfied for $E_1 > 2.5$ MeV.

Based on these arguments, $E_1 = 3$ MeV is chosen to be the minimum limit for the present calculation, and all the observables are integrated from $\vartheta_{p,min}$ (the maximum of $\vartheta_{p,min}^{(c)}$ and $\vartheta_{p,min}^{(q)}$). Screening effects which are important at low energies, are introduced in the cross section via a multiplicative factor which takes into account the resummation for many photon exchange [142]:

$$\chi = \frac{\chi_b}{e^{\chi_b} - 1}, \quad \chi_b = -2\pi \frac{\alpha}{\beta}. \quad (8.13)$$

Such a factor is larger than one for opposite charges and increases the cross section for the reaction of interest here. At the lowest energy ($E_1 = 3$ MeV) this correction is of the order of 30%.

8.2 Proton charge radius

The problem of the proton size has been recently the object of large interest and discussions, due to the disagreement which has been found between the measurements

of the proton root mean square (rms) charge radius using different methods. The rms charge radius is a fundamental static property of the nucleon as its magnetic moment. It can be measured by elastic electron scattering on protons and also inferred from the effects of finite nuclear size on electron or muon energy levels as measured in atomic (hydrogen) spectra. In the following, we give a short overview on the values of the proton rms charge radius determined by these methods. Finally we suggest a method based on the elastic proton electron scattering to measure the proton rms charge radius.

8.2.1 Hydrogen spectroscopy

According to Dirac and Schrödinger theory, the energy levels of the hydrogen electron depend only on the principal quantum number (n). In 1947, Lamb and Rutherford showed that the $2p^{1/2}$ state ($n = 2$, orbital momentum $l = 1$ and total angular momentum $j = 1/2$) is slightly lower than the $2s^{1/2}$ state ($n = 2$, $l = 0$ and $j = 1/2$) resulting in a shift of the corresponding spectral line (Lamb shift). The energy shift can be explained as a consequence of the bound-state QED effects which take into account: radiative, recoil, relativistic, binding, and nuclear structure effects.

Let us consider the effect of the nucleus finite size on the electron energy levels in the hydrogen atom. The corresponding correction to the electron energy levels is [143]:

$$\Delta E \propto \frac{2(Z\alpha)^4}{3n^3} m_r^3 \langle r_c^2 \rangle. \quad (8.14)$$

Where Z is the nuclear number, α is the fine-structure constant, $m_r = m_e M / (m_e + M)$ is the reduced mass of the electron-proton system and $\langle r_c^2 \rangle^{1/2}$ is the rms proton charge radius. Using the De Broglie relationship between energy and frequency $\Delta E = h\Delta\nu$ (h is the Planck's constant) in Eq.8.14, one can determine the proton rms charge radius by a measurement of the transition frequency of hydrogen energy levels using laser spectroscopy.

The value of the proton rms charge radius reported by the Committee on Data for Science and Technology (CODATA) in 2008 [144], $\langle r_c^2 \rangle^{1/2} = 0.8768(69)$ fm was mainly extracted from this method. The CODATA was established in 1966 as an interdisciplinary committee of the International Council for Science.

8.2.2 Muonic hydrogen spectroscopy

Muonic hydrogen is a bound system of a muon and a proton. The muon is about 200 times heavier than the electron, therefore, the atomic Bohr radius of muonic hydrogen is smaller than in ordinary hydrogen. This increases sensitivity of muonic hydrogen Lamb shift to the finite size of the proton.

Proton rms charge radius was determined at Paul Scherrer Institut (PSI) by laser spectroscopy measurement of the $^2P_{1/2}-^2S_{1/2}$ transition frequency in muonic hydrogen [145]: $\Delta\nu = 49881.88(77)$ GHz. This corresponds to an energy difference of

$\Delta E_{exp} = 206.2949(32)$ MeV. The comparison of ΔE_{exp} with the corresponding theoretical prediction based on the bound-state QED effects (Ref. [145] and references therein) gives a value for the rms proton charge radius equal to $\langle r_c^2 \rangle^{1/2} = 0.84184(67)$ fm. This number is smaller by five standard deviation compared to the CODATA value.

8.2.3 Electron proton scattering

The most direct way to extract the size of a hadron consists of measuring the electric FF (G_E) from scattering experiments. In chapter 3, the relation between G_E and $\langle r_c^2 \rangle$ was derived (Eq. 3.9). We have seen that the proton rms charge radius can be determined by the slope of $G_E(Q^2)$ at $Q^2 = 0$ ($Q^2 = -q^2$):

$$\langle r_c^2 \rangle = -6 \frac{dG_E(Q^2)}{dQ^2} \Big|_{Q^2=0}. \quad (8.15)$$

One of the issues using this method is to know how one can extract the charge radius from the measured values of $G_E(Q^2)$. In principle, from a data set, we need to find the slope at $Q^2 = 0$. The extrapolation to $Q^2 = 0$ is not simple because the functional form of $G_E(q^2)$ is unknown. The value of the extracted charge radius strongly depends on the fitting model used for the electric FF parametrization. Series expansions as Taylor series around $Q^2 = 0$, continued fraction expansion [146], and z -expansion [147], can be used to parametrize the electric FF of the proton and extract the charge radius. Another issue in the determination of the proton charge radius is related to the choice of the experimental data set, as different sets lead to systematic discrepancies.

In Ref. [146], the value extracted from the world ep scattering data, using the CF expansion for G_E , is equal to $\langle r_c^2 \rangle^{1/2} = 0.895(18)$ fm. The most recent result from electron proton elastic scattering,

$$\langle r_c^2 \rangle^{1/2} = 0.879(5)_{\text{stat}}(4)_{\text{syst}}(2)_{\text{model}}(4)_{\text{group}} \text{ fm}, \quad (8.16)$$

can be found in Ref. [148]. In this experiment, the electron-proton scattering cross section was measured at the Mainz Microtron (MAMI) up to a four momentum transfer squared of $Q^2 = 0.6 \text{ GeV}^2$, with statistical error below 0.2%. A large variety of FF models was used to fit cross section data which give different values of the proton charge radius (model dependent). The smallest value of Q^2 reached in this experiment was 0.004 GeV^2 . However the possibility to access much smaller values of Q^2 may give severe constraints to the models used for the fitting procedure at $Q^2 \sim 0$.

8.2.4 Proton charge radius measurement with pe elastic scattering

The proton rms charge radius determined from the Lamb shift in muonic hydrogen disagrees significantly with the value determined from hydrogen frequency transition as well as from elastic electron proton scattering experiments. The uncertainty of the

muonic hydrogen value is significantly smaller than the uncertainties of other values. The origin of this difference is not yet established. As far as elastic electron proton scattering experiments are concerned, one of the main issues for determining the proton radius is related to the extrapolation to $Q^2 \rightarrow 0$. It is suggested here that pe elastic scattering may give a more precise extrapolation, due to the fact that it allows to access very small Q^2 values. In this section, we illustrate the kinematics of the elastic electron proton scattering at a specific value of the proton beam kinetic energy, $E_p = 100$ MeV. This helps in reducing the hadronic background when the atomic electrons are considered as electron target: the value $E_p = 100$ is under the pion threshold in proton-proton reaction (the interaction between the proton beam and the protons of the target).

Fig. 8.2 (left) reports Q_{max}^2 as a function of the proton kinetic energy, in the hundred of MeV range. One can see that the values of transferred momenta are very small: for a proton beam with kinetic energy $E_p = 100$ MeV, $(Q^2)_{max} = 0.2 \times 10^{-6}$ GeV².

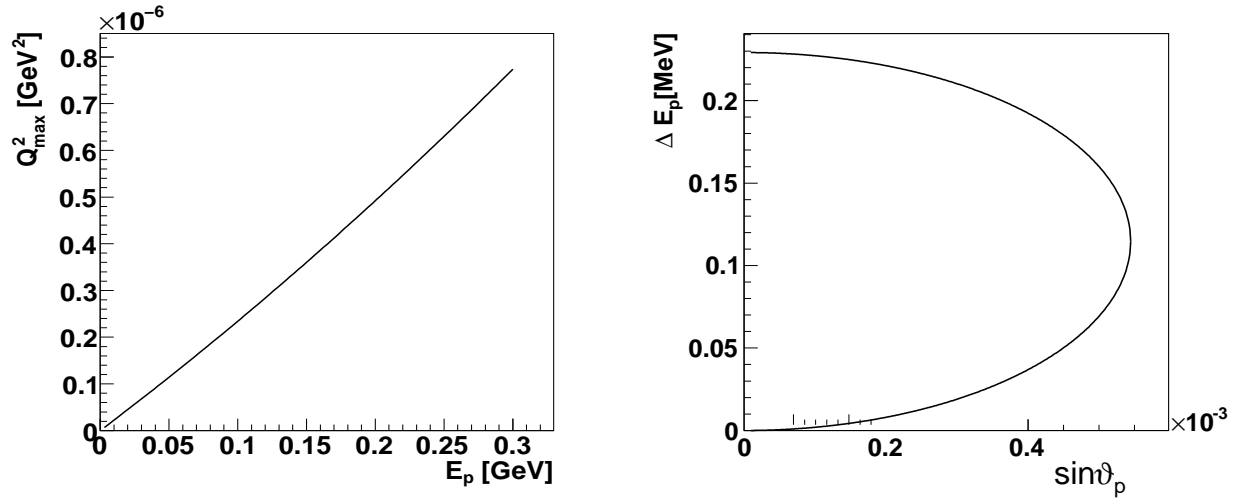


Figure 8.2: (Left) Maximum value of the four momentum transfer squared (Q^2) as a function of the proton beam kinetic energy, E_p in GeV. (Right) Difference in kinetic energy between scattered protons and incoming protons, ΔE_p , for $E_p=100$ MeV, as a function of the sine of the proton scattering angle.

The difference of energy between the scattered protons and the beam is shown in Fig. 8.2 (right) as a function of the proton scattering angles. The proton kinematics is very close to the beam ($\Delta E_p \sim 10^{-4}$ GeV), which makes the detection of the scattered protons very challenging. However a magnetic system with momentum resolution of the order of 10^{-4} could provide at least the measurement of the energy of the scattered proton. This would allow a coincidence measurement which helps to reduce the possible background.

While the proton is emitted in a narrow cone, the electron can be scattered up to 90° . The energy of the recoil electrons is shown in Fig. 8.3 (left) as a function of the cosine of the recoil angles.

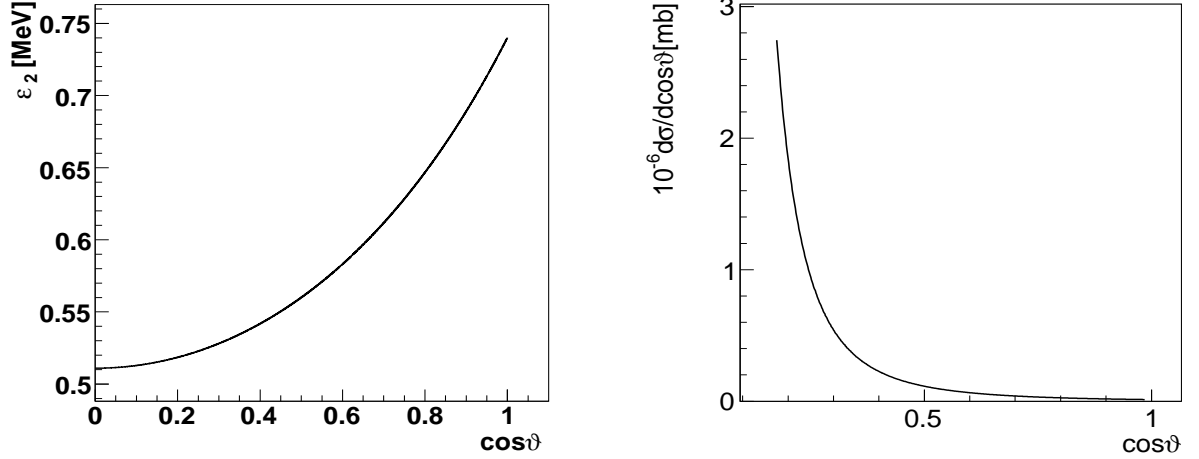


Figure 8.3: (Left) Energy of the recoil electron as a function of the cosine of the electron scattering angle for beam kinetic energy $E_p=100$ MeV. (Right) Differential cross section as a function of the cosine of the electron scattering angle for beam kinetic energy $E_p=100$ MeV.

The differential cross section as a function of $\cos \vartheta$ is shown in Fig. 8.3 (right) in the angular range $10^\circ \leq \vartheta \leq 80^\circ$. It is large when the electron angle is close to 90° and monotonically decreasing.

The cross section, integrated in this angular range, is 25×10^4 mb. Assuming a luminosity $\mathcal{L} = 10^{32} \text{ cm}^{-2} \text{ s}^{-1}$ and an ideal detector with an efficiency of 100%, a number of $\simeq 25 \times 10^9$ events can be collected in one second: the present reaction allows to reach very small momenta with huge cross section. However, its very specific kinematics requires a dedicated experiment. One possibility is to detect the correlation between angle and energy of the recoil electron. The detection of the energy of the scattered proton in coincidence is feasible, in principle, with a magnetic system.

The last point to be discussed concerning this method is how to fill the gap between the maximum value of Q^2 which can be achieved in inverse kinematics ($\sim 10^{-6} \text{ GeV}^2$) and the minimum value reached in electron proton elastic scattering ($\sim 10^{-3} \text{ GeV}^2$). In principle, if the data obtained using this method at very small Q^2 have large error bars, we are not able to constrain the slope of the parametrization function of the electric FF at $Q^2 \rightarrow 0$ using only these data. Therefore, information on the large kinematical region of low Q^2 (including the region $[10^{-3}, 10^{-6}]$) with high precision is required. This can be provided by low energy collider experiments, where the small kinetic energy of the electron target may increase the value of the momentum transfer squared from 10^{-6} GeV^2 up to 10^{-3} GeV^2 .

In summary, the main advantages of the proposed reaction are the possibility of accessing low Q^2 values with high statistics and negligible physical background. Moreover, in inverse kinematics, the electric contribution to the cross section dominates and the magnetic contribution can be safely neglected ($\tau_{max} = 0.5 \times 10^{-7}$). Therefore, there is no need of Rosenbluth separation and/or polarization method to determine G_E . This allows a precise measurement of the proton radius at very small Q^2 , decreasing the errors due to the extrapolation for $Q^2 \rightarrow 0$. For the electron target, any heavy target, *Au*, *Pb*, *W*, can be considered as a good target. For the problem of small angle scattered proton, a momentum resolution of the order of 10^{-4} for an emitted proton has been achieved in high resolution spectrometers, for example the dispersive spectrometer SPES1 (Saturne) [149]. More recently, high resolution detection for protons at zero degrees is reported at the facilities RIBF and RIKEN [150].

8.3 Polarization of high energy (anti)proton beams

Polarized antiproton beams, with high intensity and degree of polarization would open a wide domain of studies at FAIR [151]. For the case of interest here, the measurement of the single spin asymmetry in $\vec{p}p \rightarrow e^+e^-$ gives information on the relative phase of the TL proton FFs.

Different methods have been suggested, and some of them were used, to polarize antiproton beams, for example, from antihyperon decay, using spin filter or spin flip, stochastic techniques,...

In 1987, Stern-Gerlach effect in alternating quadrupole fields was proposed to polarize stored proton or heavy ion beams in storage rings by spatially separating particles with opposite spin directions [152]. This method is very demanding and seems out of reach in the GeV range. At Fermilab, a polarized antiproton beam has been produced from the decay of antihyperons. Nevertheless, at polarization degree $P > 0.35$, the achieved intensities never exceeded $\sim 1.5 \times 10^5 s^{-1}$ [12].

The idea that strong interaction might be used to polarize proton (antiproton) beams appeared first in [153] and was suggested by P. L. Gonska (1968):

“ We place a polarized proton target in a circulating beam... When passing through the target, protons with one of the two possible polarization states are scattered out of beam more often than the other... The result is that the transmitted beam becomes polarized”.

This method is called the spin filtering: due to different cross section for parallel ($\uparrow\uparrow$) and anti-parallel ($\uparrow\downarrow$) spin alignment, an unpolarized beam by multiple passage through a polarized target becomes polarized, while the intensity decreases. It was tested by FILTEX collaboration in 1992 at the TSR-Heidelberg [154] with 23 MeV stored protons on a polarized hydrogen target. In 90 minutes, the intensity of the beam was 5% of the initial one and the polarization degree amounted to 2.4%.

The rate of polarization buildup due to filtering mechanism was also estimated theoretically, taking into account only strong proton-proton (pp) interaction. This es-

timization is noticeably different (about factor 2 larger) from the experimental result. In 1994, the first theoretical interpretation of the FILTEX results was done by Meyer and Horowitz [155] where the discrepancy between theory and experiment has been attributed to three main effects: 1- the contribution of the Coulomb-nuclear interference, 2- the interaction of a projectile with the polarized electrons (pe) of the hydrogen gas target (spin flip) and 3- the scattering of a projectile on polarized protons of the target at angles smaller than the acceptance angle of the storage ring. Taken into account these contributions, the calculation showed to be in good agreement with the experiment. Based on these results it was suggested to polarize an antiproton beam by spin-flip in pp and pe scattering reactions [156].

The PAX (Polarized Antiproton eXperiments) [151] collaboration has demonstrated recently, with a dedicated experiment using the COSY electron cooling, that the spin-flip method can not provide noticeable polarization for the proton beam when protons and electrons interact at negligible relative energy [157].

In the following of this section, we will show that, in the energy range of GeV, the spin flip mechanism for pe scattering can produce polarized protons. Assuming C invariance in electromagnetic interactions, the elastic reactions $p + e$ and $\bar{p} + e^+$ are strictly equivalent: the same mechanism can be applied to polarize antiproton beams.

8.4 Polarization transfer coefficients, T_{ij} , in the $p + \vec{e} \rightarrow \vec{p} + e$ reaction

The coefficients of polarization transfer from the electron target to the proton beam can be obtained from Eq. A.20. In the frame where the initial electron is at rest, the polarization four vectors of the electron, S , and of the scattered proton, η_2 , have the following components:

$$S \equiv (0, \vec{\xi}), \quad \eta_2 \equiv \left(\frac{1}{M} \vec{p}_2 \cdot \vec{\chi}_2, \vec{\chi}_2 + \frac{\vec{p}_2(\vec{p}_2 \cdot \vec{\chi}_2)}{M(E_2 + M)} \right), \quad (8.17)$$

where $\vec{\xi}$ and $\vec{\chi}_2$ are the unit polarization three-vectors of the initial electron and scattered proton in their rest systems, respectively. In the Lab system (inverse kinematics) one can write $\vec{p}_1 = \vec{k}_2 + \vec{p}_2$ and $m + E_1 = E_2 + \epsilon_2$.

Using the P -invariance of the hadron electromagnetic interaction, one can parametrize the dependence of the differential cross section versus the polarizations of the electron target and of the scattered proton as follows:

$$\begin{aligned} \frac{d\sigma}{dq^2}(\vec{\xi}, \vec{\chi}_2) &= \left(\frac{d\sigma}{dq^2} \right)_{unpolarized} [1 + T_{\ell\ell}\xi_\ell\chi_{2\ell} + T_{nn}\xi_n\chi_{2n} + T_{tt}\xi_t\chi_{2t} + T_{\ell t}\xi_\ell\chi_{2t} \\ &\quad + T_{t\ell}\xi_t\chi_{2\ell}], \end{aligned} \quad (8.18)$$

where T_{ik} , $i, k = \ell, t, n$ are the non vanishing polarization transfer coefficients. The polarization vectors can be longitudinal (l), transverse (t) with respect to the momenta of the initial proton beam, or orthogonal (normal (n)) to the scattering plane.

At high energy, the polarization transfer coefficients depend essentially on the direction of the scattered proton polarization. Let us choose an orthogonal system with the z -axis directed along \vec{p}_1 , \vec{k}_2 lies in the xz plane and the y -axis is directed along the vector $\vec{p}_1 \times \vec{k}_2$. Therefore, in this system $\ell \parallel z$, $t \parallel x$ and $n \parallel y$. The explicit expressions for the polarization transfer coefficients are given in Appendix B. They are shown in Fig. 8.4 as a function of the incident energy for $\vartheta = 0$ mrad (black solid line), 10 mrad (red dashed line), 30 mrad (green dash-dotted line), 50 mrad (blue dotted line).

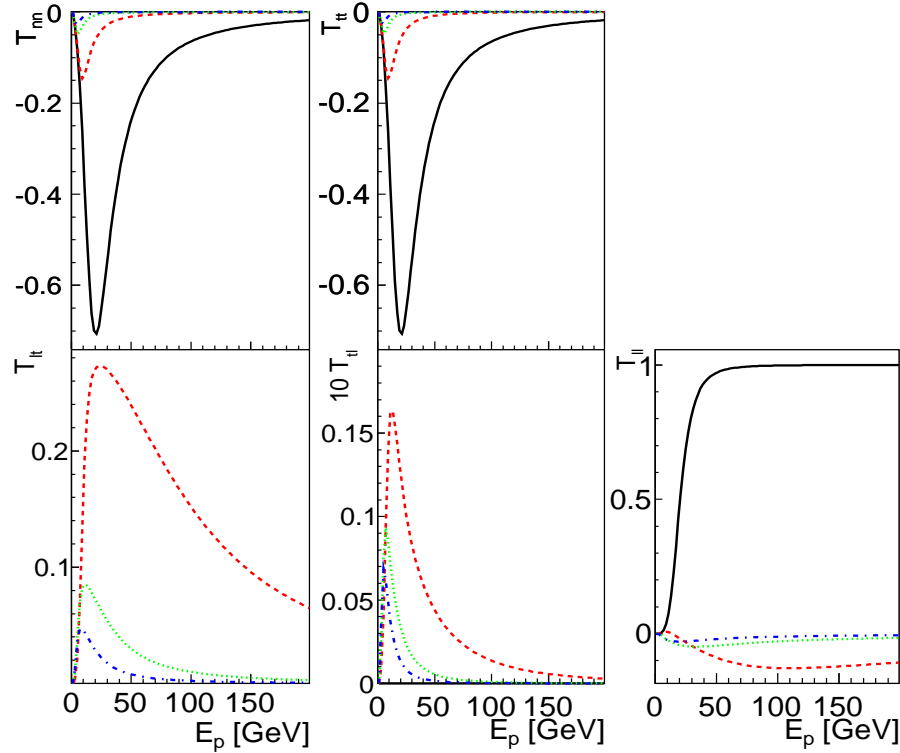


Figure 8.4: Polarization transfer coefficients as a function of E_p for different angles of the recoil electron: $\vartheta = 0$ (black solid line), 10 mrad (red dashed line), 30 mrad (green dotted line), 50 mrad (blue dash-dotted line).

One can see that in collinear kinematics, in general, either polarization observables take the maximal values or they vanish. An interesting kinematic region appears at $E_p = 20$ GeV. The value of observables depends on the angle of the recoil electron. As the maximum angle of the scattered proton is very small, well within the acceptance angle of any storage ring, all the protons scattering from electrons stay in the ring. By consequence, the effects of polarization can be evaluated from the integrated value of the polarized cross section and polarization observables in the full allowed kinematical region.

The values for the total polarized and unpolarized cross sections are reported in Ta-

ble 8.1 and for the corresponding integrated polarization coefficients in Table 8.2, at different incident energies.

E_p [GeV]	σ_{unp} [mb]	$\sigma_{t\ell}$ [mb]	$\sigma_{\ell t}$ [mb]	$\sigma_{\ell\ell}$ [mb]	$\sigma_{t\ell}$ [mb]	σ_{nn} [mb]
23×10^{-3}	4.4×10^8	26	26.7	-125.3	-16.9	-139.3
50×10^{-3}	2×10^8	11.5	12.2	-62.8	-7.4	-67
1	2.5×10^7	0.4	0.8	-5.6	-0.2	-2.9
10	1.9×10^7	9.1×10^{-3}	10.6×10^{-2}	-1.01	-0.6×10^{-2}	-0.09
50	1.8×10^7	0.4×10^{-3}	2.3×10^{-2}	-0.2	-0.3×10^{-3}	-0.5×10^{-2}

Table 8.1: Unpolarized cross section and polarized transfer cross sections (in mb) for different incident kinetic energies.

E_p [GeV]	$T_{t\ell}$	$T_{\ell t}$	$T_{\ell\ell}$	$T_{t\ell}$	T_{nn}
23×10^{-3}	1.5×10^{-12}	1.5×10^{-12}	-1.3×10^{-12}	-2.6×10^{-12}	-3.8×10^{-12}
50×10^{-3}	7.2×10^{-12}	7.5×10^{-12}	-6.3×10^{-12}	-1.2×10^{-11}	-1.8×10^{-11}
1	3.3×10^{-9}	6.8×10^{-9}	-4.8×10^{-9}	-6.8×10^{-9}	-9.2×10^{-9}
10	3.5×10^{-7}	3.9×10^{-6}	-1.4×10^{-6}	-1.1×10^{-6}	-1.2×10^{-6}
50	5.9×10^{-6}	0.3×10^{-3}	1.4×10^{-3}	-1.4×10^{-5}	-0.2×10^{-4}

Table 8.2: Integrated polarization transfer coefficients for different incident energies.

Comparing the integrated values of one of these polarization transfer coefficient, i.e. T_{nn} , at $E_p = 23$ MeV (which is in agreement with the result of the FILTEX experiment) and $E_p = 10$ GeV, one can see a difference of about 10^6 order of magnitude.

Numerical estimates showed that polarization effects may be sizable in the GeV range, and that the polarization transfer coefficients for $\vec{p} + e \rightarrow \vec{p} + e$ could be used to polarize high energy proton beams. The calculated values of the scattered proton polarization for the reaction $p + \vec{e} \rightarrow \vec{p} + e$ at proton beam energies lower than a few tens of MeV show that it is not possible to obtain sizable polarization of the antiproton beam in an experimental setup where antiprotons and electrons collide with small relative velocities. The present results confirm that the polarization of the scattered proton has large values at high proton-beam energies [158]. Thus, one could consider an experimental setup where high-energy protons (antiprotons) collide with a polarized electron (positron) target at rest to obtain polarized protons (antiprotons). The low values of momentum transfer which are involved ensure that the cross section is sizable. A practical implementation of this method has not yet been further elaborated. One may also replace the atomic target with a low energy electron collider.

8.5 High energy polarimetry

At the relativistic heavy-ion collider (RHIC), large interest has been given to the inverse kinematics (proton projectile on electron target) due to the possibility to build polarimeters, for high-energy polarized proton beams [159].

The experimental angular asymmetry for the elastic pe -scattering is given by the product of the beam P_i^p and target P_j^e polarizations along i and j directions respectively and the spin correlation coefficient C_{ij} (analyzing powers):

$$A_{ij}^{exp} = P_i^p P_j^e C_{ij}. \quad (8.19)$$

A useful process for polarimetry should have:

- Substantial analyzing power and cross section in order to produce a large figure of merit for the polarimeter.
- Well-established theoretical foundations, providing reliable calculations of the cross section and its energy dependence;

The idea to use pe elastic scattering for beam polarimetry has been first suggested in Ref. [158]. In the one photon exchange approximation, the uncertainty on the cross section comes mainly from the proton electromagnetic FFs. In the allowed domain of the momentum transfer squared, all models converge to the static values of charge and anomalous magnetic moment of the proton. It was shown [159] that the analyzing powers for the present reaction, as a functions of the proton beam energy E_p , reach a maximum for forward scattering at $E_p = 50$ GeV. The authors concluded that the concept of such a polarimeter is realistic for longitudinal as well as transverse proton-beam polarization. In that paper, explicit expressions for the analyzing powers in the Lab frame where the electron is considered at rest were not given.

In the following, the correlation coefficients of the elastic scattering of high energy polarized protons by polarized electrons, and for all possible polarization directions, are calculated explicitly in terms of proton FFs.

8.6 Polarization correlation coefficients, C_{ij} , in the $\vec{p} + \vec{e} \rightarrow p + e$ reaction

The spin correlation coefficients for the elastic $\vec{p}\vec{e}$ collisions can be obtained from the expression of Eq. A.21. In the frame where the electron target is at rest, the four-vector of the proton beam polarization η_1 , has the following components:

$$\eta_1 = \left(\frac{\vec{p}_1 \cdot \vec{\chi}_1}{M}, \vec{\chi}_1 + \frac{\vec{p}_1(\vec{p}_1 \cdot \vec{\chi}_1)}{M(E_1 + M)} \right), \quad (8.20)$$

where $\vec{\chi}_1$ is the unit vector describing the polarization of the initial proton in its rest system.

Applying the P-invariance of the hadron electromagnetic interaction, one can write the following expression for the dependence of the differential cross section on the polarization of the initial particles:

$$\begin{aligned} \frac{d\sigma}{dq^2}(\vec{\xi}, \vec{\chi}_1) = & \left(\frac{d\sigma}{dq^2} \right)_{un} [1 + C_{\ell\ell}\xi_\ell\chi_{1\ell} + C_{tt}\xi_t\chi_{1t} + C_{nn}\xi_n\chi_{1n} + C_{\ell t}\xi_\ell\chi_{1t} \\ & + C_{t\ell}\xi_t\chi_{1\ell}], \end{aligned} \quad (8.21)$$

where C_{ik} , $i, k = \ell, t, n$ are the spin correlation coefficients which characterize $\vec{p}\vec{e}$ scattering. Small coefficients (in absolute value) are expected for the transverse component of the beam polarization at high energies. This can be seen from the expression of the components of the proton beam polarization four-vector which can be approximated at large energies ($E_1 \gg M$) by:

$$\eta_{1\mu} = (0, \vec{\chi}_{1t}) + \chi_{1\ell} \left(\frac{|p_1|}{M}, \frac{\vec{p}_1}{M} \frac{E_1}{|p_1|} \right) \sim \chi_{1\ell} \frac{p_{1\mu}}{M}. \quad (8.22)$$

The effect of the transverse beam polarization appears to be smaller by a factor $1/\gamma$, $\gamma = E_1/M \gg 1$. The explicit expressions of the spin correlation coefficients are also given in Appendix B, and illustrated in Fig. 8.5.

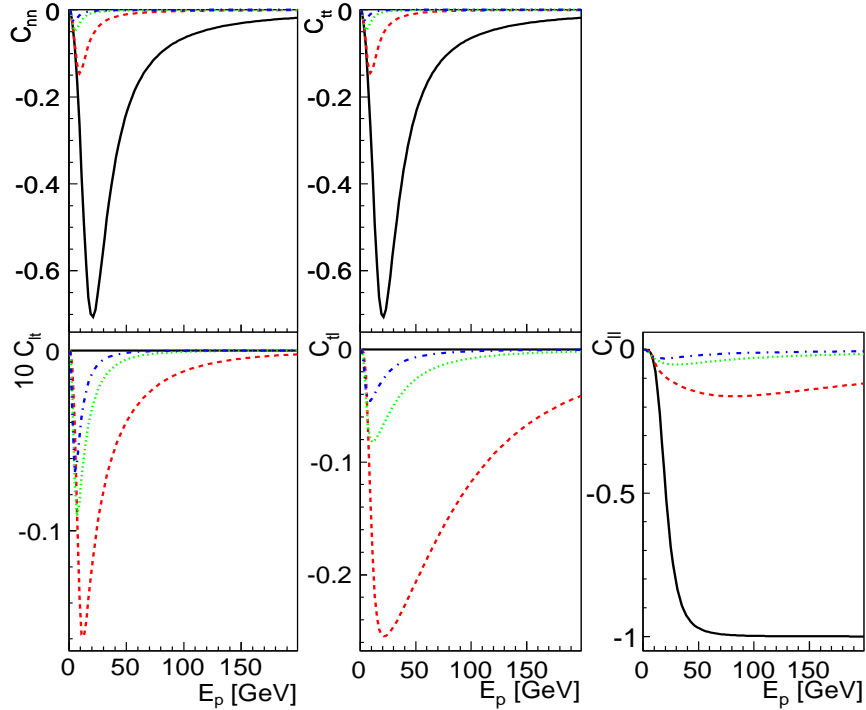


Figure 8.5: Same as Fig. 8.4 but for the spin correlation coefficients.

The effectiveness of this method in polarisation measurements can be quantified by the figure of merit. The figure of merit is a quantity used to characterize the performance of a device, system or method, and allows the comparison of different alternatives. For a polarimeter, the differential figure of merit is defined as the product of the polarimeter efficiency $\epsilon(\vartheta_p)$ and the analyzing coefficients C_{ij} :

$$\mathcal{F}^2(\vartheta_p) = \epsilon(\vartheta_p)C_{ij}^2(\vartheta_p), \quad (8.23)$$

where $\epsilon(\vartheta_p) = N_f(\vartheta_p)/N_i$ can be defined as the ratio between the number of scattered events in an interval $\Delta\vartheta_p$ around ϑ_p , and the number of the incident events.

The duration necessary for a polarization measurement in order to achieve a definite statistical error ΔP on the polarization P of the proton beam can be obtained through the relation:

$$\begin{aligned} \left(\frac{\Delta P(\vartheta_p)}{P} \right)^2 &= \frac{2}{N_i(\vartheta_p)\mathcal{F}^2(\vartheta_p)P^2} = \frac{2}{Lt_m(d\sigma/d\Omega)d\Omega C_{ij}^2(\vartheta_p)P^2} \\ &= \frac{2}{Lt_m(d\sigma/dq^2)dq^2 C_{ij}^2(q^2)P^2}, \end{aligned} \quad (8.24)$$

where t_m is the duration of measurement. The correlation coefficient squared, weighted by the differential cross section, $C_{t\ell}^2(q^2)(d\sigma/dq^2)$ and $C_{\ell\ell}^2(q^2)(d\sigma/dq^2)$ are shown in Fig. 8.6 for different electron angles.

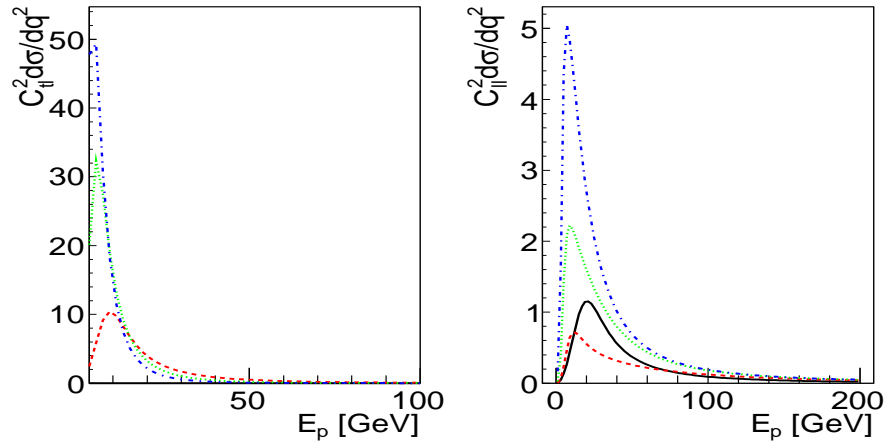


Figure 8.6: Variation of the differential quantities $C_{t\ell}^2(q^2)(d\sigma/dq^2)$ (left) and $C_{\ell\ell}^2(q^2)(d\sigma/dq^2)$ (right) [mb/GeV²] as a function of incident energy for a polarized proton beam scattering from a polarized electron target $\vec{p} + \vec{e} \rightarrow p + e$, at different angles. Notations are the same as in Fig. 8.4.

The integrated quantity

$$F^2 = \int \frac{d\sigma}{dq^2} C_{ij}^2(q^2) dq^2 \quad (8.25)$$

as a function of the incident energy is shown in Fig. 8.7. One can see that F^2 takes its maximum value for $E_p \simeq 10$ GeV. Assuming a luminosity of $10^{32} \text{ cm}^{-2} \text{ s}^{-1}$ for an ideal detector with an acceptance and efficiency of 100%, one could measure the beam polarization with an error of 1% in a time interval of 3 min.

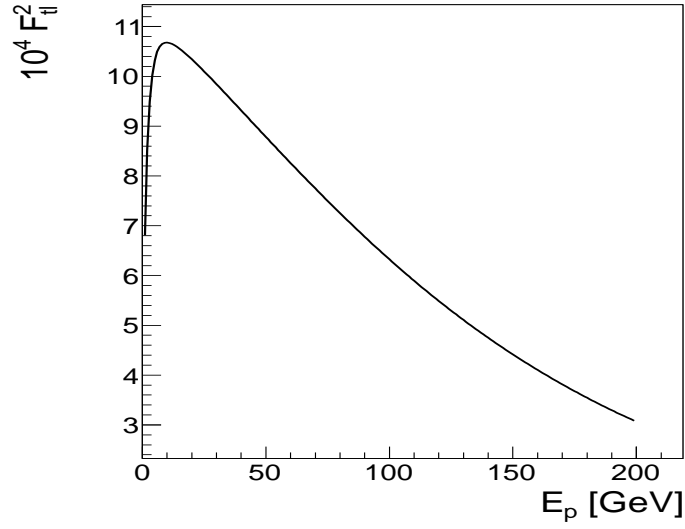


Figure 8.7: Variation of the quantity F^2 [a.u.] as a function of proton kinetic energy E_p for a transverse polarized proton beam, scattered by a longitudinally polarized electron target ($\vec{p} + \vec{e} \rightarrow p + e$).

As a conclusion, if one detects the outgoing proton, which seems more challenging because its kinematical characteristics are close to those of the beam (for the high-energy solution) one could in principle build a polarimeter based on the scattering of a polarized beam (the polarization of which should be measured) on a polarized target (with known polarization). In this case, from the azimuthal distribution, one can reconstruct the components of the polarization which are normal to the scattering plane.

Chapter 9

Proton antiproton annihilation into massive leptons

In chapter 8, model independent expressions for experimental observables associated to the elastic lepton proton scattering in the SL region are derived. In this chapter, the transition to the TL region is performed to focus on the proton-antiproton annihilation into heavy lepton pair. The unpolarized cross section and the polarization observables in terms of the proton electromagnetic FFs are calculated in a model independent formalism taking into account the mass of the heavy lepton.

The reaction $\bar{p}p \rightarrow e^+e^-$ has been first studied in Ref. [65] in connection with the possibility to extract proton FFs in the TL region assuming one photon exchange. Later, polarization observables have been derived under the assumption of an electron mass equal to zero in Ref. [160]. In 2005, model independent expressions of single and double spin observables for the reaction $\bar{p} + p \rightarrow e^- + e^+$ including the contribution of two photon exchange have been calculated in Ref. [161], still neglecting the electron mass. Here, the formalism of Ref. [161] is generalized to the case of heavier leptons, such as μ or τ for which mass can not be neglected. This induces new terms in the reaction amplitude. The interest of FFs measurement in $\bar{p} + p$ annihilation into heavier leptons is related to the following facts:

- The individual determination of the electric and magnetic proton form factors in $\bar{p}p \rightarrow \ell^+\ell^-$ requires a precise measurement of the angular distribution of the final lepton. Radiative corrections (RC) due to the emission of real and emission/absorption of virtual photons do affect the measurement of the experimental observables, in particular the differential cross section. As the photon emission from the final state is inversely proportional to the lepton mass, the higher the lepton mass the less the corresponding radiative effects. Therefore, in the case of muon or tau production, RC are suppressed as $|\vec{k}|/m_\ell$ (\vec{k} is the lepton three momentum).
- The τ lepton is an unstable particle with a decay time of $290.6 \times 10^{-15}\text{s}$. The polarization of unstable particles can be measured, in principle, through the

angular or energy distribution of their weak decay products. Consequently, the observables related to the lepton polarization may be experimentally measured without polarimeters. As it has been performed at the Large Electron Positron (LEP) collider, the ALEPH (Apparatus for LEP PHysics at CERN) collaboration measured the τ polarization in the CM of electron-positron collision from different decays such as $\tau \rightarrow \pi^- + \nu_\tau$, $\tau \rightarrow a_1 + \nu_\tau$, $\tau \rightarrow \rho + \nu_\tau$ [162, 163].

- From the relativistic definition of the particle polarization 4-vector, the observables corresponding to the transverse polarization of the lepton contain the factor m_ℓ/E (m_ℓ is the lepton mass, E is the incident energy). In the few GeV range, they are suppressed in case of electrons, whereas, in the case of τ leptons they are enhanced.

9.1 Formalism

The formalism given in the appendix A is the basis of the calculations described here. The difference in notations is related to the fact that antiparticles are now involved in the interaction (TL region). Let us consider the reaction:

$$\bar{p}(p_1) + p(p_2) \rightarrow \ell^-(k_1) + \ell^+(k_2), \quad (9.1)$$

where $\ell = e, \mu$ or τ and the four-momenta of the particles are written in parenthesis. In the Born approximation $q = k_1 + k_2 = p_1 + p_2$ is the four momentum of the exchanged virtual photon.

The spin structure of the matrix element can be written as follow:

$$\mathcal{M} = -\frac{4\pi\alpha}{q^2} j_\mu J^\mu = -\frac{4\pi\alpha}{q^2} (j_0 J_0 - \vec{j} \cdot \vec{J}). \quad (9.2)$$

The leptonic and hadronic currents are:

$$j_\mu = \bar{u}(k_1) \gamma_\mu v(k_2), \quad (9.3)$$

and

$$J^\mu = \bar{v}(p_1) \left[G_M(q^2) \gamma^\mu + \frac{P^\mu}{M} F_2(q^2) \right] u(p_2), \quad P^\mu = \frac{(p_1 - p_2)^\mu}{2} \quad (9.4)$$

The differential cross section is related to the matrix element squared (Eq. 9.2) by

$$d\sigma = \frac{(2\pi)^4}{4\mathcal{I}} |\mathcal{M}|^2 \frac{d^3\vec{k}_1 d^3\vec{k}_2}{(2\pi)^6 4\epsilon_1 \epsilon_2} \delta^4(p_1 + p_2 - k_1 - k_2), \quad (9.5)$$

where $\mathcal{I} = (p_1 \cdot p_2)^2 - p_1^2 p_2^2$ and $\epsilon_1(\epsilon_2)$ is the energy of the $\ell^-(\ell^+)$ lepton, and

$$|\mathcal{M}|^2 = \frac{e^4}{q^4} L_{\mu\nu} H^{\mu\nu}, \quad L_{\mu\nu} = j_\mu j_\nu^*, \quad H^{\mu\nu} = J^\mu (J^\nu)^*. \quad (9.6)$$

The leptonic tensor for the case of an unpolarized lepton is:

$$L_{\mu\nu}^{(0)} = 4(k_{1\mu}k_{2\nu} + k_{1\nu}k_{2\mu}) - 2q^2 g_{\mu\nu}, \quad (9.7)$$

where $g_{\mu\nu}$ is the metric tensor of the Minkowski spacetime. The contribution to the electron tensor corresponding to a polarized electron is

$$L_{\mu\nu}^{(p)} = 2im_\ell \epsilon_{\mu\nu\rho\sigma} q_\rho S_\sigma, \quad (9.8)$$

where S_σ is the polarization four-vector describing the lepton polarization, and $\epsilon_{\mu\nu\rho\sigma}$ is the unit antisymmetric tensor with $\epsilon_{0123} = 1$. We denote the mass of the lepton by m_ℓ .

The hadronic tensor for unpolarized protons is:

$$H_{\mu\nu}^{(0)} = \left(g_{\mu\nu} - \frac{q_\mu q_\nu}{q^2} \right) H_1 + P_\mu P_\nu H_2, \quad (9.9)$$

where

$$H_1 = -2q^2 |G_M|^2, H_2 = \frac{8}{\eta_p - 1} [|G_M|^2 - \eta_p |G_E|^2], \quad \eta_p = q^2/(4M^2). \quad (9.10)$$

9.2 Kinematics

In the CM system, the lepton pair is emitted back to back and each lepton carries half of the total energy. In the Lab system, the kinematics for a massive lepton, in particular for a τ -lepton, which mass is larger than the proton mass, is essentially different from the case when the lepton mass is neglected. In the case of e or μ , there is no limitation on the angular region of the produced (negative) lepton in the Lab system, and there is a unique relation between the energy (ϵ_1) and the angle (ϑ). In the limit of zero lepton mass, this relation can be written as:

$$\epsilon_1 = \frac{MW}{W - p_{\bar{p}} \cos \vartheta}, \quad W = E_1 + M, \quad (9.11)$$

where E_1 and $p_{\bar{p}}$ are respectively the energy and the momentum of the antiproton beam in the Lab frame. When the mass of the lepton exceeds the proton mass, there is a maximum limiting angle for the lepton emission (ϑ^{max}), which depends on the lepton mass and on the incident energy:

$$\cos \vartheta_1^{max} = \frac{W \sqrt{m_\ell^2 - M^2}}{m_\ell p_{\bar{p}}}, \quad (9.12)$$

and it is illustrated as vertical lines in Fig. 9.1. In the Lab system, from the conservation laws of energy and momentum one finds also that one angle corresponds to two possible values for the energy of the emitted τ^- lepton:

$$\epsilon_1^\pm = \frac{MW^2 \pm \sqrt{p_{\bar{p}}^2 \cos^2 \vartheta_1 [W^2(M^2 - m_\ell^2) + m_\ell^2 p_{\bar{p}}^2 \cos^2 \vartheta_1]}}{(W^2 - p_{\bar{p}}^2 \cos^2 \vartheta)}. \quad (9.13)$$

This is illustrated in Fig. 9.1, for three incident energies $E_1 = 6.85$ GeV, just above the kinematical threshold (blue dash-dotted line), $E_1 = 15$ GeV (black solid line) and $E_1 = 30$ GeV (red dashed line), well above threshold.

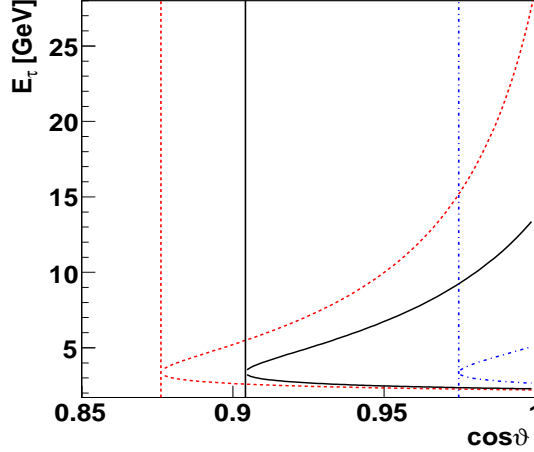


Figure 9.1: Energy of the τ^- lepton as a function of the emission angle for $E_1 = 6.85$ GeV (blue dash-dotted line), $E_1 = 15$ GeV (black solid line) and $E_1 = 30$ GeV (red dashed line), in the Lab system. The limiting angles are shown as vertical lines for the corresponding energy.

For a fixed angle ϑ , the correlated positive lepton can take two values of energy and emission angle (Fig. 9.2) according to the conservation laws.

9.3 Unpolarized cross section in the CMS

The following analysis for the unpolarized cross section and polarization observables is done in the CMS, in a coordinate frame where: the z -axis is directed along the antiproton momentum $z \parallel \vec{p}$, the y -axis is directed along the vector $\vec{p} \times \vec{k}$ (\vec{k} is the negative lepton momentum in CMS) and the x -axis in order to form a left handed coordinate system. In this frame, the four vectors of the particles are

$$p_1 = (E, \vec{p}), \quad p_2 = (E, -\vec{p}), \quad k_1 = (E, \vec{k}), \quad k_2 = (E, -\vec{k}), \quad (9.14)$$

where

$$\begin{aligned} E &= \sqrt{q^2}/2, \quad \vec{k} = \left(\sqrt{\frac{q^2}{4} - m_\ell^2} \sin \theta, 0, \sqrt{\frac{q^2}{4} - m_\ell^2} \cos \theta \right), \\ \vec{p} &= \left(0, 0, \sqrt{\frac{q^2}{4} - M^2} \right), \quad \vec{k} \cdot \vec{p} = |\vec{k}| |\vec{p}| \cos \theta, \end{aligned} \quad (9.15)$$

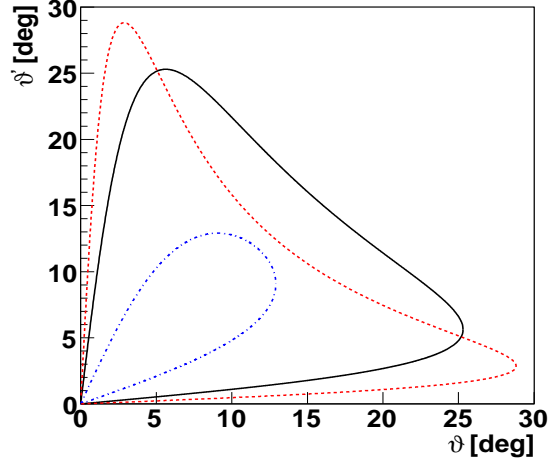


Figure 9.2: τ^+ emission angle ϑ' as a function of the τ^- angle ϑ in the Lab system. Notation as in Fig. 9.1.

and θ is the CMS angle of the negative lepton with respect to the antiproton beam.

The expression of the differential cross section for unpolarized $\bar{p}p \rightarrow \ell^-\ell^+$ is obtained from the square of the scattering amplitude by the contraction of the unpolarized leptonic and hadronic tensors ($H_{\mu\nu}^0(L^0)^{\mu\nu}$):

$$\frac{d\sigma_0^C}{d\Omega} = \frac{\alpha^2}{4q^2} \frac{\beta_\ell}{\beta_p} \mathcal{D}^C, \quad \mathcal{D}^C = \frac{|G_E|^2}{\eta_p} (1 - \beta_\ell^2 \cos^2 \theta) + |G_M|^2 (2 - \beta_\ell^2 \sin^2 \theta), \quad (9.16)$$

where $\beta_\ell^2 = 1 - 4m_\ell^2/q^2$ is the velocity squared of the lepton ℓ of mass m_ℓ ($\ell = e, \mu$ or τ) and $\beta_p^2 = 1 - 4M^2/q^2 = 1 - 1/\eta_p$ is the antiproton velocity squared. Integrating the differential cross section (Eq. 9.16) over the solid angle one finds the expression for the total cross section:

$$\sigma = \frac{\pi\alpha^2}{3q^2} \frac{\beta_\ell}{\beta_p} \left(2 + \frac{1}{\eta_\ell} \right) \left[\frac{|G_E|^2}{\eta_p} + 2|G_M|^2 \right], \quad \eta_\ell = \frac{q^2}{4m_\ell^2}, \quad (9.17)$$

which depends on the moduli squared of FFs, and does not contain any interference term. In the limit of zero lepton mass, this expression coincides with the results obtained in Ref. [75] for the case of electron:

$$\frac{d\sigma}{d\Omega}(\bar{p}p \rightarrow e^+e^-) = \frac{\alpha^2}{4q^2\beta_p} \left[\frac{|G_E|^2}{\eta_p} \sin^2 \theta + |G_M|^2 (1 + \cos^2 \theta) \right], \quad (9.18)$$

$$\sigma(\bar{p}p \rightarrow e^+e^-) = \frac{2\pi\alpha^2}{3q^2\beta_p} \left(\frac{|G_E|^2}{\eta_p} + 2|G_M|^2 \right). \quad (9.19)$$

From a comparison between Eqs. (9.16) and (9.18) one can see that the terms due to the lepton mass do not change the even nature of the differential cross section with respect to $\cos \theta$, as expected from the one photon exchange mechanism, but change the ratio of the cross section at $\theta = 0^\circ$ or 180° with respect to the cross section at $\theta = 90^\circ$ degrees.

The differential cross section (Eq. 9.16) can be expressed as a function of the angular asymmetry \mathcal{A} as:

$$\frac{d\sigma}{d\Omega} = \left(\frac{d\sigma}{d\Omega} \right)_{\pi/2} (1 + \mathcal{A} \cos^2 \theta), \quad (9.20)$$

where

$$\left(\frac{d\sigma}{d\Omega} \right)_{\pi/2} = \frac{\alpha^2}{4q^2} \frac{\beta_\ell}{\beta_p} \left[\frac{|G_E|^2}{\eta_p} + |G_M|^2 (2 - \beta_\ell^2) \right], \quad \mathcal{A} = \beta_\ell^2 \frac{\eta_p |G_M|^2 - |G_E|^2}{\eta_p |G_M|^2 (2 - \beta_\ell^2) + |G_E|^2}. \quad (9.21)$$

As in the case of electrons, the measurement of the asymmetry \mathcal{A} allows one to determine the ratio of the moduli of the FFs through the relation:

$$\left| \frac{G_E}{G_M} \right|^2 = \eta_p \frac{\beta_\ell^2 - (2 - \beta_\ell^2) \mathcal{A}}{\beta_\ell^2 + \mathcal{A}}. \quad (9.22)$$

9.3.1 Single spin observables: the analyzing power

The unpolarized cross section contains only the moduli squared of the form factors. The investigation of reaction Eq. 9.1 with polarized antiproton beam and/or polarized proton target carries information about the phase difference of the nucleon FFs, $\Phi = \Phi_M - \Phi_E$, where $\Phi_{M,E} = \arg G_{M,E}$.

Unlike elastic e^-p scattering in one-photon exchange approximation, the hadronic tensor in the reaction (9.1) contains an antisymmetric part due to the fact that nucleon FFs are complex functions [161]. Therefore, in the present case, the polarization of the antiproton may lead to nonzero spin asymmetry.

The differential cross section when only the antiproton beam is polarized can be written as:

$$\frac{d\sigma}{d\Omega} = \frac{d\sigma_0}{d\Omega} (1 + A_y^C \chi_{1y}), \quad (9.23)$$

where A_y^C is the only non vanishing single spin asymmetry (in CMS) due to the antiproton polarization and $\vec{\chi}_1$ is the polarization of the antiproton in its rest frame. This asymmetry is determined by the component of the polarization vector along y -axis which is perpendicular to the reaction plane. In the CMS, A_y^C has the form:

$$\mathcal{D}^C A_y^C = \frac{\beta_\ell^2 \sin 2\theta}{\sqrt{\eta_p}} \text{Im} G_M G_E^*. \quad (9.24)$$

Note that the single spin asymmetry, as defined in Eq. 9.24, does not depend on the polarization degree of the beam, but the polarized cross section does according to

Eq. 9.23 and reduces proportionally to the degree of the beam polarization, if the beam is not fully polarized.

One can see that taking into account the mass of the lepton leads to a factor β_ℓ^2 which decreases when the antiproton energy increases. The limit of A_y^C when the mass of leptons tends to zero, gives the known expression for the asymmetry of electron production [164]:

$$\mathcal{D}^C A_y^C(m_\ell \rightarrow 0) = \frac{\sin 2\theta}{\sqrt{\eta_p}} \text{Im} G_M G_E^*, \quad (9.25)$$

where

$$\mathcal{D}^C(m_\ell \rightarrow 0) = \frac{|G_E|^2}{\eta_p} \sin^2 \theta + |G_M|^2 (1 + \cos^2 \theta). \quad (9.26)$$

One can see from Eq. 9.24 that this asymmetry vanishes in collinear kinematics, for $\theta = 0^\circ$ or 180° . It can be explained, since in a parity conserving electromagnetic interaction the spin asymmetry is determined by a correlation of the type $\vec{\chi}_1 \cdot (\vec{p} \times \vec{k}_1)$. Therefore, it vanishes when the lepton momentum is parallel or anti-parallel to the antiproton momentum. The single-spin asymmetry does not vanish in one photon exchange approximation, due to the complex nature of FFs in the time-like region. This is a principal difference from the elastic ep scattering, where nucleon FFs are real functions.

The measurement of this asymmetry allows one to determine the phase difference of the nucleon FFs, when the moduli are determined from the unpolarized differential cross section measurements [75].

The single spin asymmetry due to the polarization of the lepton vanishes because the spin-dependent leptonic tensor does not contain any symmetric part (over the indices μ and ν). This is due to the fact that the electromagnetic interaction of the τ -lepton, as in case of e or μ , is assumed to be point-like (does not contain FFs). The measurement of this asymmetry constitutes a model independent experimental test of the point-like nature of the τ -lepton.

Note that the inclusion of the two-photon exchange mechanism may lead to a non-zero value of the single-spin asymmetry due to the τ -lepton polarization [161]. In the case of e or μ pair production, the contribution of two-photon exchange is suppressed by the presence of a factor m_ℓ/M in this asymmetry. But, in the case of τ pair production, this factor will enhance the terms due to two-photon exchange. Therefore, the measurement of the polarization of a single τ lepton in the collision of unpolarized particles is a direct test of the presence of the two-photon exchange mechanism. An advantage of this measurement is that the polarization of unstable particles can be measured through the angular distribution of their decay products as already mentioned.

9.3.2 Double spin polarization observables

The double spin observables describe the cases where two particles involved in the annihilation reaction are polarized. The expressions for the double spin observables are

combinations of $ImF_1F_2^*$, $ReF_1F_2^*$ and $|F_{1,2}|^2$. Three types of double spin observables are considered here:

- The polarization transfer coefficients T_{ij} , which describe the transfer of the polarization from the polarized antiproton beam to the produced negative lepton.
- Analyzing powers in the initial state C_{ij}^h , which describe the correlation of spin between the polarized proton target and antiproton beam.
- Correlation coefficients in the final state. These coefficients are determined by the polarization measurement of the final leptons.

The indexes i, j correspond to n, t, ℓ , according to the direction of the polarization vectors of the lepton, or to x, y, z referring to the direction of the hadron. Then the following three independent polarization four vectors describe the lepton polarization in CMS

$$s_\ell^C = \frac{1}{m_\ell}(k, E \sin \theta, 0, E \cos \theta), \quad s_t^C = (0, \cos \theta, 0, -\sin \theta), \quad s_n^C = (0, 0, 1, 0), \quad (9.27)$$

where $E(k)$ is the CMS energy (magnitude of the momentum) of the lepton.

9.3.2.1 Polarization transfer coefficients

The non-vanishing transfer polarization coefficients are:

$$\begin{aligned} T_{\ell x}^C &= \frac{2 \sin \theta}{\sqrt{\eta_p} \mathcal{D}^C} \text{Re} G_M G_E^*, \quad T_{\ell z}^C = 2 \frac{\cos \theta}{\mathcal{D}^C} |G_M|^2, \quad T_{ny}^C = 2 \frac{m_\ell}{M} \frac{\text{Re} G_E G_M^*}{\eta_p \mathcal{D}^C}, \\ T_{tx}^C &= 2 \frac{m_\ell \cos \theta}{M \eta_p \mathcal{D}^C} \text{Re} G_E G_M^*, \quad T_{tz}^C = -2 \frac{m_\ell \sin \theta}{M \sqrt{\eta_p} \mathcal{D}^C} |G_M|^2. \end{aligned} \quad (9.28)$$

These coefficients are T -even observables, and, similarly to the case of elastic lepton-nucleon scattering, they do not vanish in the one-photon exchange. The coefficients T_{ny}^C , T_{tx}^C , T_{tz}^C are proportional to the mass of the produced lepton and they are suppressed by the factor m_ℓ/M for $\ell = e$ or μ . In the case of a τ -lepton this factor constitutes an enhancement of ~ 2 . The polarization observables $T_{\ell z}^C$ and T_{tz}^C are determined by the magnetic FF only, whereas $T_{\ell x}^C$, T_{tx}^C and T_{ny}^C involve the factor $\text{Re} G_M G_E^*$. Therefore, the measurement of the coefficients $T_{\ell x}^C$, T_{ny}^C , and T_{tx}^C can give in principle information on the phase difference of the nucleon FFs. In the limit of zero lepton mass, the expressions (9.28) coincide with the corresponding results of Refs. [164] and [161], neglecting the two-photon contribution.

9.3.2.2 Analyzing powers in polarized proton-antiproton collisions

The part of the differential cross section which depends on the polarization of the antiproton beam and proton target can be written as:

$$\frac{d\sigma}{d\Omega} = \frac{d\sigma_0}{d\Omega} (1 + A_{ij}^C \chi_{1i} \chi_{2j}), \quad (9.29)$$

where $\vec{\chi}_2$ is the polarization vector of the proton in its rest frame and A_{ij}^C are the analyzing powers which have the following form in CMS:

$$\begin{aligned}
 \mathcal{D}^C A_{xx}^C &= \sin^2 \theta \beta_\ell^2 \left(\frac{|G_E|^2}{\eta_p} + |G_M|^2 \right) + \frac{|G_E|^2}{\eta_p \eta_\ell}, \\
 \mathcal{D}^C A_{yy}^C &= \sin^2 \theta \beta_\ell^2 \left(\frac{|G_E|^2}{\eta_p} - |G_M|^2 \right) + \frac{|G_E|^2}{\eta_p \eta_\ell}, \\
 \mathcal{D}^C A_{zz}^C &= -\sin^2 \theta \beta_\ell^2 \left(\frac{|G_E|^2}{\eta_p} + |G_M|^2 \right) - \frac{|G_E|^2}{\eta_p \eta_\ell} + 2|G_M|^2, \\
 \mathcal{D}^C A_{xz}^C &= \mathcal{D}^C A_{zx}^C = \frac{\sin 2\theta}{\sqrt{\eta_p}} \beta_\ell^2 \text{Re} G_M G_E^*, \quad \eta_p = \frac{q^2}{4M^2}, \quad \eta_\ell = \frac{q^2}{4m_\ell^2}
 \end{aligned} \tag{9.30}$$

One can see that at small angles the contribution of $|G_E|^2$ dominates in the analyzing powers A_{xx}^C and A_{yy}^C . This effect is enhanced when considering heavy lepton ($1/\eta_\ell = 4m_\ell^2/q^2$). The coefficient A_{xz}^C gives information about the relative phase, through the term $\cos \Phi$. Combining this coefficient and the single spin asymmetry A_y^C , one can obtain useful relation between these quantities:

$$\tan \Phi = \frac{A_y^C}{A_{xz}^C}. \tag{9.31}$$

The measurement of the analyzing powers A_{xx}^C and A_{yy}^C allows one to determine the ratio of the FF moduli through the relation:

$$\left| \frac{G_E}{G_M} \right|^2 = \frac{\eta_p \beta_\ell^2}{1 + \eta_\ell^{-1} \cot^2 \theta} \frac{1 + \mathcal{R}}{1 - \mathcal{R}}, \quad \mathcal{R} = \frac{A_{yy}^C}{A_{xx}^C}. \tag{9.32}$$

Note that the sum of the double analyzing powers A_{xx}^C and A_{yy}^C is proportional to $|G_E|^2$:

$$\mathcal{D}^C (A_{xx}^C + A_{yy}^C) = \frac{2}{\eta_p} \left(\frac{1}{\eta_\ell} + \beta_\ell^2 \sin^2 \theta \right) |G_E|^2. \tag{9.33}$$

The measurement of this sum can be considered, in principle, as a good method for the determination of $|G_E|$. The advantage of measuring the ratio of polarization observables with heavy leptons instead of the unpolarized cross section, is that systematic errors associated with the measurement essentially cancel as well as RC allowing more precise measurements.

9.3.2.3 Correlation coefficients: polarized lepton-antilepton pair

The part of the cross section which depends on the polarizations of the produced leptons can be written as:

$$\frac{d\sigma}{d\Omega} = \frac{d\sigma_0}{d\Omega} (1 + C_{ij}^C \xi_{1i} \xi_{2j}), \tag{9.34}$$

where $\vec{\xi}_1$ ($\vec{\xi}_2$) is the polarization vector of the lepton ℓ^- (ℓ^+) in its rest frame and C_{ij}^C are the polarization correlation coefficients. In this case, the indexes ℓ, t, n have the following meaning in CMS: ℓ (longitudinal polarization) means that the polarization vectors of the negative lepton ($\vec{\xi}_1$) and positive lepton ($\vec{\xi}_2$) in their rest frame are directed along the momentum of the negative lepton, t means that both polarization vectors are orthogonal to this momentum (transverse polarization) and n that both polarization vectors are normal to the reaction plane (normal polarization).

The nonzero polarization correlation coefficients, in CMS, have the following form

$$\begin{aligned}\mathcal{D}^C C_{nn}^C &= \sin^2 \theta \beta_\ell^2 \left[\frac{|G_E|^2}{\eta_p} - |G_M|^2 \right] + \frac{|G_E|^2}{\eta_p \eta_\ell}, \\ \mathcal{D}^C C_{tt}^C &= \sin^2 \theta \left(1 + \frac{1}{\eta_\ell} \right) \left(|G_M|^2 - \frac{|G_E|^2}{\eta_p} \right) + \frac{|G_E|^2}{\eta_p \eta_\ell}, \\ \mathcal{D}^C C_{ll}^C &= \sin^2 \theta \left(1 + \frac{1}{\eta_\ell} \right) \left(\frac{|G_E|^2}{\eta_p} - |G_M|^2 \right) + 2 |G_M|^2 - \frac{|G_E|^2}{\eta_p \eta_\ell}, \\ \mathcal{D}^C C_{tt}^C &= C_{t\ell}^C = \frac{\sin 2\theta}{\sqrt{\eta_\ell}} \left(\frac{|G_E|^2}{\eta_p} - |G_M|^2 \right).\end{aligned}\tag{9.35}$$

From these expressions one can see that, for the τ -lepton, the large mass leads to an increase of the $|G_E|^2$ term in the angular regions $\theta \sim 0^\circ$ and $\theta \sim 180^\circ$. This effect essentially decreases for e and μ . One can also see that these correlation coefficients do not contain information about the phase difference of nucleon FFs.

9.4 Triple spin polarization observables

Triple spin polarization observables can be accessed through two types of reactions:

- Polarization measurement of one of the two produced leptons in the polarized proton antiproton annihilation.
- Polarization measurement of the lepton pair when only the proton target or the antiproton beam is polarized.

The polarization coefficients of the production of a polarized (negative) lepton in the annihilation of polarized protons and antiprotons are denoted by M_{i0jk} . The four subscripts refer to, respectively, the negative lepton which polarization is measured, the positive lepton, the polarized antiproton, and the polarized proton target. For the case of a longitudinally polarized lepton, the nonzero coefficients are :

$$\mathcal{D}^C M_{\ell 0 zy} = \mathcal{D}^C M_{\ell 0 yz} = \frac{\sin \theta}{\sqrt{\eta_p}} \text{Im} G_M G_E^*.\tag{9.36}$$

For the transverse and normal polarizations of the lepton, we have :

$$\begin{aligned}\mathcal{D}^c M_{t0zy} &= \mathcal{D}^c M_{t0yz} = \frac{m_\ell \cos \theta}{M \eta_p} \text{Im} G_M G_E^*, \\ \mathcal{D}^c M_{n0xz} &= \mathcal{D}^c M_{n0zx} = -\frac{1}{\eta_p} \frac{m_\ell}{M} \text{Im} G_M G_E^*.\end{aligned}\quad (9.37)$$

These observables do not contain additional information about nucleon FFs. In the limit of zero lepton mass only $M_{\ell 0zy}$ and $M_{\ell 0yz}$ are nonzero, and their expressions coincide with the results obtained for the coefficients D_{zy} and D_{yz} obtained in Ref. [161] for the case of a polarized proton-antiproton pair and longitudinally polarized electrons (neglecting the two-photon contributions).

The non vanishing polarization observables in the case of annihilation of a polarized antiproton beam with unpolarized proton target, when the polarization of both lepton and antilepton is measured, can be written as:

$$\begin{aligned}\mathcal{D}^c C_{tty0} &= -\frac{\sin 2\theta}{2\sqrt{\eta_p}} \frac{\eta_\ell + 1}{\eta_\ell} \text{Im} G_M G_E^*, \\ \mathcal{D}^c C_{\ell\ell y0} &= \frac{\sin 2\theta}{2\sqrt{\eta_p}} \frac{\eta_\ell + 1}{\eta_\ell} \text{Im} G_M G_E^*, \\ \mathcal{D}^c C_{nny0} &= \frac{\sin 2\theta}{2\sqrt{\eta_p}} \beta_\ell^2 \text{Im} G_M G_E^*, \\ \mathcal{D}^c C_{\ell nx0} &= \mathcal{D}^c C_{n\ell x0} = -\frac{\cos \theta}{\sqrt{\eta_p \eta_\ell}} \text{Im} G_M G_E^*, \\ \mathcal{D}^c C_{tnx0} &= \mathcal{D}^c C_{ntx0} = \frac{\sin \theta}{\sqrt{\eta_p}} \text{Im} G_M G_E^*, \\ \mathcal{D}^c C_{\ell ty0} &= \mathcal{D}^c C_{t\ell y0} = \frac{\cos 2\theta}{\sqrt{\eta_\ell \eta_p}} \text{Im} G_M G_E^*.\end{aligned}\quad (9.38)$$

In the case of zero lepton mass, one finds $C_{\ell nx0} = C_{n\ell x0} = C_{\ell ty0} = C_{t\ell y0} = 0$.

The $\text{Im} G_M G_E^*$ can be accessed through the measurement of the single spin asymmetry. However, the measurement of the ratio of any pair of the triple spin observables can give indication of additional mechanisms beyond the Born approximation. As a matter of fact, within the one-photon exchange approximation, this ratio depends only on kinematical variables.

9.5 Numerical results

In order to illustrate the different polarization observables two parametrizations for the TL FFs are used. The first one is based on the vector meson dominance models of Ref. [165]. The second one is a pQCD inspired parametrization, based on analytical extension of the dipole formula in the TL region [166] (see chapter 3.2.3).

The ratio between the total cross section (Eq. 9.17) for heavy lepton ℓ production $\ell = \tau$ ($m_\tau=1776.82$ MeV), or $\ell = \mu$ ($m_\mu=105.66$ MeV) with respect to the cross section for the production of an electron pair ($m = 0.511$ MeV), Eq. 9.19, is written as:

$$R_\ell = \frac{\sigma(\ell^+\ell^-)}{\sigma(e^+e^-)} = \frac{1}{2}\beta_\ell(3 - \beta_\ell^2), \quad (9.39)$$

and it is illustrated in Fig. 9.3, as a function of the total energy of the system from the $\bar{p}p$ annihilation threshold, $\sqrt{q^2} = 1.8765$ GeV. The corrections to the ratio due to the mass are of the fourth order and proportional to $(m_\ell/\sqrt{q^2})^4$ [75]; therefore, beyond the kinematical threshold, the muon and electron cross sections are similar. But for τ production, the variation is significant in the energy region above the $\tau^+\tau^-$ threshold ($\sqrt{q^2} = 3.5536$ GeV).

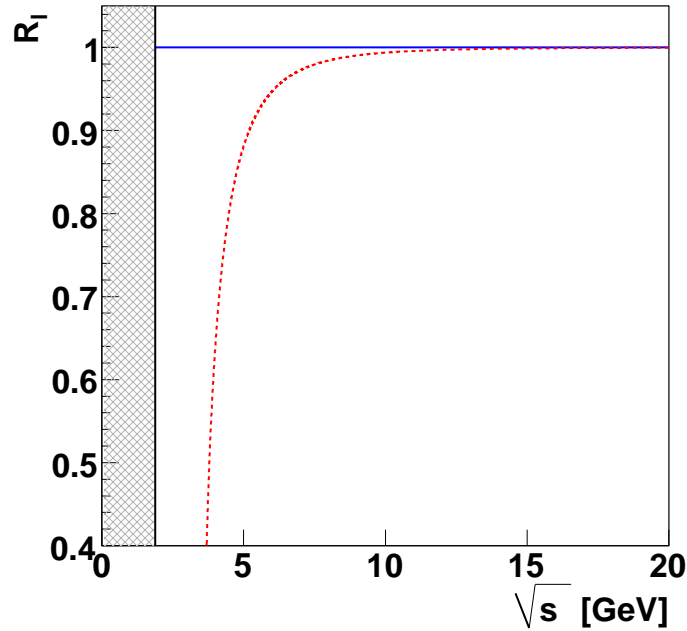


Figure 9.3: Total cross section ratios $R_\ell = \frac{\sigma(\ell^+\ell^-)}{\sigma(e^+e^-)}$, for $\ell = \tau$ (red dashed line) and $\ell = \mu$ (blue solid line) as a function of $\sqrt{q^2}$. The shaded area illustrates the region below the physical threshold for $\bar{p} + p$ annihilation.

The angular dependence of the differential cross section is shown in Fig. 9.4, at a fixed value of $q^2 = 15$ GeV². For illustration, we use here the VMD FF parametrization. As mentioned above, the effect of the mass changes the stiffness of the angular dependence of the differential cross section as a function of $\cos\theta$, as illustrated in Fig. 9.4 (left), for $q^2 = 15$ GeV². For τ -leptons, the relative contribution of the electric to magnetic term is larger. In other words, the effect of the mass changes the slope

and the intercept of the linear dependence of the differential cross section as a function of $\cos^2 \theta$, as illustrated in Fig. 9.4 (right).

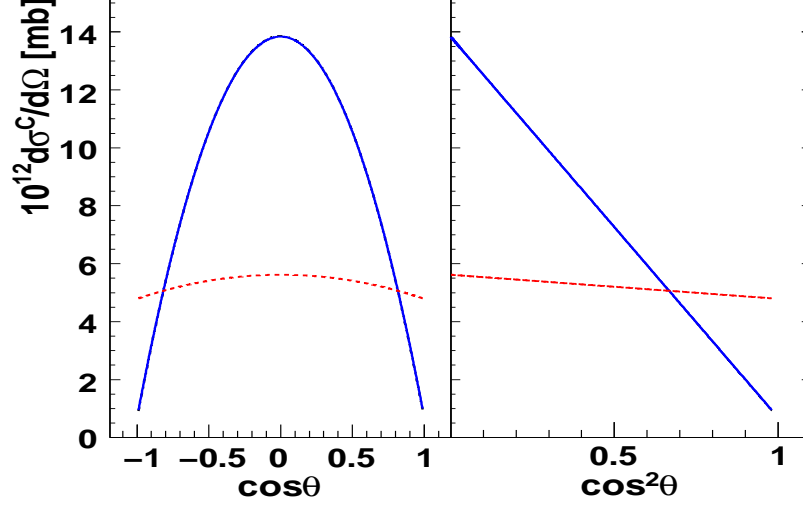


Figure 9.4: Differential cross section as a function of $\cos \theta$ (left) and $\cos^2 \theta$ (right) for $q^2=15 \text{ GeV}^2$, assuming the VMD FF parametrization [165], for $\ell = \tau$ (red dashed line), $\ell = \mu$ (blue solid line). The calculation for $\ell = e$ (black dotted-dashed line) is hardly visible since it overlaps with the μ line.

The q^2 dependence of the single spin asymmetry, as well of the triple polarization observables and of some double spin observables, is driven by the term $\text{Im} G_M G_E^*$ (besides simple kinematical coefficients); therefore it will constitute a direct test of nucleon models. The single spin asymmetry has been calculated for e , μ and τ lepton pair production, at $q^2 = 15 \text{ GeV}^2$, for the VMD FF parametrization in CMS and it is represented in Fig. 9.5 (left). It is very small for τ lepton, whereas for μ and e it exhibits a strong forward backward angular asymmetry.

To illustrate the effect of the FF parametrization, the CMS ratio of the analyzing powers A_{yy}^C/A_{xx}^C as a function of the total energy, Eq. 9.32, is shown in Fig. 9.5 (right) for $\cos \theta = 0.5$. The lines corresponding to e overlap with μ in the considered range. The parametrization [165] (thin lines) predicts a large ratio of FFs in this region, whereas for pQCD (thick lines), the FF ratio is equal to one. This difference is particularly enhanced in this specific analyzing power ratio.

The non-vanishing double spin observables are shown in Fig. 9.6 for the VMD parametrization from Ref. [165] as a function of $\cos \theta$ in CMS for $q^2 = 15 \text{ GeV}^2$. From top to bottom, from left to right are illustrated: the polarization transfer coefficients, $T_{\ell x}^C, T_{\ell z}^C, T_{ny}^C, T_{tx}^C, T_{tz}^C$, the analyzing powers in polarized proton-antiproton collisions $A_{xx}^C, A_{yy}^C, A_{zz}^C, A_{xz}^C$, and the correlation coefficients when the polarization of the lepton-antilepton pair is measured: $C_{nn}^C, C_{tt}^C, C_{\ell\ell}^C, C_{\ell t}^C$. Note that A_{yy}^C coincides with C_{nn}^C and it is not shown.

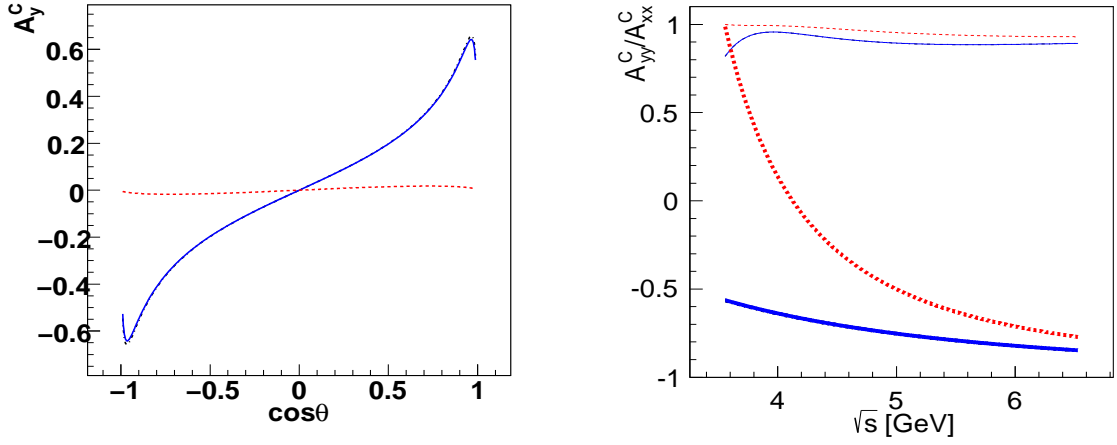


Figure 9.5: (Left) Single spin asymmetry as a function of $\cos \theta$ for $q^2=15 \text{ GeV}^2$, for the parametrization of Ref. [165]. (Right) Ratio of the analyzing powers A_{yy}^C/A_{xx}^C in the CMS as a function of the total energy, with the parametrizations [165] (thin lines) and pQCD (thick lines). Notation as in Fig. 9.4.

The observables are shown in Fig. 9.7 using the pQCD parametrization of the proton FFs assuming $|G_E| = |G_M|$. Note that this pQCD inspired parametrization does not have any imaginary part; therefore some of the observables vanish. From top to bottom, from left to right are illustrated: the polarization transfer coefficients, $T_{\ell z}^C$, T_{tz}^C , the analyzing powers in polarized proton-antiproton collisions A_{xx}^C , A_{yy}^C , A_{zz}^C , and the correlation coefficients when the polarization of the lepton-antilepton pair is measured: C_{nn}^C , C_{tt}^C , $C_{\ell\ell}^C$, $C_{\ell t}^C$.

For the τ -lepton, the effect of the mass is sizable in all the observables. The difference between the μ and e effects is tiny and it is best seen in the observables related to the transverse polarization of one lepton, such as T_{tz} , T_{tz} , T_{ny} , and $C_{\ell t}$. The mass effect is relatively larger when the incident energy is lower and it is independent from the choice of the FF parametrizations.

9.6 Conclusion

The calculation of polarization observables for the annihilation of proton-antiproton into a lepton pair was extended to the case of heavy leptons, such as τ or μ in the one-photon exchange approximation. The expressions of the observables are given in terms of the nucleon electromagnetic FFs. We investigated the dependence on the lepton mass of the unpolarized cross section, of the angular asymmetry and of various polarization observables.

Our results show an enhancement of the polarization observables of these heavy unstable particles, in particular when the transverse polarization of the leptons is con-

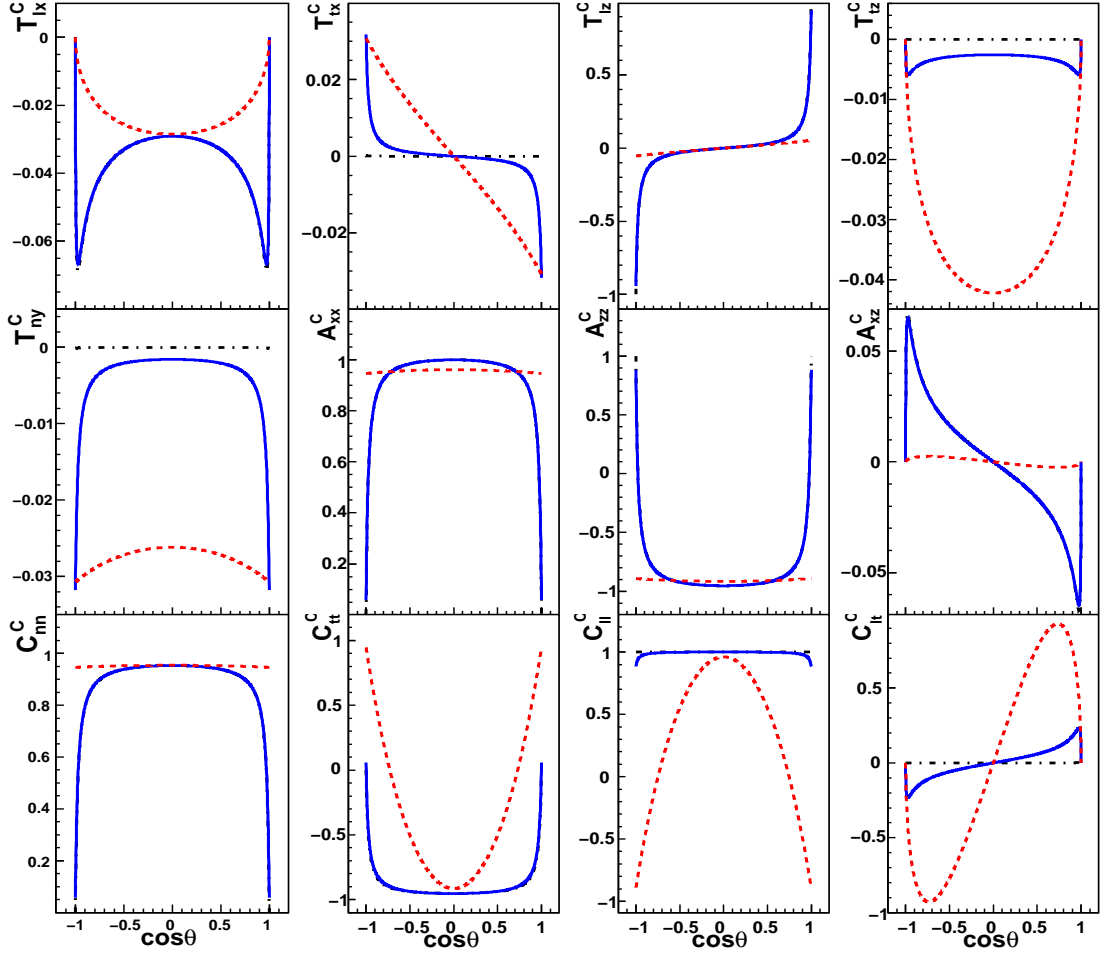


Figure 9.6: Double polarization observables as a function of $\cos \theta$, for $q^2 = 15 \text{ GeV}^2$, using the VMD parametrization from Ref. [165] in CMS. Notation as in Fig. 9.4.

sidered. The polarization measurement of heavy leptons can be done in principle through the angular distribution of its decay products. The feasibility study of TL FF measurements at PANDA using the production of heavy leptons needs to be considered in more details.

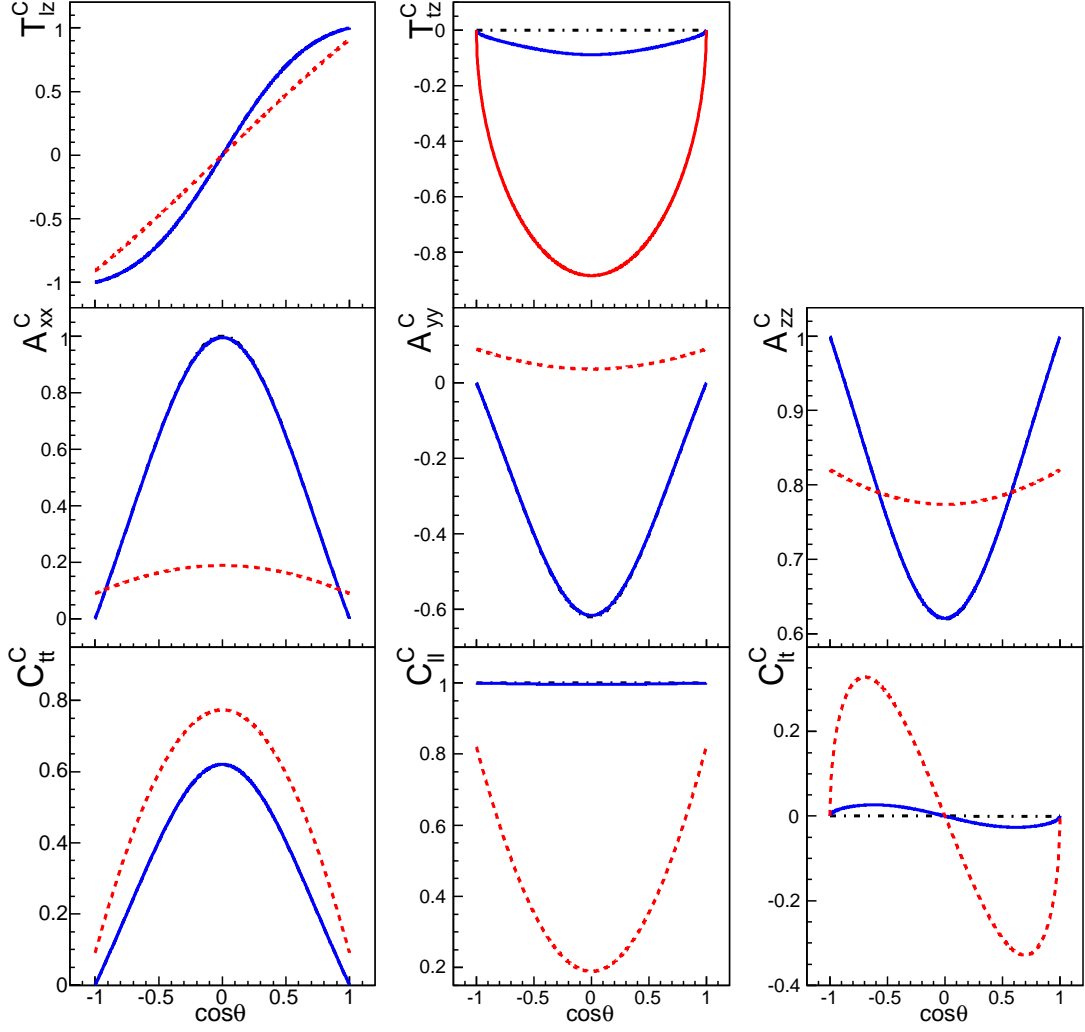


Figure 9.7: Double polarization observables as a function of $\cos\theta$, for $q^2 = 15 \text{ GeV}^2$, using the pQCD parametrization of FFs in CMS. Notation as in Fig. 9.4.

Chapter 10

Conclusions and perspectives

The internal electromagnetic structure of the proton parametrized in terms of electromagnetic FFs, was investigated in this thesis, in view of their measurement at the future PANDA experiment. After an introduction describing the scientific programme and the detector of PANDA, experimental, simulation and phenomenological studies have been considered. Experimental tests for the optical coupling in the PANDA electromagnetic calorimeter, and the corresponding simulation studies within the PANDARoot software have been performed. The annihilation of proton antiproton into leptonic channels which gives access to the electromagnetic TL FFs and the crossing symmetry reactions are described. Original results have been found. They can be summarized as follows:

- Mechanical, thermal, optical properties and radiation hardness of two commercial glues (DC3145 and RT600) have been studied in view of their use for the electromagnetic crystal calorimeter of PANDA which will be operated at low temperature (-25° C). The new aspect of this work was the study of the optical performance of the selected glues at different temperatures in combination with the mechanical strength and the overall radiation hardness. Based on the results of these measurements, the PANDA collaboration chose the glue “DC 3145” for the optical coupling in the EMC as it is a reliable and nearly perfect optical glue even for the unusual and extreme operational conditions in case of PANDA.
- Feasibility studies of measuring proton TL FFs at PANDA have been presented. Realistic Monte Carlo simulations which take into account the geometry, the material budget and the performance of the future detector, as well as tracking efficiency and particle identification have been performed. Background rejection has been studied. The results showed that the proton FF ratio can be measured at the future PANDA experiment through the annihilation reaction $\bar{p}p \rightarrow e^+e^-$ with unprecedented statistical accuracy.
- We have studied the radiative corrections for the reaction of proton antiproton annihilation into an electron pair using the PHOTOS package implemented in

PANDARoot. The precision of the radiative corrections generated by the PHOTOS package with respect to the available analytical calculations was evaluated. It is shown that odd contributions, which are important for the extraction of electromagnetic FFs should be implemented.

- The elastic scattering of protons from electrons at rest was investigated in a relativistic approach in the one photon exchange (Born) approximation. The differential cross section and various double spin polarization observables have been calculated in terms of the nucleon electromagnetic FFs. Numerical estimations showed that polarization effects are sizable in the GeV range. The reaction $p+e \rightarrow p+e$ could be used to polarize and to measure the polarization of high energy proton (antiproton) beams. We have also seen that this reaction, in general all the elastic and inelastic hadron scattering by atomic electrons (which can be considered at rest), is characterized by a small value of the transfer momentum squared Q^2 , even for relatively large energies of colliding hadrons. We illustrated the accessible kinematical range and showed that one could improve by four order of magnitudes the lower limit of Q^2 at which elastic experiments have been done. This may allow precise measurements of the proton radius, decreasing the errors due to the extrapolation to $Q^2 \rightarrow 0$.
- The calculation of polarization observables for the annihilation of proton-antiproton into a lepton pair was extended to the case of heavy leptons, such as μ and τ . In this case it is not possible to neglect the lepton mass. The calculation was performed in the one-photon exchange approximation. The expressions of the observables are given in terms of nucleon electromagnetic FFs. We investigated the dependence on the mass of the lepton of the unpolarized cross section, of the angular asymmetry and various polarization observables. It was shown that the observables related to the transverse polarization of one lepton are enhanced for heavy lepton masses.

The experience from my PhD studies has increased my motivation to continue my career in fundamental research. Having been in close contact with a large experimental collaboration and with theoreticians in this domain, I realize that many questions can be answered by experiments in the near future, in particular, the BESIII/BEPC-II and the FAIR/PANDA experiments.

The simulation studies that I carried out were related to a challenging issue for electromagnetic process measurements at PANDA consisting of the suppression of the huge hadronic background mainly coming from the $\pi^+\pi^-$ production. Other important and fundamental issues, for example the radiative corrections and their effects on the extracted values of the proton FFs, have to be considered in more details.

An important part of my thesis was focused on polarization phenomena in electromagnetic processes. Feasibility studies for a polarized proton target or antiproton beam have started in the laboratories at CERN, Mainz (Germany) and in the United States. The possibility of a transverse polarized proton target for PANDA is actually under

investigation at Mainz. The possibility of accelerating polarized antiproton beams for PANDA is also investigated by the PAX collaboration [151].

Feasibility studies to detect heavy leptons (μ and τ) in proton-antiproton annihilation at the PANDA experiment have started but more realistic simulations are required considering in parallel the improvement of the detection performance of the detectors.

Concerning hadron electromagnetic FFs, several experiments are planned or ongoing in electron accelerators and collider as JLab, Novosibirsk and BES. The main purpose is to reach higher transferred momenta and/or better precisions. In the TL region the individual determination of the electric and magnetic FFs has the highest priority. The measurement of polarization observables which would allow to determine the relative phase of the TL complex FFs represents an essential issue. PANDA will be an ideal detector to measure the TL electromagnetic FFs of the proton.

Appendix A

Lepton nucleon interaction: general formalism

In this appendix, a model independent formalism [167] for the calculation of the experimental observables associated to the elastic lepton nucleon scattering will be considered. The formula derived in this chapter, for unpolarized cross section and polarization observables, hold in any reference system and can be applied to describe:

- elastic scattering of electron beams on proton target,
- elastic scattering of muon beams on proton target,
- elastic scattering of protons on electrons at rest.

Calculations for elastic electron nucleon scattering are usually based on the formalism of A. M. Rosenbluth [57] for the unpolarized cross section and Akhiezer and Rekalo [65] for the polarization observables. In the present case, the mass of the lepton is explicitly taken into account in the calculation; the lepton mass can't be neglected for low energy interacting muons (off a proton) or when the projectile is heavier than the target (inverse kinematics).

The present derivation is limited to the first order of perturbation theory (Born approximation). The Born diagrams can be taken as the starting point of the description of the real physical process because the value of the electromagnetic fine structure constant is small ($\alpha \sim 1/137$).

A.1 The scattering amplitude

At the leading order in α , the lepton (ℓ) proton (p) elastic scattering:

$$\ell(k_1) + p(p_1) \rightarrow \ell(k_2) + p(p_2), \quad (\text{A.1})$$

occurs through the exchange of a single photon.

In Eq. A.1, the particle momenta are indicated in parenthesis and $q = k_1 - k_2 = p_2 - p_1$ is the four-momentum of the exchanged photon.

The scattering amplitude \mathcal{M} is a complex scalar. In Feynman gauge, \mathcal{M} can be written in terms of the electromagnetic current of the lepton (j_{EM}^ℓ), the nucleon (J_{EM}^N) and the photon propagator as:

$$\mathcal{M} \propto J_{EM}^N \frac{1}{q^2} j_{EM}^\ell, \quad (\text{A.2})$$

A.1.1 Leptonic current

The leptonic current, j_{EM}^ℓ , assuming no internal structure for the lepton, can be derived from the Lagrangian density of the QED as:

$$j_{EM}^\ell = \bar{u}(k_2)[-ie\gamma_\mu]u(k_1) = -iej_\mu, \quad (\text{A.3})$$

where $u(k_j)$, $j = 1, 2$ is a four component spinor of free Dirac particle describing the lepton external lines of the Born diagram.

A.1.2 Hadronic current

The structure of the hadronic current is more complicated than the leptonic current due to the complex nature of the nucleon. The Dirac gamma matrices γ_μ describing the electromagnetic interaction point for the leptons should be replaced by a vertex operator which takes into account all of the effects of the internal structure. An expression for the hadronic current can be constructed using the symmetries and properties of the electromagnetic interaction.

A compact expression for the nucleon current, J_{EM}^N , was given by L. L. Foldy [58] and G. Salzman [59], based on the assumptions:

- J_{EM}^N must be relativistically covariant and transforms as a Lorentz four-vector.
- J_{EM}^N should respect the current conservation law expressed in momentum space as $q_\mu J^\mu = 0$; the current should be orthogonal to the momentum transfer q_μ .
- The Dirac equation applies (the nucleon is on shell).

They showed that the general form of the hadronic current is:

$$J_{EM}^N = ie\bar{u}(p_2) \left[F_1(q^2)\gamma_\mu - \frac{1}{2M}F_2(q^2)\sigma_{\mu\nu}q^\nu \right] u(p_1) = ieJ_\mu. \quad (\text{A.4})$$

where the tensor $\sigma_{\mu\nu} = \frac{i}{2}[\gamma_\mu, \gamma_\nu]$. The functions $F_{1,2}(q^2)$ are the Dirac and Pauli FFs which describe the internal structure of the nucleon. In the limit of $q^2 \rightarrow 0$, they converge to the static values of the charge and the anomalous magnetic moment of the nucleon. Other covariant expressions satisfying Foldy's assumptions can be obtained for the nucleon current, however they can always be expressed in the form of Eq. A.4, using the Dirac equation.

A.2 Electromagnetic tensors

The differential cross section is proportional to the square of the scattering amplitude \mathcal{M} :

$$d\sigma \sim |\mathcal{M}|^2 = 16\pi^2 \frac{\alpha^2}{q^4} L_{\mu\nu} H^{\mu\nu}, \text{ with } L_{\mu\nu} = j_\mu j_\nu^*, \quad H^{\mu\nu} = J^\mu J^{\nu*}, \quad (\text{A.5})$$

$L_{\mu\nu}$ and $H_{\mu\nu}$ are called the leptonic and hadronic tensor respectively. The expressions of these tensors depend on the polarization states of the lepton and nucleon (spin 1/2 particles). The density matrix $\rho = u(p)\bar{u}(p)$ for a free Dirac particle of four-momentum p and mass m , taking into account the polarization, can be written as:

$$\rho = u(p)\bar{u}(p) = (\hat{p} + m) \frac{1}{2} (1 - \gamma_5 \hat{s}), \quad \hat{p} = p_\alpha \gamma^\alpha, \quad \hat{s} = s_\beta \gamma^\beta. \quad (\text{A.6})$$

For the case of antiparticles:

$$\rho = v(p)\bar{v}(p) = (\hat{p} - m) \frac{1}{2} (1 - \gamma_5 \hat{s}). \quad (\text{A.7})$$

The polarization four vector s is a pseudo-vector which satisfies $s^2 = -1$ and $s \cdot p = 0$. It is related to the unit vector along the polarization of the particle in its rest system, $\vec{\chi}$ by:

$$s_0 = \frac{\vec{p} \cdot \vec{\chi}}{m}, \quad \vec{s} = \vec{\chi} + \frac{\vec{p}(\vec{p} \cdot \vec{\chi})}{m(m + p_0)}. \quad (\text{A.8})$$

The convention of the definition of the four-vector in the Minkowski spacetime is:

$$p_\mu = (p_0, \vec{p}), \quad \text{and } \hat{p} = \gamma_\mu p^\mu = \gamma_0 p^0 - \vec{\gamma} \vec{p}. \quad (\text{A.9})$$

When $\vec{\chi}$ and \vec{p} are parallel (or anti-parallel), the particle is longitudinally polarized, and when they are orthogonal, the particle is transversally polarized. Normal polarization is obtained when $\vec{\chi}$ is normal to the scattering plane.

Eq. A.8 shows that the transverse or the normal polarization vector does not change whenever expressed in the particle rest frame, in the Lab frame or in other reference systems.

A.2.1 Leptonic tensor

The leptonic tensor for unpolarized initial and final leptons (averaging over the initial lepton spin) can be expressed in the form of traces as:

$$L_{\mu\nu}^0 = \frac{1}{2} \text{Tr}[(\hat{k}_2 + m) \gamma_\mu (\hat{k}_1 + m) \gamma_\nu] = q^2 g_{\mu\nu} + 2(k_{1\mu} k_{2\nu} + k_{1\nu} k_{2\mu}), \quad (\text{A.10})$$

where $g_{\mu\nu}$ is the metric tensor of the Minkowski spacetime.

The contribution to the leptonic tensor when the lepton is polarized, is determined by:

$$L_{\mu\nu}(S_i) = 2im \epsilon_{\mu\nu\alpha\beta} q^\alpha S_i^\beta, \quad (\text{A.11})$$

where S_i^β is the polarization four-vector for initial ($i = 1$), or outgoing ($i = 2$) lepton, and $\epsilon_{\mu\nu\alpha\beta}$ is the antisymmetric tensor with $\epsilon_{0123} = 1$.

A.2.2 Hadronic tensor

The hadronic tensor for unpolarized initial and final nucleon can be calculated in a similar way as for the lepton, using:

$$H_{\mu\nu}^0 = \frac{1}{2} \text{Tr}[(\hat{p}_2 + M)\Gamma_\mu(\hat{p}_1 + M)\Gamma_\nu^*], \quad (\text{A.12})$$

where Γ_μ is the hadronic vertex operator defined by (A.4):

$$\Gamma_\mu = F_1(q^2)\gamma_\mu - \frac{1}{2M}F_2(q^2)\sigma_{\mu\nu}q^\nu. \quad (\text{A.13})$$

Assuming P-invariance of the electromagnetic interactions and the conservation of the (electromagnetic) hadronic current, the hadronic tensor can be written in the standard form, through two unpolarized structure functions, H_1 and H_2 :

$$H_{\mu\nu}^0 = \left(-g_{\mu\nu} + \frac{q_\mu q_\nu}{q^2}\right) H_1(q^2) + P_\mu P_\nu H_2(q^2). \quad (\text{A.14})$$

Averaging over the initial proton spin, the structure functions H_i , $i = 1, 2$, can be expressed in terms of the nucleon electromagnetic FFs as:

$$\begin{aligned} H_1(q^2) &= -q^2 G_M^2(q^2), \\ H_2(q^2) &= 4M^2 \frac{G_E^2(q^2) + \tau G_M^2(q^2)}{1 + \tau}, \end{aligned} \quad (\text{A.15})$$

where $G_E(q^2) = F_1(q^2) - \tau F_2(q^2)$ is the Sachs proton electric FF and $\tau = -q^2/(4M^2)$.

Based on Eq. A.8, the hadronic tensor can be written as a sum of the unpolarized and polarized contributions terms:

$$H_{\mu\nu} = H_{\mu\nu}^0 + H_{\mu\nu}(\eta_j) + H_{\mu\nu}(\eta_1, \eta_2), \quad j = 1, 2, \quad (\text{A.16})$$

where $H_{\mu\nu}(\eta_j)$ is the contributions of the proton polarization to the hadronic tensor:

$$\begin{aligned} H_{\mu\nu}(\eta_j) &= -2iG_M(q^2)[MG_M(q^2)\epsilon_{\mu\nu\alpha\beta}q^\alpha\eta_j^\beta \\ &\quad + F_2(q^2)(P_\mu\epsilon_{\nu\alpha\beta\gamma} - P_\nu\epsilon_{\mu\alpha\beta\gamma})p_1^\alpha p_2^\beta \eta_j^\gamma], \end{aligned} \quad (\text{A.17})$$

and the four-vector η_j stands for the initial ($j = 1$) or final ($j = 2$) proton polarization.

The part of the hadronic tensor which corresponds to polarized protons in initial and final states, $H_{\mu\nu}(\eta_1, \eta_2)$, can be written as

$$\begin{aligned} H_{\mu\nu}(\eta_1, \eta_2) &= A_1\tilde{g}_{\mu\nu} + A_2P_\mu P_\nu + A_3(\tilde{\eta}_{1\mu}\tilde{\eta}_{2\nu} + \tilde{\eta}_{1\nu}\tilde{\eta}_{2\mu}) + A_4(P_\mu\tilde{\eta}_{1\nu} + P_\nu\tilde{\eta}_{1\mu}) \\ &\quad + A_5(P_\mu\tilde{\eta}_{2\nu} + P_\nu\tilde{\eta}_{2\mu}), \end{aligned} \quad (\text{A.18})$$

where

$$\tilde{g}_{\mu\nu} = g_{\mu\nu} - \frac{q_\mu q_\nu}{q^2}, \quad \tilde{\eta}_{i\mu} = \eta_{i\mu} - \frac{q \cdot \eta_i}{q^2} q_\mu, \quad i = 1, 2,$$

and A_i are written in terms of FFs as:

$$\begin{aligned} A_1 &= \frac{G_M^2}{2}(2q \cdot \eta_1 q \cdot \eta_2 - q^2 \eta_1 \cdot \eta_2), \quad A_2 = -\eta_1 \cdot \eta_2 \frac{2M^2}{1+\tau}(G_E^2(q^2) + \tau G_M^2(q^2)), \\ A_3 &= G_M^2(q^2) \frac{q^2}{2}, \quad A_4 = -MG_M(q^2) \frac{G_E(q^2) + \tau G_M(q^2)}{1+\tau} q \cdot \eta_2, \\ A_5 &= MG_M(q^2) \frac{G_E(q^2) + \tau G_M(q^2)}{1+\tau} q \cdot \eta_1. \end{aligned}$$

A.3 Polarized and unpolarized cross section

The cross section characterizes the probability that a given process occurs. The cross section is the proportionality constant between the number of final particles (N_f) issued from a definite reaction and the number of incident particles (N_i) and target particles (N_t). The cross section can be also viewed as the effective area seen by the incident particle.

In a relativistic approach, the differential cross section for any binary processes can be written in terms of the corresponding matrix element squared $|\mathcal{M}|^2$, the flux of colliding particles \mathcal{I} , and the phase space of the final particles $d\mathcal{P}$:

$$\begin{aligned} d\sigma &= \frac{|\mathcal{M}|^2}{\mathcal{I}} (2\pi)^4 \delta^4(k_1 + p_1 - k_2 - p_2) d\mathcal{P}, \\ \mathcal{I} &= 4\sqrt{(k_1 \cdot p_1)^2 - m^2 M^2}, \quad d\mathcal{P} = \frac{d^3 \vec{k}_2}{(2\pi)^3 2\epsilon_2} \frac{d^3 \vec{p}_2}{(2\pi)^3 2E_2}, \end{aligned} \quad (\text{A.19})$$

where \vec{p}_2 , E_2 (\vec{k}_2 , ϵ_2) are the momentum and energy of the final proton (lepton) respectively.

The expression of the differential cross section for unpolarized lepton-proton scattering is obtained from the square of the scattering amplitude by the contraction of the unpolarized leptonic and hadronic tensors ($H_{\mu\nu}^0(L^0)^{\mu\nu}$). The other terms in $H_{\mu\nu}$ and $L_{\mu\nu}$ lead to the expressions of polarized cross section.

The simplest polarization experiment is the polarization measurement of one of the scattered particles in unpolarized beam and target scattering, or the scattering of a polarized (unpolarized) beam on unpolarized (polarized) target without measurement of final state polarization. These experiments allow the measurement of single spin observables which are proportional to the imaginary part of the nucleon FFs ($Im F_1 F_2^*$). In the SL region, assuming the one photon exchange, FFs are real functions and the single spin observables vanish.

A.3.1 Polarization transfer coefficients $T_{ab}(S_i, \eta_j)$

The polarization transfer coefficients are double spin observables and describe the polarization transfer from a polarized target to the ejectile. The transfer coefficients are

obtained by contraction of the spin-dependent leptonic tensor $L_{\mu\nu}(S_i)$ (Eq. A.10), and the spin-dependent hadronic tensor $H_{\mu\nu}(\eta_i)$ (Eq. A.17):

$$\begin{aligned} \mathcal{D}T_{ab}(S_i, \eta_j) &= 4mMG_M(q^2)[G_E(q^2)(q \cdot S_i q \cdot \eta_j - q^2 S \cdot \eta_j) \\ &\quad - q^2 F_2(q^2)P \cdot S_i P \cdot \eta_j], \end{aligned} \quad (\text{A.20})$$

where $\mathcal{D} = H_{\mu\nu}^0(L^0)^{\mu\nu}/2$. The indices a, b can be n (normal), t (transverse), and l (longitudinal), according to the direction of the polarization vectors of each particle. The transfer polarized cross sections are defined as the product of the unpolarized cross section and the polarization transfer coefficients.

A.3.2 Polarization correlation coefficients $C_{ab}(S_1, \eta_1)$

In the reaction involving a polarized beam and a polarized target (initial lepton and nucleon are polarized), one can derive the expressions for the spin correlation coefficients through the contraction of the spin-dependent leptonic $L_{\mu\nu}(S_1)$ and hadronic $H_{\mu\nu}(\eta_1)$ terms:

$$\begin{aligned} \mathcal{D}C_{ab}(S_1, \eta_1) &= 8mMG_M(q^2)[(q \cdot S_1 q \cdot \eta_1 - q^2 S_1 \cdot \eta_1)G_E(q^2) \\ &\quad + \tau q \cdot \eta_1(q \cdot S_1 + 2p_1 \cdot S_1)F_2(q^2)]. \end{aligned} \quad (\text{A.21})$$

These coefficients are called also double analyzing powers. In the present case, the polarized cross sections are defined as the product of the unpolarized cross section and the analyzing power coefficients.

When the equations derived in this chapter are applied to elastic proton scattering on electron target, in the limit of lepton mass equal to zero, one obtains the expressions of the Rosenbluth unpolarized cross section [57] and of the polarization observables [65].

Appendix B

Polarization observables for the elastic proton electron scattering

B.1 Polarization transfer coefficients, T_{ij} , for $p + \vec{e} \rightarrow \vec{p} + e$

The explicit expressions for the polarization transfer coefficients for $p + \vec{e} \rightarrow \vec{p} + e$ are:

$$\begin{aligned}
\mathcal{D}T_{nn} &= 4mMq^2G_EG_M, \\
\mathcal{D}T_{tt} &= 4mMq^2\frac{G_M}{1+\tau}\left\{(1+\tau)G_E - \left(E+M+\frac{q^2}{2m}\right)^{-1}\left(1-\frac{q^2}{q_{max}^2}\right)\right. \\
&\quad \left.[(E_1+M+2E_1\tau)G_E - \tau(E_1+M+2M\tau)G_M]\right\}, \\
\mathcal{D}T_{t\ell} &= -2m|\vec{p}|q^2\frac{G_M}{1+\tau}\left(E_1+M+\frac{q^2}{2m}\right)^{-1}\left[-q^2\left(1-\frac{q^2}{q_{max}^2}\right)\right]^{1/2} \\
&\quad \left\{\frac{M}{m}\frac{m+M}{E-M}[(1+2\tau)G_E - \tau G_M] + \right. \\
&\quad \left.\left(1-2m\frac{E_1+m}{s}\frac{q^2}{q_{max}^2}\right)[G_E + \tau G_M]\right\}, \\
\mathcal{D}T_{\ell t} &= -4m|\vec{p}|q^2\frac{G_M}{1+\tau}\left(E_1+M+\frac{q^2}{2m}\right)^{-1}\left[-q^2\left(1-\frac{q^2}{q_{max}^2}\right)\right]^{1/2} \\
&\quad \left\{(1+\tau)G_M + \frac{E_1-M}{2M}[G_M - G_E] \right. \\
&\quad \left. - m\frac{E_1+m}{s}\frac{1}{q_{max}^2}[q^2(G_E + \tau G_M) + \right. \\
&\quad \left. 2M(E_1+M)(G_E(1+2\tau) - \tau G_M)]\right\}, \tag{B.1}
\end{aligned}$$

$$\begin{aligned}
\mathcal{DT}_{\ell\ell} = & 4mMq^2 \frac{G_M}{1+\tau} \left\{ (1+\tau) \left[\frac{E_1}{M} + \frac{xq^2}{2m}(E_1 + M + 2m) - \right. \right. \\
& \frac{(E_1 + m)^2}{s} \frac{q^2}{q_{max}^2} \left(1 + \frac{xq^2}{2m}(m - M) \right) + \frac{1}{s}(m + M)(E_1 + m)x\vec{p}^2 \frac{q^2}{q_{max}^2} \left. \right] G_E \\
& + \tau \left[x\vec{p}^2 \frac{M + m}{m} \left(1 - 3 \frac{m(E_1 + m)}{s} \frac{q^2}{q_{max}^2} \right) + \right. \\
& \left. \frac{(E_1 + m)^2}{s} \frac{q^2}{q_{max}^2} \left(1 - \frac{xq^2}{2m}(m + M) \right) - \frac{E_1 + m}{m} \right] [G_M - G_E] \left. \right\}, \quad (\text{B.2})
\end{aligned}$$

with $\tau = -q^2/(4M^2)$, $x^{-1} = M(E_1 + M + \frac{q^2}{2m})$, and $s = m^2 + M^2 + 2mE_1$ is the total energy in the proton electron elastic scattering.

B.2 Polarization correlation coefficients, C_{ij} , for $\vec{p} + \vec{e} \rightarrow p + e$

The explicit expressions of the spin correlation coefficients, as a function of the Sachs FFs can be written as:

$$\begin{aligned}
\mathcal{DC}_{nn} &= 4mMq^2 G_E G_M, \\
\mathcal{DC}_{tt} &= 4mM\tau q^2 \frac{G_M}{1+\tau} \left[\left(1 - \frac{4M^2}{q_{max}^2} \right) G_E + \left(\frac{q^2}{q_{max}^2} - 1 \right) G_M \right], \\
\mathcal{DC}_{t\ell} &= 8mM|\vec{p}| \left[-q^2 \left(1 - \frac{q^2}{q_{max}^2} \right) \right]^{1/2} \frac{G_M}{1+\tau} \left\{ \tau [G_M - G_E] \right. \\
& \quad \left. - \frac{q^2}{q_{max}^2} \frac{m(E_1 + m)}{s} [\tau G_M + G_E] \right\}, \\
\mathcal{DC}_{\ell t} &= -2mM \frac{q^2}{|\vec{p}|} \left(\frac{E_1}{M} - \frac{M}{m} \right) \left[-q^2 \left(1 - \frac{q^2}{q_{max}^2} \right) \right]^{1/2} \frac{G_M}{1+\tau} [\tau G_M + G_E], \\
\mathcal{DC}_{\ell\ell} &= 4q^2 \frac{G_M}{1+\tau} \left\{ (mE_1 - \tau M^2) G_E + \tau (M^2 + mE_1) G_M \right. \\
& \quad \left. - (M^2 + mE_1) \frac{q^2}{q_{max}^2} \frac{m(E_1 + m)}{s} [\tau G_M + G_E] \right\}. \quad (\text{B.3})
\end{aligned}$$

Appendix C

Acronyms

Alice Environment	AliEn
antiProton ANnihilation at DArmstadt	PANDA
Antiproton Decelerator	AD
Avalanche Photo Diode	APD
Center of Mass System	CMS
Central Processing Units	CPUs
Compact Muon Solenoid	CMS
Compressed Baryonic Matter	CBM
Deep Virtual Compton Scattering	DVCS
Detection of Internally Reflected Cherenkov	DIRC
Drell-Yan	DY
Dual Parton Model	DPM
Dynamical Selection Rules	DSRs
Electromagnetic Calorimeter	EMC
Facility for Antiprotons and Ion Research	FAIR
Facility for Low Antiproton and Ion Research	FLAIR
Final State Radiation	FSR
Form Factors	FFs
Forward Tracker	FT
Gas Electron Multiplier	GEM
Generalized Parton Distributions	GPDs
High Energy Storage Ring	HESR
Jefferson Laboratory	JLab
Laboratory	Lab
Large Area Avalanche Photo Diodes	LAAPDs

Lead-tungstate	PWO
Leading Logarithmic	LL
Low Energy Antiproton Ring	LEAR
Mainz Microtron	MAMI
Micro-Channel Plate Photo-Multiplier Tubes	MCP PMTs
Micro Vertex Detector	MVD
New Experimental Storage Ring	NESR
Particle IDentification	PID
Paul Scherrer Institut	PSI
perturbative Quantum ChromoDynamics	pQCD
Polarized Antiproton eXperiments	PAX
Quantum ChromoDynamics	QCD
Quantum ElectroDynamics	QED
Radiative corrections	RC
Relativistic Heavy-Ion Collider	RHIC
root mean square	rms
Space-Like	SL
Straw Tube Tracker	STT
Time-Like	TL
Time Of Flight	TOF
Transition Distribution Amplitudes	TDAs
Ultra relativistic Quantum Molecular Dynamics	UrQMD
UNIversal Linear ACcelerator	UNILAC
Vacuum Photo-Triodes	VPTs
Vector Meson Dominance	VMD
Wide Angle Compton Scattering	WACS

Appendix D

List of publications

D.1 Journal Articles

1. A. Dbeyssi, E. Tomasi-Gustafsson, G. I. Gakh and M. Konchatnyi,
Proton-antiproton annihilation into massive leptons,
Nucl. Phys. A **894** (2012) 20.
2. A. Dbeyssi, E. Tomasi-Gustafsson, G. I. Gakh and C. Adamuscin,
Experimental constraint on the ρ^- meson form factors in the time-like region,
Phys. Rev. C **85**, 048201 (2012).
3. A. Dbeyssi *et al.*,
Tests of optical glues for the PANDA electromagnetic calorimeter,
Nucl. Instrum. Meth. A **722**, 82-86 (2013).
4. G. I. Gakh, A. Dbeyssi, E. Tomasi-Gustafsson, D. Marchand and V. V. Bytev,
Proton electron elastic scattering and the proton charge radius,
arXiv:1201.2572 [nucl-th].
5. E. A. Kuraev, E. Tomasi-Gustafsson and A. Dbeyssi,
A model for space and time-like proton (neutron) form factors,
Phys. Lett. B **712**, 240 (2012).
6. G. I. Gakh, A. Dbeyssi, D. Marchand, E. Tomasi-Gustafsson and V. V. Bytev,
Polarization effects in elastic proton-electron scattering,
Phys. Rev. C **84**, 015212 (2011)
7. G. I. Gakh, E. Tomasi-Gustafsson, A. Dbeyssi and A. G. Gakh,
General analysis and numerical estimations of polarization observables in $\bar{N} + N \rightarrow \pi + e^+ + e^-$ reaction in an exclusive experimental setup,
Phys. Rev. C **86**, 025204 (2012)
8. E. A. Kuraev, Y. .M. Bystritskiy, V. V. Bytev, E. Tomasi-Gustafsson, A. Dbeyssi
and E. Tomasi-Gustafsson,

Annihilation of $\bar{p} + p \rightarrow e^+ + e^- + \pi^0$ and $\bar{p} + p \rightarrow \gamma + \pi^0$ through ω -meson intermediate state, J. Exp. Theor. Phys. **115**, 93 (2012)

9. PANDA Collaboration,

Technical design report for the PANDA (AntiProton Annihilations at Darmstadt) Straw Tube Tracker,

Eur. Phys. J. A **49**, 25 (2013).

D.2 Proceedings

1. A. Dbeyssi [PANDA Collaboration],

“Time-like proton form factors and heavy lepton production at PANDA,”
PoS QNP **2012**, 062 (2012).

2. A. Dbeyssi and E. Tomasi-Gustafsson,

“Classification of anti- $p + p$ induced reactions,”
Prob. Atomic Sci. Technol. **2012N1**, 84 (2012).

3. G. I. Gakh, A. Dbeyssi, D. Marchand, V. V. Bytev and E. Tomasi-Gustafsson,

“Polarization effects in elastic proton-electron scattering,”
Prob. Atomic Sci. Technol. **2012N1**, 79 (2012).

4. A. Dbeyssi [PANDA Collaboration],

“Hadron Electromagnetic Form Factors In Time-Like Region,”
PoS ConfinementX (2012) 289.

Bibliography

- [1] P. A. M. Dirac, Proc. Roy. Soc. (London) A126 (1930) 360-365 and Nobel Lecture, 1933.
- [2] C. D. Anderson, Phys. Rev. 43 (1933) 491.
- [3] O. Chamberlain, E. Segré, C. Wiegand and T. Ypsilantis, Phys. Rev. 100 (1955) 947.
- [4] B. Cork, G. R. Lambertson, O. Piccioni and W. A. Wenzel, Phys. Rev. 104 (1957) 1193.
- [5] R. Armenteros and B. French, High Energy Physics (ed. E.H.S. Burhop, Academic Press, New York), Vol. 4 (1969) 237-417.
- [6] LEAR webpage:
<http://home.web.cern.ch/about/accelerators/low-energy-antiproton-ring>.
- [7] E. Klempt, *et al.*, Phys. Rep. 368 (2002) 119.
- [8] The Antiproton Decelerator webpage:
<http://home.web.cern.ch/about/accelerators/antiproton-decelerator>.
- [9] T. Eriksson, Proc. LEAP05 Conf., AIP Conf Proc. 796 (2005) 389.
- [10] G. Garzoglio *et al.* [E835 Collaboration], Nucl. Instrum. Meth. A 519 (2004) 558.
- [11] T. A. Armstrong *et al.* [E835 Collaboration], Phys. Rev. D 47 (1993) 772.
- [12] D. P. Grosnick *et al.*, [FNAL-E581/704 Collaboration], Nucl. Instrum. Meth. A 290 (1990) 269.
- [13] A. Bravar *et al.*, Phys. Rev. Lett. 77 (1996) 2626.
- [14] FAIR Baseline Technical Report, GSI, 2006. Webpage:
<http://www.fair-center.eu>
- [15] NuSTAR collaboration,
http://www.gsi.de/forschung/fair_experiments/NUSTAR/projects_e.html.

BIBLIOGRAPHY

- [16] APPA collaboration,
<http://www.fair-center.org/APPA-Physics.187.0.html>.
- [17] CBM collaboration,
http://www.gsi.de/forschung/fair_experiments/CBM/1intro_e.html.
- [18] Physics Performance Report for PANDA: “ Strong Interaction Studies with Antiprotons”, The PANDA Collaboration, arXiv:0903.3905 [hep-ex], 2009.
(<http://www-panda.gsi.de/>)
- [19] C. B. Dover, T. Gutsche, M. Maruyama and A. Faessler, Prog. Part. Nucl. Phys. 29 (1992) 87.
- [20] K. Nakamura *et al.* (Particle Data Group), J. Phys. G 37 (2010) 075021,
<http://pdg.lbl.gov/>.
- [21] J. E. Enstrom *et al.*, PDG Compilation LBL-58 (1972).
- [22] <http://durpdg.dur.ac.uk/HEPDATA/>.
- [23] V. Uzhinsky *et al.*, Phys. Lett. B 705 (2011) 235 (2011).
- [24] A. A. Arkhipov, arXiv:hep-ph/9911533.
- [25] A. A. Arkhipov, arXiv:hep-ph/9909531.
- [26] A. B. Kaidalov and K. A. Ter-Martirosyan, Sov. J. Nucl. Phys. 40 (1984) 135 and Yad. Fiz. 40 (1984) 211.
- [27] A. Dbeyssi and E. Tomasi-Gustafsson, Prob. Atomic Sci. Technol. 2012N1 (2012) 84. A. Dbeyssi and E. Tomasi-Gustafsson, http://www-panda.gsi.de/db/notesDBr/AD12-121213_report-cross-sectionsPbarp.pdf
- [28] E. Fermi, Prog. Theor. Phys. 5 No. 4 (1950) 570-583.
- [29] P. Gregory *et al.*, Nucl. Phys. B (1976) 102 189.
- [30] R. Stenbacka *et al.*, Nuovo Cim. A 51 (1979) 63.
- [31] E. A. Kuraev, E. Tomasi-Gustafsson, Phys. Rev. D 81 (2010) 017501.
- [32] M. Kohno, W. Weise, Nucl. Phys. A 454 (1986) 429 .
- [33] J. Van de Wiele and S. Ong, Eur. Phys. J. A 46 (2010) 291.
- [34] BABAR collaboration, <http://www.slac.stanford.edu/BF/>
- [35] BELLE collaboration, <http://belle.kek.jp/>
- [36] BESIII collaboration, <http://bes3.ihep.ac.cn/index.htm>

- [37] Fermilab E835 webpage: <http://www.e835.to.infn.it/>.
- [38] M. Ablikim *et al.*, [BESIII Collaboration], Phys. Rev. Lett. 110 (2013) 252001.
- [39] R. Mizuk *et al.*, [Belle Collaboration], Phys. Rev. D 78 (2008) 072004.
- [40] R. Mizuk *et al.*, [Belle Collaboration], Phys. Rev. D 80 (2009) 031104(R).
- [41] M. Sudol *et al.*, Eur. Phys. J. A 44 (2010) 373.
- [42] A. V. Radyushkin, Phys. Part. Nucl. 44 (2013) 469.
- [43] A. Freund, A. V. Radyushkin, A. Schafer and C. Weiss, Phys. Rev. Lett. 90 (2003) 092001.
- [44] B. Pire and L. Szymanowski, Phys. Rev. D 71 (2005) 111501.
- [45] J. P. Lansberg, Phys. Rev. D 76 (2007) 111502.
- [46] R. L. Jaffe, Phys. Rev. Lett. 38 (1977) 195 [Erratum-ibid. 38 (1977) 617].
- [47] E. Rutherford, Philosophical Magazine Series 6, vol. 21 (1911) 669-688.
- [48] N. F. Mott: Proc. Roy. Soc. (London) A 124 (1929) 425.
- [49] W. A. McKinley, Jr., and H. Feshbach, Phys. Rev. 74 (1948) 1759.
- [50] H. Feshbach, Phys. Rev. 88 (1952) 295.
- [51] E. Guth, Anz. Akad. Wiss. Wien, Math.-Naturw. Kl., 24 (1934) 299.
- [52] M. E. Rose, Phys. Rev. 73 (1948) 279.
- [53] Ferrara International School Niccolò Cabeo, proceeding 2010,
<http://www.fe.infn.it/cabeo-school/>.
- [54] J. H. Smith, Ph.D. thesis, Cornell University, February 1951.
- [55] R. Hofstadter, Rev. Mod. Phys., 28 (1956) 214.
- [56] O. Stern. Nature, 132-103, 1933.
- [57] M. N. Rosenbluth, Phys. Rev. 79 (1950) 615-619.
- [58] L. L. Foldy, Phys. Rev. 87 (1952) 688.
- [59] G. Salzman, Phys. Rev. 99 (1955) 973.
- [60] D. R. Yennie, R. N. Wilson, and D. G. Ravenhall, Rev. Mod. Phys., 29 (1957) 144.

BIBLIOGRAPHY

- [61] G. F. Chew, R. Karplus, S. Gasiorowicz, and F. Zachariasen, Phys. Rev. 110, (1958) 265 ;
- [62] L. E. Phragmén, and E. Lindelöf, Acta Math. 31, 381 (1908); E. C. Titchmarsh, The Theory of Functions (Oxford University Press, London, 1939).
- [63] F. J. Ernst, R. G. Sachs and K. C. Wali, Phys. Rev. 119 (1960) 1105.
- [64] C. F. Perdrisat, V. Punjabi and M. Vanderhaeghen, Prog. Part. Nucl. Phys. 59 (2007) 694 [hep-ph/0612014].
- [65] A. Akhiezer, and M. Rekalov, Sov. Phys. Dokl. 13 (1968) 572 [Dokl. Akad. Nauk Ser. Fiz. 180 (1968) 1081].
- [66] A. Akhiezer, and M. Rekalov, Sov. Phys. Dokl. 4 (1974) 277 [Fiz. Elem. Chast. Atom. Yadra 4 (1973) 662].
- [67] A. J. R. Puckett, *et al.*, Phys. Rev. Lett. 104 (2010) 242301 and Refs therein.
- [68] L. Andivahis, *et al.*, Phys. Rev. D 50 (1994) 5491.
- [69] M. E. Christy *et al.*, Phys. Rev. C 70 (2004) 015206.
- [70] I. A. Qattan, J. Arrington, R. E. Segel, X. Zheng, K. Aniol, O. K. Baker, R. Beams and E. J. Brash *et al.*, Phys. Rev. Lett. 94 (2005) 142301.
- [71] M. K. Jones *et al.*, [Jefferson Lab Hall A Collaboration], Phys. Rev. Lett. 84 (2000) 1398.
- [72] O. Gayou *et al.* [Jefferson Lab Hall A Collaboration], Phys. Rev. Lett. 88 (2002) 092301.
- [73] M. Meziane *et al.*, Phys. Rev. Lett. 106 (2011) 132501.
- [74] A. J. R. Puckett *et al.*, Phys. Rev. C 85 (2012) 045203.
- [75] A. Zichichi, S. M. Berman, N. Cabibbo, R. Gatto, Nuovo Cim. 24 (1962) 170.
- [76] M. P. Rekalov, Sov. J. Nucl. Phys. 1 (1965) 760 .
- [77] G. Bardin *et al.*, Nucl. Phys. B 411 (1994) 3.
- [78] J. P. Lees *et al.*, [BaBar Collaboration], arXiv:1302.0055 [hep-ex], 2013.
- [79] M. Ambrogiani *et al.* [E835 Collaboration], Phys. Rev. D 60 (1999) 032002.
- [80] A. Antonelli *et al.*, Nucl. Phys. B 517 (1998) 3.
- [81] C. Adamuscin, E. A. Kuraev, E. Tomasi-Gustafsson and F. E. Maas, Phys. Rev. C 75 (2007) 045205.

- [82] E. A. Kuraev, Y. M. Bystritskiy, V. V. Bytev, A. Dbeyssi and E. Tomasi-Gustafsson, J. Exp. Theor. Phys. 115 (2012) 93.
- [83] G. I. Gakh, E. Tomasi-Gustafsson, A. Dbeyssi and A. G. Gakh, Phys. Rev. C 86 (2012) 025204.
- [84] J. Boucher, PhD thesis, 2011,
http://www-panda.gsi.de/db/thesesDBr/JB14-111219_thesis_J-Boucher.pdf.
- [85] M. C. Mora Espi, PhD thesis, 2012,
http://www-panda.gsi.de/db/thesesDBr/MC22-121120_MCMoraEspi_Thesis.pdf.
- [86] F. Iachello, A. D. Jackson and A. Lande, Phys. Lett. B 43 (1973) 191.
- [87] W. R. Frazer and J. R. Fulco, Phys. Rev. 117 (1960) 1609.
- [88] G. J. Gounaris and J. J. Sakurai, Phys. Rev. Lett. 21 (1968) 244.
- [89] F. Iachello and Q. Wan, Phys. Rev. C 69 (2004) 055204.
- [90] E. Tomasi-Gustafsson, G. I. Gakh and C. Adamuscin, Phys. Rev. C **73**, 045204 (2006).
- [91] C. Adamuscin, G. Gakh, and E. Tomasi-Gustafsson, Phys. Rev. C 75 (2007) 065202.
- [92] J. de Melo, and T. Frederico, Phys. Rev. C 55 (1997) 2043.
- [93] B. Aubert, *et al.*, Phys. Rev. D 78 (2008) 071103.
- [94] A. Dbeyssi, E. Tomasi-Gustafsson, G. Gakh, and C. Adamuscin, Phys. Rev. C 85 (2012) 048201.
- [95] V. A. Matveev, R. M. Muradian, and A. N. Tavkhelidze, Lett. Nuovo Cim. 7 (1973) 719.
- [96] S. J. Brodsky and G. R. Farrar, Phys. Rev. Lett. 31 (1973) 1153.
- [97] E. A. Kuraev, E. Tomasi-Gustafsson and A. Dbeyssi, Phys. Lett. B 712 (2012) 240.
- [98] R. Baldini, S. Pacetti, A. Zallo, A. Zichichi, Eur. Phys. J. A 39 (2009) 315.
- [99] W. Erni *et al.*, [PANDA Collaboration], “Technical Design Report for the PANDA Solenoid and Dipole Spectrometer Magnets”, arXiv:0907.0169 [physics.ins-det], 2009.
- [100] W. Erni *et al.*, [PANDA Collaboration], “Technical Design Report for the: PANDA Micro Vertex Detector”, arXiv:1207.6581 [physics.ins-det], 2011.

BIBLIOGRAPHY

- [101] W. Erni *et al.*, [PANDA Collaboration], “Technical design report for the PANDA Straw Tube Tracker”, Eur. Phys. J. A 49 (2013) 25.
- [102] W. Erni *et al.*, [PANDA Collaboration], “Technical Design Report for PANDA Electromagnetic Calorimeter (EMC)”, arXiv:0810.1216v1 [physics.ins-det], 2008.
- [103] M. J. Berger and S. M. Seltzer, Tables of Energy Losses and Ranges of Electrons and Positrons, National Aeronautics and Space Administration Report, NASA-SP-3012 (Washington DC 1964).
- [104] J. Beringer *et al.*, Phys. Rev. D 86 (2012) 010001, p. 320.
http://pdg.lbl.gov/2012/html/computer_read.html.
- [105] F. X. Girod *et al.* [CLAS Collaboration], Phys. Rev. Lett. 100 (2008) 162002
- [106] I. Dafinei *et al.*, Mat. Res. Soc. Symp. Proc. 348 (1994) 99.
- [107] M. Kavatsyuk *et al.* [PANDA Collaboration], Nucl. Instrum. Meth. A **648** (2011) 77.
- [108] <http://cms.web.cern.ch/>.
- [109] M. Montecchi and C. H. Q. Ingram, Nucl. Instrum. Meth. A 465 (2001) 329.
- [110] <http://www.dowcorning.com>
- [111] <http://www.wacker.com/cms/en/products-markets/productselector/product-selector.jsp>
- [112] <http://optik.heraeus-quarzglas.de>
- [113] M. Kobayashi, S. Ishimoto, S. Sugimoto and S. Kobayashi, Nucl. Instrum. Meth. A 305 (1991) 401.
- [114] S. Baccaro *et al.*, Nucl. Instrum. Meth. A 406 (1998) 276.
- [115] Technical Progress Report for $\overline{\text{P}}$ ANDA: “Strong Interaction Studies with Antiprotons”, http://www.panda.gsi.de/archive/public/panda_tpr.pdf, [PANDA Collaboration], 2005.
- [116] E. Tomasi-Gustafsson and M. P. Rekalo, Phys. Lett. B 504 (2001) 291.
- [117] <http://Fairroot.gsi.de/>
- [118] R. Brun and F. Rademakers, Nucl. Instr. Meth. A 389 (1997) 81-86.
- [119] I. Hrinacova *et al.*, Proc. of Computing in High Energy and Nuclear Physics (La Jolla) THJT00692X (2003).

- [120] CERN Program Library W5013 (1991).
- [121] S. Agostinelli *et al.* [GEANT4 Collaboration], Nucl. Instrum. Meth. A 506 (2003) 250.
- [122] D. J. Lange, Nucl. Instrum. Meth. A 462 (2001) 152.
- [123] A. Capella, U. Sukhatme, C. I. Tan, and J. Tran Thanh Van, Phys. Rep. 236 (1994) 225.
- [124] M. Bleicher *et al.*, J. Phys. G25 (1999) 1859.
- [125] A. Fontana *et al.*, International Conference on Computing in High Energy and Nuclear Physics (CHEP'07), Journal of Physics: Conference Series 119 (2008) 032018.
- [126] R. Kunne, Private communication.
- [127] M. Born and E. Wolf, "Principles of Optics", Oxford, Pergamon (1970).
- [128] M. Gumberidze, Private communication.
- [129] <https://ipngridwiki/wiki/Accueil>.
- [130] PANDA GRID sites: <http://serpiero.to.infn.it/map.jsp>
- [131] P. Buncic, A. J. Peters, P. Saiz and J. F. Grosse-Oetringhaus, CHEP 2004, Interlaken, Switzerland (2004) 440.
- [132] MonALISA portal, <http://monalisa.cern.ch>
- [133] P. Buehler, <http://panda-wiki.gsi.de/cgi-bin/viewauth/Computing/Productions>
- [134] P. Buehler *et al.*, http://www-panda.gsi.de/db/notesDB/PB12-131011_grid_etg-101013.pdf
- [135] M. Zambrana *et al.*,
<http://panda-wiki.gsi.de/pub/PANDAMainz/EventGenerators/note.pdf>
- [136] A. I. Ahmadov, V. V. Bytev, E. A. Kuraev and E. Tomasi-Gustafsson, Phys. Rev. D 82 (2010) 094016.
- [137] J. Van de Wiele and S. Ong, arXiv:1202.1114 [nucl-th], 2012.
- [138] G. I. Gakh, N. P. Merenkov and E. Tomasi-Gustafsson, Phys. Rev. C 83 (2011) 045202.
- [139] P. Golonka and Z. Was, Eur. Phys. J. C 45 (2006) 97.
- [140] E. Barberio and Z. Was, Comput. Phys. Commun. 79 (1994) 291.

BIBLIOGRAPHY

- [141] J. D. Jackson, Classical Electrodynamics, J. Wiley and Sons, New York (1975) 645.
- [142] A.D Sakharov sov. Phys Usp.34(1991) 375.
- [143] M. I. Eides, H. Grotch and V. A. Shelyuto, Phys. Rept. 342 (2001) 63 [hep-ph/0002158].
- [144] P. J. Mohr, B. N. Taylor and D. B. Newell, Rev. Mod. Phys. 80 (2008) 633.
- [145] R. Pohl, A. Antognini, *et al.*, Nature 466 (2010) 213.
- [146] I. Sick, Phys. Lett. B 576 (2003) 62 [nucl-ex/0310008].
- [147] R. J. Hill, G. Paz, Phys. Rev. D 82 (2010) 113005.
- [148] J. C. Bernauer *et al.*, [A1 Collaboration], Phys. Rev. Lett. 105 (2010) 242001.
- [149] J. Arvieux, Workshop on Production and Decay of light mesons Conference, Paris, 1988, Proceedings Ed. P. Fleury. Teaneck, N.J., World Scientific, 1988. 239p., 209-211.
- [150] Y. Shimizu *et al.*, J. Phys. Conf. Ser. 312 (2011) 052022.
- [151] V. Barone *et al.* [PAX Collaboration], arXiv:hep-ex/0505054.
- [152] T. O. Niinikoski and R. Rossmanith, Nucl. Instrum. Meth. A 255 (1987) 460.
- [153] P. L. Csonka, Nucl. Instrum. Meth. 63 (1968) 247.
- [154] F. Rathmann *et al.*, Phys. Rev. Lett. 71 (1993) 1379 .
- [155] C. J. Horowitz and H. O. Meyer, Phys. Rev. Lett. 72 (1994) 3981.
- [156] F. Rathmann *et al.*, Phys. Rev. Lett. 94 (2005) 014801.
- [157] D. Oellers *et al.*, Phys. Lett. B 674 (2009) 269 [arXiv:0902.1423 [nucl-ex]].
- [158] I. V. Glavanakov, Yu. F. Krechetov, A. P. Potylitsyn, G. M. Radutsky, A. N. Tabachenko and S. B. Nurushev, Nucl. Instrum. Meth. A 381 (1996) 275.
- [159] I. V. Glavanakov, Yu. F. Krechetov, A. P. Potylitsyn, G. M. Radutsky, A. N. Tabachenko and S. B. Nurushev, 12th International Symposium on High-energy Spin Physics (SPIN 96), Amsterdam, Netherlands, 10-14 Sep 1996; I. V. Glavanakov, Yu. F. Krechetov, G. M. Radutskii and A. N. Tabachenko, JETP Lett. 65 (1997) 131 [Pisma Zh. Eksp. Teor. Fiz. 65 (1997) 123].
- [160] S. M. Bilenkii, C. Giunti and V. Wataghin, Z. Phys. C 59 (1993) 475.
- [161] G. I. Gakh, E. Tomasi-Gustafsson, Nucl. Phys. A 761 (2005) 120.

- [162] D. Decamp *et al.* [ALEPH Collaboration], Phys. Lett. B 265 (1991) 430.
- [163] A. Heister *et al.*, [ALEPH Collaboration], Eur. Phys. J. C 20 (2001) 401.
- [164] E. Tomasi-Gustafsson, F. Lacroix, C. Duterte, G. I. Gakh, Eur. Phys. J. A 24 (2005) 419.
- [165] F. Iachello, A. D. Jackson and A. Lande, Phys. Lett. B 43 (1973) 191; F. Iachello and Q. Wan, Phys. Rev. C 69 (2004) 055204.
- [166] D. V. Shirkov and I. L. Solovtsov, Phys. Rev. Lett. 79 (1997) 1209.
- [167] G. I. Gakh, A. Dbeyssi, D. Marchand, E. Tomasi-Gustafsson and V. V. Bytev, Phys. Rev. C 84 (2011) 015212.

BIBLIOGRAPHY
